Stress-Responsive Nano- and Microcomposites Featuring Mechanophore Units

by

Elizabeth Nofen

A Dissertation Presented in Partial Fulfillment
of the Requirements for the Degree
Doctor of Philosophy

Approved May 2016 by the
Graduate Supervisory Committee:

Lenore Dai, Co-Chair
Aditi Chattopadhyay, Co-Chair
Heather Emady
Bin Mu
David Nielsen

ARIZONA STATE UNIVERSITY

August 2016

ABSTRACT

The problem of catastrophic damage purveys in any material application, and minimizing its occurrence is paramount for general health and safety. Thus, novel damage detection schemes are required that can sense the precursors to damage. Mechanochemistry is the area of research that involves the use of mechanical force to induce a chemical change, with recent study focusing on directing the mechanical force to embedded mechanophore units for a targeted chemical response. Mechanophores are molecular units that provide a measureable signal in response to an applied force, often in the form of a visible color change or fluorescent emission, and their application to thermoset network polymers has been limited. Following preliminary work on polymer blends of cyclobutane-based mechanophores and epoxy, dimeric 9-anthracene carboxylic acid (Di-AC)-based mechanophore particles were synthesized and employed to form stress sensitive particle reinforced epoxy matrix composites.

Under an applied stress, the cyclooctane-rings in the Di-AC particles revert back to their fluorescent anthracene form, which linearly enhances the overall fluorescence of the composite in response to the applied strain. The fluorescent signal further allows for stress sensing in the elastic region of the stress-strain curve, which is considered to be a form of damage precursor detection. This behavior was further analyzed at the molecular scale with corresponding molecular dynamics simulations. Following the successful application of Di-AC to an epoxy matrix, the mechanophore particles were incorporated into a polyurethane matrix to show the universal nature of Di-AC as a stress-sensitive particle filler. Interestingly, in polyurethane Di-AC could successfully detect damage with less applied strain compared to the epoxy system.

While mechanophores of varying chemistries have been covalently incorporated into elastomeric and thermoplastic polymer systems, they have not yet been covalently incorporated a thermoset network polymer. Thus, following the study of mechanophore particles as stress-sensitive fillers, two routes of grafting mechanophore units into an epoxy system to form a self-sensing nanocomposite were explored. These involved the mechanophore precursor and mechanophore, cinnamamide and di-cinnamamide, respectively. With both molecules, the free amine groups can directly bond to epoxy resin to covalently incorporate themselves within the thermoset network to form a self-sensing nanocomposite.

ACKNOWLEDGMENTS

I would first like to gratefully thank Dr. Lenore L. Dai, who has been an amazing source of mentorship, support, and inspiration not only throughout my Ph.D. studies, but during my undergraduate studies as well. I am not sure if I would have ever pursued a Ph.D. if I had not started working in her lab, so she has forever changed my life for the better and I could not be more grateful. I also acknowledge Dr. Aditi Chattopadhyay for serving as my co-advisor and allowing my research to more thoroughly integrate chemical engineering, material science, and mechanical engineering. I also gratefully thank my other committee members, Dr. Bin Mu, Dr. Heather Emady, and Dr. David Nielsen, for their support and insights regarding my research.

I have had the pleasure of working with every person that has been a part of Dr. Dai's group at ASU, and I would like to specifically thank those that have mentored me and gone before, including Drs. Huan Ma, Yanmei Song, Sriya Sanyal, Denzil Frost, Jin Zou, Mingmeng Zhang, Haobo Chen, and Prithwish Chatterjee. I have also enjoyed working with my peers and the new recruits: Stella Nickerson, Wei Gao, Ryan Gunckel, and Yifei Xu. I would also like to thank Bonsung Koo and Dr. Yingtao Liu for help with the Air Force and Army projects. I would also like to thank all of the students I have mentored throughout the years, specifically Conrad Hom, Jason Wickham, Nick Zimmer, and Avi Dasgupta for all of the long hours they helped me in the lab. It has been a privilege to work and collaborate with so many bright, passionate, and caring people, and I am deeply thankful for their contributions to my Ph.D. studies.

My wonderful friends and family have also been instrumental throughout my life, and especially during the challenges of graduate school. I would like to particularly thank

my husband Micah for being an emotional rock during this time, as well as providing me endless dinners and smiles. I would also like to acknowledge my mother, father, and sister, Catherine, Eric, and Michelle Walker, who have always maintained that I can do whatever I set my mind to and give me reason to excel at everything I do.

I would like to acknowledge the financial support from the Army Research Office, Grant Number W911NF1510072, Program Manager Dr. David Stepp, the Air Force Office of Scientific Research, grant number FA9550-12-1-0331, Program Manager Dr. David Stargel, and student support from the National Science Foundation Graduate Research Fellowship Program, and the ARCS Foundation as a Lawson Scholar. I would also like to acknowledge Dr. Bin Mu's Laboratory, the W. M. Keck Bioimaging Laboratory, the LeRoy Eyring Center for Solid Sate Science, and the Adaptive Intelligent Materials & Systems Center, all at Arizona State University, for facilities use.

TABLE OF CONTENTS

Page

CHAPTER Page

LIST OF TABLES

Table Page

LIST OF FIGURES

Figure Page

Figure Page

Figure Page

Figure Page

Figure Page

Figure Page

Figure Page

Figure Page

Figure Page

Figure Page

CHAPTER

1. INTRODUCTION

Composites pervade throughout all man-made applications, combining multiple material properties and functionalities to fulfill a targeted need. The push for smaller, more robust, “smart” sensing devices has shifted some focus away from macroscale composites and towards micro- and nanocomposites, to exploit the unique mechanical, interfacial, thermal, and electrical properties that occur at the smaller length scales [1-7]. Mechanochemistry encompasses the use of mechanical force to induce a chemical change, with specialized force-responsive molecular units, or mechanophores, being developed in the recent years to probe the mechanical nature of chemical bonds and realize reaction pathways not possible via alternative means [8-10]. The problem of catastrophic damage purveys in any material application, and minimizing its occurrence is paramount for general health and safety, with mechanochemistry offering a unique platform for the study of the precursors to damage and damage propagation. While many studies exist regarding thermoplastic and elastomeric polymer mechanochemistry, there has been limited study of mechanochemistry within the other branch of polymer chemistry, that being thermoset networks.

Chapter 2 contains the background and motivations for topics studied in this dissertation, focusing on multifunctional micro- and nanocomposites and mechanochemistry, and the intersection of these topics to yield the main work in this dissertation. Chapter 3 explains the methodology for the experimental preparation of mechanophore-embedded micro- and nanocomposites, the characterization methods of the composites, as well as an outline of the molecular dynamics simulation methodology presented.

Chapter 4 contains the results and discussion, beginning with the preparation of crosslinked cyclobutane-based mechanophore polymer-epoxy blends. This then leads into the creation of dimeric anthracene-based mechanophore particles for damage precursor detection in reinforced epoxy matrix microcomposites. As Di-AC had never been previously applied as a mechanophore and thermosets are rarely studied in mechanochemistry, this created an alternative avenue for study in the field. Under an applied stress, the cyclooctane-rings in the Di-AC particles reverted back to their fluorescent monomeric anthracene form, which linearly enhanced the overall fluorescence of the composite in response to the applied strain. The fluorescent signal further allowed for stress sensing in the elastic region of the stress-strain curve, which is considered to be a form of damage precursor detection. Overall, the incorporation of Di-AC to the epoxy matrix added the much desired stress sensing and damage precursor detection capabilities with good retention of the material properties. This section is then followed by a comparison of the dimeric anthracene experimental work and corresponding molecular dynamics simulations.

Following the successful application of Di-AC to an epoxy matrix, the mechanophore particles were incorporated into a polyurethane matrix to show the universal nature of Di-AC as a stress-sensitive particle filler. Interestingly, in polyurethane Di-AC could successfully detect damage with less applied strain compared to the epoxy system, and the underlying mechanisms regarding this improvement were probed and hypothesized to be due to enhanced interactions of the particles with the matrix, with possible surface grafting of the mechanophore particles to the polyurethane matrix. This chapter ends with the novel grafting of mechanophore units into a thermoset network polymer matrix. This study has the potential to open polymer mechanochemistry into new directions, as while

mechanophores of varying chemistries have been covalently incorporated into elastomeric and thermoplastic polymer systems, they have not yet been covalently incorporated a thermoset network polymer. Thus, two routes of grafting mechanophore units into an epoxy system to form a self-sensing nanocomposite were explored. The first involved the grafting of the mechanophore precursor molecule cinnamamide to the epoxy resin, with subsequent hardener addition and UV curing to form the mechanically sensitive cyclobutane rings. In the second route, the solution-made mechanophore di-cinnamamide grafted to the epoxy resin to allow for maximum cyclobutane concentration in the formed nanocomposites. The chemistry of the covalent bonding between the mechanophore units and the epoxy constituents was confirmed, and effect on the composite material properties was studied. Overall, there was successful formation of self-sensing nanocomposites with the early damage detection functionality achieved.

Chapter 5 includes a summary of the work on the novel development of stress-responsive, mechanophore-embedded nano- and microcomposites, as well as the proposed future work, damage detection via Fourier transform infrared spectroscopy sensing and "smart" metal-organic frameworks (MOFs). Appendices include work on particle self-assembly at ionic liquid-based interfaces including Pickering emulsions, pyrrole-based poly(ionic liquids) as efficient stabilizers for the formation of hollow MWCNT particles, experimental and molecular dynamics simulation work of iodide-based ionic liquid and water mixtures, and colloidal lattice preparation of environmentally responsive microgel particles at ionic liquid-water interfaces.

CHAPTER

2. BACKGROUND AND MOTIVATION

2.1. Multifunctional Nano- and Microcomposites

Composites are materials consisting of two or more differing components, and have been ubiquitous to human life, ever since straw and mud were first mixed to form crude bricks for building construction [11]. Concrete, a mixture of a cement binding agent and an aggregate filler, is the most widely used composite of the modern day, with roots in Ancient Rome [12]. The basic principle of composites is to achieve desirable material or functional properties not possible from the constituent materials alone. This guiding principle has made the use of composites not limited to building materials, but has opened up their use to a myriad of applications, including electronics and optics [13-18], membranes, medical devices and biological research [19-24], catalysis [25-28], energy harvesting and storage [29-35], among a multitude of others.

The structure of the individual components within a composite can vary greatly, and thus heavily influence its overall material properties and applications; examples include stacked layers, core-shell, interpenetrating networks, etc. [36-38]. However, arguably the most widespread composite structure is that of a bulk matrix component with secondary components incorporated into the matrix for reinforcement or some other functional use. Generally, these types of composites are named according to the material type of the matrix, and include ceramic matrix composites (CMCs), metal matrix composites (MMCs), and polymer matrix composites (PMCs). The secondary incorporated components commonly consist of either reinforcing particles or fibers, with a schematic of various composite types can be seen in Figure 2.1.1.

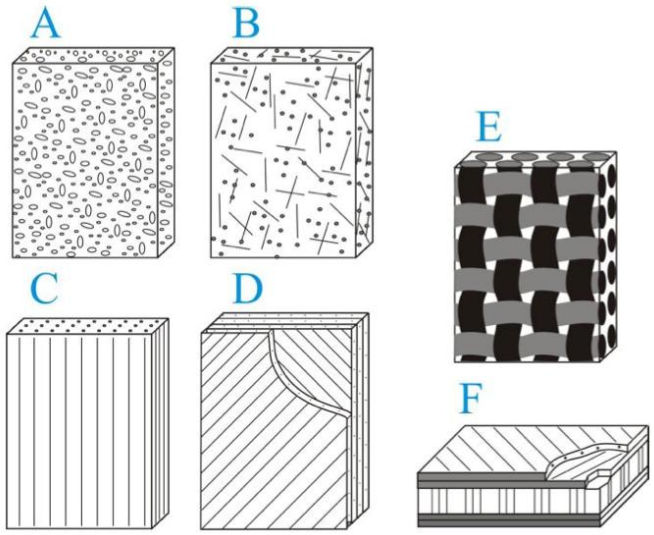

Figure 2.1.1. Schematic showing various composite types including: A. Particle reinforced composite, B. Chopped strand reinforced composite, C. Unidirectional fiber-reinforced composite, D. Fiber-reinforced laminates, E. Fabric-reinforced plastic, and F. Honeycomb structured composite. [39]

In fiber-reinforced composites, long or short, woven or unwoven fibers are incorporated into the matrix, with key examples including carbon fiber-reinforced composites (CFRCs) and glass fiber-reinforced composites (GFRCs). CFRCs and GFRCs typically utilize a polymer matrix and are currently used in various industries including aerospace, military, automobiles, structural materials, and consumer products [40]. Most notably, the transition of the size of the composite fillers from the macroscale to the micro- and nanoscales, allows for novel material properties and functionalities, and is the focus of many ongoing research efforts, moving the focus of the studies from macroscale composites to micro- and nanocomposites.

2.1.1. Microcomposites

Microcomposites are simply composites with components on the micrometer scale, or the composite itself is of this scale. As ubiquitous as composites are, microcomposites also fill novel use cases, including in many biological applications. For example, Chao et al. developed a microcomposite substrate to study the mechanical interactions between cells and a matrix, using lithography to create microfeatures in a polydimethylsiloxane (PDMS) and Collagen gel [41]. Zhang et al. created a novel ultra high molecular weight polyethylene (UHMWPE)-hyaluronan (HA) microcomposite for total joint replacements, adding HA to the traditionally used UHMWPE to decrease the friction, and thus improve the wear resistance [42]. The researchers Naik and Carpenter developed microcomposites for the targeted released of cancer drugs by coating magnetic iron core nanoparticles with a fluorescent dye, the biodegradable polymer poly(D,L-lactide-co-glycolide) (PLGA), and poly(vinyl alcohol), to form composite particles [43]. The fluorescent dye acted as a drug mimic and allowed for particle tracking and evaluation of drug release, as it can be quenched by the iron nanoparticles, the iron core nanoparticles allow for localized heating of the composite when microwaves are applied, and the degradation of the PGLA is what allows for the ultimate drug release. The goal of the entire functional microcomposite being to eliminate side effects caused by very potent cancer drugs by delivering these biodegradable particles directly to the cancer site for maximum effectiveness.

An important subcategory includes particle-reinforced composites (PRCs), in which matrixes are reinforced by particle fillers, and are ubiquitous for overall property enhancement in a wide variety of applications. Examples utilizing microparticles include

microelectronics packaging [44], polymer electrolyte membrane (PEM) fuel cells [45], and the aerospace, automotive, and construction industries [46], due to the virtually unlimited combination of matrix and particles, and the wide variety of particle types and properties.

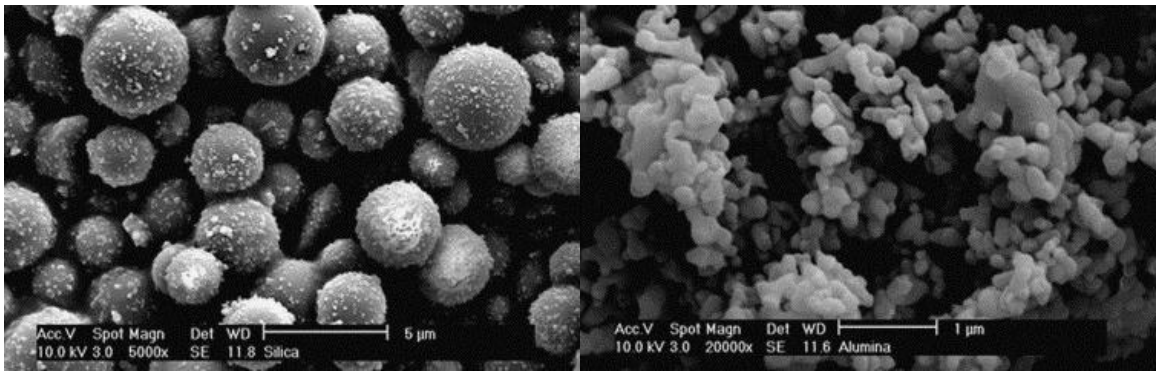

Figure 2.1.1.1. SEM images of common microparticle fillers with silica particles in the left image and alumina particles in the right image. [47]

For a more detailed particle-reinforced composite example, in microelectronics packaging, underfill is used between the microchip and the substrate to minimize thermal stresses due to the coefficient of thermal expansion (CTE) mismatch between the microchip and the substrate and to provide mechanical reinforcement of the solder joints, with the underfill usually being comprised of an epoxy polymer matrix and micro-sized particle fillers. Epoxy is a 3D network polymer thermoset commonly formed by reacting of an epoxide-containing resin with an amine-containing hardener, with both the resin and hardener having multiple reactive sites in order to form the 3D network. Thermosets generally have good mechanical properties, but have the drawback of not being able to be thermally re-processed, like their thermoplastic polymer cousins. Microparticle fillers commonly utilized in underfill include silica and alumina [47, 48]. Scanning Electron

Microscopy (SEM) images of these two common fillers can be seen in Figure 2.1.1.1, with the silica fillers being spherical and having a mean size of 3 μm and the alumina fillers having a polygon shape and a 1 μm mean size. The filler is added to the epoxy matrix to lower the overall CTE of the underfill, provide additional mechanical reinforcement and thermal stability, as well as lower the overall cost [49, 50].

In addition to the particle-reinforced microcomposite scheme, microcomposites can take the form of microparticles, commonly as functional nanoparticles incorporated into a microparticle matrix or as core-shell structures of differing materials. Titanium dioxide (TiO_2) is often utilized in nanoparticle form for its semiconducting and photocatalytic properties, nanoparticles are used instead of a bulk form as this increased the surface area for the reactions to occur. However, one issue with using TiO_2 or other nanoparticles is their tendency to aggregate, thus it can be desirable to embed the nanoparticles into a matrix to maintain the surface area. Coutinho and Gupta performed this by embedding TiO_2 nanoparticles into temperature responsive microgels of poly(N-isopropylacrylamide) with interpenetrating linear chains of poly(acrylic acid) (PAAc), with the PAAc serving to assist the loading of the TiO_2 particles within the microgels [51]. The loading of the TiO_2 was able to be varied from 10 – 75 wt%, and the composites showed rapid destabilization, allowing for facile particle recovery over that of pure TiO_2 nanoparticles. Coutinho and Gupta then added to the work by showing that the TiO_2 microcomposite gels could additionally degrade methyl orange via photocatalysis, with the reaction kinetics depending strongly on the pH affecting the TiO_2/PAAc/methyl orange interactions [52].

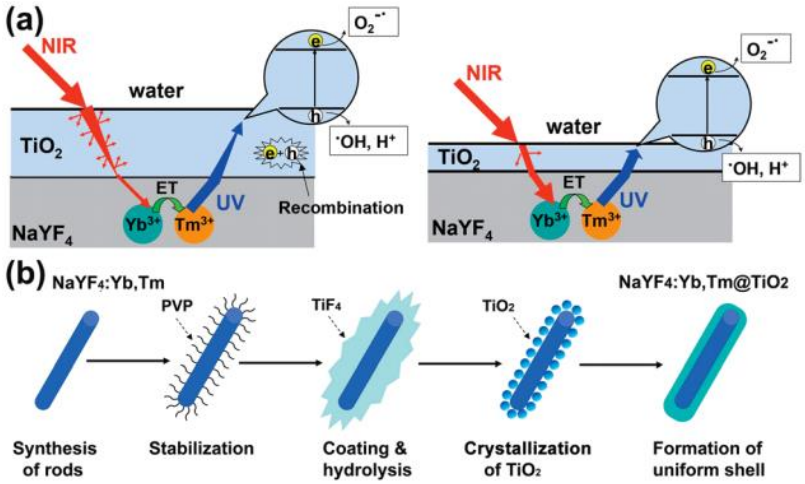

Figure 2.1.1.2. (a) Photocatalysis process with upconversion for left: a thick TiO_2 shell, right: a moderate TiO_2 shell. (b) Synthesis of the TiO_2-$NaYF_4$:Yb,Tm core–shell composites. [53]

The band gap of TiO_2 is such that it can only absorb UV light, thus many studies focus on tuning this towards the visible light spectrum, or others. Zhang et al. combined the study of lanthanide-doped materials, which can upconvert near infrared (NIR) light to UV light when properly doped, with TiO_2, to allow for the semiconductor to take advantage of this alternative spectrum of light [53]. The authors first synthesized lanthanide-doped $NaYF_4$ microrods and nanorods ($NaYF_4$:Yb,Tm), added a poly(vinylpyrrolidone) (PVP) coating, a TiF_4 Titanium precursor, with subsequent hydrothermal heating to form the TiO_2 shell, with the shell thickness playing a key role to the photocatalytic conversion (Figure 2.1.1.2). Other microcomposites designed specifically for enhanced visible light photocatalytic activity for degrading organic dye and wastewater treatment include Ag_2CO_3/CeO_2, $Ag/Ag_2O/Ag_2CO_3$, $Cu_2O/Cu_{31}S_{16}$, Ag/Cu_2O, SnO_2/reduced graphene oxide (GO), and graphene/$Bi_2O_2CO_3$ [54-59].

In the area between micro- and nanocomposites, materials from both scales can be applied in composites simultaneously to exploit their individual benefits. Tsekmes et al. probed this by adding less than 1 vol% hexagonal boron nitride and cubic boron nitride nanoparticles fillers to epoxy with 60% alumina and silica microparticles [60]. The group showed that when this small amount of nanoparticle fillers were added to the epoxy microcomposite, higher AC and DC breakdown strengths were achieved, as well as higher thermal conductivities compared to analogous microcomposites without the nanofillers. The group attributed these phenomena to interactions between the nano- and microfillers, as well as the polymer matrix, with the chemical bonds formed between the nanoparticles and matrix decreasing the mismatch in the phonon vibrations and phonon scattering at the interfaces between the materials, and the nanoparticles possibly bridging the gaps between the microparticles.

2.1.2. Nanocomposites

The scaling of the composite constituents from the microscale to the nanoscale drastically affects their properties and resulting applications. Our group pioneered a one-step core-shell composite nanoparticle synthesis method via a Pickering (solid-stabilized) emulsion technique, to first create core-shell polystyrene (PS)-silica composite nanoparticles, and to later use styrene and the thermo-responsive monomer N-isopropylacrylamide (PNIPAAm) as co-monomers to synthesize thermoresponsive PS/poly(NIPAAm)-silica core-shell nanocomposites which could release a drug loaded into the nanocomposite cores via “nanopump” action caused by a thermally driven particle size change [61-63]. These core-shell particles were able to be uptaken by human prostate cancer (PC3 and

PC3-PSMA) cells because of their nanosize, similarly formed micro-sized particles would have been too large in relation to the cell size, and thus ineffective for the desired targeted drug delivery. In this way, the size scale of the composite for the application can play a key role to its overall effectiveness.

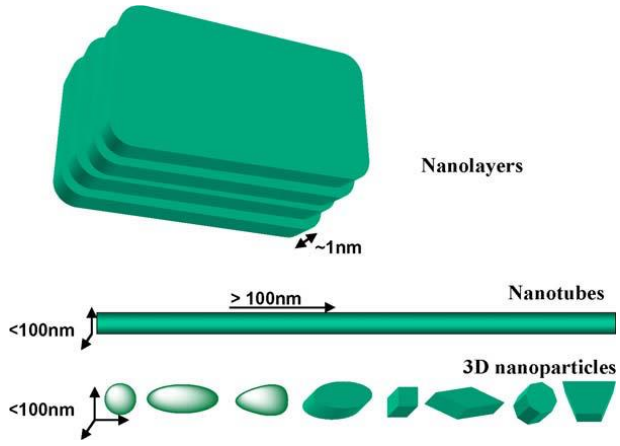

Figure 2.1.2.1. Schematic showing differing types of nanomaterials that can be incorporated into nanocomposites. [64]

Thus, nanocomposites are simply composites with one constituent on the nanometer scale. They can either have the structure of nanoparticles, as in the above core-shell example, or they can exist as bulk macroscale samples, with nano-features incorporated into it. In addition to simple spherical nanoparticles, other nanomaterials commonly incorporated into nanocomposites can be seen in Figure 2.1.2.1, and include nanolayers, nanotubes, and various shapes of nanoparticles, which considered 2D, 1D, and 0D, respectively. In terms of polymer matrix nanocomposites, the seminal work occurred in 1993 by a group of Toyota researchers in which they synthesized nanocomposites with a nylon-6 polymer matrix and montmorillonite (MMT) clay platelets intercalated or exfoliated inside [65]. Compared to the neat polymer, the nanocomposite had a 2 to 4-fold in-

crease in the Young's modulus with filler loadings of only 3 to 6 wt%, which would have required loading of 25 to 30 wt% filler in similar microcomposites [66]. These mechanical improvements of nanocomposites are attributed to the extremely large aspect ratio due to the nanosize of the fillers and strong polymer filler interactions that affect the load transfer between the polymer and nanofiller [67]. In addition to the aspect ratio, the characteristic size of the nanofillers, as well as their surface chemistry and surface charge density are key factors effecting the interaction and resulting properties of the nanocomposites. Nanocomposites featuring organoclay fillers are still widely studied, and various processing techniques as well as matrix and filler chemistry have been explored, including in epoxy matrices [68-70].

Table 2.1.2.1. Various nanofiller attributes and their resulting applications. [66]

Particle type	Particle shape and size	Applications
Carbon black	Sphere, radius $R \sim 20$ nm (primary particles)	Conductive coatings and paints
	Fractal aggregates (secondary clusters)	Automotive sealants and adhesives
Carbon nanotubes	Rods, length $L > 100$ nm, thickness $T \sim 1$ nm	Conductive coatings and materials
Silica particles	Spheres, radius $R \sim 5$–100 nm	Toughened, flame retardant polymer materials
Nanoclays	Platelets, width $H \sim 50$–5000 nm, thickness $T \sim 1$ nm	Hardened, toughened, flame retardant polymer materials
Metal (Au, Ag, Pt) nanoparticles	Spheres, radius $R \sim 2$–100 nm	Sensors, electronic applications, catalysts

Additionally, the interfaces between the particles and the matrix in particle-reinforced composites can allow for unique functionalities including the conversion between heat and electricity to create thermoelectric materials [71, 72]and for unique organic−inorganic hybrid solar cells featuring a conjugated polymer matrix and nanocrystal

particles [73]. A summary of additional commonly studied nanofillers with some example applications can be found in Table 2.1.2.1, and range from toughened and flame retardant materials to conductive coatings to sensors, electronic applications, and catalysis.

Due to these interesting properties of nanocomposites, much work is being done in the simulation realm to better explain what is happening at the nanoscale to correlate it with the macroscale properties. This includes molecular dynamics (MD) simulations, in which a direct method is used to solve Newton's equations of motion with the atoms interacting through various interatomistic potentials [64]. MD can identify atom positions, velocities, and forces and use them to calculate various other parameters such as density, Young's modulus, glass transition temperature, diffusion constants, etc., when initial conditions, interaction potentials, and the time scale for the simulation are properly set [74, 75]. Other modeling efforts for nanocomposites include analytical modeling, especially of the stiffness, and finite element modeling (FEM) using continuum methods [76-79].

Referring back to the nanomaterials seen in Figure 2.1.2.2, namely, nanolayers, nanotubes, and nanoparticles, these can correspond to the carbon derivatives: graphene, carbon nanotubes, and bucky-balls/nanodiamond/graphene oxide, respectively, which are commonly used to create various functional nanocomposites [80-82]. Graphene is the 2D allotrope of carbon that is one atomic layer thick and in which all of the atoms are sp^2 hybridized with delocalized electrons present on its surface. Graphene is the building block for all other graphitic materials, as seen in Figure 2.1.2.2. Graphene provides many desirable properties to nanocomposites when they are incorporated, including sensing capabil-

ities and improved mechanical and thermal properties, and thus this is the focus of much research [83, 84].

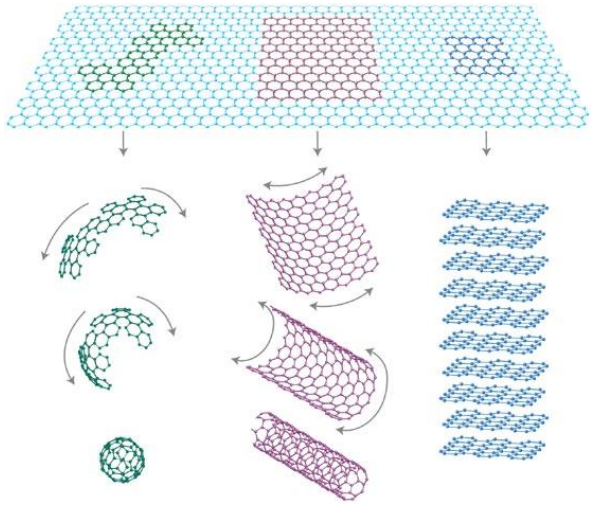

Figure 2.1.2.2. Schematic showing how graphene is the building block of all graphitic structures. From left to right: buckyball, carbon nanotube, and 3D stacked graphite. [85]

The incorporation of carbon nanotubes (CNTs) into nanocomposites has additionally attracted attention, especially incorporated into polymer matrices, due to the unique mechanical, thermal, and electrical properties of both the CNTs and the resulting composites [86, 87]. CNTs can exist as single-walled carbon nanotubes (SWCNTs), which can be thought of as a single layer of graphene rolled into a tube, as seen in Figure 2.1.2.2, or as multi-walled carbon nanotubes (MWCNTs), in which many layers of carbon nanotubes are contained concentrically within each other. Khare et al. used MD simulations to study the interactions of SWCNTs in an epoxy matrix at the nanoscale to make correlations with the calculated bulk properties [88, 89]. The group found that the addition of dispersed, pristine CNTs caused lowering of the glass transition temperature (Tg) and Young's modulus, due to the interface region being compressible and behaving like a

polymer thin film, which is the opposite result of what would be expected. The use of aggregated CNTs affected these properties less, as there were less interfaces present. The group then functionalized the CNTs with amine groups so that the CNTs would be grafted into the epoxy matrix, and found that the Tg was slightly higher than the neat epoxy, and that there was a great increase in Young's modulus overall with functionalization. Thus, the interaction of the nanofiller with the matrix was found to be crucial in terms of the overall properties.

Due to their remarkable thermal, mechanical, and electrical characteristics and low mass density, carbon nanotubes are a material of interest in a diverse set of fields. However, agglomeration of the nanotubes and their incompatibility with polymer matrices encompass some of the major challenges in their employment in many proposed applications, especially in the field of nanocomposites [90-93]. The fundamental limitations of carbon nanotubes highlight the need to focus on efficient methods for stable CNT dispersion, without reducing their desired thermal, mechanical, and electrical properties. This is because stable liquid-phase dispersions of CNTs allow for facile processing of the nanotubes for incorporation into composites.

Broadly speaking, there are two approaches to disperse CNTs: first is the mechanical dispersion method, and the second is the alteration of the surface energy of the CNTs, either physically through non-covalent treatment, or chemically by the means of covalent bonding. Previously, most of work related to dispersion of CNTs (both single walled and multi-walled) has focused on high-powered ultrasonication for dispersing the materials by using a high shear rate. The major drawback of such an approach is the decreased aspect ratio of the nanotubes during the high shear mixing process as well as lim-

ited stability [94]. Chemical methods, particularly the covalent treatment method, offer highly stable dispersions due to the chemical functionalization to increase the surface energy, providing repelling forces in between individual nanotubes, with acid groups being a common functionalization scheme [95, 96]. Although this method is efficient, it can cause structural defects in the graphene network of the nanotubes, which can significantly reduce the performance of the CNTs and their potential applications. These defects occur due to the aggressive nature of the chemical method, which includes high reaction temperatures and long reaction times, as well as the added surface pendant interrupting the π-electron cloud of the CNTs [97]. In this context, non-covalent treatment offers an appealing route to disperse CNTs, mitigating the need for harsh thermal or mechanical treatments and allowing the crucial π-electron cloud of the graphitic nanotube structure to remain completely intact.

Non-covalent surface treatment for CNT dispersions generally comprises of utilizing different types of stabilizers, typically surfactants having both a hydrophilic and hydrophobic group, which are known to facilitate the homogenization of CNTs [94, 98, 99]. One of the major drawbacks of surfactant-based stabilization is large quantity of stabilizers that must be added in relation to the amount of CNTs to prevent the aggregation. Secondly, most of the known surfactants used for this application do not share the same properties as CNTs, e.g. high conductivity or thermal stability, which interrupts the inherent properties and applications of the nanotubes when these molecules wrap around them. A new option to lessen the effect of the above disadvantages is to use ionic liquids (ILs), which are comprised solely of ions and are liquids below 100 °C, as alternatives to create stable dispersants of nanotubes. Recently, Fukushima et al. demonstrated this by

dispersing CNTs in different ionic liquids [100]. However, this mechanism of non-covalent wrapping of the CNTs in ILs does not yield very stable dispersions in water or organic solvents, which is key to their facile incorporation into nanocomposites.

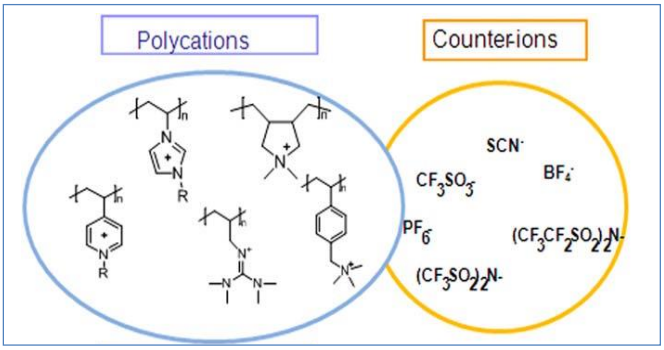

Figure 2.1.2.3. Representative chemical structures of the common cation-polymerized PILs. [101]

Polymerized ionic liquids (poly(ionic liquids), PILs) feature a polymer backbone and pendant ionic liquid groups (Figure 2.1.2.3) and can offer enhanced stability over ionic liquids for CNT dispersions. This is attributed to the longer chains of the PILs, which are hypothesized to aid in the wrapping of the CNTs and lead to more stable dispersions [102]. Apart from the stability, PILs also offer extraordinary versatility in terms of hydrophilicity/hydrophobicity, a key factor for utilizing CNTs in different liquid systems. The polarity of the PILs can be tuned by simple anion exchange reactions to produce PILs of the same polymer backbone with a variety of anions, thus PILs can be solubilized in water to many different polar and nonpolar organic solvents corresponding to the polarity of the selected anion. If this phenomenon can be applied to CNTs, it is expected that CNT dispersion in various polar and nonpolar solvents can be created for application into nanocomposite processing.

2.2. Mechanochemistry

Mechanochemistry is the area of chemistry that involves the use of mechanical force to induce a chemical change, separate from the other well-studied areas of thermochemistry, electrochemistry, and photochemistry [103]. Mechanochemistry offers the materials chemist alternative routes to obtain desired products, as the use of mechanically active groups can allow for reaction pathways not possible with traditional thermal or light-driven reactions [8]. A thorough review of the history of mechanochemistry by Dr. Laszlo Takacs can be found in Reference [104], with mechanochemistry present in the first civilizations through making fire by friction or using flint, to a 315 B.C. reference of the ancient Greeks reducing cinnabar to mercury by grinding in a copper mortar with a copper pestle, and a 1820 paper by Faraday describing the "dry way" of reducing of silver chloride by grinding with zinc, tin, iron, and copper in a mortar.

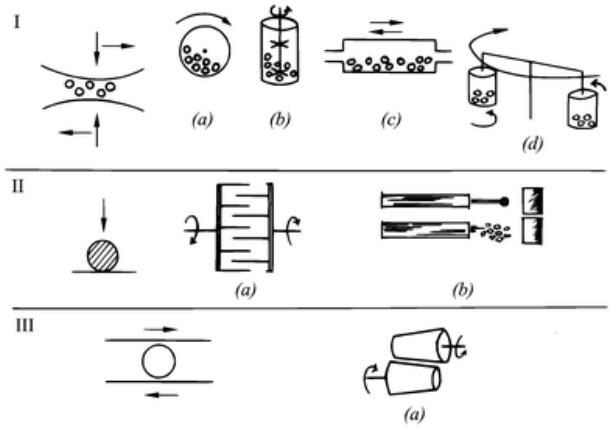

Figure 2.2.1. Different devices for mechanical treatment: I: shear and impact (a: ball mill, b: attritor, c: vibration mill, d: planetary mill); II: impact (a: pin mill, b: jet-mill); III: shear (a: rollers). [105]

As mechanochemical reactions are arguably less obvious that those carried out intentionally with heat, light, or electricity, the development of mechanochemistry occurred

in a somewhat disconnected fashion, with differing elements and applications of the field still being reconciled in modern science [105]. Due to this, different facets and research directions of mechanochemistry are notably separated in the literature in what can be thought of as two large groups, the first focusing on the different types of mechanical forces that can induce the chemical changes as a reaction mechanism (i.e. ball milling, grinding [106-108]and the other examples seen in Figure 2.2.1), with the second involving the conscious design of stress-sensitive chemistries and materials to act as signals for applied mechanical forces, such as in the relatively new and exciting field of polymer mechanophores, to be discussed below [109-111].

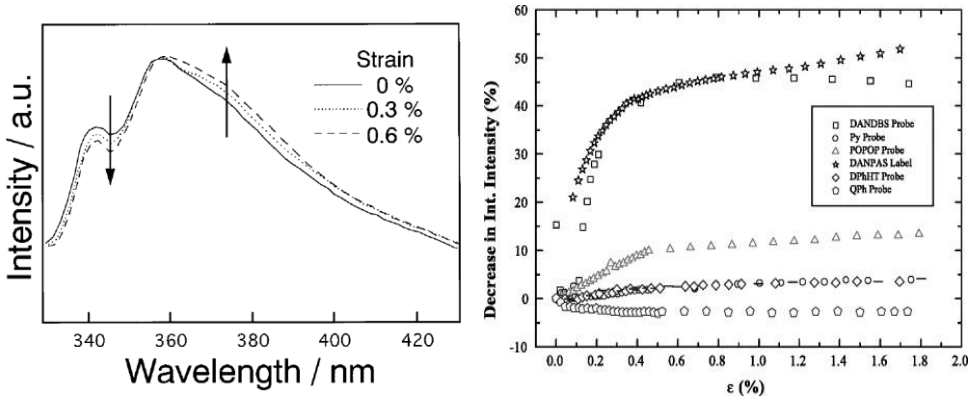

Figure 2.2.2. Left: Steady state emission spectra for the PVCz-PS film. Right: Fluorescent response of a variety of fluorophore labels in response to strain. Adapted from References [112, 113].

Mechanochromism refers to the specific phenomena of mechanically induced color changes, generally caused by incorporated chromophores or fluorophores, which show a visible light or fluorescent response to a mechanical force, respectively [114]. Fluorescence is well understood, and occurs when a suitable excitation wavelength of light excites the fluorophore from its electronic ground state to an electronic excited state

to form an excimer. The electronic excited state will then quickly fall back down to the ground state, releasing less energy that was initially applied, resulting in a photon of a longer wavelength of light, or the measured fluorescence emission [115].

As the electronic energy bands are defined by the confirmation and structure of the fluorophore, various fluorophores will have varying emission spectra and intensity of the emission, which can be observed by a fluorescence microscope or fluorometer. Fluorescence is a common property of organic molecules possessing a conjugated network, that is delocalized π-bonding in which the electrons in the p-orbitals are free to move throughout the molecule, e.g. in aromatic rings. In general, a larger conjugated system corresponds to greater fluorescent properties for the molecule. For mechanochromic species, different excimer complexes can form based on the different interactions of the fluorophore molecules when subject to induced stress or strain. Specifically, with fluorophores such as poly(N-vinylcarbazole) (PVCz), different excimers exist depending on whether there is a partial or full overlap of the carbazole groups on the polymer backbone. These excimer confirmations can be induced by changes in the local mechanical environment, and thus these fluorophores can act as a molecular sensor for applied strains, by way of changes in their fluorescent emission, as seen in Figure 2.2.2 [113]. This method can be used to non-invasively identify residual stresses and strains within polymeric materials, such as the PVCz in a PS film in Figure 2.2.2, but as the mechanism simply functions by molecular overlap and no change in the chemical bonding of the system, the fluorescent signal change disappears when the applied strain is removed [115]. In Figure 2.2.2 (right), various fluorophore probes or tags were incorporated into an epoxy matrix and the change in fluorescence intensity with an applied strain was ob-

served, simultaneously, as otherwise no change would be observed [112]. For most of the fluorophores used, there was a marked decrease in the fluorescence intensity, with one probe showing a slight increase; overall, the probe 1,4-bis(5-phenyloxazol-2-yl)benzene (POPOP) was found to have the greatest response to the applied strain.

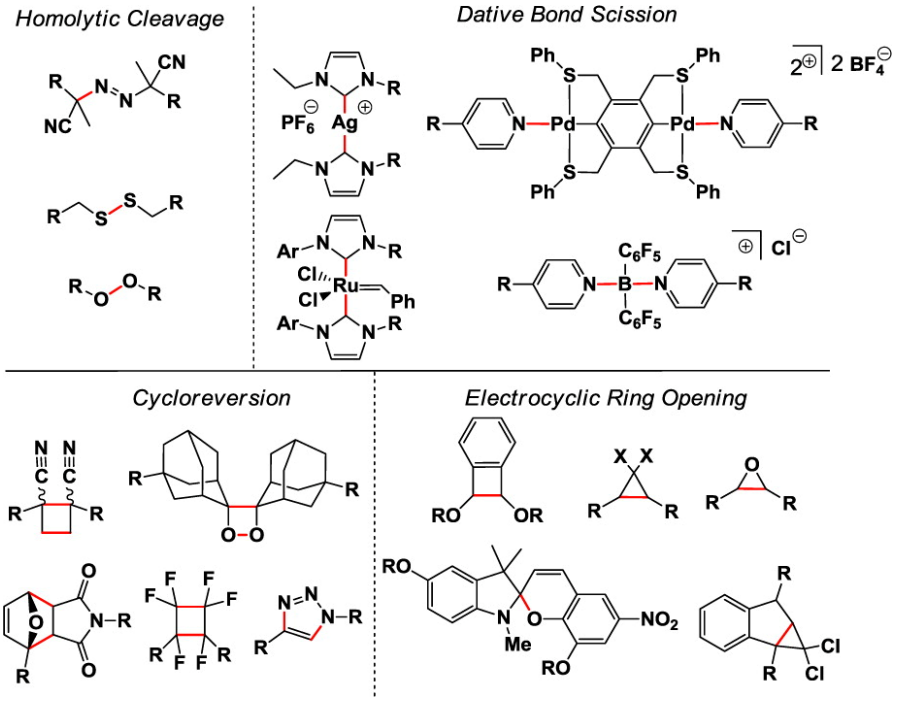

Figure 2.2.3. Generalized examples of mechanophores, with the mechanically active bonds highlighted in red. R = site of polymer attachment; X = F, Cl. [116]

Mechanophores are molecular units that undergo selective bond scission in response to an external force to provide a measureable signal to correlate to the applied force for a targeted chemical response [116-120]. The bond scission mechanism for mechanophore activation is what separates this group from the above described mechanochromic materials, as the chemical structure of latter chromophores/fluorophore tags remains intact during the mechanical response. Examples of mechanisms for various mechanophores can be found in Figure 2.2.3, and are categorized according to the func-

tional bonds, including targeted homolytic cleavage of the weaker bonds in a structure, dative bond scission for specialized bonds with inorganic elements, cycloreversion to break a cyclic ring and revert back to two separate molecules, and electrocyclic ring opening in which then ring opening retains the single molecule structure.

A recent offshoot to the mechanochemistry field is that of mechanobiochemistry, or the study of mechanically responsive biomacromolecules or biomaterials [121, 122]. In 2013, Makyla et al. published the first utilization of a fluorescent protein as a mechanophore in a polymeric material, namely at the interfaces of glass fibers and epoxy in glass fiber-reinforced composites [123]. The group used enhanced yellow fluorescent protein (eYFP) as a link between glass surfaces and epoxy, and when there was interfacial debonding of the fibers from the epoxy matrix, the proteins mechanically unfolded, causing a measurable loss of fluorescence to correlate with the applied damage. The same group then applied the eYFP to carbon fiber-reinforced epoxy composites, and were able to detect damage by the same mechanism [124]. However, the group only used single carbon fibers in a very thin 1.5 mm thick epoxy, in a full carbon fiber-reinforced composite, the black color of the fibers would likely quench any change in fluorescence. The group did discuss this issue and noted that at least 50% of the fluorescence was reduced when the fibers were incorporated into the composite, however, the protein-based mechanophores did perform better in terms of quenching when compared to the chosen reference fluorophore, amino-fluorescein, the latter being completely quenched on the carbon-fibers [124].

However, the main thrusts of mechanochemistry have been in the synthetic and material science realm, with much work in using mechanophores for sensing in polymer

mechanochemistry. An important breakthrough in the mechanophore field was made by the research group of Dr. Jeffrey Moore at the University of Illinois at Urbana-Champaign with the synthesis of spiropyran (SP)-embedded, elastomeric poly(methyl acrylate) (PMA) chains, with the SP units acting as force sensors in response to tensile loading [10]. Tensile testing and simultaneous optical spectroscopy were applied to examine the force-induced 6-electrocyclic ring-opening reaction from colorless spiropyran to colored merocyanine, resulting in a mechanically-induced visible color change, as seen in Figure 2.2.4. In the same journal article, the group additionally showed that SP could act as a functional mechanophore crosslinker in glassy poly(methyl methacrylate) (PMMA) beads [10]. As the mechanically-induced signal from SP is visible to the naked eye, many groups have used it as their mechanophore of choice in various elastomeric or thermoplastic polymer systems, including in as crosslinkers in PMMA[125], in rubber-toughened PMMA [126], and in networked elastomeric poly(dimethylsiloxane) (PDMS) [127].

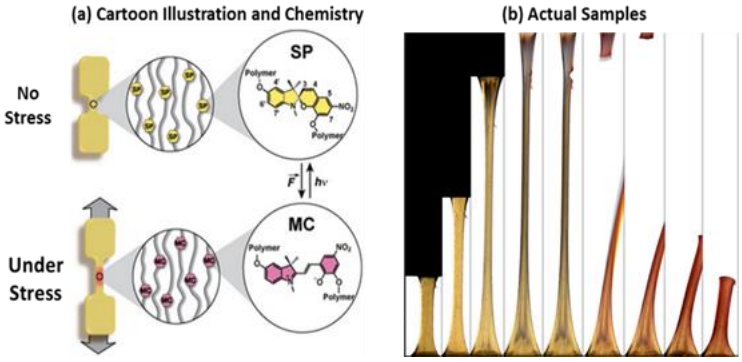

Figure 2.2.4. (a) Cartoon illustration of the activation of spiropyran mechanophores in a poly(methyl acrylate) matrix. (b) Optical images of the corresponding dog-bone samples during a tensile test. [10]

Photoirradiation as a reaction pathway, is very important, as selective, targeted excitation with UV–vis irradiation can initiate chemical reactions not otherwise possible thermally, or by other methods, or reactions which would have less efficiency due to unwanted side reactions or other effects [128]. Cycloaddition via photodimerization is a well-known mechanism, in which certain monomeric structures can dimerize into cycloalkane rings, such as cinnamoyl groups into cyclobutane via [2+2] cycloaddition [129]. The relatively facile reaction pathway of cycloaddition has been exploited to study a number of phenomena, including exploitation of the fact that photodimerization of cinnamate derivatives is enhanced in micelle solutions, with the stereochemistry of the cyclodimers being found to change with a change in the aggregated structures, allowing them to be excellent probes for determining molecular orientations [130]. Cyclobutane rings formed from the photodimerization of cinnamoyl groups can also act as mechanophore units, with the strained rings reverting back to their fluorescent, monomeric cinnamoyl form after an applied stress, as seen in Figure 2.2.5 [131-133].

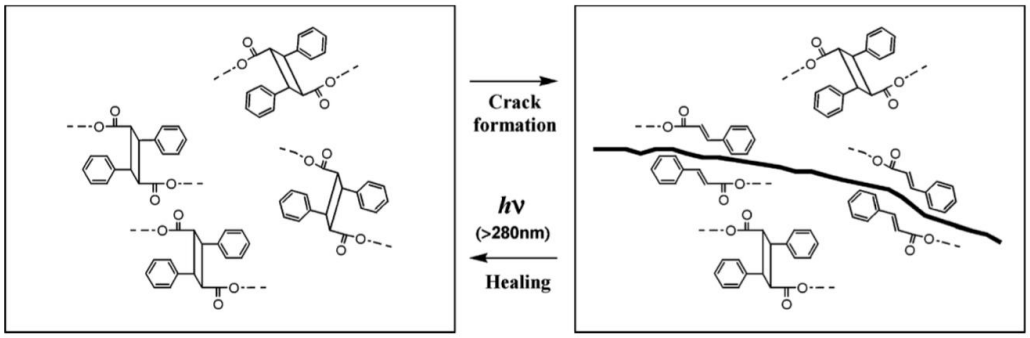

Figure 2.2.5. Left: Schematic showing polymerized cyclobutane mechanophores before an applied force/crack, Right: Reversion to fluorescent cinnamoyl groups along damaged area/crack, and healing to the left image upon the application of UV light. [132]

The strained cyclobutane ring structure has been used as a mechanophore in a number of other studies, including to produce a mendable poly(butylene adipate) network by functionalization with cinnamoyl groups [134], as masked cyanoacrylate functional groups [135], and as various mono- and di- cyano-substituted (and without cyano groups) cyclobutanes to study the collapse of cavitation bubbles [136, 137]. Cyclobutane mechanophores most commonly go through cycloreversion to create two separate alkene containing molecules in response to the applied stress. Additionally, cyclopropane has been used as mechanophores due to the greater strained nature of the ring, generally following an electrocyclic ring opening mechanism due to the small structure of the ring [138, 139].

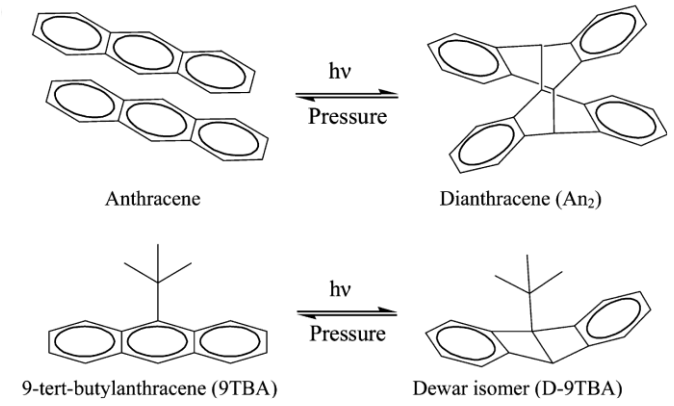

Figure 2.2.6. Top: [4 + 4] Cycloaddition of anthracene to di-anthracene. Bottom: Photoisomerization of 9-tert-butylanthracene to its Dewar isomer. [140]

Anthracene, consisting of three fused benzene rings, is a commonly used fluorophore due to its strong fluorescent signal and ease of incorporation into different molecular structures due to its carboxylic acid and other derivatives [141, 142]. Its large conjugated structure also allows for its incorporation into many optical-driven fields, including liquid crystals [143]. Upon application of UV light, anthracene derivatives can photodimerize into a number of structures, some specifically for shape memory [144] and self-

healing applications [145]. In a few recent studies, anthracene moieties have also been used as mechanophore precursors, as they have a much higher absolute fluorescence quantum yield compared to other mechanophores, and a large conjugated system, which brings the excitation/emission to longer wavelengths [146].

Anthracene derivatives can form a variety of mechanochemically active species including strained Dewar isomers in 9-tert-butylanthracene and a cyclooctane-type dimer, as seen in Figure 2.2.6 [140, 147], two cyclobutane rings via [4 + 4] cycloaddition of cyclophane bis-anthracene [148], and retro Diels-Alder reactions [127, 149]. Diels-Alder cycloadditions are primarily thermal and photochemical driven, with anthracene being able to participate in [4+2] cycloadditions with a variety of dienophiles due to its conjugated structure [150]. Retro Diels-Alder reactions, as in the previously mentions mechanically active examples, release the small molecule dienophile, resulting in a measurable signal change [151, 152]. However, these anthracene derivatives, including the force-responsive ones, have previously only been studied in solution, films, or elastomers; leaving room open for their novel application in other schemes with new chemistries.

2.3. Motivation of Work

The problem of catastrophic damage purveys in any material application, and minimizing its occurrence is paramount for general health and safety. Thus, the ability to sense applied damage and correlate it with a measurable signal is extremely desirable. Micro- and nanocomposites build on the functionality of traditional composites by providing novel functionalities and materials properties due to the shrinking of the length scales, including applications in photo and chemical catalysis, energy conversion, small

molecule sensors, barrier and anticorrosion materials, among many others [153-155]. Mechanochemistry is the field at the intersection of chemistry and mechanical engineering, allowing for the novel development and employment of unique stress-responsive materials targeted towards damage monitoring and recovering damage [156]. The use of mechanophores, molecular units that change chemically in response to an applied force, can allow for novel damage detection schemes through their ability to act as stress sensors in various polymer matrices [157, 158]. It is worthwhile to note that the previously mentioned work on spiropyran, cyclobutane/cyclopropane, and anthracene as mechanophores exclusively involve solutions, thin films, or elastomeric/thermoplastic matrices, and there is a notable gap in the literature concerning thermoset polymer systems and engineering composites, including nanocomposites, microcomposites, and fiber-reinforced composites [110, 111, 119]. Additionally, our target is damage precursor or early damage detection, so that the damage identification can occur well before ultimate material failure, so that the material can be repaired or replaced before catastrophic damage occurs. For the polymer composites studied, this damage detection must then occur before the yield point in a stress-strain curve, that is, in the linear elastic region. In this region, when the applied stress is removed, the sample returns to its original state, akin to the deformation of a Hookean spring. After the yield point, plastic deformation of the material occurs, correlating to irreversible damage than cannot be recovered. It is crucial to be able to detect damage precursors before this irreversible material damage is sustained.

Simple mechanochromic fluorophores would not be appropriate for this desired damage detection scheme, as the fluorescent signal change generated by the excimer formation only occurs when the damage is applied, reverting back to the initial state upon

removing the applied stress [112, 113]. For the damage precursor detection, it is desired that crack nucleation can be observed, and for that, the signal alluding to the damage needs to remain present after the sample has been damaged. Thus, mechanophores, which undergo bond scission under an appropriate mechanical force, would be more appropriate for this scenario as the chemical-mechanical activation mechanism can be thought to be irreversible due to the resulting chemical structure change. Thus, we have chosen to study cycloalkane-functional mechanophores that operate via cycloreversion upon damage to yield fluorescent signals. In our earlier work, we began by focusing on applying mechanochemistry to thermoset systems by creating self-sensing polymer blends of cyclobutane-based mechanophores and epoxy [159]. The two crosslinked cyclobutane-functional mechanophores studied were from the precursors 1,1,1-tris(cinnamoyloxymethyl) ethane (TCE) and poly(vinyl cinnamate) (PVCi), which both are formed by UV irradiation to dimerized the cinnamoyl groups in the molecules to the cyclobutane rings. The fluorescent signals achieved in this cyclobutane work occurred after the yield point, however, and for early damage precursor detection, it is desirable to detect damage well before this point. Thus, we continued our study by synthesizing dimeric (9-anthracene carboxylic acid) (Di-AC) particles as novel mechanophores in epoxy composites.

The use of Di-AC is expected to allow for early damage precursor detection as the material exhibits over 10 times the absolute fluorescence quantum yield compared to the cinnamoyl-containing polymers, due to the molecule containing three conjugated benzene rings [147]. Because of the superior quantum yield, an order of magnitude less individual mechanophore molecules are needed to break in DA to observe the same fluorescence that occurs with TCE or PVCi; thus, early damage when only few molecules are broken

should be able to be observed. Also, the quantum yield corresponds to the amount of damage retained in the polymer, providing a function by which to predict damage in the overall material. This high quantum yield also provides the possibility of detecting damage deep in the polymer matrix as well as the early damage precursor functionality, making the anthracene moiety more desirable to be used as a fluorescent sensor in practical applications. This functionality has been seen in that the maximum fluorescence emission wavelength has been reported to shift from 495 nm for TCE to 568 nm for anthracene [147].

As spiropyran (SP)-linked elastomeric polymers have been extensively studied in the mechanophore research, we offer a brief summary of the advantages of using cinnamoyl or anthracene cycloalkane-functional mechanophores as an alternative to SP. Spiropyran as a mechanophore is reported to be quite sensitive environmental conditions such as pH, temperature, and light [160-165]. For example, activated SP fades to the inactivate state within 30 minutes under ambient light [166]. Because the emission of the cycloalkane-functional mechanophores is the shorter-wavelength UV, this deactivation is expected to be much less under ambient conditions. Also, the cycloaddition mechanism is thermally forbidden, making the fluorescence emission to not experience a thermal fade. Additionally, the cycloalkane linkages are not pH sensitive. Notably, while the ring-opening mechanism in SP can be reversed after the application of force with white light, if the covalent bonds in the mechanophore molecules break during tension, healing is not possible. The overall behavior of a visible color sensor like SP can be considered more digital (on/off) in nature, rather than a gradual signal in response to damage. The visible color change is a more macroscopic sensor, with SP not used successfully as a mi-

crocrack sensor. Another challenge of SP as a mechanophore is the multitude of careful synthesis and washing steps to produce the final material [10]. These considerations call for the study of alternative mechanophores with differing chemistry to improve the functionality of these materials in terms of mechanical properties and environmental robustness.

In the work contained in this dissertation, we sought to study a new mechanophore chemistry in epoxy and polyurethane thermoset matrices while additionally enhancing the overall damage detection capability and creating a self-sensing mechanophore particle reinforced composite, rather than a simple polymer blend. Thus, we created PRCs with embedded dimerized 9-anthracene carboxylic acid (Di-AC) mechanophore microparticles. To the our knowledge, there has only been one other article reporting mechanophore-based particles, in which maleimide−anthracene cycloadducts were attached to silica nanoparticles via poly(methyl acrylate) chains, and were activated via sonication in solution [167]. Additionally, spiropyran-based particles have been synthesized, but they have not yet been tested for mechanical responsiveness, only light and temperature responsiveness [168-170]. Thus, we synthesized, characterized, and applied dimeric anthracene (Di-AC)-based mechanophore particles to form stress sensing particle reinforced thermoset network composites. Under an applied stress, the cyclooctane-rings in the Di-AC particles revert to their fluorescent anthracene monomeric form, enhancing the overall fluorescence of the composite, thus adding a sensing capability with good retention of the material properties. Interestingly, in the polyurethane matrix, there was an enhancement of the fluorescent signal, which was attributed to increased interactions between the matrix and the particles, with possible surface grafting occurring. We addition-

ally carried out molecular dynamics simulations in parallel to the experimental work to better understand the nanoscale precursors to damage and mechanophore activation in the self-sensing microcomposites.

We then moved from microscale mechanophore incorporate to the nanoscale by preparing novel, grafted, covalently-bonded, self-sensing mechanophore thermoset network nanocomposites. In the previously discussed work, in which the mechanophores were simply used as stress-sensing additives, the self-sensing could only occur between the stress-sensing molecules, and any damage done to the matrix polymer could not be sensed, the fluorescent nature only serving as a signal to the damage. Another notable drawback of utilizing mechanophores as additives was the significant lowering of the glass transition temperature of the system, narrowing the temperature window in which the composite can be used. Thus, we proposed to overcome these limitations by the direct covalent incorporation of the mechanophore units into an epoxy network thermoset polymer to create a novel functionalized nanocomposite system, by using the mechanophore precursor and mechanophore, cinnamamide and di-cinnamamide, respectively. This systematic and novel work also provided further fundamental understanding of mechanochemistry as a whole.

CHAPTER

3. METHODOLOGY

3.1. Experimental Preparation and Study of Micro- and Nanocomposites with Embedded Mechanophore Units

3.1.1. Materials

9-anthracene carboxylic acid (AC, Alfa Aesar), tetrahydrofuran (THF, Alfa Aesar), 1-methyl-2-pyrrolidinone (NMP, Sigma Aldrich), cinnamamide (Cinn, Sigma-Aldrich), diethyl ether (VWR International), and deuterated dimethyl sulfoxide (DMSO-d_6, Cambridge Isotope Laboratories) were used as received. The epoxy resin FS-A23 (digycidylether of bisphenol F, DGEBF) and epoxy hardener FS-B412 (diethylenetriamine, DETA) were purchased from Epoxy Systems Inc. and used as received. The thermoset polyurethane (PU) matrix used was Crystal Clear ® 200 from Smooth-On, Inc. which consisted of 4,4'-methylenedicyclohexyl diisocyanate (Part A) and a proprietary polyol (Part B).

3.1.2. Preparation of Crosslinked Cyclobutane Mechanophore Polymer Blends

The cyclobutane-based mechanophore monomer, 1,1,1-tris(cinnamoyl oxymethyl)ethane (TCE), was synthesized according to Reference [159], while the polymeric mechanophore monomer poly(vinyl cinnamate) (PVCi) was purchased from Sigma Aldrich and used as received. TCE or PVCi were incorporated into the resin by first dissolved in dichloromethane, with subsequent removal of the solvent after homogenization. Photo-curing to create the cyclobutane mechanophore linkages was then carried out with

a 302 nm wavelength UV lamp for four hours, with the samples subsequently left to finish curing in ambient overnight. The detailed procedure can be found in Reference [159].

3.1.3. Synthesis of the Mechanophore Dimers Di-AC and Di-Cinn

To form dimeric 9-anthracene carboxylic acid (Di-AC) particles, 2 g of AC were dissolved in 40 mL of THF and the mixture was homogenized via magnetic stirring, under a nitrogen purge, and put into darkness. The solution was then photoirradiated with a 302 nm wavelength UV lamp (UVP, UVM-28), with a light density of approximately 1300 μW cm^{-2} at a distance of 3 cm, for three days. A precipitate formed, which was washed with THF by gravity filtration to remove the yellow AC monomer, until the bottom solution was clear. The product was then dried to remove excess solvent. The Di-AC product was obtained as a white powder with a yield of 37%. To ensure the uniformity of the particle size, the Di-AC product was then filtered through 10 μm filter paper (EMD Millipore) with acetone, to gather particles under 10 μm. The particles were allowed to settle and the acetone was decanted off, with subsequent drying of the particles to remove any excess solvent.

To synthesize di-cinnamamide (Di-Cinn), 2 g of cinnamamide were dissolved in 40 mL of diethyl ether and the mixture was homogenized via magnetic stirring and under a nitrogen purge. The solution was then photoirradiated with a 302 nm wavelength UV lamp for two days. A white precipitate formed, which was washed with diethyl ether by gravity filtration to remove the brown cinnamamide monomer, until the bottom solution was clear. The product was then dried to remove excess solvent.

3.1.4. Chemical Characterization Methods

^{1}H Nuclear Magnetic Resonance (NMR) spectra were taken with a Bruker 400 MHz NMR spectrometer. For the NMR samples, approximately 5 mg of each sample was dissolved in 750 μL of DMSO-d_6. Fourier Transform Infrared (FTIR) spectra were taken either in the ambient atmosphere with a Nicolet iS50 FTIR Spectrometer or under vacuum in a Bruker IFS 66v/S FTIR spectrometer equipped with a Pike Diamond ATR (Attenuated Total Reflectance) accessory. 1000 nm sections of the composites were made with a Leica Ultracut R Microtome. Transmitted light images of the were taken with a Leica SP5 confocal laser-scanning microscope. The particle size of a dilute solution of 6 mg Di-AC in 5 mL THF was determined via Dynamic Light Scattering (DLS) with a PSS NICOMP 380 ZLS. A Perkin Elmer Lambda 18 UV-visible (UV-vis) spectrometer was used to gather absorption data at ambient for a dilute solution of 1 mg AC in 20 mL NMP before photoirradiation and after photoirradiating the reported times. Emission spectra were collected with a Horiba Scientific FluoroLog-3 Spectrofluorometer with an excitation wavelength of 350 nm, with quartz coverslips for the powder samples, and all slits set at 1 nm. Microscopic morphologies of the surface of the epoxy samples were taken with a FEI/Philips XL30 Environmental FEG Scanning Electron Microscope (SEM). The chemical structures were drawn with MarvinSketch.

3.1.5. Preparation of Di-AC Mechanophore-Embedded Epoxy Matrix Composites

To form the studied composites consisting of 5 wt% Di-AC particles in an epoxy matrix, 0.25 g of the 10 μm filtered Di-AC particles were added to 3.74 g of epoxy resin. These were then mixed with a small impeller mixer at 200 rpm for 10 min at room tem-

perature and checked for the particles to be well dispersed. 1.01 g of the epoxy hardener was then added (to form 5 g total of epoxy at a mass ratio of M_{Resin}: $M_{Hardener}$ = 100:27), and mixed with the impeller mixer at 200 rpm for 5 min at room temperature. After the mixture was homogenous, it was poured into silicone rubber molds sprayed with a mold release agent and allowed to cure overnight at room temperature. Neat epoxy samples were prepared in a similar manner with the same 100:27 ratio of resin to hardener.

3.1.6. Preparation of Di-AC Mechanophore-Embedded Polyurethane Matrix Composites

To form the composites consisting of 2.5 and 5 wt% Di-AC particles in a thermoset polyurethane matrix, the 10 μm filtered Di-AC particles and 4,4'-methylenedicyclohexyl diisocyanate (Part A) were mixed with an impeller mixer at 200 rpm for 5 min at room temperature so that the particles were dispersed. The proprietary polyol (Part B) was then added to the diisocyanate/Di-AC mixture at a mass ratio of $M_{Part\ A}$: $M_{Part\ B}$ = 10:9, and mixed with the impeller mixer at 200 rpm for 5 min again at room temperature. After the mixture was homogenous, it was poured into silicone rubber molds and degassed in a vacuum oven at -29 in Hg for 90 minutes. The polyurethane was then allowed to cure overnight at room temperature, and then post cured at 70 °C for 8 hr. Neat polyurethane samples were prepared in a similar manner at the same 10:9 mass ratio.

3.1.7. Preparation of Mechanophore-Grafted Epoxy Nanocomposites

To form the studied nanocomposites consisting of 10 wt% cinnamamide or 10 wt% di-cinnamamide in 5 g total epoxy, each were first reacted with the resin to ensure the covalent bond formation. 0.5 g of cinnamamide or di-cinnamamide were added to 3.704 g of epoxy resin (digycidylether of bisphenol F, DGEBF) and 20 mL of dichloromethane. This mixture was then heated at 40 ºC for 4 hr under a nitrogen purge and magnetic stirring to allow for the reaction between the epoxide rings and the amine groups. After the reaction was completed, the cinnamamide reaction solution turned fluorescent opaque yellow while the di-cinnamamide reaction solution was white and opaque. The dichloromethane solvent was then removed under reduced pressure and 0.796 g of hardener (diethylenetriamine, DETA) was added to each functionalized resin mixture (4.204 g total). The hardener/resin/mechanophore weight ratio was calculated according to the manufacturer's recommendations and the epoxide/amine equivalent weight. These mixtures were then impeller mixed at 200 rpm for 5 min at room temperature until homogenous. The mixtures were then poured into silicone rubber molds sprayed with a mold release agent and allowed to cure overnight at room temperature, with the cinnamamide epoxy being UV cured for 4 hrs under 365 nm light (UVP, UVLMS-38) prior to leaving in darkness to complete the curing. Neat epoxy samples were prepared in a similar manner with a 100:27 ratio of resin to hardener.

3.1.8. Characterization of Mechanophore -Embedded Thermoset Composites

After simple machining, the average dimensions of the samples for the compression test were 3 × 4 × 8 mm and 2 × 12 × 35 mm for the Dynamic Mechanical Analyzer

(DMA) tests. A TA Instruments Q20 Differential Scanning Calorimeter (DSC) was used to determine the glass transition temperature (Tg) of the samples in aluminum Tzero pans with lids under nitrogen, with air (an empty pan and lid) used as the reference. The sample was first heated to 70 °C to eliminate any thermal history, cooled down to −20 °C, then heated to 120 °C to determine the Tg, with all heating and cooling rates set at 10 °C/min. A TA Instruments Thermogravimetric Analyzer (TGA) Q500 was used to determine the decomposition temperatures (Td) under nitrogen. Each sample was placed in a tared platinum crucible and heated from 25 to 600 °C at a heating rate of 10 °C min^{-1}. A TA Instruments Q800 Dynamic Mechanical Analyzer (DMA) was used to measure the storage modulus, loss modulus, and tan delta for the samples over a temperature range and to calculate the crosslink density. The multi-frequency/strain method was used with the single cantilever clamp and a frequency of 1 Hz under amplitude control. The temperature was ramped from 25 to 120 °C at a heating rate of 5 °C/min, with the strain amplitude set at 25 μm. The characteristic temperatures and moduli values from DSC, TGA, and DMA were found using the built in functions in the TA Instruments Universal Analysis software. A TestResources 800L Compression Test System was used to compress the samples to different strains and obtain stress-strain plots for the samples. A small amount of petroleum jelly was applied to the samples to minimize their friction with the compression plate, and prevent unwanted shearing. The tests were run in displacement control in the longitudinal direction at a loading rate of 1 mm/min and conducted at room temperature. The fluorescence generation from the compressed samples was observed under a Nikon Eclipse TE300 inverted video fluorescence microscope, by excitation under 340–380 nm UV light, with a filter cube to capture the emission of light between

435–485 nm for the Di-AC embedded samples and 500–550 nm for the Cinn/Di-Cinn grafted samples. All images were taken with a black-and-white camera and with the same intensity of light, gain, and exposure time. The Image J (http://imagej.nih.gov/ij/) software package was used to quantify the fluorescence density of the images taken. Every image was first converted to an 8-bit image and then the "Measure" function was used to calculate the integrated intensity for the selected area of the image; this is through the software taking the sum of the pixel values in the image, and then averaging the intensity at each point. The 8-bit gray scale fluorescence images from the fluorescence microscope were subsequently pseudocolored green with ImageJ with the built-in "Green" LUT, and the fluorescent images published in this paper were all further enhanced by increasing both the brightness and contrast by 40% for better viewing. A UVP UV Transilluminator, Model M-20, with an 8 watt and 302 nm wavelength UV light source was used to take macroscopic pictures of the Di-AC epoxy compression test samples and these images were also pseudocolored green with ImageJ.

3.2. Hybrid MD Simulation Modeling Framework

The bond dissociation energy (BDE) calculation was performed according to our previous work [171] and using the constrained geometry external force (COGEF) method developed by Beyer et al. [172]. A local work analysis, which was also implemented in our previous work [171], was performed to simulate mechanophore activation of the smart material. The MD simulation unit cell ($15 \times 15 \times 15$ nm^3) was constructed with randomly distributed molecules of the constituents. The weight percentages of the constituents were: 74.8 wt% DEGBF, 20.2 wt% DETA, and 5 wt% Di-AC. The epoxy-based

matrix had an extensively crosslinked structure. The epoxy resin and hardener were cured using the covalent bond generation protocol performed by the classical force field (Merck Molecular Force Field) [75]. Periodic boundary conditions were applied to the boundaries of the unit cell. Conjugate gradient energy minimization was performed first. Subsequently, NPT (isobaric-isothermal) ensemble equilibration was conducted on the unit cell at 300 K and 1 atm for 1 ns using the Nose‑Hoover thermostat and barostat to control the temperature and pressure. After equilibration, the epoxy curing simulation was performed. Subsequently, the system was stabilized to reduce the augmented potential energy caused by the newly generated bonds. A uniaxial loading simulation was performed to analyze the local force experienced by the mechanophore molecules in the cured unit cell. Tensile loading tests were performed with a very high strain rate (1013 s^{-1}) by a deformation method adapting a quasi-continuum approach to decouple thermal molecular vibrations which may relax bond elongations during the deformation test [173]. While the tensile loading test was performed, the [4+4] cyclodimers were stretched by the applied local forces, and the C-C bond lengths were monitored at every step. The mechanophore activation simulation using the atoms' trajectory data was conducted in a way to change the color from red to green when the C-C bonds are stretched beyond the critical bond length (2.16 Å) which was determined from the BDE of Di-AC. In order to analyze the mechanophore activation quantitatively, the local work done by the local force on the C-C bonds is calculated. It was proved that local force analysis itself was not relevant to capture mechanophore activation as the unit cell deforms [171].

CHAPTER

4. RESULTS AND DISCUSSION

4.1. Polymer Blends of Crosslinked Cyclobutane-based Mechanophore Polymers and Epoxy for Damage Detection in Thermoset Systems

In our group's first foray into the study of stress-sensing materials, we created polymer blends of crosslinked cyclobutane based mechanophores and epoxy matrices to observe the change in fluorescent emission with applied stress[159]. The mechanophores studied were generated by UV photodimerization of the crosslinkable, cinnamoyl-functionalized 1,1,1-tris(cinnamoyloxymethyl) ethane (TCE) and poly(vinyl cinnamate) (PVCi). The cyclobutane sensing units were produced by [2+2] cycloaddition of the carbon-carbon double bond in the cinnamoyl functional groups of TCE and PVCi. The TCE monomer was synthesized according to literature, and as each TCE monomer molecule consisted of three active cinnamoyl cites, photoirradiation of the monomer yielded a crosslinked polymer. PVCi was purchased from Sigma Aldrich, and consists of a linear polyethylene chain with cinnamoyl functional groups at the vinyl position. Photoirradiation of PVCi leads to the polymer chains crosslinking with each other.

The cycloaddition reaction was confirmed by Fourier transform infrared (FTIR) spectroscopy, by observing the change in specific peaks before and after the application of UV light, as seen in Figure 4.1.1. The spectra is of a TCE film on a potassium bromide (KBr) disk, and before photoirradiation of TCE, peaks at 1713 and 1637 cm^{-1} are present, corresponding to the conjugated C=O and C=C stretching vibrations of the cinnamoyl monomer. After photoirradiation, the C=C peak disappears due to the formation of the cyclobutane rings by photodimerization at the alkene position, consuming the cinnamoyl

groups. Additionally, the C=O peak shifted to a higher wavenumber with decreasing absorbance, which was attributed to the loss of π–conjugation from the C=C double bond.

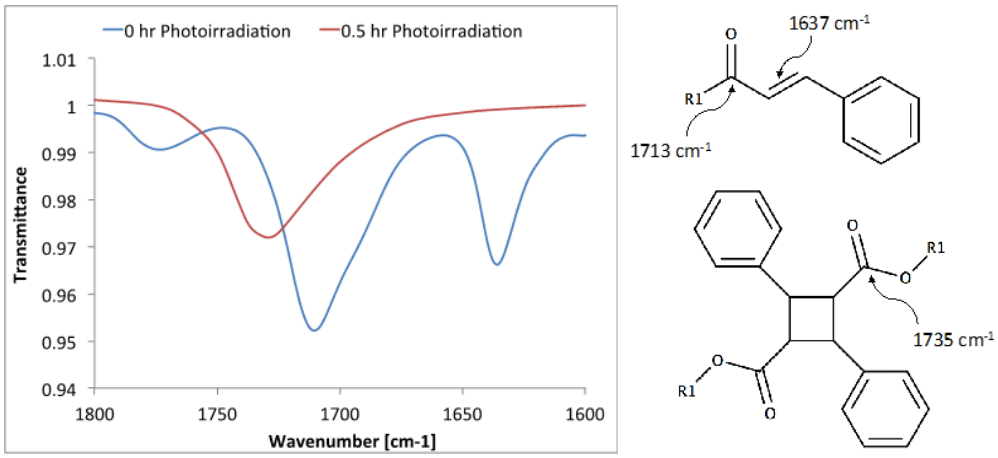

Figure 4.1.1. FTIR spectra of solution cast TCE on a KBr disk before and after photoirradiation with the respective chemical structures.

After confirmation of the formation of the cyclobutane mechanophore units via photodimerization, polymer blends of the mechanophores and epoxy were prepared. The mechanophore monomer, either TCE or PVCi, was dispersed into the epoxy resin, followed by addition of the hardener. The epoxy then underwent UV curing to create the cyclobutane mechanophore units. This thus created simple polymer blends of epoxy and the crosslinked mechanophores, which were found to be miscible via Scanning Electron Microscopy (SEM) and Differential Scanning Calorimetry (DSC), or the mechanophores can be thought of as additives in the epoxy.

When the blended system underwent crack formation and propagation, via compression tests, the cyclobutane units were mechanochemically cleaved to afford the monomeric structure. This cinnamoyl structure was capable of fluorescent emission, which indicated the location of the cracks in the epoxy when viewed with a fluorescent micro-

scope. Figure 4.1.2 shows the stress-strain curve of the compression test for a 10 wt% TCE-epoxy polymer blend. At each of the strain values denoted with green x's visible light and fluorescent images of the sample were taken to evaluate the extent of the damage detection.

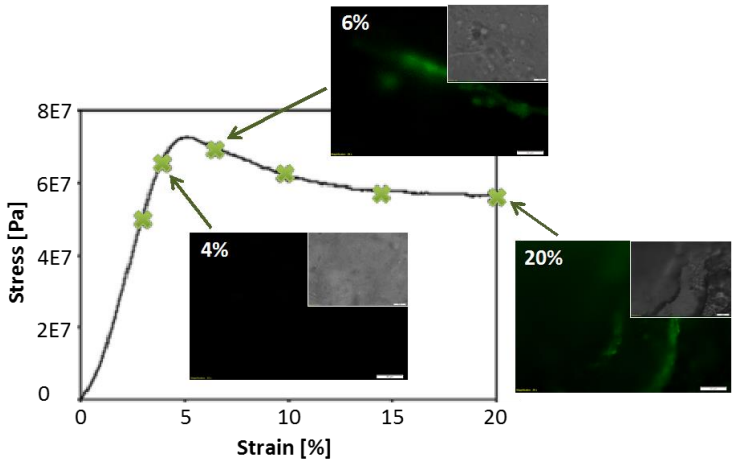

Figure 4.1.2. Stress-strain curve of 10 wt% TCE-epoxy polymer blend with overlayed representative fluorescent images for selected strain values. Scale bars are 50

For all visible light images taken, the damage/microcracks formed could not be observed. For strains below the yield strength, such as 4% strain, no fluorescent emission was observed, implying that the mechanophores could not be activated without plastic deformation. However, immediately after the yield point, at 6% strain, fluorescent microcracks were observed, the number of fluorescent microcracks increasing as the strain increased. In order to quantify the amount of fluorescence observed, for each strain level, multiple fluorescent images were taken and the average fluorescent intensity over each group of images was calculated via ImageJ. Figure 4.1.3 shows the resulting curve with respective standard deviations. It can be seen that while there is no statistical difference between 3 and 4% strain, there is a difference between 4 and 6% strain, the latter occur-

ring after the yield point. As previously mentioned, before the yield point, there was no fluorescence, so the intensity value from ImageJ for the 3 and 4% strain correlates to this. Thus the large standard deviation for 6% strain is due to there being both fluorescently activate and inactive regions on the sample, as would be expected when the mechanophores first begin to break. It can also be seen that the overall fluorescence intensity increased with the applied strain, as expected, as more mechanophore units are activated by increasing the applied force.

In this previous work, there were notable drawbacks caused by using the mechanophores as additives to create polymer blends, including the significant lowering of the glass transition temperature (Tg) of the material system by 28 °C for the TCE-epoxy blend, depression of the mechanical properties, including the yield strength, and inability to detect damage before the yield point. Thus, we sough to overcome these limitations by focusing on not only a different mechanophore chemistry, but a different composite structure as well, namely a particle-reinforced composite.

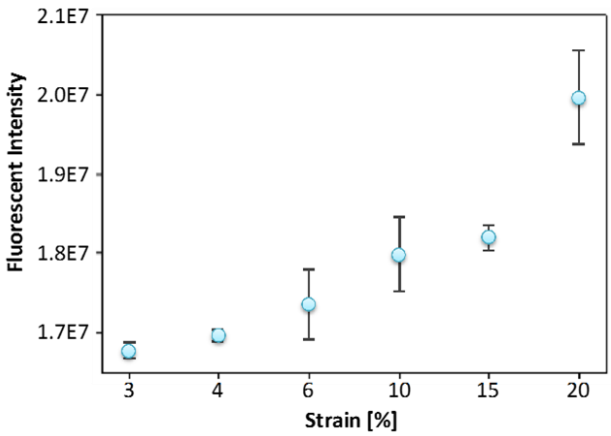

Figure 4.1.3. Fluorescence intensity values corresponding to various strains from the stress-strain curve for the 10 wt% TCE-epoxy polymer blend.

4.2. Dimeric Anthracene-based Mechanophore Particles for Damage Precursor Detection in Reinforced Epoxy Matrix Composites

4.2.1. Anthracene Photodimerization for Mechanophore Formation

It is well known that 9-substituted anthracene derivatives, including 9-anthracene carboxylic acid (AC), form prominently head-to-tail structures when photodimerized in solution under UV light via [4 + 4] cycloaddition to form a cyclooctane-type ring [174]. A schematic of this reaction to form the dimerized 9-anthracene carboxylic acid (Di-AC), which can be recovered as a pure white powder, and can be seen in Figure 4.2.1(a); the head-to-tail structure being preferred due to steric hindrance between the carboxylic acid side chains during dimerization. This dimerization reaction has also been studied in the solid-state, where molecular confinement can allow for the formation of the head-to-head dimer [175, 176]. Additionally, the solid-state [4 + 4] photodimerization phenomenon has allowed for the creation of AC molecular-crystal nanorods that can undergo reversible bending [177, 178]. Figure 4.2.1(a) also shows the subsequent incorporation of the Di-AC particles into an epoxy matrix for fluorescent stress sensing via reversion to the AC monomers after stress is applied.

In this study, AC was dissolved in THF and the mixture was homogenized via magnetic stirring, purged with nitrogen, and put into darkness. The solution was then photoirradiated with a 302 nm wavelength UV lamp to carry out the [4 + 4] cycloaddition. The Di-AC white powder precipitate formed, was washed with THF to remove any unreacted yellow AC monomer, and dried. After the photodimerization reaction and purification, the resulting Di-AC powder product was filtered through 10 μm filter paper to remove any large aggregates and capture Di-AC particles of a reasonable particle size.

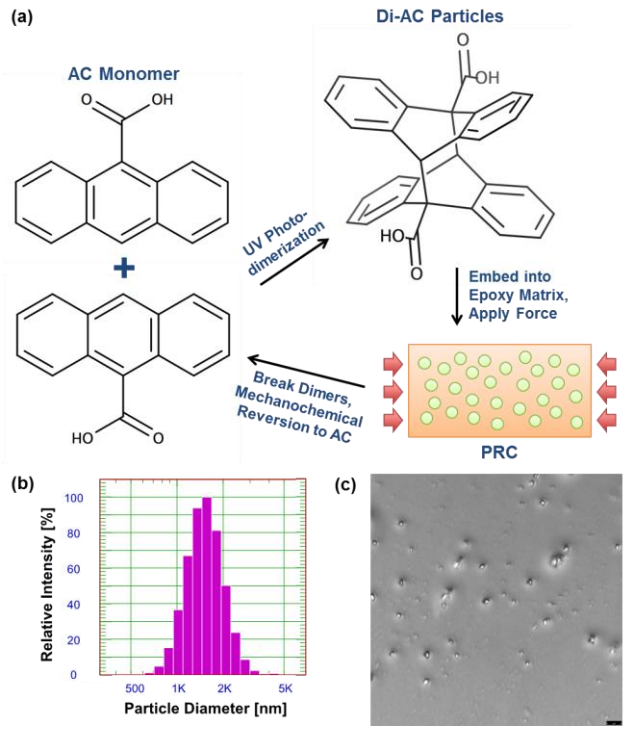

Figure 4.2.1. (a) An overview showing the conversion of the AC monomer to Di-AC particles under UV light, the subsequent embedding of the particles into an epoxy matrix to form a PRC, and, upon application of force, reversion of the Di-AC particles to the AC monomeric form to enhance the overall fluorescence of the PRC for stress sensing. (b) Representative DLS histogram showing the distribution of the Di-AC particle size. (c) Transmitted light image via confocal microscopy showing the resulting Di-AC particles (scale bar is 5 μm).

Dynamic light scattering (DLS) was used to confirm the particle size, which was found to be 1553 ± 739 nm in diameter, with a Gaussian distribution. This distribution can be seen with a corresponding relative intensity graph in Figure 4.2.1(b). Transmitted light images captured with a confocal laser-scanning microscope confirmed the particle size found from DLS (Figure 4.2.1(c)).

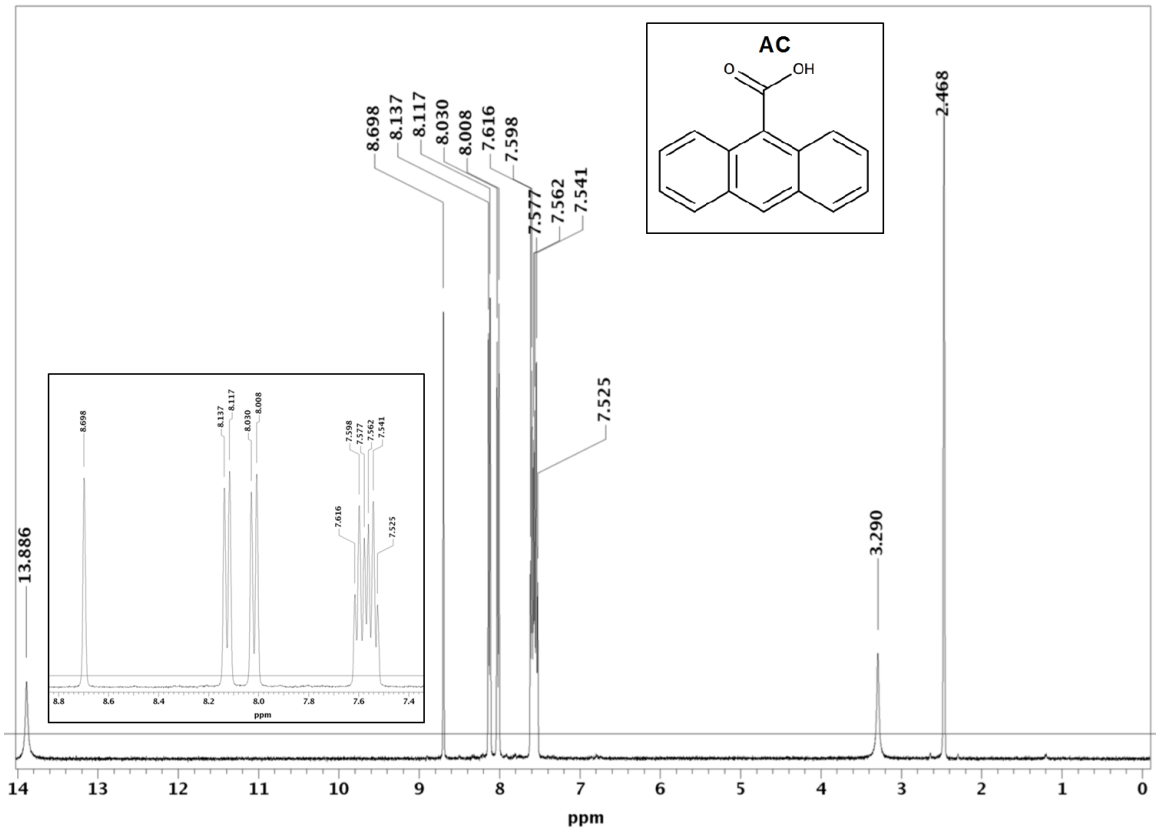

Figure 4.2.2. ^{1}H NMR spectra of 9-anthracene carboxylic acid (AC) in DMSO-d_6.

After confirming the creation of uniform Di-AC particles, the chemistry was also confirmed via nuclear magnetic resonance (NMR) and Fourier transform infrared (FTIR) spectroscopy, comparing AC with Di-AC. The ^{1}H NMR spectra for AC and Di-AC can be seen in Figures 4.2.2 and 4.2.3. Both AC and Di-AC showed a peak at 2.5 ppm, which was characteristic to the DMSO-d_6 solvent and a peak at 3.3 ppm that was characteristic of residual water in the sample. For AC, the peaks from 9 – 7 ppm correspond to the aromatic hydrogen atoms on the anthracene ring, with another peak at 13.9 ppm for the hydrogen on the carboxylic acid. For Di-AC, the peaks for the aromatic hydrogen atoms shifted to 7 – 6 ppm, the carboxylic acid peak shifted slightly to 13.5 ppm, but the distin-

guishing peak is at 5.6 ppm, which corresponds to the hydrogen atom on the newly formed cyclooctane ring – confirming the dimerized structure.

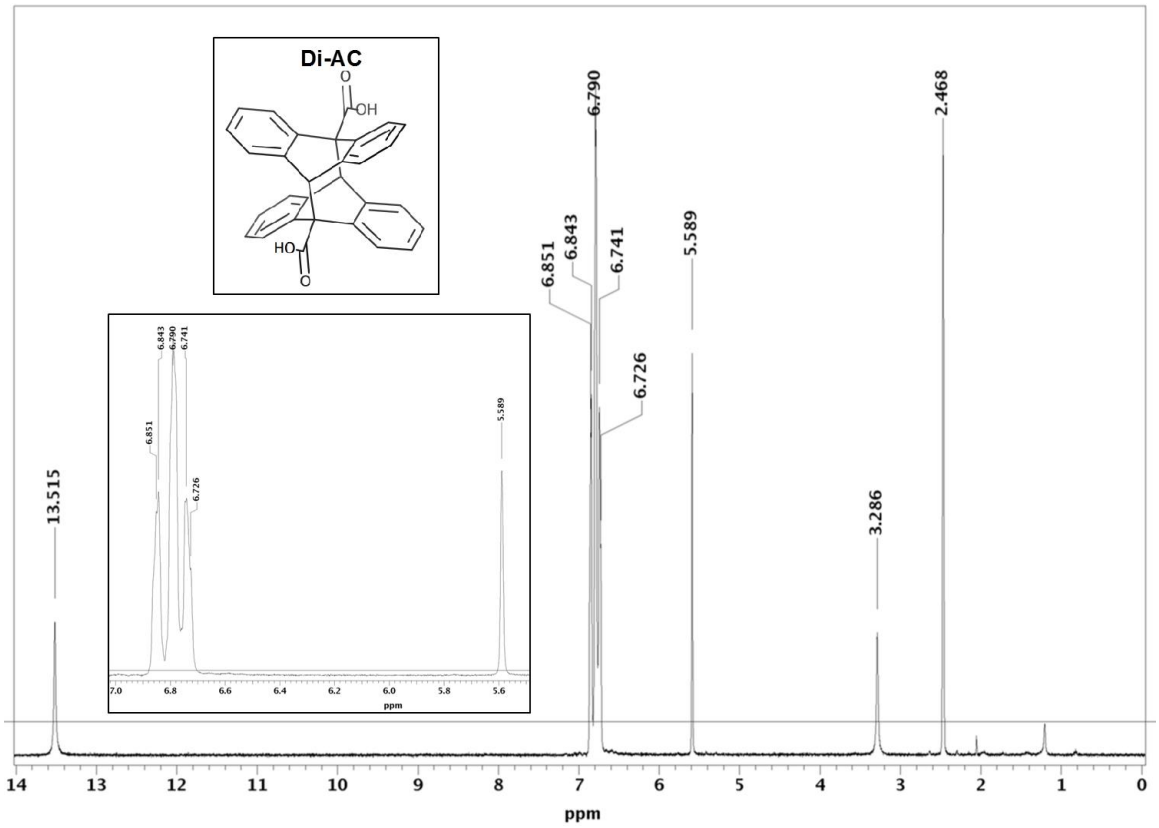

Figure 4.2.3. ^{1}H NMR spectra of dimeric 9-anthracene carboxylic acid (Di-AC) in DMSO-d_6.

Figure 4.2.4(a) shows the comparison of the FTIR spectra for AC and Di-AC, zoomed in to focus on the characteristic peaks. The full FTIR spectra from 4,000 – 400 cm^{-1} can be found in Figure 4.2.5. There are a few important characteristic peaks in the spectra, the first is for the carbonyl stretch ($\nu_{C=O}$) blue shifted from 1,685 cm^{-1} for AC to 1,698 cm^{-1} for Di-AC, indicating a cleavage of some hydrogen bonds when AC transitions to Di-AC and its 3-D structure drastically changes [175]. A new sharp peak formed at 1,393 cm^{-1}, corresponding to the newly formed alkane hydrogen (ν_{C-H}) on the cyclooc-

tane ring in Di-AC. Additionally, peaks at 1,340 and 1,225 cm^{-1} for AC corresponding to the transition band of the phenyl ring were bleached out [175].

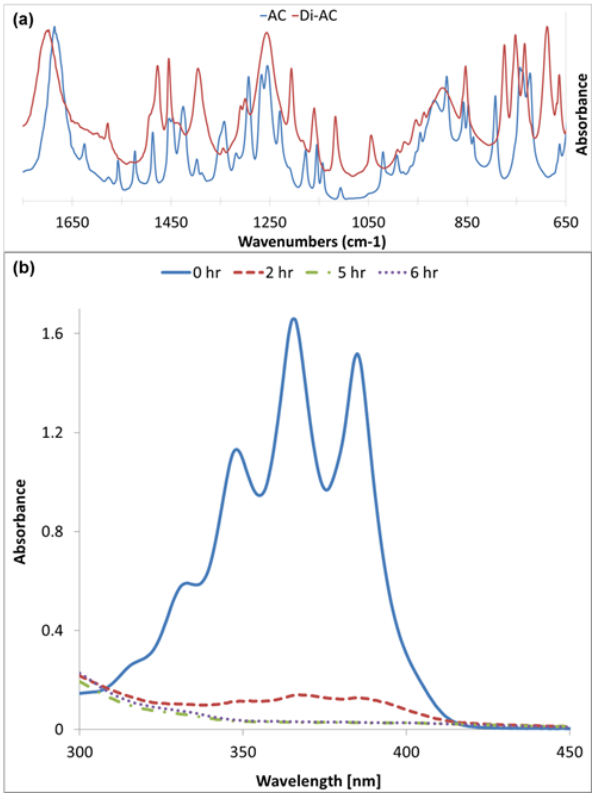

Figure 4.2.4. (a) FTIR spectra comparing the AC monomer with the Di-AC mechanophore product. (b) UV-vis spectra showing the decrease in absorbance over time.

The dimerization reaction was further studied by utilizing UV-vis spectroscopy in order to analyze the conversion of AC to Di-AC, as seen in Figure 4.2.4(b). This analysis is important, as with UV light driven reactions; the addition of light can drive both the forward and reverse reactions, resulting in low conversions. The initial solution (at 0 hr) consisted of 1 mg AC in 20 mL NMP, and showed fingerlike absorption bands between 320 and 420 nm, representing vibronic substructures, which are characteristic for anthracene derivatives [175]. 302 nm UV light was applied to the solution and samples were

taken at 2, 5, and 6 hr to probe the change in the absorbance over time. After 2 hr photoirradiation, the absorbance value decreased drastically, with the conversion for the peak at the 365 nm wavelength being 0.92. With the longer application of light, the conversion for the 365 nm peak leveled off at 0.98 for 5 and 6 hr.

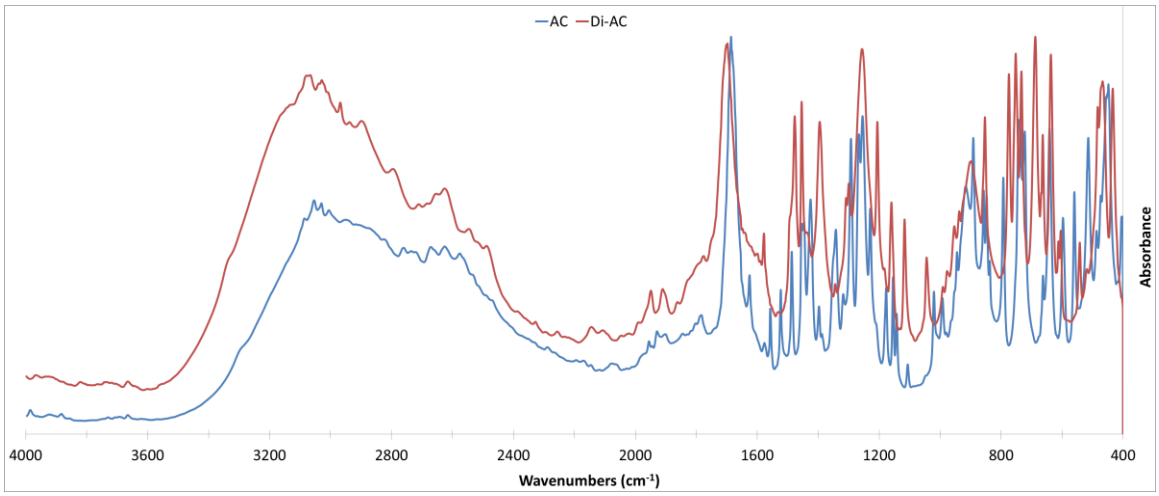

Figure 4.2.5. Full FTIR spectra comparing the unreacted AC monomer with the Di-AC mechanophore product.

The conversion never reaches 1, as some percentage of the dimers are driven back to the monomeric form under UV light, as previously mentioned. However, 0.98 is a very high conversion for this type of reaction, and is likely due to the relatively small size of the dimers and their freedom to move in the dilute solution. Additionally, after the dimerization occurs to produce the Di-AC needed for the composites, the very small amount of unreacted AC remaining is easily washed out, resulting in a quite pure product. This is an important result, as the mechanical sensing function of the Di-AC works by reversion to the AC monomer, so if there were many AC molecules incorporated in the epoxy before stress is applied, the sensing signal may have been confounded.

As the sensing action of the Di-AC mechanophore involves fluorescent emission, it is important to generate emission curves to determine where the emission lies. Figure 4.2.6(a) shows the comparison of the fluorescent emission for AC and Di-AC under 350 nm excitation. AC has very strong emission between 365 and 415 nm, with an additional peak at 435 nm. In comparison, Di-AC has a small peak at 378 nm, a large peak at 414 nm, after which it drops off sharply. This shows that while AC has more fluorescence in this region, Di-AC has some fluorescence of its own, albeit less. Following this result, we wanted to see how the fluorescence of Di-AC would affect the overall fluorescence of epoxy when it was incorporated into it.

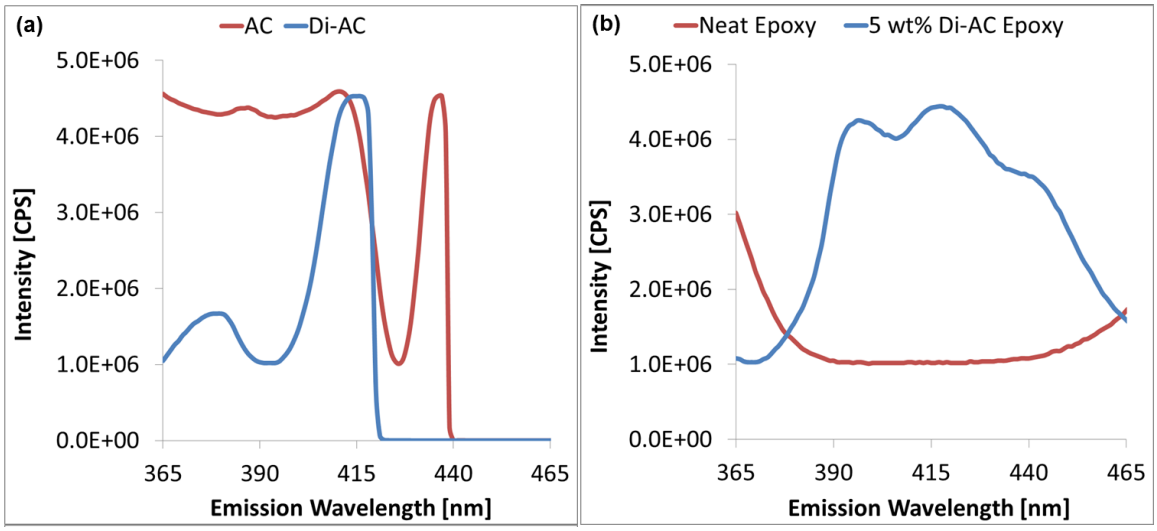

Figure 4.2.6. (a) Emission spectra of AC (red) and Di-AC (blue) for an excitation wavelength of 350 nm. (b) Emission spectra of neat epoxy (red) and epoxy embedded with 5 wt% Di-AC for an excitation wavelength of 350 nm.

With the confirmed chemistry of the mechanophore through NMR and FTIR, and the confirmed regular particle size from DLS and confocal images, epoxy composites containing 5 wt% Di-AC particles were synthesized. To form the mechanophore-

embedded epoxy, the Di-AC powder with an approximate particle diameter of 1.5 μm was impeller mixed with the epoxy resin so that it would be evenly dispersed throughout the composite. The hardener was then impeller mixed into the resin-particle mixture to obtain a mixture that was viscous and a single phase. This was then poured into rubber molds to create the samples for testing and cured at room temperature overnight. The composition of 5 wt% of Di-AC in the composite was chosen, as this was the least amount of mechanophore that could be used to still generate the desired stress sensing signal. The least amount of mechanophore was desired as incorporating the particles into epoxy interrupts the network formed between the resin and hardener when the epoxy cures, impacting the resulting thermal and mechanical properties of the composite. It is worthwhile to note that this is a very low amount of mechanophore, with other sensing systems requiring 10, 20%, or more to generate measureable signals [147, 159]. Figure 4.2.6(b) shows the comparison of the fluorescent emission for neat epoxy and the 5 wt% Di-AC epoxy composite under 350 nm excitation. The neat epoxy showed a low, flat fluorescence value in the 390 to 440 nm region, while the Di-AC composite showed broad fluorescence in this region. This emission is markedly different to the emission for the pure Di-AC powder. This can be likely attributed to thermal or mechanical stresses which occurred while the epoxy cured around the Di-AC particles, resulting in some activation of the mechanophore to revert back to the more fluorescent AC form. With this in mind, baseline fluorescence values were taken before the epoxy was stressed during the compression tests, and as long as there was a significant increase in the fluorescence compared to the stress, this method of creating the epoxy composites still produces the desired self-sensing result.

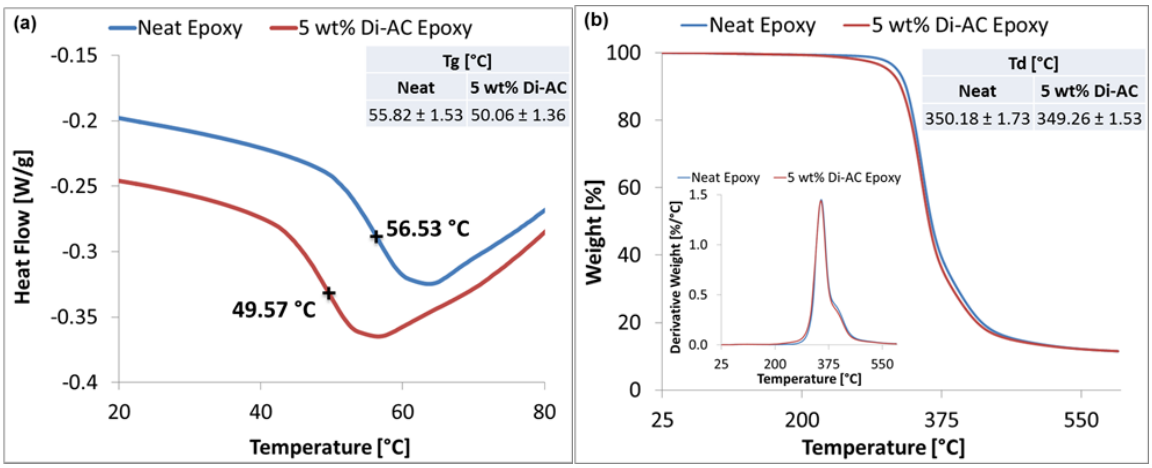

Figure 4.2.7. (a) Representative DSC scans showing the glass transition for neat epoxy (red) and the 5 wt% Di-AC epoxy composite (blue), with the resulting Tg values (as an average of 4 runs) inset on the bottom left. (b) Representative TGA curves showing the decomposition of neat epoxy (red) and the 5 wt% Di-AC epoxy composite (blue), with the resulting major Td values (as an average of 4 runs) inset on the top right. The inset left shows the respective DTG curves to determine the Td values.

4.2.2. Thermal and Mechanical Properties of Di-AC Particle Reinforced Epoxy Composites

After the more fundamental characterization of the chemistry related to the Di-AC mechanophore, the thermal and mechanical properties of the embedded composite were evaluated in order to determine the effect of adding the mechanophore. Differential Scanning Calorimetry (DSC) is a commonly used material characterization method to determine the glass transition temperature (Tg) of various samples be comparing the heat flow required to keep the desired sample and a reference sample (usually air) at the same temperature. Representative DSC scans for the neat and Di-AC composite epoxy can be seen in Figure 4.2.7(a), the Tgs calculated at the step-wise transition in the curves via the

built in TA Universal Analysis software. The average and standard deviation values for the Tg over 4 runs were 55.82 ± 1.53 °C for the neat epoxy and 50.06 ± 1.36 °C for the composite epoxy, for a difference of approximately 6 °C. This slight decrease in Tg is expected as the incorporation of the particles can disrupt the intrinsic epoxy network, as previously mentioned. The decrease of the Tg by 6 °C is much improved upon over previous work incorporating crosslinked cyclobutane polymers into epoxy via polymer blends, as that depressed the Tg by 17 to 28 °C [159]. In the previous work, at least 10 wt% of mechanophore was required for sensing, so lowering the weight percent to 5 wt% allowed for a better retention of the material properties. As the current and our previous work are the first incorporating mechanophores into epoxy matrices, it will be interesting to see what work can come out of exploring the stress sensing in this system.

Figure 4.2.7(b) shows representative Thermogravimetric Analysis (TGA) for the samples, with the corresponding Differential Thermal Gravimetry (DTG) curves in the inset left. These tests were run under nitrogen to eliminate weight loss due to oxidation, and thus purely capture the thermal decomposition of the bonds within the epoxy samples. The main decomposition temperatures (Td) were found via the peaks in the DTG curves, and were 350.18 ± 1.73 °C for the neat epoxy and 349.26 ± 1.53 °C for the composite epoxy. These values are not statistically different from each other, so it can be said that the addition of the mechanophore did not change the Td. Additionally, on the DTG curves, a small shoulder for both samples can be seen around 411 °C. It is worthwhile to note that the Td of the pure Di-AC powder (prior to embedding) was found to be 238.84 ± 4.43 °C, with a small shoulder at 302.67 ± 2.18 °C. The relatively high Td of the pure Di-AC likely contributed to its addition not affecting the Tg of the embedded composite.

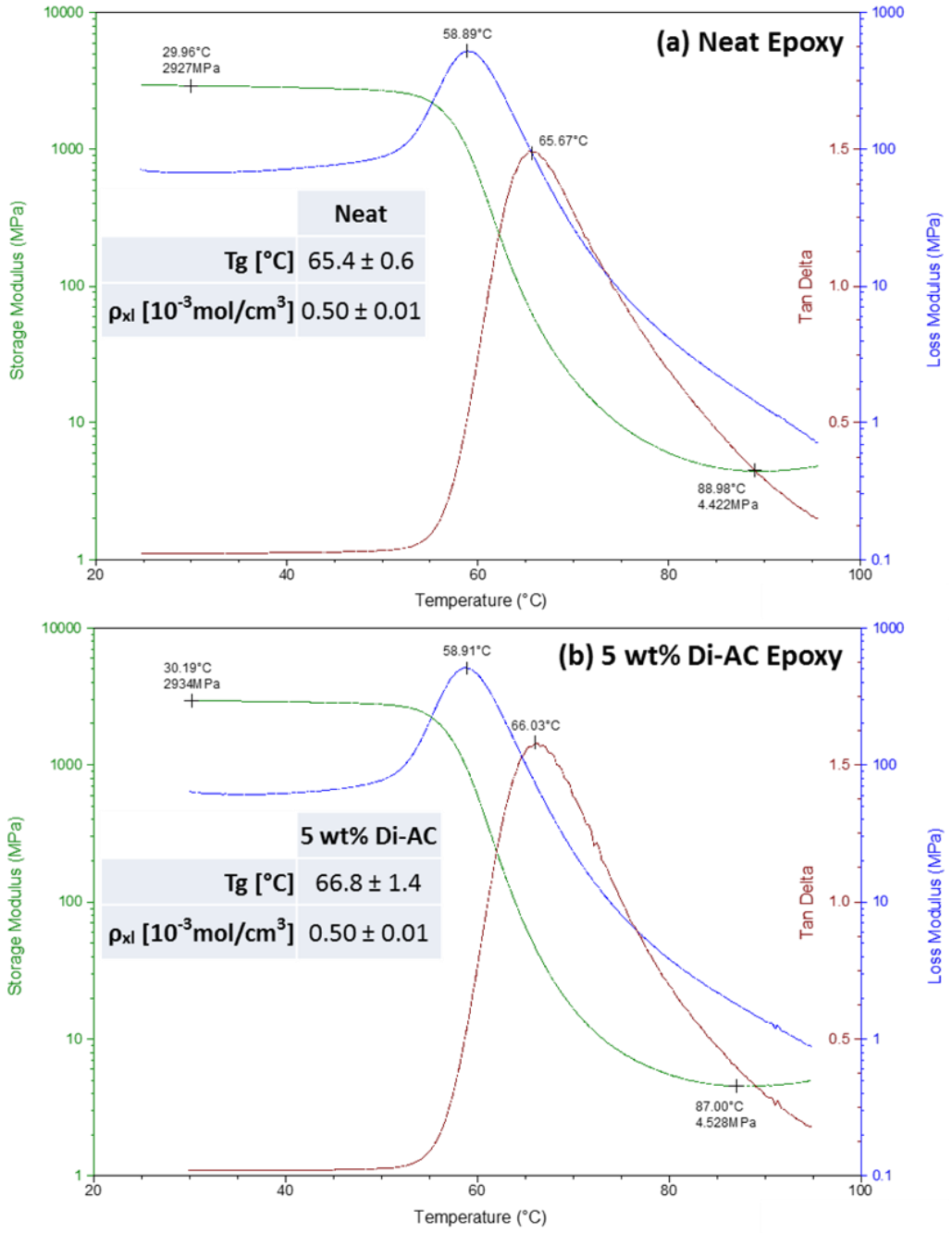

Figure 4.2.8. DMA curves showing the Storage Modulus (green), Loss Modulus (blue), and Tan Delta (maroon) of the (a) neat epoxy and (b) 5 wt% Di-AC composite samples, respectively. The inset tables show the average Tg and ρ_{xl} of the samples over 4 runs, determined from the DMA curves.

In addition to DSC, dynamic mechanical analysis (DMA) can be used to determine Tg values, as well as determine the crosslink density of the epoxy samples. The DMA measures the storage and loss moduli of a sample by physically oscillating the sample, the ratio of the two being defined as tan delta (tan δ). When heat is applied to the sample, eventually there will be a peak in the tan δ, representing the Tg. Figure 4.2.8 shows representative DMA curves for the neat and Di-AC epoxy, the Tgs values being 65.4 ± 0.6 °C and 66.8 ± 1.4 °C, respectively. It is worth noting that while the values for the two are quite comparable, the Di-AC composite shows a higher standard deviation compared to the neat epoxy, possibly due to more variation in the sample in terms of location of particles and curing. Interestingly, the 6 °C difference in Tg values found for the DSC results was not present for the DMA results. This is likely due to the fact that the Tg values were gathered from very different methods, purely thermal for DSC and mechanical for DMA. According to the DMA however, the neat epoxy and the mechanophore composite are very similar, which shows good retention of the material properties, even when the sensing feature is added. Additionally, compared to the DSC, the Tg for the neat epoxy is about 10 °C higher for the DMA, and is about 17 °C higher for the Di-AC epoxy. This has been seen previously when comparing the two methods, and is again due to the methods utilizing different mechanisms to determine the values.

DMA can also be used to calculate crosslink density for a given sample, according to the theory of rubber elasticity [179], $\rho_{xl} = \frac{G'}{3RT}$, where ρ_{xl} is the crosslink density expressed in moles of elastically effective network chains per cm^3 of sample, G' is the rubbery plateau modulus, R is the Gas Constant, and T is the absolute temperature at which the rubbery plateau modulus is determined. The rubbery plateau modulus is de-

fined where the storage modulus curve flattens out after the Tg is reached, and was 4.42 MPa at 89.0 °C for the neat epoxy and 4.53 MPa at 87.0 °C for the Di-AC epoxy. Utilizing these values and Equation 1, the crosslink densities were calculated to be 0.50 ± 0.01 × 10^3 mol/cm^3 and 0.50 ± 0.01 × 10^3 mol/cm^3. The crosslink density corresponds to how many crosslinks are able to form between the resin and hardener molecules in the epoxy during curing, and theoretically adding the mechanophore should lower the crosslink density due to the particles disrupting the network. However, this was not seen and the values were essentially the same between the neat and Di-AC embedded epoxy samples. Thus for the thermal characterization of the neat and Di-AC composite samples, while the DSC did show a slight difference in the Tg values, the Tg, Td, and crosslink density values between two from TGA and DMA showed that adding the mechanophore did little to alter the material properties, providing a benefit for Di-AC PRCs as stress sensors.

To apply the damage to the mechanophore-embedded epoxy samples to observe the resulting fluorescent signal, compression tests were performed and stress-strain curves were generated. Figure 6 shows the resulting stress-strain curves for both samples. The Young's modulus values in the linear elastic region of the curve were found to be 2.57 ± 0.06 GPa and 2.46 ± 0.06 GPa for the neat and Di-AC epoxy samples, respectively, which were in good agreement of each other. The yield strength values were 102.77 ± 0.28 MPa and 91.22 ± 1.57 MPa for the neat and Di-AC epoxy samples, respectively. The depression of the yield strength can again be attributed to the particles disrupting the epoxy network. The middle right inset of Figure 4.2.9 is a UV transilluminator picture under UV light of the compression test samples, neat epoxy on the left and Di-AC composite on the right, showing the macroscopic view of the samples. The samples have each

been compressed to 15% strain and the bright green color of the Di-AC sample reflects its much higher bulk fluorescent property.

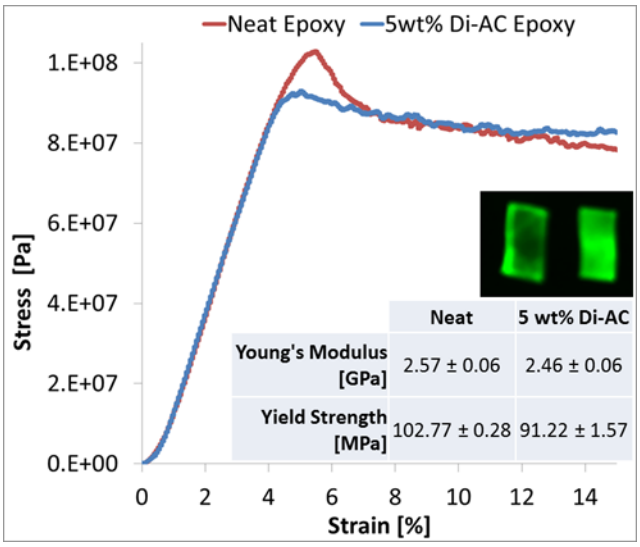

Figure 4.2.9. Stress-strain curves for the neat epoxy (red) and 5 wt% Di-AC epoxy (blue), with the lower right inset showing the resulting Young's Modulus and Yield strength values. The inset center right image shows a UV transilluminator picture of the test samples, neat epoxy (left) and epoxy with 5 wt% of Di-AC (right), both compressed to 15% strain. The enhanced fluorescence of the Di-AC epoxy relative to the neat epoxy under UV light can be clearly seen.

4.2.3. Early Damage Detection via Mechanophore Fluorescent Signaling

With the full characterization complete for the synthesized mechanophore and mechanophore-embedded composite, its functionality as a stress sensor was evaluated. Compression tests were completed on the mechanophore-embedded composite and at each of the selected strain values; 0, 2, 4, 6, 10, and 15%; ten fluorescence microscopy images were taken representative of the entire sample face in order to quantify any increase of fluorescence. Figure 4.2.10(a) shows the locations of the chosen strain values

on the stress strain curve, along with representative fluorescence images for selected strains. The 0% strain is prior to any compression, and provided a baseline for the testing. The 2% strain is clearly in the elastic region, with the 4% strain also being in the elastic region, but right before the yield point. 6% strain is immediately after the yield point, with 10 and 15% strain well into the plastic region. It should be noted that the same testing was performed on the neat epoxy, but no change in fluorescence was observed, as expected.

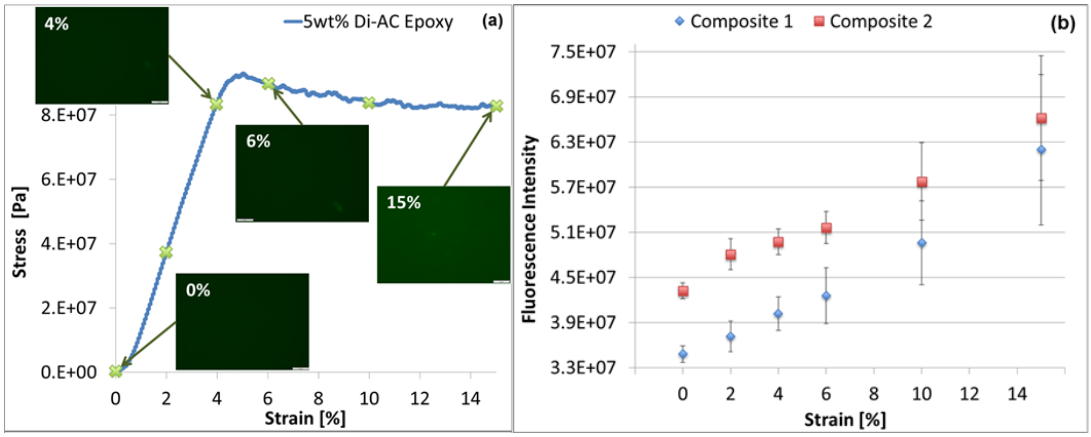

Figure 4.2.10. (a) Stress-strain curve for the mechanophore-embedded composite identifying the strain values for which fluorescence images were taken, with representative fluorescence images for 0, 4, 6, and 15% strain. (b) Average fluorescence intensity values for each strain value calculated via ImageJ, with each color representing two separate batches of Di-AC embedded epoxy. Each fluorescence intensity value was averaged over 10 pictures for each strain.

For each selected strain percentage, the ten fluorescence images were imported into the ImageJ software, and the software calculated average fluorescence intensity values for each image. The values from all ten images were then averaged and plotted with the

standard deviations, as seen in Figure 4.2.10(b). Figure 4.2.10(b) shows fluorescence data from two separate batches of the Di-AC embedded composite. It was found that the two separate batches had different fluorescence intensity values initially, but both increased with the strain in a similar way. This shows that Di-AC can be used as a mechanophore in this system, and that applying increasing strain increases the fluorescence emission, due to the breaking of the cyclooctane bonds in the Di-AC particles, causing reversion to the fluorescent monomeric form.

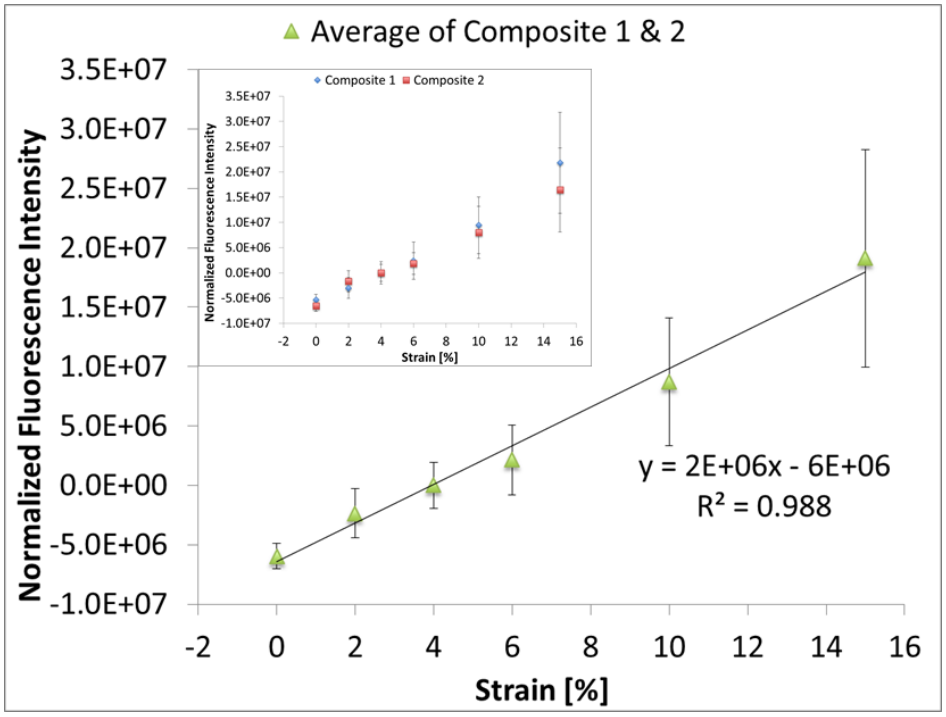

Figure 4.2.11. The resulting plot from taking the average intensity of the two composite batches for each strain value, plotted with a linear trendline, with the fluorescence intensity values for the two composite batches normalized to the 4% strain value, showing the overlaying of the curves in the inset.

Additionally, as the strain was increased, the error bars also increased. We believe this is due to the fact that as the strain was increased, plastic deformation took place in

the samples and deformed the surfaces of the epoxy, thus when the fluorescence images were taken, the emission from the mechanophore was altered due to surface roughness. This difference in initial intensity can be due to a number of factors, including the microscope having different light intensity on different days simply due to light source ageing, differences in the purity of the Di-AC incorporated, differences in how the epoxy cured and activated the particles, etc.

Regardless, when the data is normalized, the same trend is seen. Figure 4.2.11(a) shows the same data, normalized to the 4% strain value. This was done simply subtracting the corresponding 4% average fluorescence intensity value from each strain value, making the 4% strain value 0. Doing this overlays the two curves nicely, showing that even if the samples have different fluorescence initially, the overall trend is still the same. From this curve, it is clear that the 0% and 4% fluorescence values are statistically different. In order to make the curve easier to read, for each normalized strain value the ten images from each batch (20 images total) to create an overall average and overall standard deviation, as seen in Figure 4.2.11(b). This further highlights the definite statistical difference between 0% and 4% strain, and as seen in Figure 4.2.10(a), 4% strain is still in the elastic region, which means Di-AC can act as a damage precursor detector. As the region after the yield point in a stress-strain curve corresponds to plastic deformation, where irreparable damage has already taken place, it is ideal to instead achieve the damage precursor detection. In this scheme, a signal alerts to the impending material failure before the yield point (in the elastic region), so the material can be repaired or replaced. For the application of this, if an epoxy part that was incorporated with the mechanophore reached a certain fluorescence value relative to the initial fluorescence, corresponding to

4% strain, it would be known that the part is not damaged yet (it is still in the elastic region), but upon further strain, the yield point would be reached. This is a great improvement to our previous cyclobutane-based mechanophores and epoxy polymer blends, as in that system we were only able to sense damage immediately after the yield point, rather than before[159]. It could be argued that 0 and 2 % are also statically different, but there is some overlap of the error bars in the overlayed graph in the inset of Figure 8. It was also seen that the 6% intensity value was slightly higher that 4%, with the 10 and 15% values being much higher. Additionally, this characterization of the mechanochemistry is unique in that the fluorescence imaging and resulting analysis allows us to take a look at the microscale signal rather than just macroscale signal popular with visible color change mechanophores.

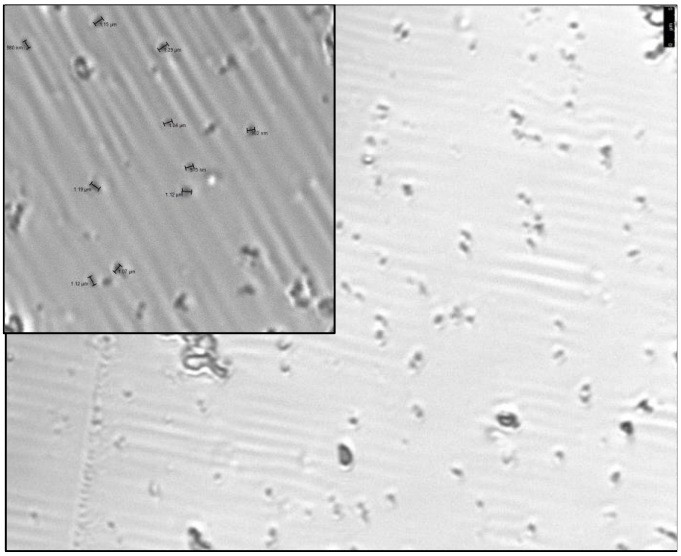

Figure 4.2.12. Confocal microscopy image of 500 μm slices of 5 wt% Di-AC epoxy, scale bar is 5 μm. Inset has approximately 1 μm scale bars at various particle locations.

There has only been one other study on the mechanochemical reversion of these cyclooctane rings formed from the photodimerization of AC back to the monomeric form

[147]. Interestingly, that group only reported successful damage detection when the cyclooctane rings were anchored onto connecting poly(vinyl alcohol) (PVA) chains, and reported no mechanophore property for the pure Di-AC powder, recording no change in the NMR spectra when the powder was ground by hand. Another group that studied the pressure-sensitivity of the strained Dewar isomer of 9-tert-butylanthracene similarly reported no pressure sensitivity for untethered dimeric anthracene [140]. Our hypothesis is that the pure Di-AC particles are held together by hydrogen bonding within the carboxylic acid group, and simple grinding of the mechanophore alone would only break these weaker bonds to form smaller particles through sliding of the particles against one another. This mechanism would thus not allow for sensing, but when the particles are embedded in an epoxy matrix, the thermoset network is formed around the particles, restraining their movement and forcing the cyclooctane rings to be broken under compression. This restraint is thus required for stress sensing with these cycloalkane rings to ensure breakage of the desired bonds.

Additionally, Figure 4.2.11 shows that a linear fit can be generated for the curve, resulting in a good fit with an R^2 value of 0.988. This implies that with the Di-AC mechanophore embedded in epoxy for stress sensing, a linear relationship can be generated between applied strain or damage and the resulting fluorescence emission, adding another novel feature to this stress sensing scheme. To ensure that the Di-AC particles remained intact in the epoxy matrix even after curing, microtome slices 500 μm thick were cut and observed under confocal microscopy (Figure 4.2.12). The particles were seen to be intact with an average particle size of 1.05 ± 0.11 μm over approximately 20 particles measured, lining up well with the DLS result of 1.5 μm.

4.3. Comparison of the Experimental and Computational Study of a Dimeric Anthracene-based Mechanophore for Early Damage Detection in Thermoset Polymer Matrices

Material failure depends on many stochastic and multiscale variables, and limited research is available on understanding the precursors to damage in complex polymeric material systems. In tandem to our groups' previous experimental research concerning cyclobutane mechanophores, computational molecular dynamics studied were performed to examine the mechanophore activation phenomena at the nanoscale while comparing experimental and simulation material property values, including the glass transition temperature [75, 171]. MD simulations were again performed for the experimental dimeric (9-anthracene carboxylic acid) particle mechanophore work in Chapter 4.2 to observe the nanoscale activation as well as to probe why Di-AC is able to detect early damage before the yield point while the cyclobutane mechanophores cannot.

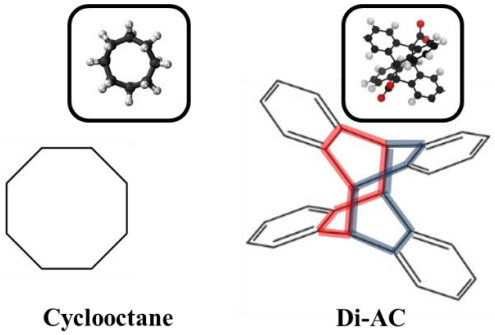

Figure 4.3.1. Chemical structure of cyclooctane (left) and di-anthracene (right).

To complete these goals, the hybrid MD simulations performed three major tasks including generating covalent bonds to simulate the epoxy curing, capturing covalent bond dissociation in the mechanophore units, and quantifying the energy required to break the covalent bonds, or bond dissociation energy (BDE), when virtual loading tests were applied. The hybrid MD simulation methodology consists of both a classical force

field and a bond order based force field (ReaxFF), as the former cannot describe covalent bond breakage while the latter can. The epoxy curing simulation was conducted through a covalent bond generation protocol using the classical force field while an appropriate bond order force field was employed to calculate BDE of the hydrocarbon compounds. Di-AC has been considered to have a "cyclooctane" type dimer, as eight carbons make up the structure between the two anthracene molecules, as seen in Figure 4.3.1.

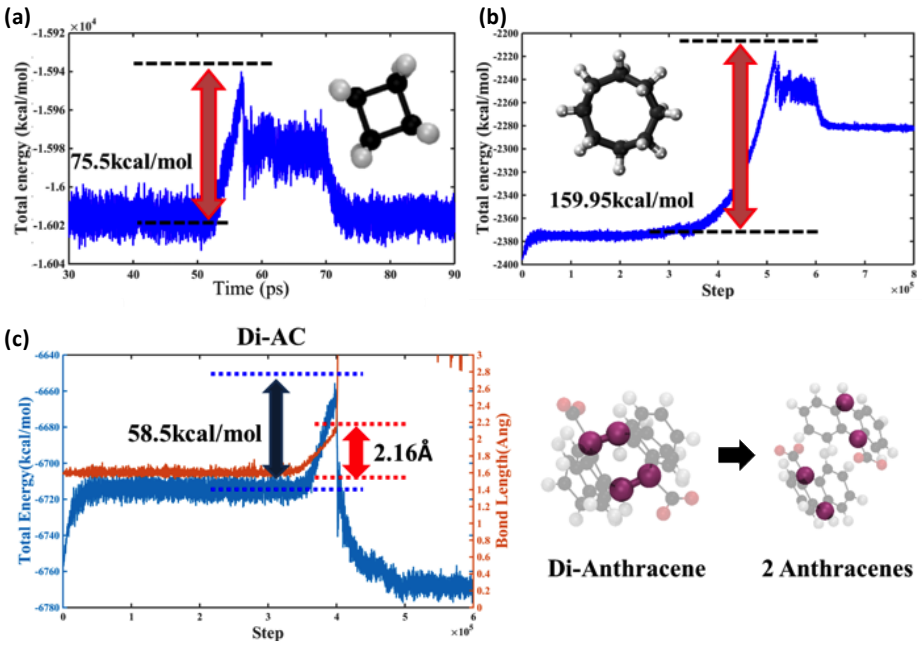

Figure 4.3.2. Bond dissociation energies of (a) cyclobutane and (b) cyclooctane. (c) Bond dissociation energy and critical length of Di-AC.

However, as the figure shows, the structure is quite different from a traditional cyclooctane ring. A cyclobutane ring is much more strained (ring strain of 26.4 kcal/mol) than a conventional cyclooctane ring (ring strain of 9.6 kcal/mol) [180]. By this reasoning, Di-AC rings should be harder to break than cyclobutane rings, however, Di-AC functioned as a better mechanophore, detecting damage earlier on. To understand the strength

of the rings in question, BDE calculations were carried out, which determine the amount of energy required to break certain bonds in the molecules. Figure 4.3.2 shows the results of the calculations, with the BDE of cyclobutane and cyclooctane being 75.5 kcal/mol and 159 kcal/mol, respectively, as would be expected since it would take more energy to break the more stable cyclooctane ring. The BDE of Di-AC was the found to be 58.5 kcal/mol with a critical length before bond breakage of 2.16 Å. This value is much lower than the BDE of cyclobutane, and thus it takes less energy to break apart a Di-AC ring, aligning with the experimental result that Di-AC has improved sensitivity than cyclobutane in that it requires less applied force to activate the dimers.

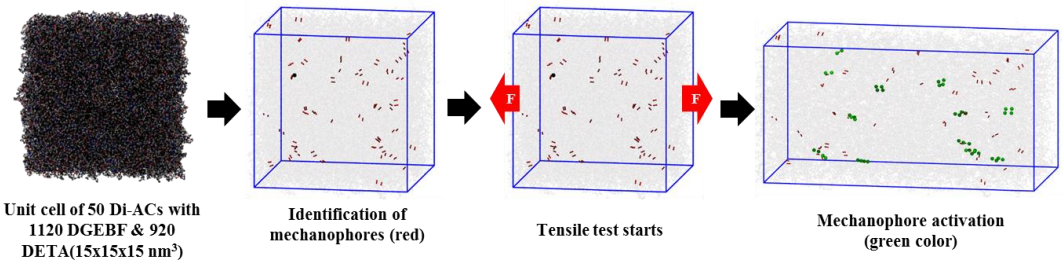

Figure 4.3.3. Procedure for simulation of mechanophore activation.

A local work analysis was performed to simulate the mechanophore activation in the composite, which showed that the number of activated mechanophores gradually increased during the deformation test (Figure 4.3.3). Due to the vast difference in length scales experiment and atomistic simulation and the much greater strain rate of strain rate of 10^{10} s^{-1}, the magnitude of yield strain and stress do not correlate well with the experimental results, however, various other properties do correlate well.

Figure 4.3.4 shows the resulting stress-strain curves from the MD simulations for both the neat and Di-AC incorporated epoxies. From the experimental work, adding the

Di-AC particles depressed the yield strength by 11.5 MPa, and from the computational work, the particles depressed it by 12.5 MPa, in good alignment. The hybrid MD methodology also captured the critical strain for mechanophore activation, before the yield strain, as seen in the left of Figure 4.3.4. For neat epoxy, the Young's modulus was found to be 2.57 ± 0.06 GPa and 2.51 ± 0.3 experimentally and from simulations, respectively, with an error of 2.3%. For the 5 wt% Di-AC composite, the Young's modulus was found to be 2.46 ± 0.06 GPa and 2.41 ± 0.3 GPa, respectively, with an error of 2.2%. Thus, the good correlation of the simulation and experimental results shows that the modeling framework can effectively guide the experimental design by estimating the effects of variability in the design parameters on material properties with some level of accuracy. The fixed design parameters for the simulations included weight fraction, curing condition (temperature/pressure), types of epoxy resin/hardener and mechanophores, thus it is anticipated that the simulations can be utilized to optimize design parameters to experimentally improve material properties such as stiffness, toughness, sensitivity or intensity of mechanophore, self-healing capability, etc., while reducing the number of experiments.

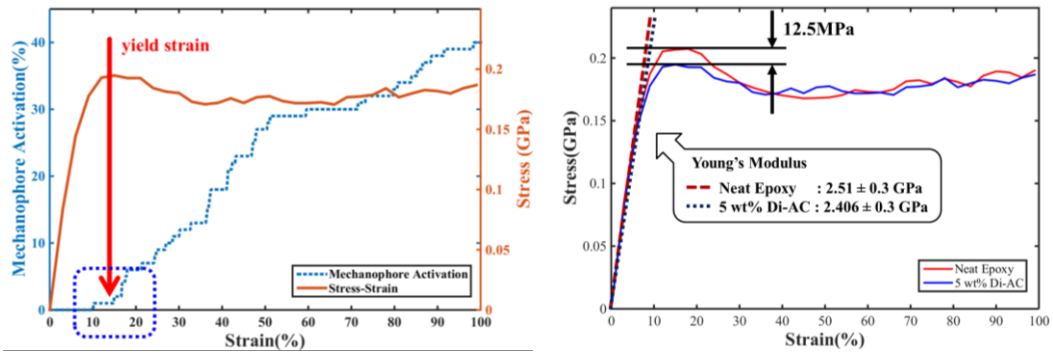

Figure 4.3.4. MD generated stress-strain curve vs. mechanophore activation plot for (left) 5 wt% Di-AC and (right) of neat-epoxy and 5 wt% Di-AC.

4.4. Universal Stress-Sensing Dimeric Anthracene-based Mechanophore Particle Fillers Incorporated into Polyurethane Thermoset Matrices

4.4.1. Formation and Material Properties of Di-AC Embedded PU Composites

Polymer mechanochemistry using mechanophores as stress sensors is a relatively new field, and little work has been done in the realm of thermosets. Following our previous work on a mechanophore particle reinforced epoxy matrix composite for damage precursor detection [181], we sought to prove the use of these novel particles as universal stress sensitive particles in thermoset matrices. There have only been a handful journal articles involving the incorporation of mechanophores into a polyurethane matrix, specifically spiropyran, dioxetane, oxanorbornadiene, diarylbibenzofuranone, and rhodamine, and all used thermoplastic/elastomeric polyurethane, rather than a thermoset [10, 182-186]. In elastomeric systems, the samples typically must be stretched to 100% or more of their initial length to activate the incorporated mechanophores, whereas we desire early damage detection of less than 4% strain in our systems. Polyurethane is an important engineering polymer, due to its robust chemical and physical properties, and the tunability of these properties by varying the chosen chemistries. Elastomeric/thermoplastic polyurethane can additionally be synthesized to contain soft (long chain polyol) and hard (diisocyanate groups and a chain extender) segments, and covalent mechanophore incorporation into these segments has been shown to be successful previously [182, 183, 185]. However, the particle incorporation method described in this work is synthetically more facile, as it simply involves mixing the mechanophore particles with the two parts of the polyurethane system to yield a particle reinforced composite with additional stress responsive capabilities. Additionally, this is the first study of an anthracene-functional mechanophore in a polyurethane matrix.

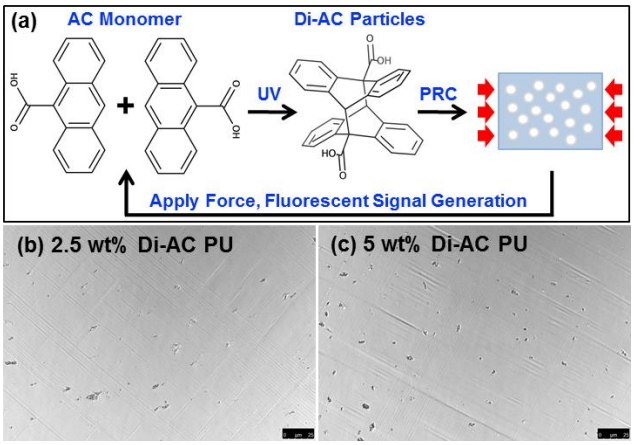

Figure 4.4.1. The top schematic shows an overview of the study, including photodimerization of the fluorescent AC monomer to the Di-AC particle mechanophore, followed by incorporation of the particles into a polyurethane matrix, with subsequent compression for the fluorescent mechanochemical activation. The bottom two confocal microscopy images show microtome sections of both the 2.5 and 5% Di-AC polyurethane composites to show the dispersion of the particles within the matrix. The scale bars are 25 μm.

9-anthracene carboxylic acid (AC) was photodimerized in solution under UV light via [4 + 4] cycloaddition to form cyclooctane-type rings, with prominently head-to-tail structures [174]. A schematic of this reaction to form the dimerized 9-anthracene carboxylic acid (Di-AC), which can be recovered as a pure white powder, can be seen in Figure 4.4.1. Di-AC is a known mechanophore, with its cyclooctane-type dimer reverting back to the fluorescent anthracene form under an applied force [147, 181]. In this work, the recovered Di-AC powered was filtered through 10 μm filter paper to remove any large aggregates and capture Di-AC particles of a micro-scale particle size. Dynamic light scattering (DLS) determined the particle size to have a Gaussian distribution for the diameter at 1512 ± 1328 nm. Figure 4.4.1 also shows the incorporation of the Di-AC particles into

a polyurethane matrix for fluorescent stress sensing under compression. The bottom two confocal microscopy images of Figure 4.4.1 show 1000 nm microtome sections of both the 2.5 and 5% Di-AC polyurethane composites, and the dispersion of the particles within the matrix can be seen. To form the mechanophore-embedded polyurethane composites, the Di-AC particles were first impeller mixed with the diisocyanate so that it would be evenly dispersed throughout the composite. The polyol was then impeller mixed into the diisocyanate-particle mixture to obtain a final homogenous mixture. This mixture was then poured into rubber molds, vacuum degassed, cured at room temperature overnight, following by thermal post curing. The compositions of 2.5 and 5 wt% Di-AC in the composites was chosen as these were the least amounts of mechanophore that could be used to still generate the desired stress sensing signal. The least amount of mechanophore was desired as incorporating the particles into polyurethane interrupts the network formed between the diisocyanate and polyol when the polyurethane cures, impacting the resulting thermal and mechanical properties of the composites.

Figure 4.4.2 shows the ATR-FTIR spectra of the pure Di-AC power mechanophore, the neat polyurethane, and the 2.5 and 5 wt% Di-AC PU composites in order to evaluate the chemical interaction between the Di-AC particles and the polyurethane matrix. The use of ATR-FTIR allows for some quantitative analysis of the peak heights generated as the entirety of the light passing through the sample and the ATR diamond is able to be detected. As polyurethane forms its thermoset crosslinked network by the reaction of diisocyanate groups with hydroxyl groups, it can be hypothesized that the diisocyanate groups can react with the –OH on the free carboxylic acid groups in Di-AC.

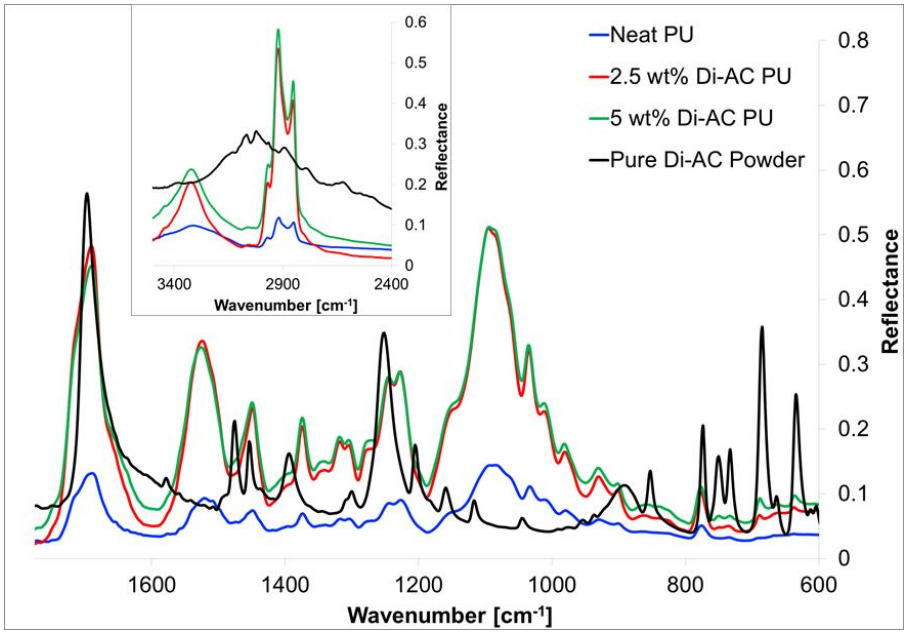

Figure 4.4.2. ATR-FTIR spectra of the pure Di-AC power mechanophore (black), the neat polyurethane (blue), and the 2.5 and 5 wt% Di-AC PU composites (red and green, respectively), with the main image being the range of wavenumbers from 1700 to 600 cm^{-1} and the inset being the range of wavenumbers from 3500 to 2400 cm^{-1}.

As Di-AC is in a microparticle form, likely held together by hydrogen bonding between its molecules, the free carboxylic acid sites that could react with the diisocyanate groups would be on the surface of the particles. Even if only a portion of the carboxylic acid groups reacted with the polyurethane matrix, this covalently embedding of the particles into the matrix could enhance the particles mechanochemical response, as the deformation of the matrix could more readily be transferred to the particles and interfacial effects would be lessened. The FTIR spectra in the inset of Figure 4.4.2 show this behavior, as the broad carboxylic acid –OH peak seen in Di-AC from 3400 – 2400 cm^{-1}, is not seen in the Di-AC composite spectra, providing evidence that at least some of the Di-AC carboxylic acid groups have reacted with the matrix [187, 188]. In this region, it can addi-

tionally be seen that the intensities of the alcohol –OH peak near 3317 cm^{-1} and the alkane C-H peaks from 3000 – 2800 cm^{-1} have been increased upon addition of the Di-AC particles. In the main image in Figure 4.4.2, multiple characteristic peaks can be observed, including the enhancement of the C=O peak near 1695 – 1685 cm^{-1} with addition of the Di-AC particles, and the strong aromatic peaks at 685 and 633 cm^{-1} in the Di-AC spectra, not present in the neat polyurethane spectra, being faintly incorporated into the composite Di-AC PU spectra. In general, all peaks present in the neat polyurethane spectra had an increased intensity when the Di-AC particles were added.

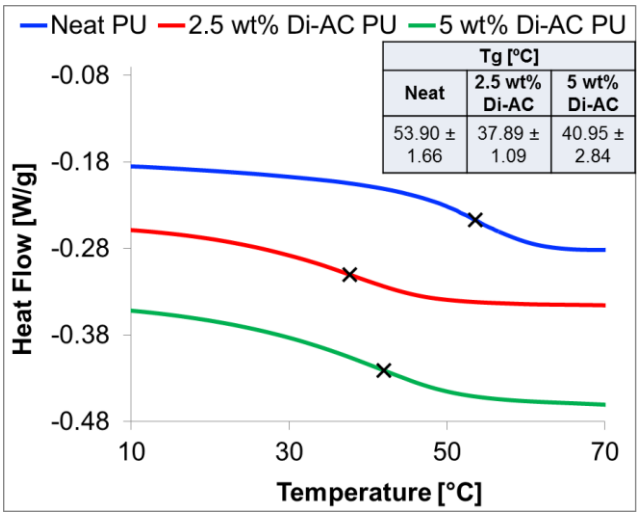

Figure 4.4.3. Representative DSC scans showing the glass transition for the neat polyurethane (blue) and the 2.5 and 5 wt% Di-AC PU composites (red and green, respectively), with the resulting Tg values (as an average of 4 runs) inset on the top right.

The thermal and mechanical properties of the Di-AC embedded composites were then obtained in order to determine the effect of adding the mechanophore on these properties. Differential Scanning Calorimetry (DSC) was used to determine the glass transition temperature (Tg) of the various samples. Representative DSC scans for the neat and

Di-AC polyurethane composites can be seen in Figure 4.4.3, the Tgs were calculated at the step-wise transition in the curves using the TA Universal Analysis software. The average Tg values over 4 runs were 53.90 ± 1.66 °C, 37.89 ± 1.09 °C, and 40.95 ± 2.84 °C, for the neat, 2.5 wt% Di-AC, and 5 wt% Di-AC polyurethane samples, respectively. This results in a decrease of the Tg from the neat of approximately 13 to 16 °C for 5 and 2.5 wt% particle addition, respectively. This Tg depression can be expected as the particles interrupt the thermoset network formation.

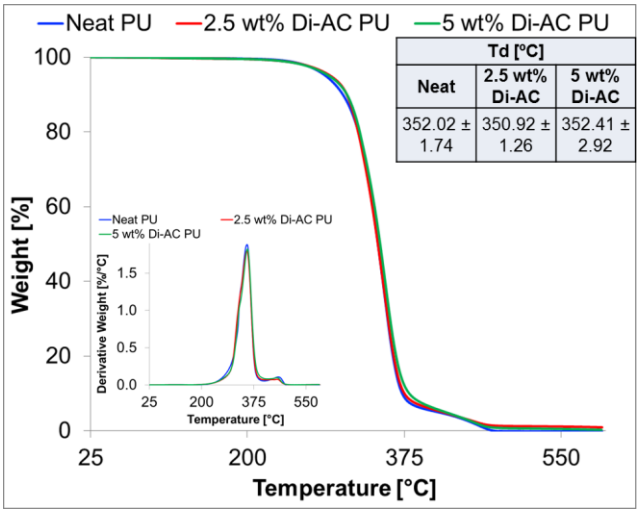

Figure 4.4.4. Representative TGA curves showing the thermal decomposition of the neat polyurethane (blue) and the 2.5 and 5 wt% Di-AC PU composites (red and green, respectively), with the resulting Td values (as an average of 4 runs) inset on the top right.

Figure 4.4.4 shows representative Thermogravimetric Analysis (TGA) for the samples, with the corresponding Differential Thermal Gravimetry (DTG) curves in the inset left. These tests were run under nitrogen to eliminate weight loss due to oxidation, and thus purely capture the thermal decomposition of the bonds within the polyurethane samples. The main decomposition temperatures (Td) were found via the peaks in the

DTG curves, and were 352.02 ± 1.74 °C, 350.92 ± 1.26 °C, and 352.41 ± 2.92 °C, for the neat, 2.5 wt% Di-AC, and 5 wt% Di-AC polyurethane samples, respectively. These values are not statistically different from each other, thus the addition of the mechanophore particles did not significantly change the Td. It is worthwhile to note that the main Td of the pure Di-AC powder (prior to embedding) was found to be 244.50 ± 1.83 °C, which is relatively high and likely contributed to the particle addition not significantly affecting the Td of the embedded composite.

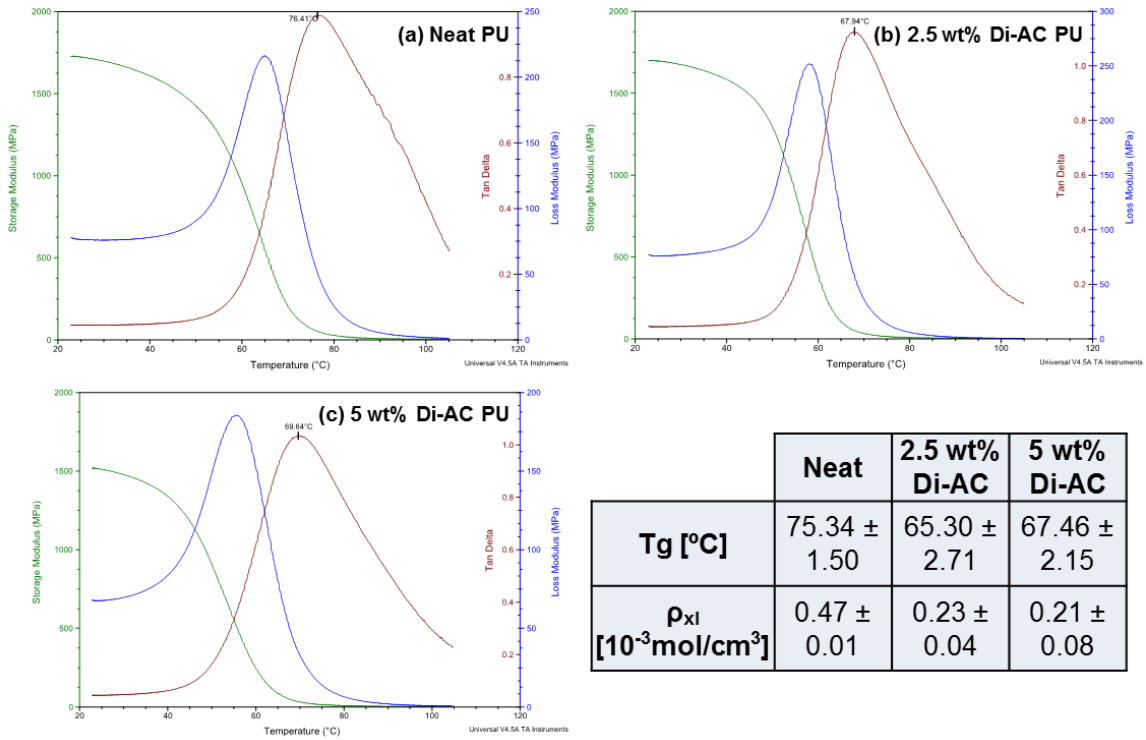

	Neat	2.5 wt% Di-AC	5 wt% Di-AC
Tg [°C]	75.34 ± 1.50	65.30 ± 2.71	67.46 ± 2.15
ρ_{xl} [10^{-3}mol/cm^3]	0.47 ± 0.01	0.23 ± 0.04	0.21 ± 0.08

Figure 4.4.5. DMA curves showing the Storage Modulus (green), Loss Modulus (blue), and Tan Delta (maroon) of the (a) neat polyurethane, (b) 2.5 wt% Di-AC composite, and (c) 5 wt% Di-AC composite, respectively. The inset table shows the average Tg and ρ_{xl} of the samples determined from the DMA curves.

Dynamic Mechanical Analysis (DMA) can be used in addition to DSC to determine Tg values, as well as determine the crosslink density of the polyurethane samples (Figure 4.4.5). The DMA measures the storage and loss moduli of a sample by physically oscillating the sample, with the ratio of the two being defined as tan delta (tan δ). The peak of the tan δ curve is then used to determine the Tg value for the sample. From DMA, the Tg values over 4 runs of each sample were 75.34 ± 1.50 °C, 65.30 ± 2.71 °C, and 67.46 ± 2.15 °C, for the neat, 2.5 wt% Di-AC, and 5 wt% Di-AC polyurethane samples, respectively. This makes for an approximate depression of the Tg by 10 and 8 °C for the 2.5 and 5 wt% Di-AC composites from the neat, respectively. It should be noted that this depression is slightly less than what was seen with the DSC, and that all of the Tg values are greater with the DMA compared to the DSC. Additionally, there was an approximate 2 °C increase in the Tg for the 5 wt% Di-AC PU compared to the 2.5 wt% Di-AC PU. These results can be hypothesized to be from the mechanical determination of the Tg in DMA, rather than the thermal determination in DSC. This mechanical determination then can allow for some small particle reinforcement behavior in the 5 wt% value that was not seen in the DSC measurements. To calculate the crosslink density, the theory of rubber elasticity can be utilized [179], $\rho_{xl} = \frac{G'}{3RT}$, where ρ_{xl} is the crosslink density expressed in moles of elastically effective network chains per cm^3 of sample, G' is the rubbery plateau modulus, R is the Gas Constant, and T is the absolute temperature at which the rubbery plateau modulus is determined. The crosslink densities were thus calculated to be 0.47 ± 0.01 × 10^3 mol/cm^3, 0.23 ± 0.04 × 10^3 mol/cm^3, and 0.21 ± 0.08 × 10^3 mol/cm^3, for the neat, 2.5 wt% Di-AC, and 5 wt% Di-AC polyurethane samples, re-

spectively. Thus, there was a significant decrease in the crosslink density upon addition of the Di-AC particles due to the disruption of the polyurethane network formation.

4.4.2. Mechanochemical Fluorescence Signal Generation for Damage Precursor Detection

A compressive force was used to apply measurable and repeatable damage to the thermoset polyurethane samples, and certain strain values were chosen to determine the resulting mechanochemical response. From these compression tests, stress-strain curves of the neat and composite polyurethane samples were generated to identify whether certain strain values were in the elastic or plastic deformation region of the curve, and to evaluate the change in the mechanical properties after Di-AC particle incorporation. Figure 4.4.6 shows the resulting stress-strain curves for all three sample types. The Young's modulus values in the linear elastic region of the curve were found to be 1.48 ± 0.02 GPa, 0.97 ± 0.10 GPa, and 1.27 ± 0.09 GPa for the neat, 2.5 wt% Di-AC, and 5 wt% Di-AC polyurethane samples, respectively. Thus, there was a notable decrease in the Young's modulus upon 2.5 wt% particle addition, but recovery of some of this loss upon increasing the particle content to 5 wt%. Similarly, the yield strength values were 62.19 ± 0.30 MPa, 39.08 ± 0.78 MPa, and 50.93 ± 0.16 MPa for the neat, 2.5 wt% Di-AC, and 5 wt% Di-AC polyurethane samples, respectively. The depression of the Young's modulus and yield strength values can be attributed to the particles disrupting the polyurethane network, however, when 5 wt% particles are added, there is some particle reinforcement behavior, and thus some recovery of the mechanical properties.

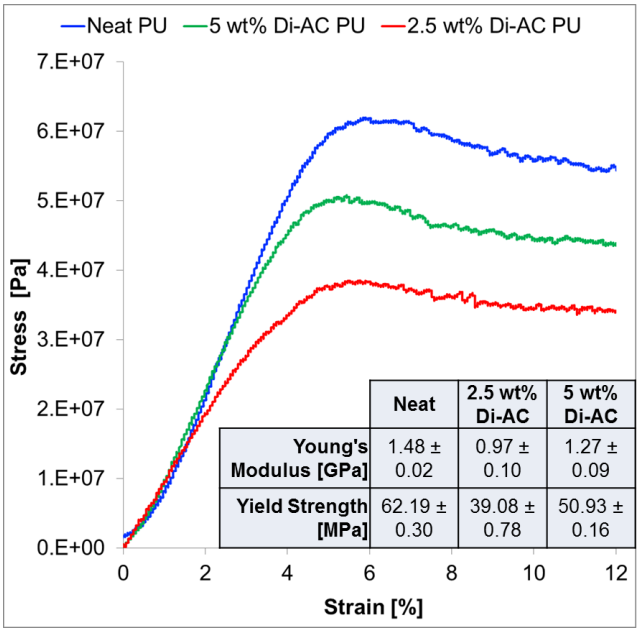

Figure 4.4.6. Stress-strain curves for the neat polyurethane (red) and the 2.5 and 5 wt% Di-AC PU composites (red and green, respectively), with the lower right inset showing the resulting Young's Modulus and Yield strength values.

The selected strain values from the compression tests for the fluorescence imaging were 0, 2, 4, 6, 10, and 15%, and representative images for these strains for both the 2.5 and 5 wt% Di-AC composites can been seen in Figure 4.4.7a and b, respectively. These images were taken under excitation of 340–380 nm UV light, with a filter cube to capture the light emission between 435–485 nm. The 8-bit gray scale fluorescence images from the microscope were subsequently pseudocolored green with the built-in "Green" LUT in ImageJ, and all of the images seen in Figure 4.4.7 were further enhanced by increasing both the brightness and contrast by 40% for better visualization of the increase in fluorescence with an increase of the strain applied. Correlating the selected strain values seen in Figure 4.4.7 with the compression test curves, 0% strain is prior to compression, to provide a baseline for the testing, and 2% and 4% strain are in elastic region, with

2% in the approximate middle of the region and 4% immediately before the yield point. 6% strain is immediately after the yield point, and 10 and 15% strain are well into the plastic region.

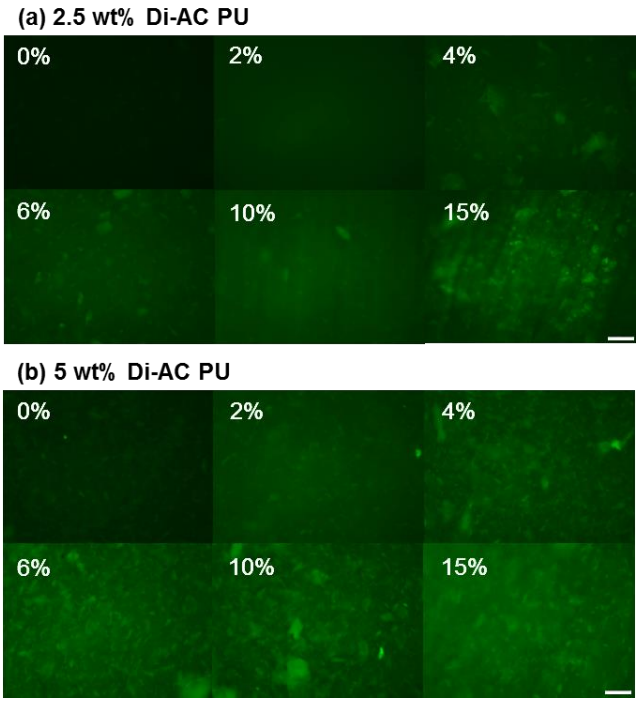

Figure 4.4.7. Representative fluorescence images for the mechanophore-embedded polyurethane composites identifying the strain values for which the images were taken, for (a) 2.5 wt% Di-AC and (b) 5 wt% Di-AC. Scale bars are 50 μm. The images were pseudo-colored green and the brightness and contrast were increased by 40% to enhance the visual analysis of the images.

Comparing each strain value between the 2.5 and 5 wt% Di-AC composites, it can be seen that the 5 wt% Di-AC composite has slightly higher fluorescent emission overall compared to the 2.5 wt%, which is expected as some baseline fluorescence exists for the Di-AC mechanophore on its own, thus using more of it increases the overall fluorescence. For both weight percents studied, an obvious increase in the fluorescence for the

2% compared to the 0% strain can be seen visually, and this fluorescent increase can be seen with the increasing applied strain. This visualization of the fluorescence change at 2% is a form of very early damage detection, as 2% strain is firmly in the elastic region of the stress-strain curve. Additionally, for 2.5 wt% Di-AC, in the 0 and 2% strain images, individual particles are not seen, but with the 4% strain and above, clear activated particle aggregates can be observed, along with the overall increase in the background fluorescence. For the 5 wt% Di-AC, particle aggregates can be faintly observed in the 0% strain image, with their fluorescence increasing over the applied strain. This difference is simply due to the increase in particles used in the 5 wt% composite compared to the 2.5 wt% composite.

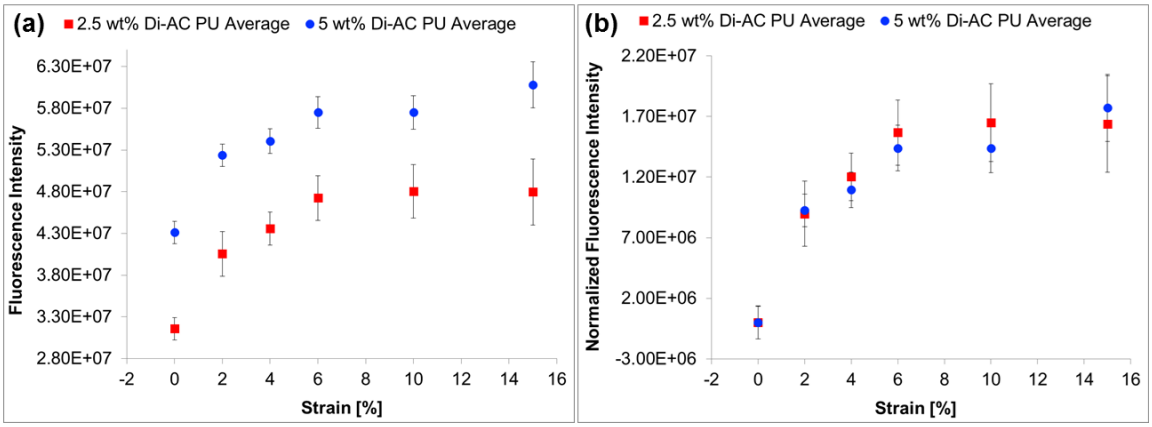

Figure 4.4.8. (a) Average fluorescence intensity values for each strain value calculated via ImageJ, for the 2.5 and 5 wt% Di-AC PU composites (red and blue, respectively). Each fluorescence intensity value was averaged over 32 pictures for each strain. (b) By normalizing both curves to the 0% strain value, the overlaying of the curves shows the same trend regardless of the weight fraction of Di-AC used.

In order to fully evaluate the functionality of the synthesized mechanophore-embedded composites for damage precursor detection, quantification of the change in the fluorescence intensity with the applied strain was required, and can be seen in Figure 4.4.8. To quantify the fluorescence intensity at each of the studied strain values, the "Measure" function in ImageJ was used on the raw 8-bit grayscale images obtained from the fluorescence microscope. The ImageJ software generated an average fluorescence intensity value for each of the images by taking the sum of the pixel values in the image and then averaging the intensity at each point. At each of the selected strain values from the compression tests, eight fluorescence microscopy images were taken for each sample, representative of the entire sample face. Four samples were used per each strain value (2 each from 2 separate composite batches), thus each point seen in Figure 4.4.8 is the average of 32 fluorescence images with the corresponding standard deviation values. Reinforcing the qualitative trend seen with the fluorescence images in Figure 4.4.7, Figure 4.4.8 clearly shows the enhancement in fluorescence with applied strain for both the 2.5 and 5 wt% Di-AC composites. Figure 4.4.8a shows the raw fluorescence intensity values calculated from ImageJ, and it can be seen that the 5 wt% Di-AC composite indeed has a higher overall fluorescence, due to the increased amount of particles used. For both weight percents used, there is a marked increase in the fluorescence intensity between 0 and 2% strain, with a lesser increase when moving up to 4 and 6% strain, leveling off after the 6% strain. This extreme increase in the observed fluorescence after only 2% strain shows this system's capability for damage precursor detection, in which the sample has not been irreversibly deformed at all, but the clear fluorescent signal is present, even with a very low mechanophore particle concentration of 2.5 wt%. In our previous work with

Di-AC in epoxy, 5 wt% of the Di-AC particles were required to observe the mechanophore activation, and there was not such a clear signal at 2%, with 4% identified as the early damage detection point [181]. Additionally, the epoxy and polyurethane systems had similar starting fluorescence values comparatively, so it is hypothesized that this increase in the fluorescent signal observed is due to some interaction with the Di-AC particles in polyurethane rather than epoxy, as discussed for the FTIR spectra for the Di-AC polyurethane composites in Figure 4.4.2 of this work. This is likely due to the possibility of some of the carboxylic acid groups on the surface of the Di-AC particles being able to react with the diisocyanate groups of the polyurethane, while the epoxide-amine reaction in epoxy is favored over reaction of the Di-AC carboxylic acid groups and the epoxide rings [189]. Covalent bonding of the particles to the polyurethane matrix would then cause an increased fluorescence response as any deformation to the matrix would be more efficiently transferred to the stress-sensitive particles, and interfacial effects would be lessened. Figure 4.4.8b shows the overlay of the 2.5 and 5 wt% Di-AC polyurethane curves by normalizing both curves to their respective 0% strain values, and there is very good agreement for all values between the two weight percents, especially for the 2% strain. This analysis shows that this behavior is intrinsic to the Di-AC particle mechanophore used, and not dependent on the weight fraction of particles. However, while the used of the lesser value of 2.5 wt% is appealing, the reduction in the thermal and mechanical properties of these composites makes the use of the 5 wt% composites more desirable, as the damage detection functionality is present with a comparative increase of the thermal and mechanical properties.

4.5. Stress-Sensing Thermoset Polymer Network via Grafted Cinnamoyl/Cyclobutane Mechanophore Units in Epoxy

4.5.1. Formation of the Mechanophore-Grafted Self-Sensing Thermoset Network Polymer

As previously mentioned, the incorporation of mechanophores into networked thermosets, such as epoxy, is notably missing from the mechanochemistry literature, which focuses on more traditional thermoplastics and elastomers. Thermosets find ubiquitous use due to their excellent mechanical and physical properties, including in printed circuit boards, high-performance adhesives, military personal protective equipment (PPE), and various marine, aerospace, and other applications. Cured epoxy resins are generally quite brittle, with a propensity to crack if exposed to sufficient stress and strain, leading to irreversible damage such as microcracking. Several studies incorporate SP and other mechanophores into the backbone of linear, thermoplastic or elastomeric polymers such as PMA, causing the mechanophore activation in these systems to require a relatively large deformation [190]. Also, when a mechanophore is incorporated into polymer chains, it requires an appropriate position relative to the polymer backbone, because mechanophores can only be force-activated if the force can be effectively transferred through the bulk material to individual chains, then to the cleavable bonds on the mechanophore units [191]. The networked polymer nature of thermosets thus provides a unique platform to study mechanochemistry, due to their ubiquitous use, superior physical properties, and unique molecular architecture. In this work, we proposed and completed the novel direct covalent grafting of photoactive mechanophore units into an epoxy matrix (a two-part network polymer), to create a self-sensing thermoset network, linked by both epoxide and mechanophore bonds. The goals of this work include being able to detect of microcracks by fluorescent spectroscopy, being able to link the degree of

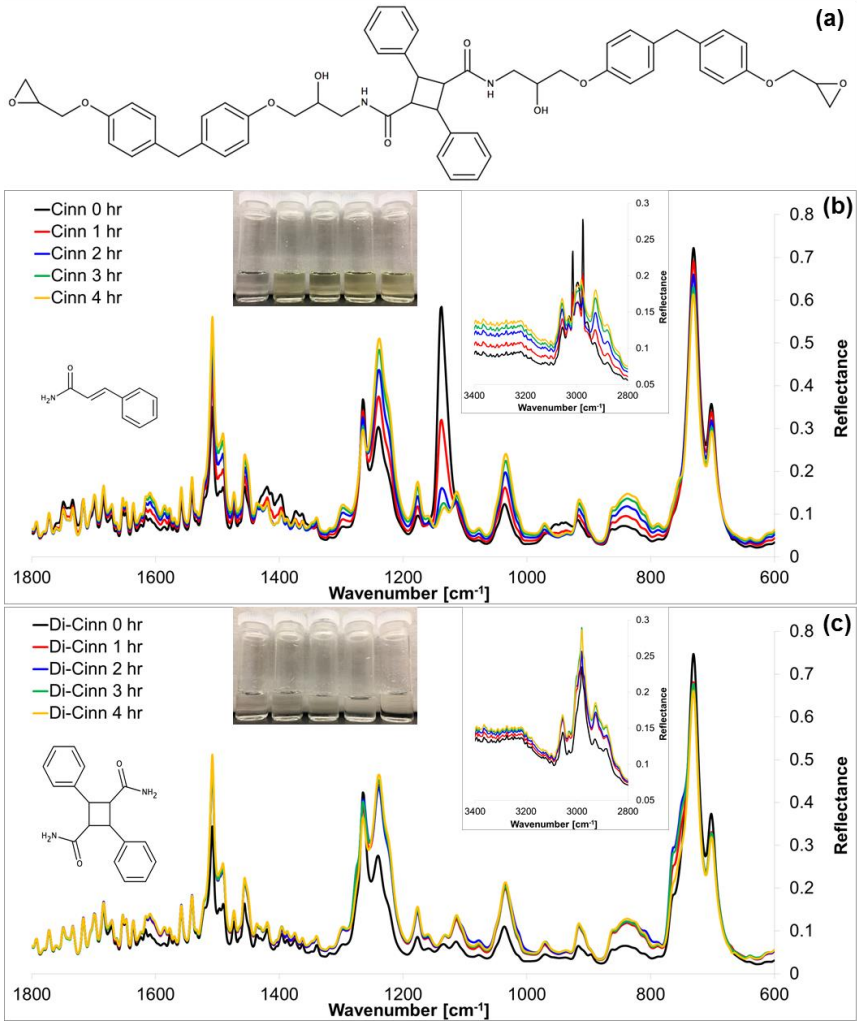

Figure 4.5.1. (a) Chemical structure of a cinnamamide dimer di-substituted with the epoxy resin diglycidyl ether of bisphenol F. (b) ATR-FTIR spectra for the reaction of cinnamamide (chemical structure inset left) with DGEBF over reaction time, inset macroscopic image of the reaction solution over reaction time, inset ATR-FTIR spectra of the region between 3400 and 2900 cm^{-1}. (c) ATR-FTIR spectra for the reaction of di-cinnamamide (chemical structure inset left) with DGEBF over reaction time, inset macroscopic image of the reaction solution over reaction time, inset ATR-FTIR spectra of the region between 3400 and 2900 cm^{-1}.

damage with the fluorescence quantum yield, early damage precursor detection, environmental robustness, and excellent retention of the mechanical and thermal properties of the composite. This systematic and novel work will also provide further fundamental understanding of mechanochemistry as a whole.

In our previous work, which utilized photodimerization of cinnamoyl functional groups to create cyclobutane stress-sensing moieties [159], the mechanophores were simply used as additives in the polymer blends, thus the self-sensing could only occur between the stress-sensing molecules, and any damage done to the matrix polymer could not be sensed, the fluorescent nature only serving as a signal to the damage. Another notable drawback of utilizing mechanophores as additives was the significant lowering of the glass transition temperature of the system, narrowing the temperature window in which the composite can be used. Thus, we proposed to overcome these limitations by the direct covalent incorporation of the mechanophore units into an epoxy network thermoset polymer to create a novel functionalized nanocomposite system.

For this study, the mechanophore precursor chosen was cinnamamide (Cinn, chemical structure in Figure 4.5.1b inset left), as it is commercially available and its amine group can covalently bond to the epoxy resin chosen (diglycidyl ether of bisphenol F, DGEBF), in a similar matter to the crosslinking of the resin with the chosen hardener (diethylenetriamine, DETA) in the neat epoxy system. Cinnamamide is known to be able to form a cyclobutane type dimer (di cinnamamide, Di-Cinn, chemical structure in Figure 4.5.1c inset left) under UV photoirradiation via [2 + 2] cycloaddition. Thus two routes are studied in this work for the mechanophore covalent incorporation into an epoxy matrix, the first being the reaction of the cinnamamide mechanophore precursor with DGEBF to

ensure covalent bond formation, with subsequent hardener addition. The epoxy mixture is then UV cured so that the cyclobutane mechanophore units can be formed via photodimerization, while the conventional resin-hardener curing is taking place. The second route is to first form di-cinnamamide in solution under UV light, then to react it with DGEBF, with subsequent hardener addition and conventional epoxy bond formation. In this second method, it is expected that more cyclobutane rings will be present in the final nanocomposite, as Di-Cinn is theoretically 100% dimerized prior to addition. In this route, the penetration depth for curing an epoxy sample and the UV curing efficiency do not play a role. In the Cinn-containing composite, this dimerization occurs in the viscous epoxy resin-hardener solution, and thus there is competition between the two types of crosslink formation as well as a physical impedance for the cinnamoyl groups to find each other in the mixture and dimerize, compared to simple dimerization in solution.

To form the studied nanocomposites, the cinnamamide dimer was first synthesized by dissolving cinnamamide in diethyl ether under magnetic stirring and a nitrogen purge. The solution was then photoirradiated with a 302 nm wavelength UV lamp for two days to carry out the [2+2] cycloaddition for the formation of the cyclobutane rings. The white Di-Cinn precipitate was then washed and dried to obtain a pure product. To form the studied nanocomposites consisting of covalently bonded 10 wt% cinnamamide or 10 wt% di-cinnamamide in epoxy, each were first reacted with the resin to ensure the covalent bond formation between the amine hydrogens in Cinn or Di-Cinn and the epoxide rings of DGEBF. This was performed by adding cinnamamide or di-cinnamamide to DGEBPF with dichloromethane as a solvent. This mixture was then heated at 40 ºC for 4 hr under a nitrogen purge and magnetic stirring to promote the reaction between the

epoxide rings and the amine groups. The dichloromethane solvent was then removed under reduced pressure and the diethylenetriamine hardener was added to each functionalized resin mixture, with the hardener/resin/mechanophore weight ratio calculated according to the manufacturer's recommendations and the epoxide/amine equivalent weight. The amount of mechanophore vs. epoxide crosslinks must be balanced in order to allow for the desired sensing signal while not depressing the thermal and mechanical properties of the matrix. These mixtures were then impeller mixed at room temperature until homogenous and subsequently poured into silicone rubber molds and allowed to cure overnight at room temperature, with the cinnamamide epoxy being UV cured for 4 hr under 365 nm light prior to leaving in darkness to complete the curing. Neat epoxy samples were prepared in a similar manner with a 100:27 ratio of resin to hardener.

The chemical structure in Figure 4.5.1a shows a cinnamamide dimer disubstituted with DGEBF, with the resin containing two active epoxide ring end groups than can covalently bond with an amine hydrogen active site. Theoretically, each amine from a cinnamamide group has two free active hydrogen sites that could participate in this reaction (with 4 total for a di-cinnamamide molecule), but as seen in Figure 4.5.1a, sterical hindrance of the reaction should be taken into account. Because the cinnamamide or di-cinnamamide first reacts with the resin molecule, there is a higher probability for increased covalent bonding to occur (compared to if this reaction happened in the epoxy *in situ*), however there is likely a higher substitution occurring with cinnamamide compared to di-cinnamamide, due to the steric hindrance. Thus, to evaluate the amount of substitution, ATR-FTIR was performed on the reaction solutions of cinnamamide/di-cinnamamide and DGEBF in dichloromethane, as seen in Figure 4.5.1b and c, respective-

ly. Interestingly, in the reaction solutions for either chemistry, the primary amine hydrogen peaks representative of Cinn and Di-Cinn at 3367 and 3157 cm^{-1} (seen in Figure 4.5.2a) are not present in the FTIR scans. However, there are other important functional group peaks present to evaluate the mechanophore-resin grafting over the reaction time. As the Attenuated Total Reflectance FTIR accessory was used on these samples, some quantitative analysis regarding the change in peak height over the reaction time can be made. For both the cinnamamide- and di-cinnamamide-resin reaction FTIR spectra in Figure 4.5.1b and c, important functional group peak changes over reaction time include a slight reduction of the 730 and 700 cm^{-1} peaks for the aromatic C-H bend, attributed to the change in aromaticity upon grafting; the dramatic increase of the peak at 1032 cm^{-1}, for the formation of new C-OH bonds upon opening of the epoxide rings; an increase at 1175 cm^{-1}, again for the new C-OH stretch; a dramatic increase near 1237 cm^{-1} for the for the C-O-C ether stretch in DGEBF change in conjugation; a decrease at 1265 cm^{-1} for the removal of the C-O stretch in the epoxides; an increase at 1454 cm^{-1} for the C-H aliphatic hydrogens; and increases at 1490, 1508, and 1606 cm^{-1} for the benzene ring, due to its change in conjugation over the reaction time. In only the cinnamamide-resin reaction FTIR spectra, there is a dramatic reduction of the peak at 1140 cm^{-1}, which can be correlated to the loss of the C-N amine peak, specifically for primary amines [192-195].

In the inset spectra in Figure 4.5.1b and c showing the wavenumbers from 3400 and 2900 cm^{-1}, there is an overlaying of the peaks for the C-H bonds of the aromatics, alkanes, and epoxide rings. For both cinnamamide and di-cinnamamide, there is an increase of the 3055, 2980, and 2924 cm^{-1} peaks, and for cinnamamide, there is a clear removal of the 2976 and 3015 cm^{-1} peaks after the reaction is completed. As the conjuga-

tion and interactions of the molecules can obscure the specific identification of theses peaks, the simple change in peak intensity and the removal of certain peaks in this region will provide the additional evidence of the procession of the mechanophore-resin reaction, with the more defined evidence from the spectra at the smaller wavenumbers.

A macroscopic viewing of the functionalization is additionally seen in the inset images of Figure 4.5.1b and c, which shows diluted reaction solution aliquots taken at 0, 1, 2, 3, and 4 hr from left to right. At 0 hr, before the reaction occurred, both Cinn and Di-Cinn reaction solutions were colorless, due to the solubility of both in dichloromethane. However, after only 1 hr reaction, cinnamamide reaction solution turned fluorescent opaque yellow, with the amount yellow color increasing as the reaction proceeded. This color change is a visible signal of the resin-mechanophore functionalization, as the UV fluorescence of the cinnamamide is shifted to the longer visible wavelengths upon reaction with the large resin molecules. The di-cinnamamide reaction solution turned white and opaque as the reaction proceeded, with is expected as the functionalized di-cinnamamide resin should not have intrinsic fluorescence unless the dimers are broken under a mechanical stress.

The ATR-FTIR spectra of the pure cinnamamide crystals and di-cinnamamide power can been seen in Figure 4.5.2a, with the important primary amine hydrogen peaks at 3367 and 3157 cm^{-1}. Other defining peaks for the spectrum include the C=O carbonyl stretch, and various aromatic peaks, below 1700 cm^{-1}. Figure 4.5.2c shows the resulting ATR-FTIR spectra for the neat epoxy, and the 10 wt% Cinn and 10 wt% Di-Cinn epoxy nanocomposites, with the Cinn composite having undergone UV curing. A macroscopic image of the epoxy samples on a light blue background can be seen in the inset of Figure

4.5.2c, with the neat epoxy being translucent, the 10 wt% Di-Cinn epoxy being opaque white, and the 10 wt% Cinn epoxy being opaque yellow; the fluorescent yellow color of the Cinn composite being a visual indicator of its intrinsic fluorescence even before damage is applied, due to the lower amount of cyclobutane formation as a result of UV dimerization in curing epoxy mixture. In the neat and composite epoxy FTIR spectra, the clear, broad –OH peak near 3300 cm^{-1} is present, due to the opening of the epoxide rings during epoxy curing. It should be noted that the 10 wt% Di-Cinn composite spectrum exhibits flattening out of this peak and small peak at 3350 cm^{-1} compared to the other spectra, which can be evidence that the Di-Cinn composite still retains some of its amine hydrogens, likely only moving from the primary amine to the secondary amine form, due to the increase in the steric hindrance in the Di-Cinn-DGEBF reaction, as compared to the Cinn-DGEBF reaction. The smooth nature of the Cinn peak in the region implies that all or most of its amine hydrogens were removed during its reaction with the resin. This difference in the bonding between Cinn and Di-Cinn with the epoxy matrix can result in differences in the mechanochemical response discussed below. Compared to the neat epoxy, the Cinn and Di-Cinn composites exhibit additional peaks at 2916 and 2846 cm^{-1}, with an additional peak for Cinn at 2941 cm^{-1}. These peaks are representative of newly present aromatic and alkane C-H bonds in the nanocomposites. Other important functional group peaks can be seen below 1700 cm^{-1}, and are similar to the peaks discussed above in Figure 4.5.1. Overall, from the ATR-FTIR spectra of the reaction between the cinnamamide and di-cinnamamide and DGEBF, along with the spectra for the final nanocomposites, there is sufficient evidence for the covalent grafting of the mechanophore units into the thermoset epoxy network.

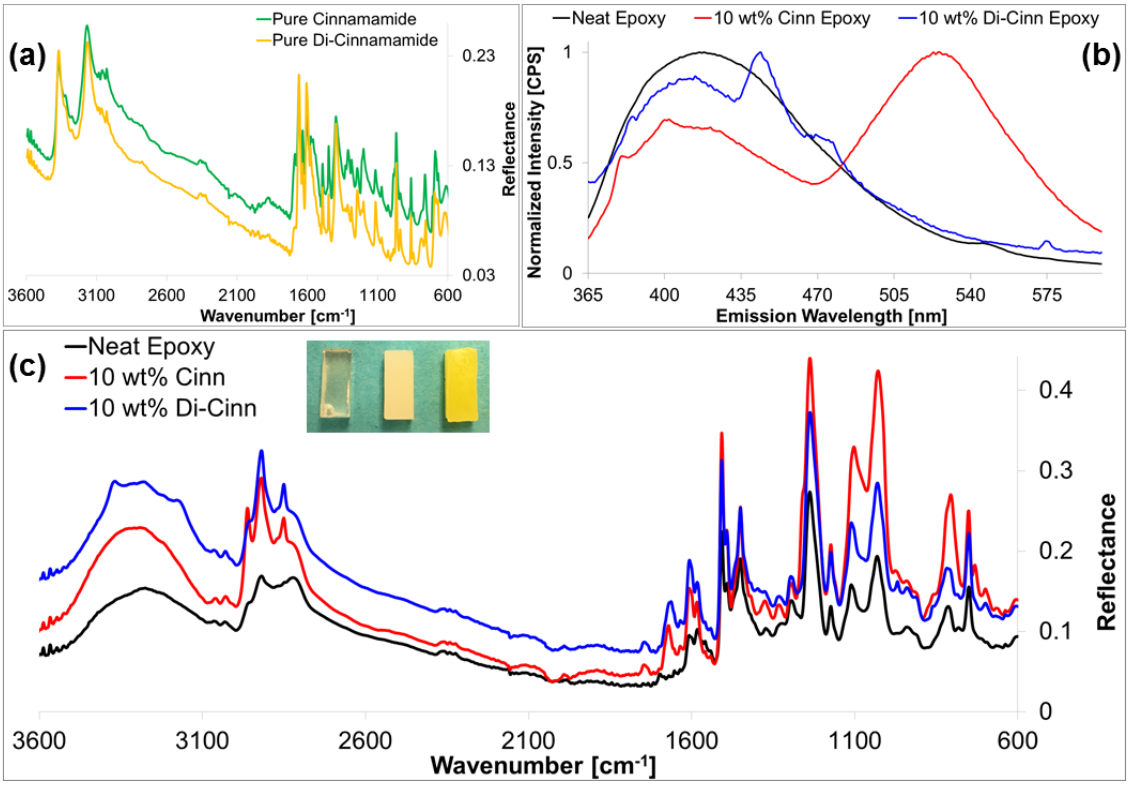

Figure 4.5.2. (a) ATR-FTIR spectra comparing cinnamamide (green) with di-cinnamamide (orange). (b) Emission spectra the neat epoxy (black), 10 wt% Cinn epoxy (red), 10 wt% Di-Cinn epoxy (blue) for an excitation wavelength of 350 nm. (c) ATR-FTIR spectra comparing the neat epoxy (black), with the 10 wt% Cinn epoxy (red) and 10 wt% Di-Cinn epoxy (blue), with the inset image showing the neat epoxy, the 10 wt% Di-Cinn epoxy, and the 10 wt% Cinn epoxy samples (from left to right).

Figure 4.5.2b shows the comparison of the fluorescent emission for the neat epoxy, and the Cinn and Di-Cinn composites under 350 nm excitation, with each curve normalized to its maximum emission. Both the neat and Di-Cinn epoxy samples have similar emission with the maximum between 370 and 470 nm, while the Cinn epoxy have its maximum emission at the higher wavelength range of 500 to 600 nm. This confirms the macroscopic fluorescent visualization of the composite samples mentioned above,

and as the emission wavelengths gathered in the subsequent fluorescence microscopy imaging are between 500 and 550 nm, it is expected that the neat and Di-Cinn samples will have a much lower intrinsic or baseline fluorescence as compared to the Cinn samples.

4.5.2. Effects of Mechanophore-Grafting on the Nanocomposite Material Properties

As the newly formed nanocomposites feature covalent incorporation of the mechanophore units, it is desired to evaluate their effect on the material properties. Differential Scanning Calorimetry (DSC) was used to determine the glass transition temperature (Tg) of the neat and mechanophore incorporated samples. A representative DSC scan for the neat epoxy can be seen in Figure 4.5.3a, with scans for the 10 wt% Cinn and Di-Cinn composites in Figure 4.5.3b. The Tg values were calculated at the step transition in the curves with the TA Universal Analysis software. The average Tg values over 4 runs were 47.85 ± 3.01 °C, 41.46 ± 0.82 °C, and 42.28 ± 1.22 °C, for the neat, 10 wt% Cinn, and 10 wt% Di-Cinn samples, respectively. This results in a decrease of the Tg from the neat of approximately 6 °C for both the mechanophore nanocomposites. This Tg depression can be expected as the newly formed mechanophore bonds are not as thermally stable as the neat epoxy network, however a 6 °C lowering relatively low compared to other work regarding mechanophore incorporated composites. Figure 4.5.3c shows SEM images of the neat and composite samples, with some difference in the surface morphology observed, but not a significant enough different to imply phase separation. Additionally, as the DSC scan only reported one Tg, it is additionally confirmed that the mechanophore units are successfully grafted and miscible with the matrix.

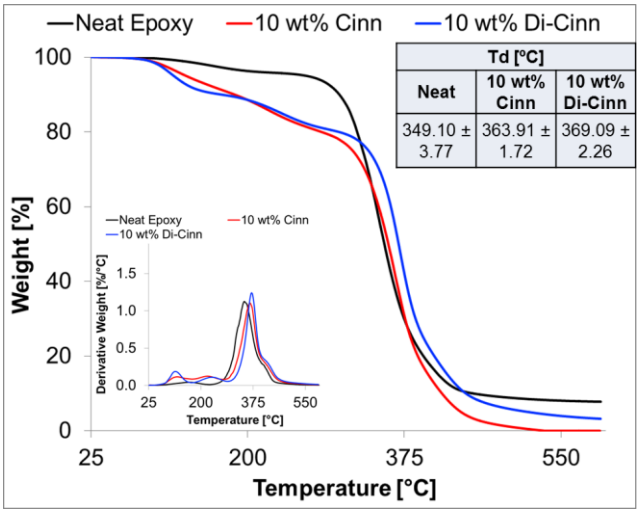

Figure 4.5.4. Representative TGA curves showing the decomposition of neat epoxy (black), and the 10 wt% Cinn (red) and 10 wt% Di-Cinn (blue) epoxy composites, with the resulting major Td values (as an average of 4 runs) inset on the top right. The inset left shows the respective DTG curves to determine the Td values.

Figure 4.5.4 shows representative Thermogravimetric Analysis (TGA) for the samples, with the corresponding Differential Thermal Gravimetry (DTG) curves in the inset left. These tests were run under nitrogen to prevent weight loss due to oxidation, and thus purely capture the thermal decomposition of the bonds within the epoxy samples. The main decomposition temperatures (Td) were found via the tallest peaks in the DTG curves, and were 349.10 ± 3.77 °C, 363.91 ± 1.72 °C, and 369.09 ± 2.26 °C, for the neat, 10 wt% Cinn, and 10 wt% Di-Cinn samples, respectively. The addition of the mechanophore did shift the main decomposition temperature higher than the neat by approximately 15 to 20 °C, for the Cinn and Di-Cinn mechanophores, respectively. However, there is a notable weight loss in the mechanophore containing composites of approximately 20% from 90 to 310 °C, followed by the main degradation. From the DTG curves,

it also appears that there are two small peaks before the main Td at 120 and 236 °C. The Td values of the pure cinnamamide and di-cinnamamide (prior to embedding) were found to be 249.15 ± 1.24 °C and 251.68 ± 7.45 °C, respectively, and occurred in one sharp decomposition step, with little to no weight loss before 200 °C. This degradation of the mechanophores themselves help to explain the second slight decomposition step near 236 °C in the composites, thus the first small decomposition step near 120 °C is likely due to the breaking of the bonds between the mechanophore units and the epoxy matrix. This step is more pronounced in the Di-Cinn sample, and is likely due to the lessened conjugation of the dimer with the matrix initially, due to di-substitution of the dimers, rather than the full substitution seen with the cinnamamide-resin reaction.

In addition to DSC to determine Tg values, Dynamic Mechanical Analysis (DMA) can be used, with representative curves seen in Figure 4.5.5. The peak of the tan delta (tan δ) curve in DMA is used to determine the Tg value for the sample, with tan δ being defined as the ratio between the loss and storage moduli. From DMA, the Tg values over 4 runs of each sample were 60.83 ± 1.50 °C, 52.66 ± 2.80 °C, and 52.23 ± 2.05 °C, for the neat epoxy, and the 10 wt% cinnamamide di-cinnamamide composites, respectively. This makes for a lowering of the Tg from the neat by about 9 °C for the mechanophore grafted samples, with the mechanophore grafted samples having statistically similar Tg values. It should be noted that this depression is slightly more than what was seen with the DSC, and overall, all of the Tg values are greater with the DMA compared to the DSC. These results can be hypothesized to be from the mechanical determination of the Tg in DMA, rather than the thermal determination in DSC.

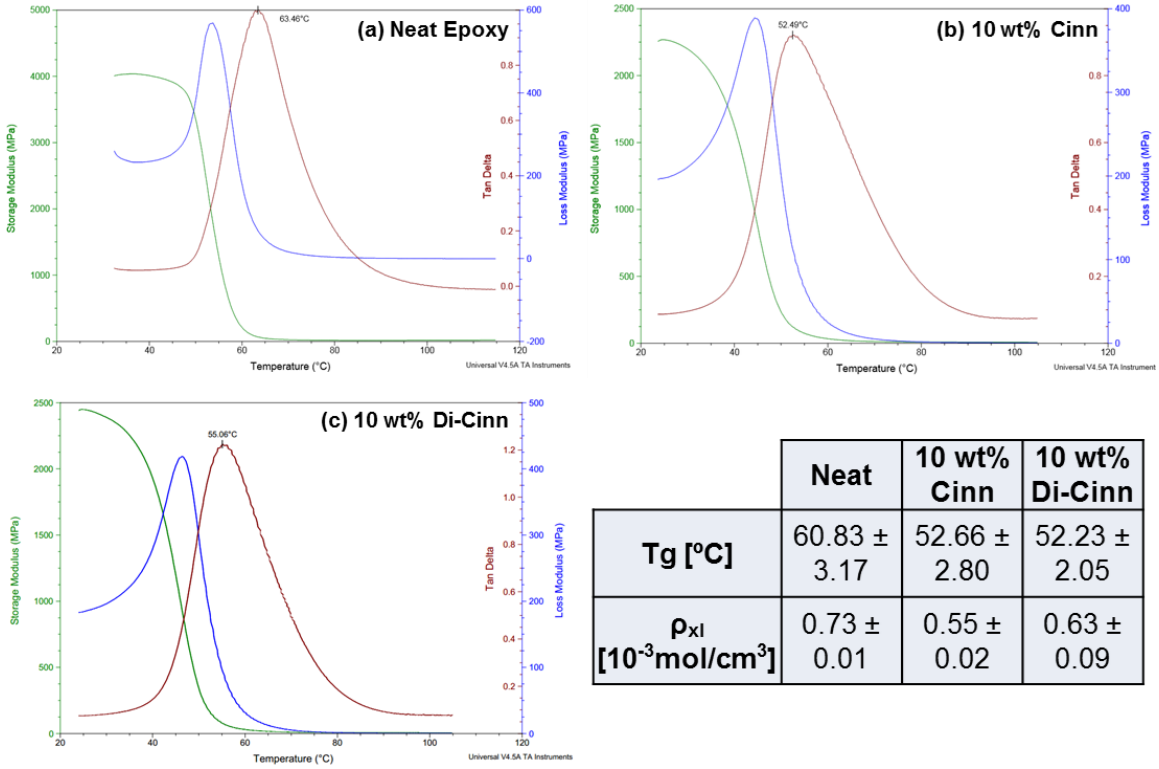

	Neat	10 wt% Cinn	10 wt% Di-Cinn
Tg [°C]	60.83 ± 3.17	52.66 ± 2.80	52.23 ± 2.05
ρ_{xl} [10^{-3}mol/cm^3]	0.73 ± 0.01	0.55 ± 0.02	0.63 ± 0.09

Figure 4.5.5. DMA curves showing the Storage Modulus (green), Loss Modulus (blue), and Tan Delta (maroon) of the (a) neat epoxy, (b) 10 wt% Cinnamamide composite, and (c) 10 wt% Di- Cinnamamide composite, respectively. The inset table shows the average Tg and ρ_{xl} of the samples determined from the DMA curves.

DMA can also be used to calculate crosslink density for a given sample, according to the theory of rubber elasticity [179], $\rho_{xl} = \frac{G'}{3RT}$, where ρ_{xl} is the crosslink density expressed in moles of elastically effective network chains per cm^3 of sample, G' is the rubbery plateau modulus, R is the Gas Constant, and T is the absolute temperature at which the rubbery plateau storage modulus is determined. The crosslink densities were thus calculated to be 0.73 ± 0.01 × 10^3 mol/cm^3, 0.55 ± 0.02 × 10^3 mol/cm^3, and 0.63 ± 0.09 × 10^3 mol/cm^3 for the neat epoxy, and the 10 wt% cinnamamide di-cinnamamide

composites, respectively. Similar to the other thermomechanical property comparisons, the neat epoxy was expected to be more highly crosslinked, with the Di-Cinn being more crosslinked than the Cinn due to the cyclobutane crosslinks being formed prior to addition into the epoxy.

4.5.3. Compressive Mechanochemical Activation and Observed Fluorescent Response

To evaluate the mechanochemical response of the mechanophore-grafted nanocomposites, compression tests were used to apply repeatable and quantifiable damage to the thermoset samples. From these compression tests, stress-strain curves were obtained for each of the different sample types, as seen in Figure 4.5.6. The Young's modulus values were calculated from the slope in the linear elastic region of the curves, and were found to be 2.21 ± 0.01 GPa, 1.36 ± 0.09 GPa, and 1.89 ± 0.09 GPa for the neat epoxy, 10 wt% Cinn and 10 wt% Di-Cinn epoxy composites, respectively. Thus, there was a notable decrease in the Young's modulus upon 10 wt% cinnamamide mechanophore incorporation, but the use of 10 wt% di-cinnamamide notably increases the Young's modulus value. Similarly, the yield strength values were 95.61 ± 1.26 MPa, 57.32 ± 0.73 MPa, and 77.44 ± 1.77 MPa for the neat, 10 wt% Cinn, and 10 wt% Di-Cinn epoxy samples, respectively. This increase in the mechanical properties when Di-Cinn is used as opposed to Cinn is, again, likely due to the higher crosslink density in the Di-Cinn composites from the mechanophore cyclobutane dimers being formed prior to incorporating in to the epoxy mixture.

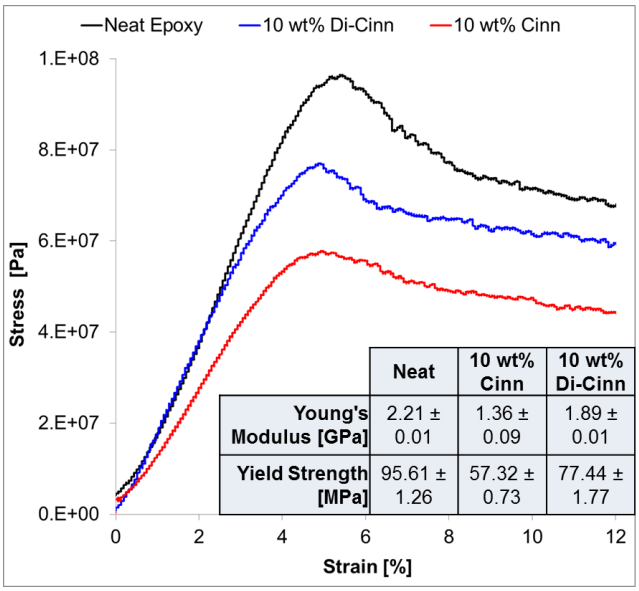

Figure 4.5.6. Stress-strain curves for the neat epoxy (black), and the 10 wt% Cinn (red) and 10 wt% Di-Cinn (blue) epoxy composites, with the lower right inset showing the resulting Young's Modulus and Yield strength values.

Fluorescence microscopy was then used in tandem with the compression tests to evaluate the fluorescent response of the self-sensing thermoset network composites, with fluorescence images taken at the strain values of 0, 2, 4, 6, 10, and 15%. From the compression test curves, 0% strain is the baseline value prior to compression, while 2% and 4% strain are in elastic region, with 4% immediately before the yield point. 6% strain is immediately after the yield point, and 10 and 15% strain are well into the plastic region. Representative images for the selected strain values for the 10 wt % Cinn and Di-Cinn epoxy nanocomposites can be seen in Figure 4.5.7a and b, respectively. These images were taken under excitation of 340–380 nm UV light, capturing the fluorescent emission between 500–550 nm. The raw 8-bit gray scale fluorescence images were pseudocolored green and the brightness and contrast were increased by 40% for better visualization in

Figure 4.5.7. It can be clearly seen that the 10 wt% Cinn composite has a much higher fluorescent emission overall compared to the 10 wt% Di-Cinn composite, which was further confirmed by the macroscale visualization of the samples and the fluorimeter data.

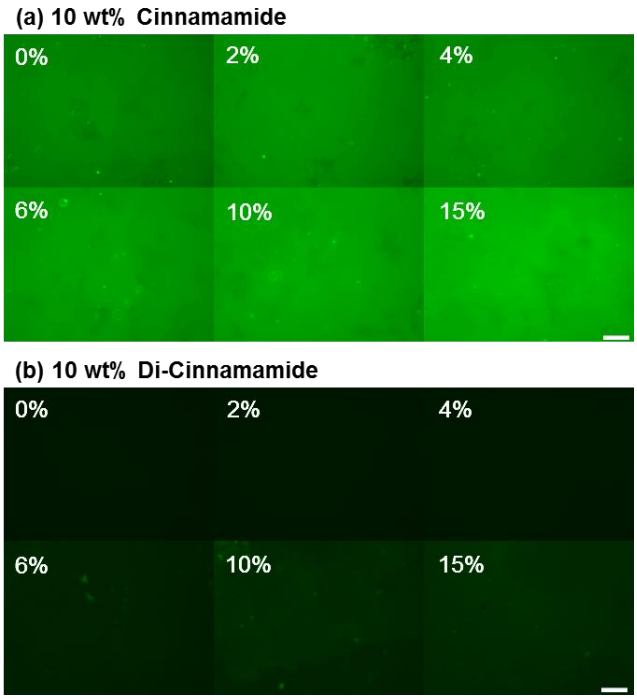

Figure 4.5.7. Representative fluorescence images for the mechanophore-embedded epoxy composites identifying the strain values for which the images were taken, for (a) 10 wt% Cinnamamide and (b) 10 wt% Di-Cinnamamide. Scale bars are 50 μm. The images were pseudocolored green and the brightness and contrast were increased by 40% to enhance the visual analysis of the images.

This reinforces the hypothesis that the cinnamamide groups in this composite are much less crosslinked, and less mechanically sensitive cyclobutane units are formed, than when the di-cinnamamide is incorporated into the epoxy. For both of the composites studied, there is an overall increase in the fluorescence with an increase of the strain applied, however, there is not a clear difference between the 0, 2, and 4% strains, which would be

required for damage precursor detection. There seems to be a noticeable difference between the 4 and 6% strain values, thus quantification of the fluorescence via ImageJ was performed to analyze the phenomenon further.

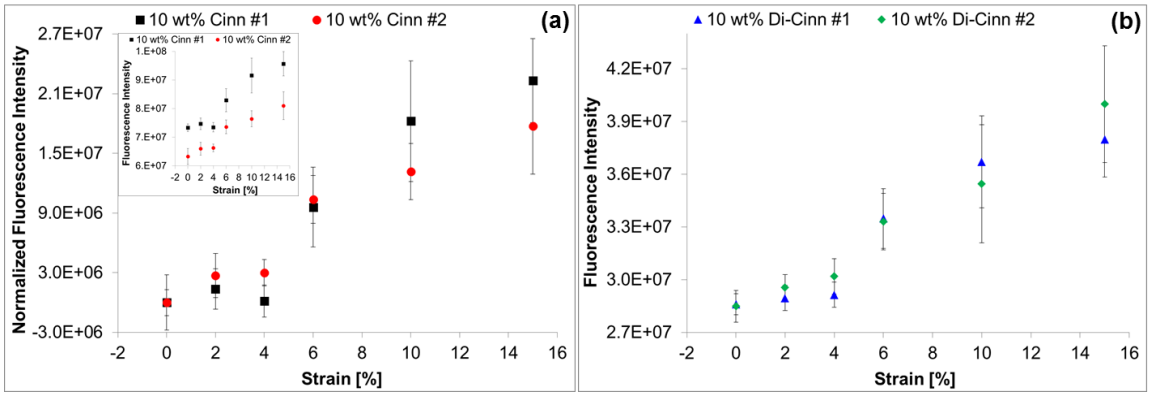

Figure 4.5.8. Average fluorescence intensity values for each strain calculated via ImageJ from the obtained fluorescence microcopy images, with each point being an average of 20 images and 2 samples per batch. (a) Upper left inset shows the raw fluorescence intensity data for 2 batches of the 10 wt% Cinn epoxy composite, while the main image shows the overlay of the two curves by normalizing the intensity to the 0% strain value. (b) Raw fluorescence intensity data for 2 batches of the 10 wt% Di-Cinn epoxy composite, showing good agreement between the batches.

For each sample analyzed, the ten fluorescence images were taken representative of the sample face and the ImageJ software calculated average fluorescence intensity values for each image. For each composite batch made, two samples for each strain percentage would be analyzed, thus each point shown in Figure 4.5.8 is an average of 20 images. The upper left inset of Figure 4.5.8 shows the raw fluorescence intensity data for 2 batches of the 10 wt% Cinn epoxy composite, which were found to have slightly different fluorescence intensity values initially, likely due to the variation in the UV curing of the

epoxy samples, which could be attributed to the light penetration depth, among other factors. However, when the curves are overlaid by normalizing the intensities to the 0% strain value, there is good agreement in the shape of the curve and the strains at which damage can be detected, as seen in the main image of Figure 4.5.8a. There is no significant different in the fluorescent intensity values between the 0, 2, and 4% strains, but there is a marked increase in the fluorescence intensity at the 6% strain mark, which is immediately after the yield point, and can serve as early damage detection. The 10 and 15% strain values show a further increase in the intensity with the applied strain, as expected.

Similarly, Figure 4.5.8b shows the raw fluorescence intensity data for two batches of the 10 wt% Di-Cinn epoxy composite, with no normalization, showing good agreement between the batches. Both batches has nearly identical starting fluorescences, and there is not a significant increase in the intensity for the batches for 2 or 4% strain. However, akin to the 10% Cinn composite batches, there is a marked statistical increase in the fluorescence at the 6% strain, with the intensity increasing with the application of 10 or 15% strain. This early damage detection at 6% strain reinforces our previous work, which involved photodimerization of cinnamoyl functional groups to create cyclobutane stress-sensing moieties within polymer blends of crosslinked-cyclobutane containing polymers and epoxy [159]. Thus, despite covalent incorporation into the epoxy network, there is not an improvement in the occurrence of the fluorescent response, likely due to the limitation of the cinnamoyl chemistry in terms of its fluorescence quantum yield. This shows that Cinn or Di-Cinn can be covalently grafted into a thermoset epoxy network and can additionally be used as a stress-responsive mechanophore via fluorescent signal genera-

tion, and that applying increasing strain increases the fluorescence emission, due to the breaking of the formed cyclobutane dimers, causing reversion to the fluorescent monomeric form.

To improve on the early damage detection scheme and sense earlier on in the stress-strain curve, the mechanophore chemistry would have to be change. A similar reaction scheme to the Cinn/Di-Cinn systems could take place with an amine containing anthracene moiety, such as 2- or 9-aminoanthracene, to form a grafted thermoset matrix while reaping the benefits of the anthracene chemistry. This would ultimately form cyclooctane as the force-responsive unit, and as previously mentioned, anthracene would be expected to offer the advantage of early damage precursor detection over the cinnamoyl mechanophores stemming from the enhanced fluorescence quantum yield and the previous results with the Di-AC particles.

Additionally, molecular dynamics simulations are being performed in tandem to the experimental work to observe grafting at the nanoscale and to help ascertain which mechanophores would be more easily activated, how much mechanophore must be incorporated to achieve the desired fluorescent signals, and what effect certain weight percentages of mechanophore incorporation will have on the overall the material properties. To perform this comparison, several characterization methods are being utilized, with the glass transition temperature of the resulting epoxy networks experimentally and as calculated by MD as one example. Similarly, the experimentally measured Young's modulus from the stress/strain test and the elastic modulus and crosslink density will also be compared to those generated from the simulations.

CHAPTER

5. SUMMARY AND PROPOSED WORK

5.1. Summary

Mechanochemistry is still a relatively new and exciting field, and the pervasive nature of damage makes it an important one, with thermoset composites being rarely studied for stress sensing. We successfully synthesized, characterized, and applied dimeric 9-anthracene carboxylic acid (Di-AC)-based mechanophore particles to form stress sensing particle reinforced epoxy matrix composites, with Di-AC having never been applied as a mechanophore on its own previously, and compared them with our cyclobutane polymer blends. The particles were found to have a regular 1.5 μm diameter, and the reaction of AC to Di-AC was thoroughly studied via NMR, FTIR, UV-vis, and fluorescence spectroscopy. The 5 wt% Di-AC embedded epoxy composites were found to have a slightly lower Tg in the DSC scans, but highly comparable materials properties when studied with the TGA, DMA, and compression test. Under the applied stress, the cyclooctane-rings in the Di-AC particles reverted back to their fluorescent anthracene monomeric form, which linearly enhanced the overall fluorescence of the composite in response to the applied strain. The fluorescent signal further allowed for stress sensing in the elastic region of the stress-strain curve, which is considered to be a form of damage precursor detection. MD simulations of the Di-AC composites were compared to the experimental work and yielded additional knowledge about the nanoscale mechanophore activation. Overall, the incorporation of Di-AC to the epoxy matrix created a robust composite system with a minor deviation from the mechanical and thermal properties of the neat epoxy, with the much-desired added benefit of stress sensing and damage precursor detection.

We then extended the work by employing the Di-AC microparticles in a thermoset polyurethane matrix to study their application as universal stress-sensing fillers in network polymer matrix composites. Under a compressive force, there was bond breakage in the mechanically weak cyclooctane photodimers of Di-AC, such that there is reversion to the fluorescent anthracene-type monomers. This fluorescent emission was then correlated to the applied strain, and the precursors to damage were detected with a noticeable fluorescent signal change at an applied strain of only 2%. This early damage detection was additionally possible at very low particle loadings of 2.5 and 5 wt%, with the 5 wt% loading showing enhanced material properties compared to the 2.5 wt%, due to particle reinforcement in the composite. Overall, the synthesis of Di-AC as a stress-sensitive particle filler allows for facile addition of advanced functionality to these ubiquitous thermoset composites.

We then proposed and completed the novel direct covalent grafting of photoactive mechanophore units into an epoxy matrix, to create a self-sensing thermoset network, linked by both epoxide and mechanophore bonds. The mechanophore precursor chosen was cinnamamide (Cinn), as its amine group can covalently bond to the epoxy resin chosen, in a similar matter to the crosslinking of the resin with the chosen hardener in the neat epoxy system. Cinnamamide is known to be able to form a cyclobutane type dimer (di cinnamamide, Di-Cinn) under UV photoirradiation via [2 + 2] cycloaddition. Thus two routes were studied for the mechanophore covalent incorporation into an epoxy matrix, the first being the reaction of the cinnamamide mechanophore precursor with DGEBF to ensure covalent bond formation, with subsequent hardener addition. The epoxy mixture is then UV cured so that the cyclobutane mechanophore units can be

formed via photodimerization, while the conventional resin-hardener curing is taking place. The second route is to first form di-cinnamamide in solution under UV light, then to react it with DGEBF, with subsequent hardener addition and conventional epoxy bond formation. In this second method, there were more cyclobutane rings present in the final nanocomposite, as Di-Cinn was theoretically 100% dimerized prior to addition, and this effected the resulting material properties of the composites. Overall, both the routes of mechanophore incorporation were successful in creating grafted, self-sensing thermoset network composites, which were capable of early damage detection via fluorescent emission.

5.2. Proposed Work

5.2.1. Cycloalkane Mechanophore Application to Carbon-containing Composites at the System Level via Fourier Transform Infrared Spectroscopy (FTIR) Sensing

To the best of our knowledge, stress-sensing mechanophores, functioning by fluorescent emission or a color change, have not been fully applied to the carbon-embedded composite system level as early damage detectors. This application would be highly desired as the embedded material in these composites, including carbon fibers, carbon black, and carbon nanotubes, are widely used due to their enhanced mechanical, thermal, and electrical properties, as previously discussed. Our group has successfully applied cyclobutane- and cyclooctane-based mechanophore sensors for damage detection as blends and particles in epoxy matrices, which worked well due to the transparent nature of the epoxy. The fluorescent signals upon damage are readily observed when the matrix medium remains translucent. The application of this sensing mechanism to structural composites presents additional challenges, especially when the fillers are black, quenching the fluorescent signals. Current damage quantification schemes for carbon-containing composites include electrical resistance/impedance tomography [196, 197], ultrasound [198], x-ray reflection topography [199], and thermography [200-202]. However, these methods often require probes to be attached to the sample, the samples removed from their use, or cannot detect damage precursors. Additionally, the penetration depth of the damage detection in the mechanophore-embedded composites create by our group remains unclear. Further understanding of this phenomenon is key to assessing overall damage of these composites. Thus, the study of the mechanophore responsiveness and penetration depth of the fluorescent signals with samples of increasing thickness and various embedded

carbon-based materials would allow for the system level application of these sensors. Additionally, the ease of incorporation and sensing, robustness, and functionality of the synthesized mechanophore sensors should be further investigated.

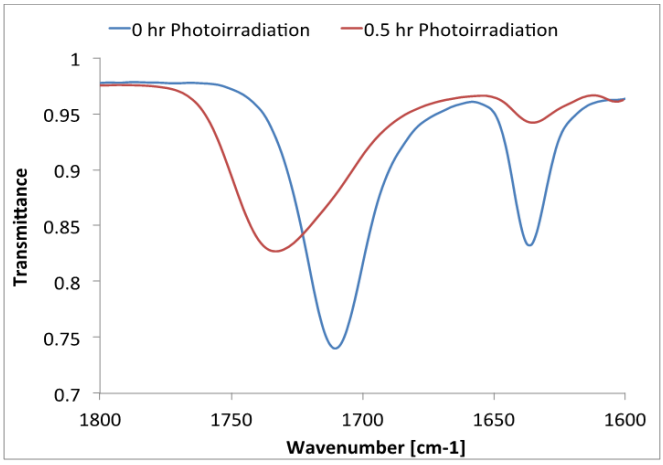

Figure 5.2.1.1. FTIR spectra of solution cast PVCi on a KBr disk before and after photoirradiation.

In our current work, we apply stress to break the cyclobutane/cyclooctane rings in the mechanophore units and subsequently revert back to the fluorescent cinnamoyl/anthracene moieties, observing this fluorescence via fluorescent microscopy. In order to overcome the challenge for system level application of carbon black, nanotubes or fibers, we propose the use of Attenuated Total Reflectance Fourier Transform Infrared Spectroscopy (ATR-FTIR) as an alternative method to observe the stress induced signal produced by the mechanophore. As mentioned previously, visible light detection methods are not feasible for stress sensing in these carbon-based composites; however, FTIR has been applied as a means for probing the chemistry of carbon-based composites, although it has not been previously used for stress sensing [203].

ATR-FTIR was developed by J. Fahrenfort in 1961, in which a crystal of high refractive index is placed in contact with a sample, and a beam of infrared light passes from the crystal and into the sample several times in an evanescent wave[204]. The entirety of the reflections is then collected for the 2 to 4 micron control volume probed. This method allows for quantitative analysis to be generated from the resulting spectra, in that the ATR-FTIR spectral peak ratios can be proportional to concentration of certain bonds based on height of the peak [205]and area underneath the peak [206]. This method has been successfully used to study and compare conformational changes of proteins in solution [207, 208] and mixtures of pharmaceutical polymorphs [209]. An IR microscope could be additionally used to generate 2D spectra of the damaged surface to pinpoint the damaged areas, and complementary data can be gathered via FT Raman Spectroscopy. We perform FTIR in our mechanophore work to confirm the formation of the mechanophore units during UV curing, with Figure 5.2.1.1 showing the curves for the poly(vinyl cinnamate) (PVCi) mechanophore. Before photoirradiation of PVCi, peaks at 1711 and 1635 cm^{-1} are present, and correspond to the conjugated C=O and C=C stretching vibrations of the cinnamoyl monomer. After photoirradiation, the C=C peak reduces drastically due to the formation of the cyclobutane rings by photodimerization at the alkene position. Additionally, the C=O peak shifts to a higher wavenumber with decreasing absorbance, which is attributed to the loss of π–conjugation from the C=C double bond [159].

It is thus hypothesized that the comparison of the FTIR spectra before and after damage should show the recovery of the conjugated cinnamoyl group by reappearance of the C=C peak and shifting of the C=O, and by fixing the penetration depth of the incident IR beam via ATR-FTIR, the location and intensity of the characteristic peaks can be cor-

related to the amount of damage. Additionally, it will be explored whether it is possible to quantify mechanophore activation based on peak ratios and the area under the peaks in the ATR-FTIR spectra. As a preliminary experiment, 10 wt% PVCi was incorporated into an epoxy blend, due to the ease of acquisition and incorporation of this mechanophore, and the ATR-FTIR spectra of irradiated and compressed samples were compared, as seen in Figure 5.2.1.2.

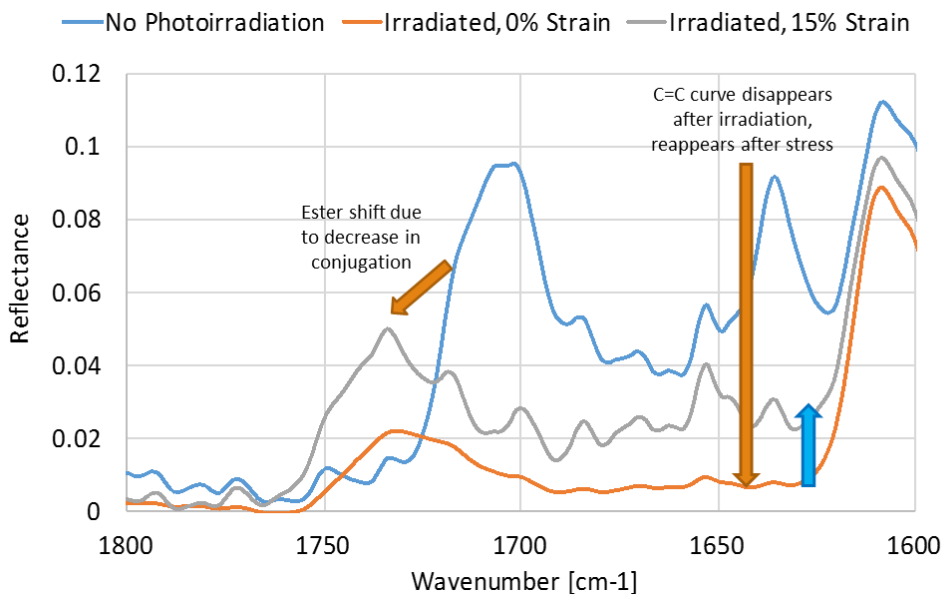

Figure 5.2.1.2. FTIR spectra of 10 wt% PVCi epoxy blend, blue: without photoirradiation, orange: after photoirradiation and before compression, gray: after photoirradiation and after 15% strain compression.

For the all spectra, the rubber band baseline correlation was used and all of the peaks were scaled to an aromatic C=C peak at 1508 cm^{-1}, as it was found not to vary with irradiation or compression. For the not irradiated samples, the peaks at 1711 and 1635 cm^{-1} for C=O and C=C are clearly present, and after photoirradiation, the 1711 cm^{-1} for C=O was seen to shift and the C=C peak disappeared, as expected. After compression of

the irradiated sample to 15% strain, the C=O peak was seen to remain shifted, and there was some recovery of the C=C peak, alluding to the cyclobutane ring breakage and cinnamoyl reversion. This preliminary data will be compared to further batches and additionally compared to an epoxy control, in order to confirm the result. The factors of scaling peak selection and the creation of ratios of peak heights, area under the curves, and peak shifts, will be fully considered in order to yield reliable FTIR signal vs. strain relationships for damage quantification. Additionally, 0.5% of carbon black or carbon nanotubes will be added to the 10 wt% PVCi epoxy composites to evaluate the presence of the signal with these black, fluorescence quenching materials, in order to realize the entire goal of the study. Alternatively, Di-AC mechanophore particle can be incorporated as the mechanophore as they may be more appropriate for enhanced signal detection and damage precursor detection. This route, consisting of ATR-FTIR for stress sensing in carbon-containing composites would allow for the first successful experimental application of these types of mechanophores at this system level and a novel damage detection scheme, with goals for early damage detection.

5.2.2. Synthesis of "Smart" Polymer Metal-Organic Frameworks (polyMOFs)

Metal-organic frameworks (MOFs) are porous, crystalline materials with metal ions/clusters and organic ligands as building blocks to form 2D or 3D frameworks. [210-212] Their unique porous and hybrid nature makes them excellent materials for various catalytic, gas absorption, and separation applications, among a multitude of others. [213-215] A very recent development in the MOF research field has been the synthesis of polymer-metal-organic frameworks (polyMOFs), in which linear, amorphous polymers were

used as the organic-ligand portion of the MOF to go from a simple one-dimensional linear polymer scheme to a 3D, organized, crystalline MOF network, with only a handful of studies being currently published. [216-218] Figure 5.2.2.1 shows a comparison of the synthesis of dimeric and polymeric ligands for MOF formation, we the brominated chain being the site of polymer incorporation into the ligand. With this new development in MOF chemistry, we propose the novel synthesis of "smart," environmentally responsive MOFs via the incorporation of temperature, pH, and stress responsive polymer units into the frameworks.

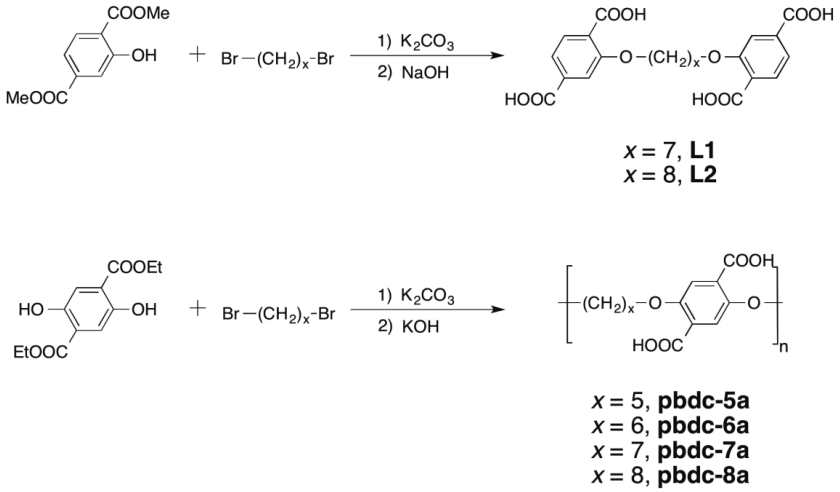

Figure 5.2.2.1. Schematic of the formation of dimeric and polymeric-ligands for MOF formation (top and bottom, respectively). [216]

Our research group focuses on environmentally responsive polymer systems, including thermally responsive, pH responsive, and stress responsive, among others. [159, 181, 219, 220] Our thermally responsive polymer of choice has been poly(N-Isopropylacrylamide) (polyNIPAM), which exhibits a transition temperature at 32 °C, in which the polymer shrinks due to a coil to globule transformation causing by a change in

the hydrogen bonding interactions. [221] One of the pH responsive monomers studied has been dimethylaminopropyl methacrylamide (DMAPMA), which, when co-polymerized with NIPAM, adds the pH responsive functionality due to changes in the charge state. This dissertation contains more details of the stress-responsive mechanophores studied by our group, which can also be incorporated into a MOF scheme. There has only been one journal article combining both the functionality of MOFs and environmentally responsive polymers, and the author's simply synthesized MOF particles with thermally responsive polymers grafted on their surfaces, rather than incorporating the "smart" polymers within in MOF network itself. [222]

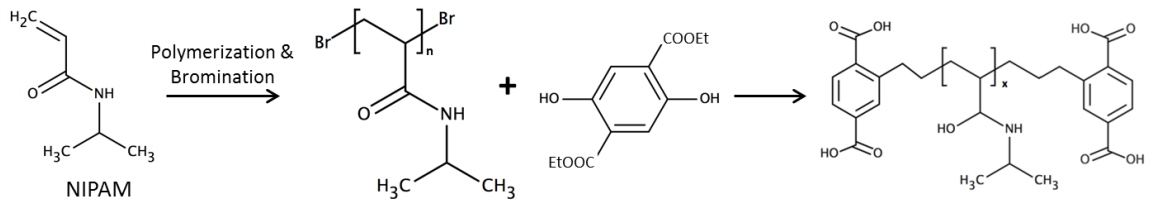

Figure 5.2.2.2. Synthesis scheme for a temperature-responsive polymer ligand for polyMOF formation.

Figure 5.2.2.2 shows a synthesis scheme for a temperature-responsive polymer ligand for polyMOF formation by brominating polyNIPAM and adding carboxylic acid containing MOF ligands to the end groups. Additionally, pH responsiveness can been added by using both NIPAM and DMAPMA in the organic ligand, as seen in Figure 5.2.2.3. Mechanochemistry has been used in the synthesis of MOFs, in reaction schemes involving grinding, etc., but little work has been done regarding stress-responsive MOFs than can emit a measureable signal upon applied damage. [223] Poly(vinyl cinnamate) (PVCi) could thus be brominated and UV dimerized within the MOF to create stress-

responsive cyclobutane units. Additionally, the mechanophore dimeric 9-anthracene carboxylic acid (Di-AC) could be used on its own as a stress-responsive MOF linker due to it containing reactive carboxylic acid groups. Overall, the addition of environmentally responsive polymers and functional groups into the MOF research field allows for novel discoveries and new possibilities for applications in a multitude of fields.

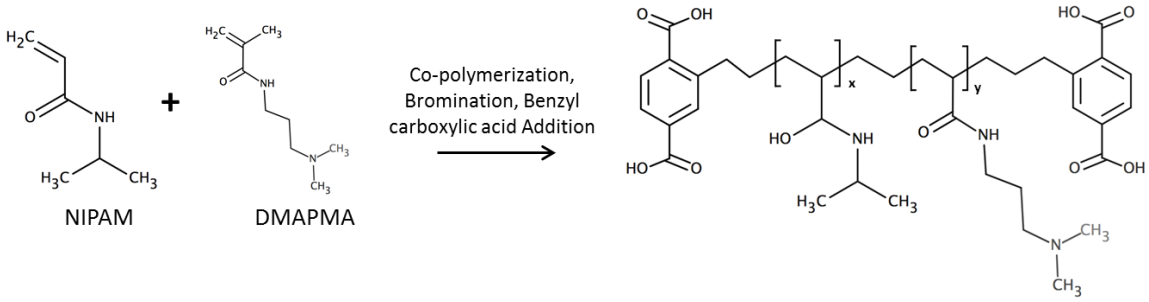

Figure 5.2.2.3. Synthesis scheme for a pH-responsive polymer ligand for polyMOF formation.

REFERENCES

1. Hess, A. E.; Capadona, J. R.; Shanmuganathan, K.; Hsu, L.; Rowan, S. J.; Weder, C.; Tyler, D. J.; Zorman, C. A. Development of a stimuli-responsive polymer nanocomposite toward biologically optimized, MEMS-based neural probes. *J Micromech Microengineering* **2011**, *21*, 054009.

2. Singha, S.; Thomas, M. J. Dielectric properties of epoxy nanocomposites. *IEEE Trans. Dielectr. Electr. Insul.* **2008**, *15*, 12-23.

3. Chozhan, C. K.; Alagar, M.; Gnanasundaram, P. Synthesis and characterization of bis(3-vinyl ester-2-hydroxy propane) ether-terminated poly(dimethysiloxane) toughened epoxy-clay hybrid nanocomposites. *Polym. Polym. Compos.* **2008**, *16*, 331-341.

4. Sajjad, M.; Feichtenschlager, B.; Pabisch, S.; Svehla, J.; Koch, T.; Seidler, S.; Peterlik, H.; Kickelbick, G. Study of the effect of the concentration, size and surface chemistry of zirconia and silica nanoparticle fillers within an epoxy resin on the bulk properties of the resulting nanocomposites. *Polym. Int.* **2012**, *61*, 274-285.

5. Khanam, P. N.; Ponnamma, D.; AL-Madeed, M. In *Electrical Properties of Graphene Polymer Nanocomposites;* Sadasivuni, K. K., Ponnamma, D., Kim, J. and Thomas, S., Eds.; Springer International Publishing: 2015; pp 25-47.

6. Chen, Z.; Dai, X. J.; Magniez, K.; Lamb, P. R.; Leal, D. R. d. C.; Fox, B. L.; Wang, X. Improving the mechanical properties of epoxy using multiwalled carbon nanotubes functionalized by a novel plasma treatment. *Composites Part A-Applied Science and Manufacturing* **2013**, *45*, 145-152.

7. Matias Chiacchiarelli, L.; Martin Escobar, M.; Maria Kenny, J.; Torre, L.; Vazquez, A. The Role of the Interphase on the Shear Induced Failure of Multiwall Carbon Nanotubes Reinforced Epoxy Nanocomposites. *J Appl Polym Sci* **2015**, *132*, 41364.

8. Hickenboth, C. R.; Moore, J. S.; White, S. R.; Sottos, N. R.; Baudry, J.; Wilson, S. R. Biasing reaction pathways with mechanical force. *Nature* **2007**, *446*, 423-427.

9. Black, A. L.; Lenhardt, J. M.; Craig, S. L. From molecular mechanochemistry to stress-responsive materials. *Journal of Materials Chemistry* **2011**, *21*, 1655-1663.

10. Davis, D. A.; Hamilton, A.; Yang, J.; Cremar, L. D.; Van Gough, D.; Potisek, S. L.; Ong, M. T.; Braun, P. V.; Martinez, T. J.; White, S. R.; Moore, J. S.; Sottos, N. R. Force-induced activation of covalent bonds in mechanoresponsive polymeric materials. *Nature* **2009**, *459*, 68-72.

11. Oates, D. Innovations in mud-brick: Decorative and structural techniques in ancient Mesopotamia. *World archaeology* **1990**, *21*, 388-406.

12. Jackson, M.; Marra, F.; Hay, R.; Cawood, C.; Winkler, E. THE JUDICIOUS SELECTION AND PRESERVATION OF TUFF AND TRAVERTINE BUILDING STONE IN ANCIENT ROME*. *Archaeometry* **2005**, *47*, 485-510.

13. Stankovich, S.; Dikin, D. A.; Dommett, G. H. B.; Kohlhaas, K. M.; Zimney, E. J.; Stach, E. A.; Piner, R. D.; Nguyen, S. T.; Ruoff, R. S. Graphene-based composite materials. *Nature* **2006**, *442*, 282-286.

14. Dabbousi, B.; RodriguezViejo, J.; Mikulec, F.; Heine, J.; Mattoussi, H.; Ober, R.; Jensen, K.; Bawendi, M. (CdSe)ZnS core-shell quantum dots: Synthesis and characterization of a size series of highly luminescent nanocrystallites. *J Phys Chem B* **1997**, *101*, 9463-9475.

15. Sun, W.; Chen, L.; Wang, Y.; Zhou, Y.; Meng, S.; Li, H.; Luo, Y. Synthesis of Highly Conductive PPy/Graphene/MnO2 Composite Using Ultrasonic Irradiation. *Synth. React. Inorg. Met. -Org. Nano-Metal Chem.* **2016**, *46*, 437-444.

16. Zhang, B.; Kang, F.; Tarascon, J.; Kim, J. Recent advances in electrospun carbon nanofibers and their application in electrochemical energy storage. *Prog. Mater. Sci.* **2016**, *76*, 319-380.

17. Nadeem, Q.; Rizwan, M.; Gill, R.; Rafique, M.; Shahid, M. Fabrication of alumina based electrically conductive polymer composites. *J Appl Polym Sci* **2016**, *133*, 42939.

18. Bouazizi, N.; Ajala, F.; Bettaibi, A.; Khelil, M.; Benghnia, A.; Bargougui, R.; Louhichi, S.; Labiadh, L.; Ben Slama, R.; Chaouachi, B.; Khirouni, K.; Houas, A.; Azzouz, A. Metal-organo-zinc oxide materials: Investigation on the structural, optical and electrical properties. *J. Alloys Compounds* **2016**, *656*, 146-153.

19. Hench, L. Bioceramics. *J Am Ceram Soc* **1998**, *81*, 1705-1728.

20. Sackmann, E. Supported membranes: Scientific and practical applications. *Science* **1996**, *271*, 43-48.

21. Farid, M. M.; Goudini, L.; Piri, F.; Zamani, A.; Saadati, F. Molecular imprinting method for fabricating novel glucose sensor: Polyvinyl acetate electrode reinforced by MnO2/CuO loaded on graphene oxide nanoparticles. *Food Chem.* **2016**, *194*, 61-67.

22. Banerjee, S.; Kar, K. K. Synergistic effect of aluminium phosphate and tungstophosphoric acid on the physicochemical properties of sulfonated poly ether ether ketone nanocomposite membrane. *J Appl Polym Sci* **2016**, *133*, 42952.

23. Chang, W.; Chen, H. Physical properties of bacterial cellulose composites for wound dressings. *Food Hydrocoll.* **2016**, *53*, 75-83.

24. Ulbricht, M. Advanced functional polymer membranes. *Polymer* **2006**, *47*, 2217-2262.

25. Haruta, M. Size- and support-dependency in the catalysis of gold. *Catal. Today* **1997**, *36*, 153-166.

26. Bobrova, L. N.; Bobin, A. S.; Mezentseva, N. V.; Sadykov, V. A.; Thybaut, J. W.; Marin, G. B. Kinetic assessment of dry reforming of methane on Pt plus Ni containing composite of fluorite-like structure. *Applied Catalysis B-Environmental* **2016**, *182*, 513-524.

27. Song, X.; Hu, Y.; Zheng, M.; Wei, C. Solvent-free in situ synthesis of g-C3N4/{001}TiO2 composite with enhanced UV- and visible-light photocatalytic activity for NO oxidation. *Applied Catalysis B-Environmental* **2016**, *182*, 587-597.

28. Yuan, Y.; Yu, Z.; Li, Y.; Lu, H.; Chen, X.; Tu, W.; Ji, Z.; Zou, Z. A MoS2/6,13-pentacenequinone composite catalyst for visible-light-induced hydrogen evolution in water. *Applied Catalysis B-Environmental* **2016**, *181*, 16-23.

29. YU, G.; GAO, J.; HUMMELEN, J.; WUDL, F.; HEEGER, A. Polymer Photovoltaic Cells - Enhanced Efficiencies Via a Network of Internal Donor-Acceptor Heterojunctions. *Science* **1995**, *270*, 1789-1791.

30. Park, S. H.; Roy, A.; Beaupre, S.; Cho, S.; Coates, N.; Moon, J. S.; Moses, D.; Leclerc, M.; Lee, K.; Heeger, A. J. Bulk heterojunction solar cells with internal quantum efficiency approaching 100%. *Nat. Photonics* **2009**, *3*, 297-U5.

31. Thompson, B. C.; Frechet, J. M. J. Organic photovoltaics - Polymer-fullerene composite solar cells. *Angew. Chem. -Int. Edit.* **2008**, *47*, 58-77.

32. Bruce, P. G.; Scrosati, B.; Tarascon, J. Nanomaterials for rechargeable lithium batteries. *Angew. Chem. -Int. Edit.* **2008**, *47*, 2930-2946.

33. Kim, J. Y.; Lee, K.; Coates, N. E.; Moses, D.; Nguyen, T.; Dante, M.; Heeger, A. J. Efficient tandem polymer solar cells fabricated by all-solution processing. *Science* **2007**, *317*, 222-225.

34. Rowsell, J.; Yaghi, O. Strategies for hydrogen storage in metal-organic frameworks. *Angew. Chem. -Int. Edit.* **2005**, *44*, 4670-4679.

35. Simon, K. A.; Warren, N. J.; Mosadegh, B.; Mohammady, M. R.; Whitesides, G. M.; Armes, S. P. Disulfide-Based Diblock Copolymer Worm Gels: A Wholly-Synthetic Thermoreversible 3D Matrix for Sheet-Based Cultures. *Biomacromolecules* **2015**, *16*, 3958.

36. Kovtyukhova, N. I.; Ollivier, P. J.; Martin, B. R.; Mallouk, T. E.; Chizhik, S. A.; Buzaneva, E. V.; Gorchinskiy, A. D. Layer-by-layer assembly of ultrathin composite films from micron-sized graphite oxide sheets and polycations. *Chemistry of Materials* **1999**, *11*, 771-778.

37. Mei, Y.; Lu, Y.; Polzer, F.; Ballauff, M.; Drechsler, M. Catalytic activity of palladium nanoparticles encapsulated in spherical polyelectrolyte brushes and core-shell microgels. *Chemistry of Materials* **2007**, *19*, 1062-1069.

38. Mandal, A.; Chakrabarty, D. Characterization of nanocellulose reinforced semi-interpenetrating polymer network of poly(vinyl alcohol) & polyacrylamide composite films. *Carbohydr. Polym.* **2015**, *134*, 240-250.

39. Kokcharov, I.; Burov, A. In *Composites;* Structural Integrity Analysis; Amazon Digital Services: 2013; .

40. Fard, M. Y.; Sadat, S. M.; Raji, B. B.; Chattopadhyay, A. Damage characterization of surface and sub-surface defects in stitch-bonded biaxial carbon/epoxy composites. *Composites Part B-Engineering* **2014**, *56*, 821-829.

41. Chao, P. G.; Sheng, S.; Chang, W. Micro-composite substrates for the study of cell-matrix mechanical interactions. *Journal of the Mechanical Behavior of Biomedical Materials* **2014**, *38*, 232-241.

42. Zhang, M.; Pare, P.; King, R.; James, S. P. A novel ultra high molecular polyethylene-hyaluronan micr use in total joint replacements. II. Mechanical and tribological property weight ocomposite for evaluation. *Journal of Biomedical Materials Research Part a* **2007**, *82A*, 18-26.

43. Naik, S.; Carpenter, E. E. Poly(D,L-lactide-co-glycolide) microcomposite containing magnetic iron core nanoparticles as a drug carrier. *J. Appl. Phys.* **2008**, *103*, 07A313.

44. Zhang, Z.; Wong, C. Recent advances in flip-chip underfill: Materials, process, and reliability. *IEEE Trans. Adv. Packag.* **2004**, *27*, 515-524.

45. Heo, S. I. Influence of particle size and shape on electrical and mechanical properties of graphite reinforced conductive polymer composites for the bipolar plate of PEM fuel cells. *Advanced composite materials* **2006**, *15*, 115-126.

46. Durand, J. M.; Vardavoulias, M.; Jeandin, M. Role of Reinforcing Ceramic Particles in the Wear Behavior of Polymer-Based Model Composites. *Wear* **1995**, *181*, 833-839.

47. Lee, W. S.; Han, I. Y.; Yu, J.; Kim, S. J.; Byun, K. Y. Thermal characterization of thermally conductive underfill for a flip-chip package using novel temperature sensing technique. *Thermochimica Acta* **2007**, *455*, 148-155.

48. He, Y.; Moreira, B. E.; Overson, A.; Nakamura, S. H.; Bider, C.; Briscoe, J. F. Thermal characterization of an epoxy-based underfill material for flip chip packaging. *Thermochimica Acta* **2000**, *357–358*, 1-8.

49. Qu, J. M.; Wong, C. P. Effective elastic modulus of underfill material for flip-chip applications. *Ieee Transactions on Components and Packaging Technologies* **2002**, *25*, 53-55.

50. Wu, X.; Wang, Y.; Xie, L.; Yu, J.; Liu, F.; Jiang, P. Thermal and electrical properties of epoxy composites at high alumina loadings and various temperatures. *Iranian Polymer Journal* **2013**, *22*, 61-73.

51. Coutinho, C. A.; Gupta, V. K. Formation and properties of composites based on microgels of a responsive polymer and TiO2 nanoparticles. *J. Colloid Interface Sci.* **2007**, *315*, 116-122.

52. Coutinho, C. A.; Gupta, V. K. Photocatalytic degradation of methyl orange using polymer-titania microcomposites. *J. Colloid Interface Sci.* **2009**, *333*, 457-464.

53. Zhang, Y.; Hong, Z. Synthesis of lanthanide-doped NaYF4@TiO2 core-shell composites with highly crystalline and tunable TiO2 shells under mild conditions and their upconversion-based photocatalysis. *Nanoscale* **2013**, *5*, 8930-8933.

54. Wu, C. Synthesis of Ag2CO3/CeO2 microcomposite with visible light-driven photocatalytic activity. *Mater Lett* **2015**, *152*, 76-78.

55. Wu, C. Facile one-step hydrothermal synthesis of Ag/Ag2O/Ag2CO3 microcomposite with visible light-driven photocatalytic activity. *Mater Lett* **2015**, *160*, 291-293.

56. Liu, X.; Li, Z.; Zhang, Q.; Li, F. Controllable synthesis and enhanced photocatalytic properties of Cu2O/Cu31S16 composites. *Mater. Res. Bull.* **2012**, *47*, 2631-2637.

57. Yang, J.; Li, Z.; Zhao, C.; Wang, Y.; Liu, X. Facile synthesis of Ag-Cu2O composites with enhanced photocatalytic activity. *Mater. Res. Bull.* **2014**, *60*, 530-536.

58. Liu, H.; Liu, T.; Zhang, Z.; Dong, X.; Liu, Y.; Zhu, Z. Simultaneous conversion of organic dye and Cr(VI) by SnO2/rGO microcomposites. *J. Mol. Catal. A-Chem.* **2015**, *410*, 41-48.

59. Madhusudan, P.; Yu, J.; Wang, W.; Cheng, B.; Liu, G. Facile synthesis of novel hierarchical graphene-Bi2O2CO3 composites with enhanced photocatalytic performance under visible light. *Dalton Transactions* **2012**, *41*, 14345-14353.

60. Tsekmes, I. A.; Morshuis, P. H. F.; Smit, J. J.; Kochetov, R. Enhancing the Thermal and Electrical Performance of Epoxy Microcomposites with the Addition of Nanofillers. *IEEE Electr. Insul. Mag.* **2015**, *31*, 32-42.

61. Ma, H.; Dai, L. L. Synthesis of polystyrene–silica composite particles via one-step nanoparticle-stabilized emulsion polymerization. *J. Colloid Interface Sci.* **2009**, *333*, 807-811.

62. Ma, H.; Luo, M.; Sanyal, S.; Rege, K.; Dai, L. L. The One-Step Pickering Emulsion Polymerization Route for Synthesizing Organic-Inorganic Nanocomposite Particles. *Materials* **2010**, *3*, 1186-1202.

63. Sanyal, S.; Huang, H.; Rege, K.; Dai, L. L. Thermo-Responsive Core-Shell Composite Nanoparticles Synthesized via One-Step Pickering Emulsion Polymerization for Controlled Drug Delivery. *Journal of Nanomedicine and Nanotechnology* **2011**, *2*, 126.

64. Hu, H.; Onyebueke, L.; Abatan, A. Characterizing and Modeling Mechanical Properties of Nanocomposites-Review and Evaluation. *Journal of Minerals and Materials Characterization and Engineering* **2010**, *9*, 275-319.

65. Kojima, Y.; Usuki, A.; Kawasumi, M.; Okada, A.; Kurauchi, T.; Kamigaito, O. Synthesis of Nylon-6-Clay Hybrid by Montmorillonite Intercalated with Epsilon-Caprolactam. *Journal of Polymer Science Part A-Polymer Chemistry* **1993**, *31*, 983-986.

66. AnonymousEncyclopedia of Polymer Blends: Volume 1: Fundamentals. *M2 Presswire* **2010**.

67. Mittal, V. *Optimization of Polymer Nanocomposite Properties;* John Wiley and Sons: US, 2009; , pp 123.

68. Huang, W.; Zeng, S.; Liu, J.; Sun, L. Bi-axially oriented polystyrene/montmorillonite nanocomposite films. *Rsc Advances* **2015**, *5*, 58191-58198.

69. Chandramohan, A.; Vengatesan, M. R.; Devaraju, S.; Dinakaran, K.; Alagar, M. Organoclay-Filled Vinyl Ester Monomer Toughened Epoxy-Intercrosslinked Matrix Materials. *International Journal of Polymeric Materials and Polymeric Biomaterials* **2013**, *62*, 301-308.

70. Paul, D. R.; Robeson, L. M. Polymer nanotechnology: Nanocomposites. *Polymer* **2008**, *49*, 3187-3204.

71. He, M.; Ge, J.; Lin, Z.; Feng, X.; Wang, X.; Lu, H.; Yang, Y.; Qiu, F. Thermopower enhancement in conducting polymer nanocomposites via carrier energy scattering at the organic-inorganic semiconductor interface. *Energy & Environmental Science* **2012**, *5*, 8351-8358.

72. He, M.; Qiu, F.; Lin, Z. Towards high-performance polymer-based thermoelectric materials. *Energy & Environmental Science* **2013**, *6*, 1352-1361.

73. He, M.; Qiu, F.; Lin, Z. Toward High-Performance Organic-Inorganic Hybrid Solar Cells: Bringing Conjugated Polymers and Inorganic Nanocrystals in Close Contact. *Journal of Physical Chemistry Letters* **2013**, *4*, 1788-1796.

74. Frost, D. S.; Nofen, E. M.; Dai, L. L. Particle self-assembly at ionic liquid-based interfaces. *Adv. Colloid Interface Sci.* **2014**, *206*, 92-105.

75. Koo, B.; Liu, Y.; Zou, J.; Chattopadhyay, A.; Dai, L. L. Study of glass transition temperature (T-g) of novel stress-sensitive composites using molecular dynamic simulation. *Modell Simul Mater Sci Eng* **2014**, *22*, 065018.

76. Termonia, Y. Structure–property relationships in nanocomposites. *Polymer* **2007**, *48*, 6948-6954.

77. Michler, G. H.; Baltá-Calleja, F. J. *Mechanical Properties of Polymers based on Nanostructure and Morphology;* CRC Press: Hoboken, 2005; .

78. Wang, G.; Liu, H.; Yu, Z.; Mai, Y. Evaluation of Methods for Stiffness Predictions of Polymer/Clay Nanocomposites. *J Reinf Plast Compos* **2009**, *28*, 1625-1649.

79. Fornes, T. D.; Paul, D. R. Modeling properties of nylon 6/clay nanocomposites using composite theories. *Polymer* **2003**, *44*, 4993-5013.

80. Novoselov, K. S.; Geim, A. K.; Morozov, S. V.; Jiang, D.; Zhang, Y.; Dubonos, S. V.; Grigorieva, I. V.; Firsov, A. A. Electric field effect in atomically thin carbon films. *Science* **2004**, *306*, 666-669.

81. Iijima, S. Helical Microtubules of Graphitic Carbon. *Nature* **1991**, *354*, 56-58.

82. Kroto, H. W.; Allaf, A. W.; Balm, S. P. C60 - Buckminsterfullerene. *Chem. Rev.* **1991**, *91*, 1213-1235.

83. Wan, Y.; Tang, L.; Gong, L.; Yan, D.; Li, Y.; Wu, L.; Jiang, J.; Lai, G. Grafting of epoxy chains onto graphene oxide for epoxy composites with improved mechanical and thermal properties. *Carbon* **2014**, *69*, 467-480.

84. Song, Y.; Luo, Y.; Zhu, C.; Li, H.; Du, D.; Lin, Y. Recent advances in electrochemical biosensors based on graphene two-dimensional nanomaterials. *Biosens. Bioelectron.* **2016**, *76*, 195-212.

85. Geim, A. K.; Novoselov, K. S. The rise of graphene. *Nature Materials* **2007**, *6*, 183-191.

86. Pötschke, P.; Fornes, T. D.; Paul, D. R. Rheological behavior of multiwalled carbon nanotube/polycarbonate composites. *Polymer* **2002**, *43*, 3247-3255.

87. Moniruzzaman, M.; Winey, K. I. Polymer nanocomposites containing carbon nanotubes. *Macromolecules* **2006**, *39*, 5194-5205.

88. Khare, K. S.; Khare, R. Effect of Carbon Nanotube Dispersion on Glass Transition in Cross-Linked Epoxy-Carbon Nanotube Nanocomposites: Role of Interfacial Interactions. *J Phys Chem B* **2013**, *117*, 7444-7454.

89. Khare, K. S.; Khabaz, F.; Khare, R. Effect of Carbon Nanotube Functionalization on Mechanical and Thermal Properties of Cross-Linked Epoxy-Carbon Nanotube Nanocomposites: Role of Strengthening the Interfacial Interactions. *Acs Applied Materials & Interfaces* **2014**, *6*, 6098-6110.

90. Cha, S. I.; Kim, K. T.; Arshad, S. N.; Mo, C. B.; Hong, S. H. Extraordinary strengthening effect of carbon nanotubes in metal-matrix nanocomposites processed by molecular-level mixing. *Adv Mater* **2005**, *17*, 1377-+.

91. Geng, Y.; Liu, M. Y.; Li, J.; Shi, X. M.; Kim, J. K. Effects of surfactant treatment on mechanical and electrical properties of CNT/epoxy nanocomposites. *Composites Part A-Applied Science and Manufacturing* **2008**, *39*, 1876-1883.

92. Cha, S. I.; Kim, K. T.; Lee, K. H.; Mo, C. B.; Hong, S. H. Strengthening and toughening of carbon nanotube reinforced alumina nanocomposite fabricated by molecular level mixing process. *Scr. Mater.* **2005**, *53*, 793-797.

93. Gojny, F. H.; Nastalczyk, J.; Roslaniec, Z.; Schulte, K. Surface modified multi-walled carbon nanotubes in CNT/epoxy-composites. *Chemical Physics Letters* **2003**, *370*, 820-824.

94. Lu, K. L.; Lago, R. M.; Chen, Y. K.; Green, M. L. H.; Harris, P. J. F.; Tsang, S. C. Mechanical damage of carbon nanotubes by ultrasound. *Carbon* **1996**, *34*, 814-816.

95. Najafi, E.; Kim, J.; Han, S.; Shin, K. UV-ozone treatment of multi-walled carbon nanotubes for enhanced organic solvent dispersion. *Colloids and Surfaces A-Physicochemical and Engineering Aspects* **2006**, *284*, 373-378.

96. Xing, Y. C.; Li, L.; Chusuei, C. C.; Hull, R. V. Sonochemical oxidation of multiwalled carbon nanotubes. *Langmuir* **2005**, *21*, 4185-4190.

97. Bikiaris, D.; Vassiliou, A.; Chrissafis, K.; Paraskevopoulos, K. M.; Jannakoudakis, A.; Docoslis, A. Effect of acid treated multi-walled carbon nanotubes on the mechanical, permeability, thermal properties and thermo-oxidative stability of isotactic polypropylene. *Polym. Degrad. Stab.* **2008**, *93*, 952-967.

98. Vaisman, L.; Wagner, H. D.; Marom, G. The role of surfactants in dispersion of carbon nanotubes. *Adv. Colloid Interface Sci.* **2006**, *128*, 37-46.

99. Vaisman, L.; Marom, G.; Wagner, H. D. Dispersions of surface-modified carbon nanotubes in water-soluble and water-insoluble polymers. *Advanced Functional Materials* **2006**, *16*, 357-363.

100. Fukushima, T.; Kosaka, A.; Ishimura, Y.; Yamamoto, T.; Takigawa, T.; Ishii, N.; Aida, T. Molecular ordering of organic molten salts triggered by single-walled carbon nanotubes. *Science* **2003**, *300*, 2072-2074.

101. Mecerreyes, D. Polymeric ionic liquids: Broadening the properties and applications of polyelectrolytes. *Progress in Polymer Science* **2011**, *36*, 1629-1648.

102. Zhao, L.; Li, Y.; Liu, Z.; Shimizu, H. Carbon Nanotube-Conducting Polymer Core-Shell Hybrid Using an Imidazolium-Salt-Based Ionic Liquid As a Linker: Designed As a Potential Platinum Electrode Alternative Material for Large-Scale Solution Processing. *Chemistry of Materials* **2010**, *22*, 5949-5956.

103. Takacs, L. Mechanochemistry and the Other Branches of Chemistry: Similarities and Differences. *Acta Physica Polonica a* **2012**, *121*, 711-714.

104. Takacs, L. The historical development of mechanochemistry. *Chem. Soc. Rev.* **2013**, *42*, 7649-7659.

105. Boldyreva, E. Mechanochemistry of inorganic and organic systems: what is similar, what is different? *Chem. Soc. Rev.* **2013**, *42*, 7719-7738.

106. Rojac, T.; Segedin, P.; Kosec, M. In *Using Infrared Spectroscopy to Identify New Amorphous Phases - A Case Study of Carbonato Complex Formed by Mechanochemical Processing;* Infrared Spectroscopy - Materials Science, Engineering and Technology; InTech: 2012; pp 13.

107. Liu, X.; Shao, Y.; Zhang, Y.; Meng, G.; Zhang, T.; Wang, F. Using high-temperature mechanochemistry treatment to modify iron oxide and improve the corrosion performance of epoxy coating - I. High-temperature ball milling treatment. *Corros. Sci.* **2015**, *90*, 451-462.

108. James, S. L.; Adams, C. J.; Bolm, C.; Braga, D.; Collier, P.; Friscic, T.; Grepioni, F.; Harris, K. D. M.; Hyett, G.; Jones, W.; Krebs, A.; Mack, J.; Maini, L.; Orpen, A. G.; Parkin, I. P.; Shearouse, W. C.; Steed, J. W.; Waddell, D. C. Mechanochemistry: opportunities for new and cleaner synthesis. *Chem. Soc. Rev.* **2012**, *41*, 413-447.

109. Brantley, J. N.; Wiggins, K. M.; Bielawski, C. W. Polymer mechanochemistry: the design and study of mechanophores. *Polym. Int.* **2013**, *62*, 2-12.

110. Li, J.; Nagamani, C.; Moore, J. S. Polymer Mechanochemistry: From Destructive to Productive. *Acc. Chem. Res.* **2015**, *48*, 2181-2190.

111. Sottos, N. R. POLYMER MECHANOCHEMISTRY Flex, release and repeat. *Nature Chemistry* **2014**, *6*, 381-383.

112. Olmos, D.; Aznar, A.; Gonzalez-Benito, J.; Baselga, J. A fluorescence method to estimate the distribution of stresses in polymer materials. *J. Mater. Process. Technol.* **2003**, *143*, 495-500.

113. Ikawa, T.; Shiga, T.; Okada, A. Fluorescence from poly(N-vinylcarbazole) in uniaxially stretched polymer films. *J Appl Polym Sci* **1997**, *66*, 1569-1573.

114. Beyer, M. K.; Clausen-Schaumann, H. Mechanochemistry: The mechanical activation of covalent bonds. *Chem. Rev.* **2005**, *105*, 2921-2948.

115. Roberts, D. R. T.; Holder, S. J. Mechanochromic systems for the detection of stress, strain and deformation in polymeric materials. *J. Mater. Chem.* **2011**, *21*, 8256-8268.

116. Larsen, M. B.; Boydston, A. J. "Flex-Activated" Mechanophores: Using Polymer Mechanochemistry To Direct Bond Bending Activation. *J. Am. Chem. Soc.* **2013**, *135*, 8189-8192.

117. Silberstein, M. N.; Min, K.; Cremar, L. D.; Degen, C. M.; Martinez, T. J.; Aluru, N. R.; White, S. R.; Sottos, N. R. Modeling mechanophore activation within a crosslinked glassy matrix. *J. Appl. Phys.* **2013**, *114*, 023504.

118. Black, A. L.; Lenhardt, J. M.; Craig, S. L. From molecular mechanochemistry to stress-responsive materials. *Journal of Materials Chemistry* **2011**, *21*, 1655-1663.

119. Brantley, J. N.; Wiggins, K. M.; Bielawski, C. W. Polymer mechanochemistry: the design and study of mechanophores. *Polym. Int.* **2013**, *62*, 2-12.

120. Potisek, S. L.; Davis, D. A.; Sottos, N. R.; White, S. R.; Moore, J. S. Mechanophore-linked addition polymers. *J. Am. Chem. Soc.* **2007**, *129*, 13808-13809.

121. Brantley, J. N.; Bailey, C. B.; Wiggins, K. M.; Keatinge-Clay, A. T.; Bielawski, C. W. Mechanobiochemistry: harnessing biomacromolecules for force-responsive materials. *Polymer Chemistry* **2013**, *4*, 3916-3928.

122. Brantley, J. N.; Bailey, C. B.; Cannon, J. R.; Clark, K. A.; Vanden Bout, D. A.; Brodbelt, J. S.; Keatinge-Clay, A. T.; Bielawski, C. W. Mechanically Modulating the Photophysical Properties of Fluorescent Protein Biocomposites for Ratio- and Intensiometric Sensors. *Angewandte Chemie-International Edition* **2014**, *53*, 5088-5092.

123. Makyla, K.; Mueller, C.; Loercher, S.; Winkler, T.; Nussbaumer, M. G.; Eder, M.; Bruns, N. Fluorescent Protein Senses and Reports Mechanical Damage in Glass-Fiber-Reinforced Polymer Composites. *Adv Mater* **2013**, *25*, 2701-2706.

124. Loercher, S.; Winkler, T.; Makyla, K.; Ouellet-Plamondon, C.; Burgert, I.; Bruns, N. Mechanical unfolding of a fluorescent protein enables self-reporting of damage in carbon-fibre-reinforced composites. *Journal of Materials Chemistry a* **2014**, *2*, 6231-6237.

125. Kingsbury, C. M.; May, P. A.; Davis, D. A.; White, S. R.; Moore, J. S.; Sottos, N. R. Shear activation of mechanophore-crosslinked polymers. *J. Mater. Chem.* **2011**, *21*, 8381-8388.

126. Celestine, A. N.; Beiermann, B. A.; May, P. A.; Moore, J. S.; Sottos, N. R.; White, S. R. Fracture-induced activation in mechanophore-linked, rubber toughened PMMA. *Polymer* **2014**, *55*, 4164-4171.

127. Gossweiler, G. R.; Hewage, G. B.; Soriano, G.; Wang, Q.; Welshofer, G. W.; Zhao, X.; Craig, S. L. Mechanochemical Activation of Covalent Bonds in Polymers with Full and Repeatable Macroscopic Shape Recovery. *ACS Macro Lett.* **2014**, *3*, 216-219.

128. He, D.; Susanto, H.; Ulbricht, M. Photo-irradiation for preparation, modification and stimulation of polymeric membranes. *Progress in Polymer Science* **2009**, *34*, 62-98.

129. Nakamura, T.; Takagi, K.; Itoh, M.; Fujita, K.; Katsu, H.; Imae, T.; Sawaki, Y. Photodimerization of cinnamic acids controlled by molecular assemblies of surfactant amine N-oxides. *Journal of the Chemical Society-Perkin Transactions 2* **1997**, 2751-2755.

130. Takagi, K.; Itoh, M.; Usami, H.; Imae, T.; Sawaki, Y. Organized Photodimerization of Unsaturated Carboxylates - Selectivity Control by Normal and Reversed Micelles. *Journal of the Chemical Society-Perkin Transactions 2* **1994**, 1003-1009.

131. Cho, S.; Kim, J.; Chung, C. A fluorescent crack sensor based on cyclobutane-containing crosslinked polymers of tricinnamates. *Sensors and Actuators B-Chemical* **2008**, *134*, 822-825.

132. Cho, S.; Kim, J.; Chung, C. Photochemical Crack Healing in Cinnamate-Based Polymers. *Journal of Nanoscience and Nanotechnology* **2010**, *10*, 6972-6976.

133. Chung, C.; Roh, Y.; Cho, S.; Kim, J. Crack healing in polymeric materials via photochemical [2+2] cycloaddition. *Chem. Mat.* **2004**, *16*, 3982-3984.

134. Oya, N.; Sukarsaatmadja, P.; Ishida, K.; Yoshie, N. Photoinduced mendable network polymer from poly(butylene adipate) end-functionalized with cinnamoyl groups. *Polym. J.* **2012**, *44*, 724-729.

135. Kryger, M. J.; Ong, M. T.; Odom, S. A.; Sottos, N. R.; White, S. R.; Martinez, T. J.; Moore, J. S. Masked Cyanoacrylates Unveiled by Mechanical Force. *J. Am. Chem. Soc.* **2010**, *132*, 4558-4559.

136. Cintas, P.; Cravotto, G. MECHANOCHEMISTRY Measuring the force of sound. *Nature Chemistry* **2012**, *4*, 77-78.

137. Kryger, M. J.; Munaretto, A. M.; Moore, J. S. Structure-Mechanochemical Activity Relationships for Cyclobutane Mechanophores. *J. Am. Chem. Soc.* **2011**, *133*, 18992-18998.

138. Lenhardt, J. M.; Black, A. L.; Craig, S. L. gem-Dichlorocyclopropanes as Abundant and Efficient Mechanophores in Polybutadiene Copolymers under Mechanical Stress. *J. Am. Chem. Soc.* **2009**, *131*, 10818-10819.

139. Ramirez, A. L. B.; Kean, Z. S.; Orlicki, J. A.; Champhekar, M.; Elsakr, S. M.; Krause, W. E.; Craig, S. L. Mechanochemical strengthening of a synthetic polymer in response to typically destructive shear forces. *Nature Chemistry* **2013**, *5*, 757-761.

140. Tong, F.; Cruz, C. D.; Jezowski, S. R.; Zhou, X.; Zhu, L.; Al-Kaysi, R.; Chronister, E. L.; Bardeen, C. J. Pressure Dependence of the Forward and Backward Rates of 9-tert-Butylanthracene Dewar Isomerization. *J Phys Chem A* **2014**, *118*, 5349-5354.

141. Ma, Z.; Yang, F.; Wang, Z.; Jia, X. Mechanically induced color change based on the chromophores of anthracene and rhodamine 6G. *Tetrahedron Lett.* **2015**, *56*, 393-396.

142. Brichkin, S. B.; Razumov, V. F.; Bogdanova, L. M.; Rozenberg, B. A. Luminescent labels for the study of phase separation in cured epoxy polymer systems. *Polymer Science Series a* **2000**, *42*, 516-521.

143. Sagara, Y.; Yamane, S.; Mutai, T.; Araki, K.; Kato, T. A Stimuli-Responsive, Photoluminescent, Anthracene-Based Liquid Crystal: Emission Color Determined by Thermal and Mechanical Processes. *Advanced Functional Materials* **2009**, *19*, 1869-1875.

144. Defize, T.; Riva, R.; Jerome, C.; Alexandre, M. Multifunctional Poly(epsilon-caprolactone)-Forming Networks by Diels-Alder Cycloaddition: Effect of the Adduct on the Shape-Memory Properties. *Macromolecular Chemistry and Physics* **2012**, *213*, 187-197.

145. Froimowicz, P.; Frey, H.; Landfester, K. Towards the Generation of Self-Healing Materials by Means of a Reversible Photo-induced Approach. *Macromolecular Rapid Communications* **2011**, *32*, 468-473.

146. Xing, J.; Zheng, M.; Chen, W.; Dong, X.; Takeyasu, N.; Tanaka, T.; Zhao, Z.; Duan, X.; Kawata, S. C-2v symmetrical two-photon polymerization initiators with anthracene core: synthesis, optical and initiating properties. *Phys. Chem. Chem. Phys.* **2012**, *14*, 15785-15792.

147. Song, Y.; Lee, K.; Hong, W.; Cho, S.; Yu, H.; Chung, C. Fluorescence sensing of microcracks based on cycloreversion of a dimeric anthracene moiety. *J. Mater. Chem.* **2012**, *22*, 1380-1386.

148. Jezowski, S. R.; Zhu, L.; Wang, Y.; Rice, A. P.; Scott, G. W.; Bardeen, C. J.; Chronister, E. L. Pressure Catalyzed Bond Dissociation in an Anthracene Cyclophane Photodimer. *J. Am. Chem. Soc.* **2012**, *134*, 7459-7466.

149. Yoshie, N.; Saito, S.; Oya, N. A thermally-stable self-mending polymer networked by Diels-Alder cycloaddition. *Polymer* **2011**, *52*, 6074-6079.

150. Atherton, J. C. C.; Jones, S. Diels-Alder reactions of anthracene, 9-substituted anthracenes and 9,10-disubstituted anthracenes. *Tetrahedron* **2003**, *59*, 9039-9057.

151. Johns, V. K.; Shi, Z.; Dang, W.; McInnis, M. D.; Weng, Y.; Liao, Y. Photo Retro-Diels-Alder Reactions. *Journal of Physical Chemistry a* **2011**, *115*, 8093-8099.

152. Gostl, R.; Sijbesma, R. P. pi-extended anthracenes as sensitive probes for mechanical stress. *Chem. Sci.* **2016**, *7*, 370.

153. Som, T.; Troppenz, G. V.; Wendt, R. R.; Wollgarten, M.; Rappich, J.; Emmerling, F.; Rademann, K. Graphene Oxide/alpha-Bi2O3 Composites for Visible-Light Photocatalysis, Chemical Catalysis, and Solar Energy Conversion. *Chemsuschem* **2014**, *7*, 854-865.

154. Hou, K.; Huang, L.; Qi, Y.; Huang, C.; Pan, H.; Du, M. A bisphenol A sensor based on novel self-assembly of zinc phthalocyanine tetrasulfonic acid-functionalized graphene nanocomposites. *Materials Science & Engineering C-Materials for Biological Applications* **2015**, *49*, 640-647.

155. Piazza, D.; Lorandi, N. P.; Pasqual, C. I.; Scienza, L. C.; Zattera, A. J. Influence of a microcomposite and a nanocomposite on the properties of an epoxy-based powder coating. *Materials Science and Engineering: A* **2011**, *528*, 6769-6775.

156. Kaupp, G. Mechanochemistry: the varied applications of mechanical bond-breaking. *Crystengcomm* **2009**, *11*, 388-403.

157. Chen, Y.; Spiering, A. J. H.; Karthikeyan, S.; Peters, G. W. M.; Meijer, E. W.; Sijbesma, R. P. Mechanically induced chemiluminescence from polymers incorporating a 1,2-dioxetane unit in the main chain. *Nature Chemistry* **2012**, *4*, 559-562.

158. Ramirez, A. L. B.; Schmitt, A. K.; Mahanthappa, M. K.; Craig, S. L. Enhancing covalent mechanochemistry in bulk polymers using electrospun ABA triblock copolymers. *Faraday Discuss.* **2014**, *170*, 337-344.

159. Zou, J.; Liu, Y.; Shan, B.; Chattopadhyay, A.; Dai, L. L. Early damage detection in epoxy matrix using cyclobutane-based polymers. *Smart Mater. Struct.* **2014**, *23*, 095038.

160. Harada, J.; Kawazoe, Y.; Ogawa, K. Photochromism of spiropyrans and spirooxazines in the solid state: low temperature enhances photocoloration. *Chem. Commun.* **2010**, *46*, 2593-2595.

161. Shiraishi, Y.; Itoh, M.; Hirai, T. Thermal isomerization of spiropyran to merocyanine in aqueous media and its application to colorimetric temperature indication. *Phys. Chem. Chem. Phys.* **2010**, *12*, 13737-13745.

162. Aakeroy, C. B.; Hurley, E. P.; Desper, J.; Natali, M.; Douglawi, A.; Giordani, S. The balance between closed and open forms of spiropyrans in the solid state. *Crystengcomm* **2010**, *12*, 1027-1033.

163. Klajn, R. Spiropyran-based dynamic materials. *Chem. Soc. Rev.* **2014**, *43*, 148-184.

164. Hammarson, M.; Nilsson, J. R.; Li, S.; Beke-Somfai, T.; Andreasson, J. Characterization of the Thermal and Photoinduced Reactions of Photochromic Spiropyrans in Aqueous Solution. *J Phys Chem B* **2013**, *117*, 13561-13571.

165. Samat, A.; Metzger, J.; Mentienne, F.; Garnier, F.; Dubois, J. E.; Guglielmetti, R. Structure Effect on the Fading Rate of Photochromic 3-Substituted Benzothiazolinic Spiropyrans. *The Journal of Physical Chemistry* **1972**, *76*, 3554-3558.

166. Davis, D. A. Spiropyrans as color-generating mechanophores, ProQuest Dissertations Publishing, 2010.

167. Li, J.; Shiraki, T.; Hu, B.; Wright, R. A. E.; Zhao, B.; Moore, J. S. Mechanophore Activation at Heterointerfaces. *J. Am. Chem. Soc.* **2014**, *136*, 15925-15928.

168. Zhu, M. Q.; Zhu, L. Y.; Han, J. J.; Wu, W. W.; Hurst, J. K.; Li, A. D. Q. Spiropyran-based photochromic polymer nanoparticles with optically switchable luminescence. *J. Am. Chem. Soc.* **2006**, *128*, 4303-4309.

169. Huang, C.; Wang, Y.; Hong, C.; Pan, C. Spiropyran-Based Polymeric Vesicles: Preparation and Photochromic Properties. *Macromolecular Rapid Communications* **2011**, *32*, 1174-1179.

170. Su, J.; Chen, J.; Zeng, F.; Chen, Q.; Wu, S.; Tong, Z. Synthesis and photochromic property of nanoparticles with spiropyran moieties via one-step miniemulsion polymerization. *Polymer Bulletin* **2008**, *61*, 425-434.

171. Koo, B.; Chattopadhyay, A.; Dai, L. Atomistic Modeling Framework for a Cyclobutane-Based Mechanophore-Embedded Nanocomposite for Damage Precursor Detection. *Smart Mater. Struct.* **Under Review**.

172. Beyer, M. K. The mechanical strength of a covalent bond calculated by density functional theory. *J. Chem. Phys.* **2000**, *112*, 7307-7312.

173. Koo, B.; Subramanian, N.; and Chattopadhyay, A. An Atomistic Simulation Methodology to Model Damage in Amorphous Thermoset Polymer. *Computational Materials Science* **Under Review**.

174. Ito, Y.; Olovsson, G. Use of linker for preparation of missing solid-state photoproducts: Head-to-head photodimerization of anthracene-9-propionic acid in its crystalline double salt with cyclohexane-l,2-diamine. *Journal of the Chemical Society-Perkin Transactions 1* **1997**, 127-133.

175. More, R.; Busse, G.; Hallmann, J.; Paulmann, C.; Scholz, M.; Techert, S. Photodimerization of Crystalline 9-Anthracenecarboxylic Acid: A Nontopotactic Autocatalytic Transformation. *Journal of Physical Chemistry C* **2010**, *114*, 4142-4148.

176. Zouev, I.; Cao, D.; Sreevidya, T. V.; Telzhensky, M.; Botoshansky, M.; Kaftory, M. Photodimerization of anthracene derivatives in their neat solid state and in solid molecular compounds. *Crystengcomm* **2011**, *13*, 4376-4381.

177. Good, J. T.; Burdett, J. J.; Bardeen, C. J. Using Two-Photon Excitation to Control Bending Motions in Molecular-Crystal Nanorods. *Small* **2009**, *5*, 2902-2909.

178. Zhu, L.; Al-Kaysi, R. O.; Dillon, R. J.; Tham, F. S.; Bardeen, C. J. Crystal Structures and Photophysical Properties of 9-Anthracene Carboxylic Acid Derivatives for Photomechanical Applications. *Crystal Growth & Design* **2011**, *11*, 4975-4983.

179. Nielsen, L. E. Cross-Linking-Effect on Physical Properties of Polymers. *Journal of Macromolecular Science-Reviews in Macromolecular Chemistry* **1969**, *C3*, 69-103.

180. Wiberg, K. B. The Concept of Strain in Organic-Chemistry. *Angewandte Chemie-International Edition in English* **1986**, *25*, 312-322.

181. Nofen, E. M.; Wickham, J.; Koo, B.; Chattopadhyay, A.; Dai, L. L. Dimeric anthracene-based mechanophore particles for damage precursor detection in reinforced epoxy matrix composites. *Mater. Res. Express* **2016**, *3*, 035701.

182. Lee, C. K.; Beiermann, B. A.; Silberstein, M. N.; Wang, J.; Moore, J. S.; Sottos, N. R.; Braun, P. V. Exploiting Force Sensitive Spiropyrans as Molecular Level Probes. *Macromolecules* **2013**, *46*, 3746-3752.

183. Chen, Y.; Sijbesma, R. P. Dioxetanes as Mechanoluminescent Probes in Thermoplastic Elastomers. *Macromolecules* **2014**, *47*, 3797-3805.

184. Larsen, M. B.; Boydston, A. J. Successive Mechanochemical Activation and Small Molecule Release in an Elastomeric Material. *J. Am. Chem. Soc.* **2014**, *136*, 1276-1279.

185. Imato, K.; Kanehara, T.; Ohishi, T.; Nishihara, M.; Yajima, H.; Ito, M.; Takahara, A.; Otsuka, H. Mechanochromic Dynamic Covalent Elastomers: Quantitative Stress Evaluation and Autonomous Recovery. *Acs Macro Letters* **2015**, *4*, 1307-1311.

186. Wang, Z.; Ma, Z.; Wang, Y.; Xu, Z.; Luo, Y.; Wei, Y.; Jia, X. A Novel Mechanochromic and Photochromic Polymer Film: When Rhodamine Joins Polyurethane. *Adv Mater* **2015**, *27*, 6469-+.

187. Hirose, S.; Hatakeyama, T.; Hatakeyama, H. Thermal Properties of Epoxy Resins from Ester-Carboxylic Acid Derivatives of Mono- and Disaccharides. *Netsu Sokutei* **2003**, *30*, 154-160.

188. Hirose, S.; Hatakeyama, T.; Hatakeyama, H. Curing and glass transition of epoxy resins from ester-carboxylic acid derivatives of mono- and disaccharides, and alcoholysis lignin. *Macromolecular Symposia* **2005**, *224*, 343-353.

189. Auvergne, R.; Caillol, S.; David, G.; Boutevin, B.; Pascault, J. Biobased Thermosetting Epoxy: Present and Future. *Chem. Rev.* **2014**, *114*, 1082-1115.

190. Beiermann, B. A.; Davis, D. A.; Kramer, S. L. B.; Moore, J. S.; Sottos, N. R.; White, S. R. Environmental effects on mechanochemical activation of spiropyran in linear PMMA. *Journal of Materials Chemistry* **2011**, *21*, 8443-8447.

191. Caruso, M. M.; Davis, D. A.; Shen, Q.; Odom, S. A.; Sottos, N. R.; White, S. R.; Moore, J. S. Mechanically-Induced Chemical Changes in Polymeric Materials. *Chem. Rev.* **2009**, *109*, 5755-5798.

192. Lambert, J. B. *Introduction to organic spectroscopy;* New York : Macmillan: 1987; .

193. Gonzalez, M.; Carlos, J.; Baselg, J. Applications of FTIR on Epoxy Resins - Identification, Monitoring the Curing Process, Phase Separation and Water Uptake. *Infrared Spectroscopy - Materials Science, Engineering and Technology* **2012**.

194. Henbest, H. B.; Meakins, G. D.; Nicholls, B.; Taylor, K. J. Detection of the Epoxide Group by Infrared Spectroscopy. *Journal of the Chemical Society* **1957**, 1459-1462.

195. Evtushenko, Y. M.; Ivanov, V. M.; Zaitsev, B. E. Determination of epoxide and hydroxyl groups in epoxide resins by IR spectrometry. *Journal of Analytical Chemistry* **2003**, *58*, 347-350.

196. Wen, J.; Xia, Z.; Choy, F. Damage detection of carbon fiber reinforced polymer composites via electrical resistance measurement. *Composites Part B-Engineering* **2011**, *42*, 77-86.

197. Tallman, T. N.; Gungor, S.; Wang, K. W.; Bakis, C. E. Damage detection and conductivity evolution in carbon nanofiber epoxy via electrical impedance tomography. *Smart Mater. Struct.* **2014**, *23*, 045034.

198. Kaczmarek, H.; Maison, S. Comparative Ultrasonic Analysis of Damage in Cfrp Under Static Indentation and Low-Velocity Impact. *Composites Sci. Technol.* **1994**, *51*, 11-26.

199. Trappe, V.; Harbich, K. -. Intralaminar fatigue behaviour of carbon fibre reinforced plastics. *Int. J. Fatigue* **2006**, *28*, 1187-1196.

200. Bai, W.; Wong, B. S. Evaluation of defects in composite plates under convective environments using lock-in thermography. *Meas Sci Technol* **2001**, *12*, 142-150.

201. Borazjani, E.; Spinello, D.; Necsulescu, D. In *In Design of infrared non-destructive testing for damage detection in multi-layer materials;* 11th International Conference on Quantitative InfraRed Thermography; 2012; .

202. Usamentiaga, R.; Venegas, P.; Guerediaga, J.; Vega, L.; Lopez, I. Automatic detection of impact damage in carbon fiber composites using active thermography. *Infrared Phys. Technol.* **2013**, *58*, 36-46.

203. Ju, C.; Wang, Y.; He, D.; Gao, Q.; Gao, L.; Fu, M. Study on the Infrared Property of Polyaniline/Multi-Wall Carbon Nanotube Composite. *Journal of Nanoscience and Nanotechnology* **2012**, *12*, 6558-6561.

204. Fahrenfort, J. Attenuated Total Reflection - a New Principle for the Production of Useful Infra-Red Reflection Spectra of Organic Compounds. *Spectrochimica Acta* **1961**, *17*, 698-&.

205. vanSoest, J. J. G.; Tournois, H.; deWit, D.; Vliegenthart, J. F. G. Short-range structure in (partially) crystalline potato starch determined with attenuated total reflectance Fourier-transform IR spectroscopy. *Carbohydr. Res.* **1995**, *279*, 201-214.

206. Feng, L. L.; Berglund, K. A. ATR-FTIR for determining optimal cooling curves for batch crystallization of succinic acid. *Crystal Growth & Design* **2002**, *2*, 449-452.

207. van de Weert, M.; Haris, P. I.; Hennink, W. E.; Crommelin, D. J. A. Fourier transform infrared spectrometric analysis of protein conformation: Effect of sampling method and stress factors. *Anal. Biochem.* **2001**, *297*, 160-169.

208. Oberg, K. A.; Fink, A. L. A new attenuated total reflectance Fourier transform infrared spectroscopy method for the study of proteins in solution. *Anal. Biochem.* **1998**, *256*, 92-106.

209. Salari, A.; Young, R. E. Application of attenuated total reflectance FTIR spectroscopy to the analysis of mixtures of pharmaceutical polymorphs. *Int. J. Pharm.* **1998**, *163*, 157-166.

210. Eddaoudi, M.; Moler, D. B.; Li, H. L.; Chen, B. L.; Reineke, T. M.; O'Keeffe, M.; Yaghi, O. M. Modular chemistry: Secondary building units as a basis for the design of highly porous and robust metal-organic carboxylate frameworks. *Acc. Chem. Res.* **2001**, *34*, 319-330.

211. Kitagawa, S.; Kitaura, R.; Noro, S. Functional porous coordination polymers. *Angewandte Chemie-International Edition* **2004**, *43*, 2334-2375.

212. Li, H.; Eddaoudi, M.; O'Keeffe, M.; Yaghi, O. M. Design and synthesis of an exceptionally stable and highly porous metal-organic framework. *Nature* **1999**, *402*, 276-279.

213. Seo, J. S.; Whang, D.; Lee, H.; Jun, S. I.; Oh, J.; Jeon, Y. J.; Kim, K. A homochiral metal-organic porous material for enantioselective separation and catalysis. *Nature* **2000**, *404*, 982-986.

214. Lee, J.; Farha, O. K.; Roberts, J.; Scheidt, K. A.; Nguyen, S. T.; Hupp, J. T. Metal-organic framework materials as catalysts. *Chem. Soc. Rev.* **2009**, *38*, 1450-1459.

215. Li, J.; Kuppler, R. J.; Zhou, H. Selective gas adsorption and separation in metal-organic frameworks. *Chem. Soc. Rev.* **2009**, *38*, 1477-1504.

216. Zhang, Z.; Ha Thi Hoang Nguyen; Miller, S. A.; Cohen, S. M. polyMOFs: A Class of Interconvertible Polymer-Metal-Organic-Framework Hybrid Materials. *Angewandte Chemie-International Edition* **2015**, *54*, 6152-6157.

217. Lee, S.; Choi, E.; Lee, S.; Kim, S.; Kwon, O. -. Unusual Transformation from a Solvent-Stabilized 1D Coordination Polymer to a Metal-Organic Framework (MOF)-Like Cross-Linked 3D Coordination Polymer. *Chemistry-a European Journal* **2015**, *21*, 15570-15574.

218. Allen, C. A.; Boissonnault, J. A.; Cirera, J.; Gulland, R.; Paesani, F.; Cohen, S. M. Chemically crosslinked isoreticular metal-organic frameworks. *Chemical Communications* **2013**, *49*, 3200-3202.

219. Zhang, M.; Ngo, T. H.; Rabiah, N. I.; Otanicar, T. P.; Phelan, P. E.; Swaminathan, R.; Dai, L. L. Core-Shell and Asymmetric Polystyrene-Gold Composite Particles via One-Step Pickering Emulsion Polymerization. *Langmuir* **2014**, *30*, 75-82.

220. Chen, H.; Kelley, M.; Guo, C.; Yarger, J. L.; Dai, L. L. Adsorption and release of surfactant into and from multifunctional zwitterionic poly(NIPAm-co-DMAPMA-co-AAc) microgel particles. *J. Colloid Interface Sci.* **2015**, *449*, 332-340.

221. Destribats, M.; Eyharts, M.; Lapeyre, V.; Sellier, E.; Varga, I.; Ravaine, V.; Schmitt, V. Impact of pNIPAM Microgel Size on Its Ability To Stabilize Pickering Emulsions. *Langmuir* **2014**, *30*, 1768-1777.

222. Liu, H.; Zhu, H.; Zhu, S. Reversibly Dispersible/Collectable Metal-Organic Frameworks Prepared by Grafting Thermally Responsive and Switchable Polymers. *Macromolecular Materials and Engineering* **2015**, *300*, 191-197.

223. Friscic, T.; Halasz, I.; Strukil, V.; Eckert-Maksic, M.; Dinnebier, R. E. Clean and Efficient Synthesis Using Mechanochemistry: Coordination Polymers, Metal-Organic Frameworks and Metallodrugs. *Croat. Chem. Acta* **2012**, *85*, 367-378.

224. Luo, M.; Dai, L. L. Molecular dynamics simulations of surfactant and nanoparticle self-assembly at liquid–liquid interfaces. *Journal of Physics: Condensed Matter* **2007**, *19*, 375109; 375109.

225. Luo, M.; Mazyar, O. A.; Zhu, Q.; Vaughn, M. W.; Hase, W. L.; Dai, L. L. Molecular Dynamics Simulation of Nanoparticle Self-Assembly at a Liquid-Liquid Interface. *Langmuir* **2006**, *22*, 6385-6390.

226. Binks, B. P.; Lumsdon, S. O. Influence of Particle Wettability on the Type and Stability of Surfactant-Free Emulsions. *Langmuir* **2000**, *16*, 8622-8631.

227. Binks, B. P.; Horozov, T. S. *Colloidal particles at liquid interfaces;* Cambridge University Press: Cambridge; New York, 2006; , pp 503.

228. Niu, Z.; He, J.; Russell, T. P.; Wang, Q. Synthesis of Nano/Microstructures at Fluid Interfaces. *Angew. Chem. Int. Ed.* **2010**, *49*, 10052-10066.

229. Bresme, F.; Oettel, M. Nanoparticles at fluid interfaces. *Journal of Physics: Condensed Matter* **2007**, *19*, 413101.

230. Ramsden, W. *Proc. R. Soc. London* **1903**, *91*, 940.

231. Pickering, S. U. Emulsions. *J. Chem. Soc. Trans.* **1907**, *91*, 2001-2021.

232. Betancourt, O. J.; McLean, A. Y. Changes in Chemical Composition and Physical Properties of a Heavy Residual Oil Weathering under Natural Conditions. *Journal of the Institute of Petroleum* **1973**, *59*, 223-230.

233. Mackay, G. D. M.; McLean, A. Y.; Betancourt, O. J.; Johnson, B. D. Formation of Water-in-Oil Emulsions Subsequent to an Oil Spill. *Journal of the Institute of Petroleum* **1973**, *59*, 164-172.

234. Chieu, J. N.; Gloyna, E. F.; Schechter, R. S. Coalescence of Emulsified oily Wastewater by Fibrous Beds. *Proceedings of the Industrial Waste Conference* **1977**, *30*, 611-620.

235. Van Boekel, M. A. J. S.; Walstra, P. Stability of Oil-in-Water Emulsions with Crystals in the disperse Phase. *Colloids and Surfaces* **1981**, *3*, 109-118.

236. Jaynes, E. N. In *Chapter 6: Applications in Food Industry II;* Becher, P., Ed.; Encyclopedia of Emulsion Technology; Marcel Dekker: New York, 1983; Vol. 2, .

237. Corcorran, S.; Lochhead, R. Y.; McKay, T. Particle-Stabilized Emulsions: A Brief Overview. *Cosmetics and Toiletries* **2004**, *119*, 47-50.

238. Stiller, S.; Gers-Barlag, H.; Lergenmueller, M.; Pflücker, F.; Schulz, J.; Wittern, K. P.; Daniels, R. Investigation of the stability in emulsions stabilized with different surface modified titanium dioxides. *Colloids Surf. Physicochem. Eng. Aspects* **2004**, *232*, 261-267.

239. Fuller, G. G.; Lask, M.; Melle, S. Pickering Emulsions with Controllable Stability. *Langmuir* **2005**, *21*, 2158-2162.

240. Velev, O.; Furusawa, K.; Nagayama, K. Assembly of latex particles by using emulsion droplets as templates 2. Ball-like and composite aggregates. *Langmuir* **1996**, *12*, 2385-2391.

241. Dinsmore, A. D.; Hsu, M. F.; Nikolaides, M. G.; Marquez, M.; Bausch, A. R.; Weitz, D. A. Colloidosomes: Selectively Permeable Capsules Composed of Colloidal Particles. *Science* **2002**, *298*, pp. 1006-1009.

242. Faria, J.; Ruiz, M. P.; Resasco, D. E. Phase-Selective Catalysis in Emulsions Stabilized by Janus Silica Nanoparticles. *Adv. Synth. Catal.* **2010**, *352*, 2359-2364.

243. Crossley, S.; Faria, J.; Shen, M.; Resasco, D. E. Solid nanoparticles that catalyze biofuel upgrade reactions at the water/oil interface. *Science* **2010**, *327*, 68-72.

244. He, Y. Preparation of polyaniline/nano-ZnO composites via a novel Pickering emulsion route. *Powder Technol* **2004**, *147*, 59-63.

245. Voorn, D.; Ming, W.; van Herk, A. Polymer-clay nanocomposite latex particles by inverse pickering emulsion polymerization stabilized with hydrophobic montmorillonite platelets. *Macromolecules* **2006**, *39*, 2137-2143.

246. Tarimala, S.; Dai, L. L. Structure of Microparticles in Solid-Stabilized Emulsions. *Langmuir* **2004**, *20*, 3492-3494.

247. Dai, L. L.; Tarimala, S.; Wu, C.; Guttula, S.; Wu, J. The Structure and Dynamics of Microparticles at Pickering Emulsion Interfaces. *Scanning* **2008**, *30*, 87.

248. Ma, H.; Dai, L. L. Structure of Multi-Component Colloidal Lattices at Oil-Water Interfaces. *Langmuir* **2009**, *25*, 11210-11215.

249. Plechkova, N. V.; Seddon, K. R. Applications of ionic liquids in the chemical industry. *Chem. Soc. Rev.* **2008**, *37*, 123-150.

250. Walden, P. *Bull. Acad. Imper. Sci. St. Petersbourg* **1914**, *8*, 405-422.

251. Chum, H. L.; Koch, V. R.; Miller, L. L.; Osteryoung, R. A. Electrochemical scrutiny of organometallic iron complexes and hexamethylbenzene in a room temperature molten salt. *J. Am. Chem. Soc.* **1975**, *97*, 3264-3265.

252. Holbrey, J. D.; Seddon, K. R. The phase behaviour of 1-alkyl-3-methylimidazolium tetrafluoroborate; ionic liquids and ionic crystals. *J. Chem. Soc. Dalton Trans.* **1999**, 2133.

253. Seddon, K. R. *Kinet. Catal.* **1996**, *37*, 693-697.

254. Bonhote, P.; Dias, A.; Papageorgiou, N.; Kalyanasundaram, K.; Gratzel, M. Hydrophobic, Highly Conductive Ambient-Temperature Molten Salts. *Inorg. Chem.* **1996**, *35*, 1168-1178.

255. Huddleston, J. G.; Visser, A. E.; Reichert, W. M.; Willauer, H. D.; Broker, G. A.; Rogers, R. D. Characterization and comparison of hydrophilic and hydrophobic room temperature ionic liquids incorporating the imidazolium cation. *Green Chem.* **2001**, *3*, 156-164.

256. Seddon, K. R.; Stark, A.; Torres, M. J. Influence of chloride, water, and organic solvents on the physical properties of ionic liquids. *Pure Appl. Chem.* **2000**, *72*, 2275-2287.

257. Chaumont, A.; Schurhammer, R.; Wipff, G. Aqueous Interfaces with Hydrophobic Room-Temperature Ionic Liquids: A Molecular Dynamics Study. *J Phys Chem B* **2005**, *109*, 18964.

258. Ranke, J.; Othman, A.; Fan, P.; Müller, A. Explaining ionic liquid water solubility in terms of cation and anion hydrophobicity. *International journal of molecular sciences* **2009**, *10*, 1271-1289.

259. Brennecke, J. F.; Maginn, E. J. Ionic liquids: Innovative fluids for chemical processing. *AIChE J.* **2001**, *47*, 2384-2389.

260. Goodrich, B. F.; de, l. F.; Gurkan, B. E.; Lopez, Z. K.; Price, E. A.; Huang, Y.; Brennecke, J. F. Effect of Water and Temperature on Absorption of CO 2 by Amine-Functionalized Anion-Tethered Ionic Liquids. *The Journal of Physical Chemistry B* **2011**, *115*, 9140-9150.

261. Schneider, W. F.; Brennecke, J. F.; Maginn, E. J.; Mindrup, E.; Gurkan, B.; Price, E.; Goodrich, B. WO2011056895A1, 2011.

262. Gurkan, B. E.; de, l. F.,Juan C.; Mindrup, E. M.; Ficke, L. E.; Goodrich, B. F.; Price, E. A.; Schneider, W. F.; Brennecke, J. F. Equimolar CO2 Absorption by Anion-Functionalized Ionic Liquids. *J. Am. Chem. Soc.* **2010**, *132*, 2116-2117.

263. Cadena, C.; Anthony, J. L.; Shah, J. K.; Morrow, T. I.; Brennecke, J. F.; Maginn, E. J. Why Is CO2 So Soluble in Imidazolium-Based Ionic Liquids? *J. Am. Chem. Soc.* **2004**, *126*, 5300-5308.

264. Gupta, K. M.; Chen, Y.; Hu, Z.; Jiang, J. Metal-organic framework supported ionic liquid membranes for CO2 capture: anion effects. *Phys. Chem. Chem. Phys.* **2012**, *14*, 5785-5794.

265. Joskowska, M.; Kopczynska, I.; Debski, B.; Holownia-Kedzia, D.; Aranowski, R.; Hupka, J. Wetting of supports by ionic liquids used in gas separation processes. *Physicochem. Probl. Miner. Process.* **2012**, *48*, 129-140.

266. Gurkan, B. E.; de la Fuente, J. C.; Mindrup, E. M.; Ficke, L. E.; Goodrich, B. F.; Price, E. A.; Schneider, W. F.; Maginn, E.; Brennecke, J. F. Chemically complexing ionic liquids for post-combustion CO2 capture. *Int. Tech. Conf. Clean Coal Fuel Syst.* **2010**, *35*, 931-937.

267. Luebke, D.; Nulwala, H.; Wickramanayake, S.; Hopkinson, D.; Myers, C. In *In Supported ionic liquid membranes for CO2 capture;* American Chemical Society: 2012; , pp 172.

268. Tempel, D. J.; Henderson, P. B.; Brzozowski, J. R. US Patent 2006060817, 2006.

269. Tempel, D. J.; Henderson, P. B.; Brzozowski, J. R.; Pearlstein, R. M.; Cheng, H. High Gas Storage Capacities for Ionic Liquids through Chemical Complexation. *J. Am. Chem. Soc.* **2008**, *130*, 400-401.

270. Welton, T. Room-Temperature Ionic Liquids. Solvents for Synthesis and Catalysis. *Chem. Rev.* **1999**, *99*, 2071-2084.

271. Hallett, J. P.; Welton, T. Room-Temperature Ionic Liquids: Solvents for Synthesis and Catalysis. 2. *Chem. Rev.* **2011**, *111*, 3508-3576.

272. Haugland, R. *Handbook of fluorescent probes and research products. 9th ed;* Molecular Probes, Inc: Eugene, Oregon, 2002; .

273. Berendsen, H. J. C.; van, d. S.; van Drunen, R. GROMACS: A message-passing parallel molecular dynamics implementation. *Comput. Phys. Commun.* **1995**, *91*, 43-56.

274. Lindahl, E.; Hess, B.; Van der Spoel, D. GROMACS 3.0: a package for molecular simulation and trajectory analysis. *J. Mol. Model.* **2001**, *7*, 306.

275. Van, D. S.; Lindahl, E.; Hess, B.; Groenhof, G.; Mark, A. E.; Berendsen, H. J. C. GROMACS: Fast, flexible, and free. *J.Comput.Chem.* **2005**, *26*, 1701-1718.

276. Jorgensen, W. L.; Madura, J. D.; Swenson, C. J. Optimized intermolecular potential functions for liquid hydrocarbons. *J. Am. Chem. Soc.* **1984**, *106*, 6638-6646.

277. Lopes, J. N. C.; Padua, A. A. H. Molecular force field for ionic liquids composed of triflate or bistriflylimide anions. *J Phys Chem B* **2004**, *108*, 16893.

278. Lopes, J. N. C.; Deschamps, J.; Padua, A. A. H. Modeling Ionic Liquids Using a Systematic All-Atom Force Field. *J Phys Chem B* **2004**, *108*, 2038.

279. Bhargava, B. L.; Balasubramanian, S. Refined potential model for atomistic simulations of ionic liquid [bmim][PF6]. *J. Chem. Phys.* **2007**, *127*, 114510.

280. Berendsen, H. J. C.; Grigera, J. R.; Straatsma, T. P. The missing term in effective pair potentials. *J. Phys. Chem.* **1987**, *91*, 6269-6271.

281. Mazyar, O. A.; Hase, W. L. Dynamics and Kinetics of Heat Transfer at the Interface of Model Diamond {111} Nanosurfaces. *J Phys Chem A* **2006**, *110*, 526.

282. van Gunsteren, W. F.; Billeter, S. R.; Eising, A. A.; Huenberger, P. H.; Kruger, P.; Mark, A. E.; Scott, W. R. P.; Tironi, I. G. *Biomolecular Simulation: The GROMOS 96 Manual and User Guide;* Verlag der Fachvereine: Zurich, 1996; .

283. Berendsen, H. J. C.; Postma, J. P. M.; van Gunsteren, W. F.; Hermans, J. *Intermolecular Forces;* Reidel: Dordrecht, 1981; .

284. Frost, D. S.; Dai, L. L. Molecular dynamics simulations of charged nanoparticle self-assembly at ionic liquid-water and ionic liquid-oil interfaces. *J. Chem. Phys.* **2012**, *136*, 084706.

285. Frost, D. S.; Machas, M.; Dai, L. L. Molecular Dynamics Studies on the Adaptability of an Ionic Liquid in the Extraction of Solid Nanoparticles. *Langmuir* **2012**, *28*, 13924-13932.

286. Frost, D. S.; Dai, L. L. Molecular Dynamics Simulations of Nanoparticle Self-Assembly at Ionic Liquid-Water and Ionic Liquid-Oil Interfaces. *Langmuir* **2011**, *27*, 11339-11346.

287. Wensink, E. J. W.; Hoffmann, A. C.; Apol, M. E. F.; Berendsen, H. J. C. Properties of Adsorbed Water Layers and the Effect of Adsorbed Layers on Interparticle Forces by Liquid Bridging. *Langmuir* **2000**, *16*, 7392-7400.

288. Frost, D. S.; Schoepf, J. J.; Nofen, E. M.; Dai, L. L. Understanding droplet bridging in ionic liquid-based Pickering emulsions. *J. Colloid Interface Sci.* **2012**, *383*, 103-109.

289. Lynden-Bell, R. M.; Del Popolo, M. G.; Youngs, T. G. A.; Kohanoff, J.; Hanke, C. G.; Harper, J. B.; Pinilla, C. C. Simulations of Ionic Liquids, Solutions, and Surfaces. *Acc. Chem. Res.* **2007**, *40*, 1138.

290. Sarangi, S. S.; Reddy, S. K.; Balasubramanian, S. Low frequency vibrational modes of room temperature ionic liquids. *J. Phys. Chem. B* **2011**, *115*, 1874-1880.

291. Lynden-Bell, R. M. Gas—liquid interfaces of room temperature ionic liquids. *Mol. Phys.* **2003**, *101*, 2625.

292. Binks, B. P.; Fletcher, P. D. I.; Dyab, A. K. F. Novel emulsions of ionic liquids stabilised solely by silica nanoparticles. *Chem. Commun.* **2003**, 2540-2541.

293. Binks, B. P.; Dyab, A. K. F.; Fletcher, P. D. I. Contact angles in relation to emulsions stabilised solely by silica nanoparticles including systems containing room temperature ionic liquids. *Phys. Chem. Chem. Phys.* **2007**, *9*, 6391-6397.

294. Ma, H.; Dai, L. Particle Self-Assembly in Ionic Liquid-in-Water Pickering Emulsions. *Langmuir* **2011**, *27*, 508-512.

295. Poole, C. F.; Poole, S. K. Extraction of organic compounds with room temperature ionic liquids. *J. Chromatogr. A* **2010**, *1217*, 2268.

296. Wei, G.; Yang, Z.; Lee, C.; Yang, H.; Wang, C. R. C. Aqueous-Organic Phase Transfer of Gold Nanoparticles and Gold Nanorods Using an Ionic Liquid. *J. Am. Chem. Soc.* **2004**, *126*, 5036-5037.

297. Hub, J. S.; de Groot, B. L.; van, d. S. g_wham - A Free Weighted Histogram Analysis Implementation Including Robust Error and Autocorrelation Estimates. *Journal of Chemical Theory and Computation* **2010**, *6*, 3713-3720.

298. Kumar, S.; Bouzida, D.; Swendsen, R. H.; Kollman, P. A.; Rosenberg, J. M. THE weighted histogram analysis method for free-energy calculations on biomolecules. I. The method. *J. Comput. Chem.* **1992**, *13*, 1011.

299. Hogshead, C. G.; Manias, E.; Williams, P.; Lupinsky, A.; Painter, P. Studies of Bitumen-Silica and Oil-Silica Interactions in Ionic Liquids. *Energy Fuels* **2011**, *25*, 293-299.

300. Painter, P.; Williams, P.; Lupinsky, A. Recovery of Bitumen from Utah Tar Sands Using Ionic Liquids. *Energy Fuels* **2010**, *24*, 5081-5088.

301. Painter, P.; Pulati, N.; Cetiner, R.; Sobkowiak, M.; Mitchell, G.; Mathews, J. Dissolution and Dispersion of Coal in Ionic Liquids. *Energy Fuels* **2010**, *24*, 1848-1853.

302. Williams, P.; Lupinsky, A.; Painter, P. Recovery of Bitumen from Low-Grade Oil Sands Using Ionic Liquids. *Energy Fuels* **2010**, *24*, 2172-2173.

303. Penn State Materials Research Institute New process cleanly extracts oil from tar sands and fouled beaches. *Science Daily* **2011**.

304. Cheung, D. L.; Bon, S. A. F. Interaction of Nanoparticles with Ideal Liquid-Liquid Interfaces. *Phys. Rev. Lett.* **2009**, *102*, 066103.

305. Cheung, D. Molecular dynamics study of nanoparticle stability at liquid interfaces: Effect of nanoparticle-solvent interaction and capillary waves. *J. Chem. Phys.* **2011**, *135*, 054704.

306. H Lehle and, M. O. Stability and interactions of nanocolloids at fluid interfaces: effects of capillary waves and line tensions. *Journal of Physics: Condensed Matter* **2008**, *20*, 404224.

307. Walker, E. M.; Frost, D. S.; Dai, L. L. Particle self-assembly in oil-in-ionic liquid Pickering emulsions. *J. Colloid Interface Sci.* **2011**, *363*, 307-313.

308. Thareja, P. Particle-induced bridging in immiscible polymer blends. *Rheologica acta* **2006**, *46*, 405-412.

309. Horozov, T. S. Particle-Stabilized Emulsions: A Bilayer or a Bridging Monolayer? *Angewandte Chemie International Edition* **2006**, *45*, 773-776.

310. Bon, S. A. F.; Mookhoek, S. D.; Colver, P. J.; Fischer, H. R.; van der Zwaag, S. Route to stable non-spherical emulsion droplets. *Eur. Poly* **2007**, *43*, 4839-4842.

311. Aveyard, R.; Clint, J. H.; Horozov, T. S. Aspects of the stabilisation of emulsions by solid particles: Effects of line tension and monolayer curvature energy. *Phys. Chem. Chem. Phys.* **2003**, *5*, 2398-2409.

312. Subramaniam, A. B.; Mejean, C.; Abkarian, M.; Stone, H. A. Microstructure, Morphology, and Lifetime of Armored Bubbles Exposed to Surfactants. *Langmuir* **2006**, *22*, 5986-5990.

313. Subramaniam, A. B.; Abkarian, M.; Stone, H. A. Controlled assembly of jammed colloidal shells on fluid droplets. *Nature Materials* **2005**, *4*, 553-556.

314. Bala Subramaniam, A.; Abkarian, M.; Mahadevan, L.; Stone, H. A. Colloid science: Non-spherical bubbles. *Nature* **2005**, *438*, 930-930.

315. Fedorov, M. V.; Lynden-Bell, R. Probing the neutral graphene-ionic liquid interface: insights from molecular dynamics simulations. *Phys. Chem. Chem. Phys.* **2012**, *14*, 2552-2556.

316. Rodriguez-Perez, L.; Coppel, Y.; Favier, I.; Teuma, E.; Serp, P.; Gomez, M. Imidazolium-based ionic liquids immobilized on solid supports: effect on the structure and thermostability. *Dalton Trans.* **2010**, *39*, 7565-7568.

317. Dragoni, D.; Manini, N.; Ballone, P. Interfacial Layering of a Room-Temperature Ionic Liquid Thin Film on Mica: A Computational Investigation. *Chemphyschem* **2012**, *13*, 1772-1780.

318. Crowhurst, L.; Mawdsley, P. R.; Perez-Arlandis, J.; Salter, P. A.; Welton, T. Solvent-solute interactions in ionic liquids. *Phys. Chem. Chem. Phys.* **2003**, *5*, 2790-2794.

319. Lui, M. Y.; Crowhurst, L.; Hallett, J. P.; Hunt, P. A.; Niedermeyer, H.; Welton, T. Salts dissolved in salts: ionic liquid mixtures. *Chem. Sci.* **2011**, *2*, 1491.

320. Simon, P.; Gogotsi, Y. Materials for electrochemical capacitors. *Nature Materials* **2008**, *7*, 845-854.

321. Armand, M.; Endres, F.; MacFarlane, D. R.; Ohno, H.; Scrosati, B. ionic-liquid materials for the electrochemical challenges of the future. *Nature Materials* **2009**, *8*, 621-629.

322. Perkin, S.; Crowhurst, L.; Niedermeyer, H.; Welton, T.; Smith, A.; Gosvami, N. Self-assembly in the electrical double layer of ionic liquids. *Chem. Commun.* **2011**, *47*, 6572-6574.

323. Ballone, P.; Del Pópolo, M. G.; Bovio, S.; Podestà, A.; Milani, P.; Manini, N. Nanoindentation of a room-temperature ionic liquid film on silica: a computational experiment. *Phys. Chem. Chem. Phys.* **2012**, *14*, 2475-2482.

324. Bovio, S.; Podestà, A.; Milani, P.; Ballone, P.; Del Pópolo, M. G. Nanometric ionic-liquid films on silica: a joint experimental and computational study. *Journal of Physics: Condensed Matter* **2009**, *21*, 424118.

325. Shimizu, K.; Pensado, A.; Malfreyt, P.; Pádua, A. A. H.; Canongia Lopes, J. N. 2D or not 2D: Structural and charge ordering at the solid-liquid interface of the 1-(2-hydroxyethyl)-3-methylimidazolium tetrafluoroborate ionic liquid. *Faraday Discuss.* **2011**, *154*, 155-169.

326. Niedermeyer, H.; Hallett, J. P.; Villar-Garcia, I.; Hunt, P. A.; Welton, T. Mixtures of ionic liquids. *Chem. Soc. Rev.* **2012**.

327. Arce, A.; Earle, M. J.; Katdare, S. P.; Rodriguez, H.; Seddon, K. R. Application of mutually immiscible ionic liquids to the separation of aromatic and aliphatic hydrocarbons by liquid extraction: a preliminary approach. *Phys. Chem. Chem. Phys.* **2008**, *10*, 2538-2542.

328. Arce, A.; Earle, M.; Katdare, S.; Rodriguez, H.; Seddon, K. Mutually immiscible ionic liquids. *Chemical Communications* **2006**, 2548-2550.

329. Cheng, S.; Zhang, J.; Zhang, Z.; Han, B. Novel microemulsions: ionic liquid-in-ionic liquid. *Chemical Communications* **2007**, 2497-2499.

330. Gittins, D. I.; Caruso, F. Spontaneous Phase Transfer of Nanoparticulate Metals from Organic to Aqueous Media. *Angew. Chem. Int. Ed.* **2001**, *40*, 3001-3004.

331. Wang, Y.; Wong, J. F.; Teng, X.; Lin, X. Z.; Yang, H. "Pulling" Nanoparticles into Water: Phase Transfer of Oleic Acid Stabilized Monodisperse Nanoparticles into Aqueous Solutions of α-Cyclodextrin. *Nano Lett.* **2003**, *3*, 1555-1559.

332. Liu, J.; Alvarez, J.; Ong, W.; Roman, E.; Kaifer, A. E. Phase Transfer of Hydrophilic, Cyclodextrin-Modified Gold Nanoparticles to Chloroform Solutions. *J. Am. Chem. Soc.* **2001**, *123*, 11148-11154.

333. Neil R., C. High internal phase emulsion templating as a route to well-defined porous polymers. *Polymer* **2005**, *46*, 1439-1449.

334. Zhao, C.; Danish, E.; Cameron, N.; Kataky, R. Emulsion-templated porous materials (PolyHIPEs) for selective ion and molecular recognition and transport: applications in electrochemical sensing. *J. Mater. Chem.* **2007**, *17*, 2446-2453.

335. Bokhari, M.; Carnachan, R.; Przyborski, S.; Cameron, N. Emulsion-templated porous polymers as scaffolds for three dimensional cell culture: effect of synthesis parameters on scaffold formation and homogeneity. *J. Mater. Chem.* **2007**, *17*, 4088-4094.

336. Su, F.; Bray, C. L.; Tan, B.; Cooper, A. I. Rapid and Reversible Hydrogen Storage in Clathrate Hydrates Using Emulsion-Templated Polymers. *Adv Mater* **2008**, *20*, 2663-2666.

337. Lee, K. Y.; Kim, M.; Hahn, J.; Suh, J. S.; Lee, I.; Kim, K.; Han, S. W. Assembly of metal nanoparticle-carbon nanotube composite materials at the liquid/liquid interface. *Langmuir* **2006**, *22*, 1817-1821.

338. Russell, J. T.; Lin, Y.; Böker, A.; Su, L.; Carl, P.; Zettl, H.; He, J.; Sill, K.; Tangirala, R.; Emrick, T.; Littrell, K.; Thiyagarajan, P.; Cookson, D.; Fery, A.; Wang, Q.; Russell, T. P. Self-assembly and cross-linking of bionanoparticles at liquid-liquid interfaces. *Angewandte Chemie International Edition in English* **2005**, *44*, 2420-2426.

339. Kaur, G.; He, J.; Xu, J.; Pingali, S.; Jutz, G.; Bolker, A.; Niu, Z.; Li, T.; Rawlinson, D.; Emrick, T.; Lee, B.; Thiyagarajan, P.; Russell, T. P.; Wang, Q. Interfacial Assembly of Turnip Yellow Mosaic Virus Nanoparticles. *Langmuir* **2009**, *25*, 5168-5176.

340. Cha, S. I.; Kim, K. T.; Arshad, S. N.; Mo, C. B.; Hong, S. H. Extraordinary Strengthening Effect of Carbon Nanotubes in Metal-Matrix Nanocomposites Processed by Molecular-Level Mixing. *Adv Mater* **2005**, *17*, 1377-1381.

341. Xing, Y.; Li, L.; Chusuei, C. C.; Hull, R. V. Sonochemical Oxidation of Multiwalled Carbon Nanotubes. *Langmuir* **2005**, *21*, 4185-4190.

342. Zhao, L.; Li, Y.; Liu, Z.; Shimizu, H. Carbon Nanotube-Conducting Polymer Core-Shell Hybrid Using an Imidazolium-Salt-Based Ionic Liquid As a Linker: Designed As a Potential Platinum Electrode Alternative Material for Large-Scale Solution Processing. *Chemistry of Materials* **2010**, *22*, 5949-5956.

343. Dehaen, W.; Hassner, A. Cycloadditions. 45. Annulation of heterocycles via intramolecular nitrile oxide-heterocycle cycloaddition reaction. *J. Org. Chem.* **1991**, *56*, 896-900.

344. Zhang, W.; Li, Y.; Lin, C.; An, Q.; Tao, C.; Gao, Y.; Li, G. Electrochemical polymerization of imidazolum-ionic liquids bearing a pyrrole moiety. *J. Polym. Sci. Pol. Chem.* **2008**, *46*, 4151-4161.

345. Zhao, J.; Yan, F.; Chen, Z.; Diao, H.; Chu, F.; Yu, S.; Lu, J. Microemulsion Polymerization of Cationic Pyrroles Bearing an Imidazolum-Ionic Liquid Moiety. *J. Polym. Sci. Pol. Chem.* **2009**, *47*, 746-753.

346. Hofft, O.; Bahr, S.; Kempter, V. Investigations with Infrared Spectroscopy on Films of the Ionic Liquid [EMIM][Tf2N]. *Langmuir* **2008**, *24*, 11562-11566.

347. Liu, Y.; Yu, L.; Zhang, S.; Yuan, J.; Shi, L.; Zheng, L. Dispersion of multiwalled carbon nanotubes by ionic liquid-type Gemini imidazolium surfactants in aqueous solution. *Colloids Surf. Physicochem. Eng. Aspects* **2010**, *359*, 66-70.

348. Di Crescenzo, A.; Demurtas, D.; Renzetti, A.; Siani, G.; De Maria, P.; Meneghetti, M.; Prato, M.; Fontana, A. Disaggregation of single-walled carbon nanotubes (SWNTs) promoted by the ionic liquid-based surfactant1-hexadecyl-3-vinyl-imidazolium bromide in aqueous solution. *Soft Matter* **2009**, *5*, 62-66.

349. Zhou, X.; Wu, T.; Ding, K.; Hu, B.; Hou, M.; Han, B. The dispersion of carbon nanotubes in water with the aid of very small amounts of ionic liquid. *Chemical Communications* **2009**, 1897.

350. Moore, V. C.; Strano, M. S.; Haroz, E. H.; Hauge, R. H.; Smalley, R. E.; Schmidt, J.; Talmon, Y. Individually Suspended Single-Walled Carbon Nanotubes in Various Surfactants. *Nano Letters* **2003**, *3*, 1379-1382.

351. Chiappe, C.; Pieraccini, D. Ionic liquids: solvent properties and organic reactivity. *Journal of Physical Organic Chemistry* **2005**, *18*, 275-297.

352. Shen, M.; Resasco, D. E. Emulsions Stabilized by Carbon Nanotube-Silica Nanohybrids. *Langmuir* **2009**, *25*, 10843-10851.

353. Gao, L.; Yin, H.; Wang, D. Ionic liquids assisted formation of an oil/water emulsion stabilised by a carbon nanotube/ionic liquid composite layer. *Phys.Chem.Chem.Phys.* **2010**, *12*, 2535.

354. Panhuis, M. I. H.; Paunov, V. N. Assembling carbon nanotubosomes using an emulsion-inversion technique. *Chemical Communications* **2005**, 1726-1728.

355. Belieres, J.; Angell, C. A. Protic Ionic Liquids: Preparation, Characterization, and Proton Free Energy Level Representation. *J Phys Chem B* **2007**, *111*, 4926-4937.

356. Ohno, H. Importance and Possibility of Ionic Liquids. *Ohno/Electrochemical Aspects of Ionic Liquids* **2005**, 1-3.

357. Lu, J.; Yan, F.; Texter, J. Advanced applications of ionic liquids in polymer science. *Progress in Polymer Science* **2009**, *34*, 431-448.

358. Kubisa, P. Application of ionic liquids as solvents for polymerization processes. *Progress in Polymer Science* **2004**, *29*, 3-12.

359. Han, X.; Armstrong, D. W. Ionic Liquids in Separations. *Acc. Chem. Res.* **2007**, *40*, 1079-1086.

360. Yang, Z.; Yue, Y.; Xing, M. Effect of ionic liquids on enzyme catalysis. *J. Biotechnol.* **2008**, *136*, S394-S395.

361. Chen Renjie, Zhang Haiqin,Wu Feng Applications of Ionic Liquids in Batteries. *Progress in Chemistry* **2011**, *23*, 366.

362. Wakeham, D.; Hayes, R.; Warr, G. G.; Atkin, R. Influence of Temperature and Molecular Structure on Ionic Liquid Solvation Layers. *J Phys Chem B* **2009**, *113*, 5961-5966.

363. Wang, Y.; Wei, L.; Li, K.; Ma, Y.; Ma, N.; Ding, S.; Wang, L.; Zhao, D.; Yan, B.; Wan, W.; Zhang, Q.; Wang, X.; Wang, J.; Li, H. Lignin dissolution in dialkylimidazolium-based ionic liquid-water mixtures. *Bioresour. Technol.* **2014**, *170*, 499-505.

364. Sciarini, L. S.; Rolland-Sabata, A.; Guilois, S.; Decaen, P.; Leroy, E.; Le Bail, P. Understanding the destructuration of starch in water-ionic liquid mixtures. *Green Chem.* **2015**, *17*, 291-299.

365. Brandt, A.; Ray, M. J.; To, T. Q.; Leak, D. J.; Murphy, R. J.; Welton, T. Ionic liquid pretreatment of lignocellulosic biomass with ionic liquid-water mixtures. *Green Chem.* **2011**, *13*, 2489.

366. Jeon, J.; Kim, H.; Goddard, W. A.; Pascal, T. A.; Lee, G.; Kang, J. K. The Role of Confined Water in Ionic Liquid Electrolytes for Dye-Sensitized Solar Cells. *J.Phys.Chem.Lett.* **2012**, *3*, 556-559.

367. Liu, Z.; Abedin, S. Z.; Endres, F. Electrodeposition of zinc films from ionic liquids and ionic liquid/water mixtures. *Electrochim. Acta* **2013**, *89*, 635-643.

368. Woodward, C. E.; Harris, K. R. A lattice-hole theory for conductivity in ionic liquid mixtures: application to ionic liquid + water mixtures. *Phys.Chem.Chem.Phys.* **2010**, *12*, 1172-1176.

369. Efimova, A.; Hubrig, G.; Schmidt, P. Thermal stability and crystallization behavior of imidazolium halide ionic liquids. *Thermochimica Acta* **2013**, *573*, 162-169.

370. Zhao, Y.; Wang, L.; Byon, H. R. High-performance rechargeable lithium-iodine batteries using triiodide/iodide redox couples in an aqueous cathode. *Nature Communications* **2013**, *4*, 1896.

371. Huang, H.; Agafonov, V.; Yu, H. Molecular Electric Transducers as Motion Sensors: A Review. *Sensors* **2013**, *13*, 4581-4597.

372. Garcia, G.; Aparicio, S.; Ullah, R.; Atilhan, M. Deep Eutectic Solvents: Physicochemical Properties and Gas Separation Applications. *Energy Fuels* **2015**, *29*, 2616-2644.

373. Wang, P.; Zakeeruddin, S. M.; Moser, J.; Gratzel, M. A New Ionic Liquid Electrolyte Enhances the Conversion Efficiency of Dye-Sensitized Solar Cells. *The Journal of Physical Chemistry B* **2003**, *107*, 13280-13285.

374. Maerzke, K. A.; Goff, G. S.; Runde, W. H.; Schneider, W. F.; Maginn, E. J. Structure and Dynamics of Uranyl(VI) and Plutonyl(VI) Cations in Ionic Liquid/Water Mixtures via Molecular Dynamics Simulations. *The Journal of Physical Chemistry B* **2013**, *117*, 10852-10868.

375. Jiang, W.; Wang, Y.; Voth, G. A. Molecular Dynamics Simulation of Nanostructural Organization in Ionic Liquid/Water Mixtures. *The Journal of Physical Chemistry B* **2007**, *111*, 4812-4818.

376. Wojnarowska, Z.; Grzybowska, K.; Hawelek, L.; Swiety-Pospiech, A.; Masiewicz, E.; Paluch, M.; Sawicki, W.; Chmielewska, A.; Bujak, P.; Markowski, J. Molecular Dynamics Studies on the Water Mixtures of Pharmaceutically Important Ionic Liquid Lidocaine HCl. *Mol. Pharmaceutics* **2012**, *9*, 1250-1261.

377. Hanke, C. G.; Lynden-Bell, R. A Simulation Study of Water-Dialkylimidazolium Ionic Liquid Mixtures. *The Journal of Physical Chemistry B* **2003**, *107*, 10873-10878.

378. Lindahl, E.; Hess, B.; van, d. S. GROMACS 3.0: a package for molecular simulation and trajectory analysis. *Molecular modeling annual , 7*, 306-317.

379. Bhargava, B. L.; Balasubramanian, S. Insights into the Structure and Dynamics of a Room-Temperature Ionic Liquid: Ab Initio Molecular Dynamics Simulation Studies of 1-n-Butyl-3-methylimidazolium Hexafluorophosphate ([bmim][PF6]) and the [bmim][PF6] CO2 Mixture. *J Phys Chem B* **2007**, *111*, 4477-4487.

380. Hess, B. P-LINCS: A Parallel Linear Constraint Solver for Molecular Simulation. *J.Chem.Theory Comput.* **2008**, *4*, 116-122.

381. Hess, B.; Bekker, H.; Berendsen, H. J. C.; Fraaije, J. G. E. M. LINCS: A linear constraint solver for molecular simulations. *J.Comput.Chem.* **1997**, *18*, 1463-1472.

382. Buhl, M.; Chaumont, A.; Schurhammer, R.; Wipff, G. Ab Initio Molecular Dynamics of Liquid 1,3-Dimethylimidazolium Chloride. *The Journal of Physical Chemistry B* **2005**, *109*, 18591-18599.

383. Morrow, T. I.; Maginn, E. J. Molecular Dynamics Study of the Ionic Liquid 1- n -Butyl-3-methylimidazolium Hexafluorophosphate. *The Journal of Physical Chemistry B* **2002**, *106*, 12807-12813.

384. Sieffert, N.; Wipff, G. The [BMI][Tf2N] Ionic Liquid/Water Binary System: A Molecular Dynamics Study of Phase Separation and of the Liquid-Liquid Interface. *The Journal of Physical Chemistry B* **2006**, *110*, 13076-13085.

385. Zhao, W.; Eslami, H.; Cavalcanti, W. L.; Maller-Plathe, F. A Refined All-Atom Model for the Ionic Liquid 1- n -Butyl 3-Methylimidazolium bis(Trifluoromethylsulfonyl)imide [bmim][Tf2N]. *Zeitschrift far Physikalische Chemie* **2007**, *221*, 1647-1662.

386. Frost, D. S.; Machas, M.; Perea, B.; Dai, L. L. Nonconvective Mixing of Miscible Ionic Liquids. *Langmuir* **2013**, *29*, 10159-10165.

387. Youngs, T. G. A.; Hardacre, C. Application of Static Charge Transfer within an Ionic-Liquid Force Field and Its Effect on Structure and Dynamics. *ChemPhysChem* **2008**, *9*, 1548-1558.

388. Liu, H.; Maginn, E. A molecular dynamics investigation of the structural and dynamic properties of the ionic liquid 1-n-butyl-3-methylimidazolium bis(trifluoromethanesulfonyl)imide. *J. Chem. Phys.* **2011**, *135*, 124507.

389. Berendsen, H. J. C. Molecular dynamics with coupling to an external bath. *J. Chem. Phys.* **1984**, *81*, 3684.

390. Parrinello, M. Polymorphic transitions in single crystals: A new molecular dynamics method. *J. Appl. Phys.* **1981**, *52*, 7182.

391. Humphrey, W.; Dalke, A.; Schulten, K. VMD: Visual molecular dynamics. *J. Mol. Graph.* **1996**, *14*, 33-38.

392. Yu, G.; Zhao, D.; Wen, L.; Yang, S.; Chen, X. Viscosity of ionic liquids: Database, observation, and quantitative structure-property relationship analysis. *AIChE J.* **2011**, *58*, 2885-2899.

393. Domaska, U.; Kralikowska, M. Density and Viscosity of Binary Mixtures of Thiocyanate Ionic Liquids + Water as a Function of Temperature. *Journal of Solution Chemistry* **2012**, *41*, 1422-1445.

394. Rodriguez, H.; Brennecke, J. F. Temperature and Composition Dependence of the Density and Viscosity of Binary Mixtures of Water + Ionic Liquid. *Journal of Chemical & Engineering Data* **2006**, *51*, 2145-2155.

395. Redlich, O.; Kister, A. T. Algebraic Representation of Thermodynamic Properties and the Classification of Solutions. *Ind.Eng.Chem.* **1948**, *40*, 345-348.

396. Mokhtarani, B.; Sharifi, A.; Mortaheb, H. R.; Mirzaei, M.; Mafi, M.; Sadeghian, F. Density and viscosity of pyridinium-based ionic liquids and their binary mixtures with water at several temperatures. *The Journal of Chemical Thermodynamics* **2009**, *41*, 323-329.

397. Ngo, H. L.; LeCompte, K.; Hargens, L.; McEwen, A. B. Thermal properties of imidazolium ionic liquids. *Thermochim. Acta* **2000**, *357-358*, 97-102.

398. Earle, M. J.; Esperanca, J. M. S. S.; Gilea, M. A.; Lopes, J. N. C.; Rebelo, L. P. N.; Magee, J. W.; Seddon, K. R.; Widegren, J. A. The distillation and volatility of ionic liquids. *Nature* **2006**, *439*, 831-834.

399. Maton, C.; De Vos, N.; Stevens, C. V. Ionic liquid thermal stabilities: decomposition mechanisms and analysis tools. *Chem. Soc. Rev.* **2013**, *42*, 5963-5977.

400. Chancelier, L.; Diallo, A. O.; Santini, C. C.; Marlair, G.; Gutel, T.; Mailley, S.; Len, C. Targeting adequate thermal stability and fire safety in selecting ionic liquid-based electrolytes for energy storage. *Phys. Chem. Chem. Phys.* **2014**, *16*, 1967-1976.

401. Fox, D. M.; Gilman, J. W.; Morgan, A. B.; Shields, J. R.; Maupin, P. H.; Lyon, R. E.; De Long, H. C.; Trulove, P. C. Flammability and Thermal Analysis Characterization of Imidazolium-Based Ionic Liquids. *Ind. Eng. Chem. Res* **2008**, *47*, 6327-6332.

402. O'Mahony, A.; Silvester, D.; Aldous, L.; Hardacre, C.; Compton, R. Effect of Water on the Electrochemical Window and Potential Limits of Room-Temperature Ionic Liquids. *J. Chem. Eng. Data* **2008**, *53*, 2884-2891.

403. Hayyan, M.; Mjalli, F. S.; Hashim, M. A.; AlNashef, I. M.; Mei, T. X. Investigating the electrochemical windows of ionic liquids. *J. Ind. Eng. Chem.* **2013**, *19*, 106-112.

404. Heym, F.; Haber, J.; Korth, W.; Etzold, B. J. M.; Jess, A. Vapor Pressure of Water in Mixtures with Hydrophilic Ionic Liquids - A Contribution to the Design of Processes for Drying of Gases by Absorption in Ionic Liquids. *Chem. Eng. Technol.* **2010**, *33*, 1625-1634.

405. Rebelo, L. P. N.; Canongia Lopes, J. N.; Esperanca, J. M. S. S.; Filipe, E. On the Critical Temperature, Normal Boiling Point, and Vapor Pressure of Ionic Liquids. *J. Phys. Chem. B* **2005**, *109*, 6040-6043.

406. Liu, J.; Jiang, G.; Liu, J.; Jonsson, J. A. Application of ionic liquids in analytical chemistry. *Trends Anal. Chem.* **2005**, *24*, 20-27.

407. Deng, Y.; Zhang, Q.; Zhang, S. Recent advances in ionic liquid catalysis. *Green Chem.* **2011**, *13*, 2619-2637.

408. Welton, T. Room-Temperature Ionic Liquids. Solvents for Synthesis and Catalysis. *Chem. Rev.* **1999**, *99*, 2071-2084.

409. Brennecke, J. F.; Maginn, E. J. Ionic liquids: Innovative fluids for chemical processing. *AIChE J.* **2001**, *47*, 2384-2389.

410. Goodrich, B. F.; de la Fuente, J. C.; Gurkan, B. E.; Lopez, Z. K.; Price, E. A.; Huang, Y.; Brennecke, J. F. Effect of Water and Temperature on Absorption of CO2 by Amine-Functionalized Anion-Tethered Ionic Liquids. *J. Phys. Chem. B* **2011**, *115*, 9140-9150.

411. Plechkova, N. V.; Seddon, K. R. Applications of ionic liquids in the chemical industry. *Chem. Soc. Rev.* **2008**, *37*, 123-150.

412. Tempel, D. J.; Henderson, P. B.; Brzozowski, J. R.; Pearlstein, R. M.; Cheng, H. High Gas Storage Capacities for Ionic Liquids through Chemical Complexation. *J. Am. Chem. Soc.* **2008**, *130*, 400-401.

413. Huddleston, J. G.; Willauer, H. D.; Swatloski, R. P.; Visser, A. E.; Rogers, R. D. Room temperature ionic liquids as novel media for 'clean' liquid-liquid extraction. *Chem. Commun.* **1998**, 1765-1766.

414. Wei, G.; Yang, Z.; Chen, C. Room temperature ionic liquid as a novel medium for liquid/liquid extraction of metal ions. *Anal. Chim. Acta* **2003**, *488*, 183-192.

415. Nakashima, T.; Kawai, T. Quantum dots-ionic liquid hybrids: efficient extraction of cationic CdTe nanocrystals into an ionic liquid. *Chem. Commun.* **2005**, 1643-1645.

416. Mao, Q.; Wang, H.; Shu, Y.; Chen, X.; Wang, J. A dual-ionic liquid microemulsion system for the selective isolation of hemoglobin. *RSC Adv.* **2014**, *4*, 8177-8182.

417. Sun, Y.; Yan, K.; Huang, X. Formation, characterization and enzyme activity in water-in-hydrophobic ionic liquid microemulsion stabilized by mixed cationic/nonionic surfactants. *Colloids Surf. B* **2014**, *122*, 66-71.

418. Kakiuchi, T. Electrochemical Aspects of Ionic-Liquid|Water Two-Phase Systems. *Anal. Chem.* **2007**, *79*, 6442-6449.

419. Nakashima, T.; Kimizuka, N. Water/Ionic Liquid Interfaces as Fluid Scaffolds for the Two-Dimensional Self-Assembly of Charged Nanospheres. *Langmuir* **2011**, *27*, 1281-1285.

420. Taylor, P. Ostwald ripening in emulsions. *Adv. Colloid Interface Sci.* **1998**, *75*, 107-163.

421. Freire, M. G.; Neves, C. M. S. S.; Carvalho, P. J.; Gardas, R. L.; Fernandes, A. M.; Marrucho, I. M.; Santos, L. M. N. B. F.; Coutinho, J. A. P. Mutual Solubilities of Water and Hydrophobic Ionic Liquids. *J. Phys. Chem. B* **2007**, *111*, 13082-13089.

422. Young, G.; Nippgen, F.; Titterbrandt, S.; Cooney, M. J. Lipid extraction from biomass using co-solvent mixtures of ionic liquids and polar covalent molecules. *Sep. Purif. Technol.* **2010**, *72*, 118-121.

423. Kim, Y.; Choi, Y.; Park, J.; Lee, S.; Yang, Y.; Kim, H. J.; Park, T.; Hwan Kim, Y.; Lee, S. H. Ionic liquid-mediated extraction of lipids from algal biomass. *Bioresour. Technol.* **2012**, *109*, 312-315.

424. Zhao, H.; Xia, S.; Ma, P. Use of ionic liquids as 'green' solvents for extractions. *J. Chem. Technol. Biotechnol.* **2005**, *80*, 1089-1096.

425. Matsumoto, M.; Mochiduki, K.; Fukunishi, K.; Kondo, K. Extraction of organic acids using imidazolium-based ionic liquids and their toxicity to Lactobacillus rhamnosus. *Sep. Purif. Technol.* **2004**, *40*, 97-101.

426. Goklen, K. E.; Hatton, T. A. Liquid-Liquid Extraction of Low Molecular-Weight Proteins by Selective Solubilization in Reversed Micelles. *Sep. Sci. Technol.* **1987**, *22*, 831-841.

427. Pei, Y.; Wang, J.; Wu, K.; Xuan, X.; Lu, X. Ionic liquid-based aqueous two-phase extraction of selected proteins. *Sep. Purif. Technol.* **2009**, *64*, 288-295.

428. Du, Z.; Yu, Y.; Wang, J. Extraction of Proteins from Biological Fluids by Use of an Ionic Liquid/Aqueous Two-Phase System. *Chem. - Eur. J.* **2007**, *13*, 2130-2137.

429. Style, R. W.; Isa, L.; Dufresne, E. R. Adsorption of soft particles at fluid interfaces. *Soft Matter* **2015**, *11*, 7412-7419.

430. Monteillet, H.; Workamp, M.; Li, X.; Schuur, B.; Kleijn, J. M.; Leermakers, F. A. M.; Sprakel, J. Multi-responsive ionic liquid emulsions stabilized by microgels. *Chem. Commun.* **2014**, *50*, 12197-12200.

431. Geisel, K.; Henzler, K.; Guttmann, P.; Richtering, W. New Insight into Microgel-Stabilized Emulsions Using Transmission X-ray Microscopy: Nonuniform Deformation and Arrangement of Microgels at Liquid Interfaces. *Langmuir* **2015**, *31*, 83-89.

432. Richtering, W. Responsive Emulsions Stabilized by Stimuli-Sensitive Microgels: Emulsions with Special Non-Pickering Properties. *Langmuir* **2012**, *28*, 17218-17229.

433. Schmitt, V.; Ravaine, V. Surface compaction versus stretching in Pickering emulsions stabilised by microgels. *Curr. Opin. Colloid Interface Sci.* **2013**, *18*, 532-541.

434. Ngai, T.; Auweter, H.; Behrens, S. H. Environmental Responsiveness of Microgel Particles and Particle-Stabilized Emulsions. *Macromolecules* **2006**, *39*, 8171-8177.

435. Binks, B. P.; Murakami, R.; Armes, S. P.; Fujii, S. Effects of pH and salt concentration on oil-in-water emulsions stabilized solely by nanocomposite microgel particles. *Langmuir* **2006**, *22*, 2050-2057.

436. Charman, W. N.; Christy, D. P.; Geunin, E. P.; Monkhouse, D. C. Interaction between calcium, a model divalent cation, and a range of poly (Acrylic Acid) resins as a function of solution pH. *Drug Dev. Ind. Pharm.* **1991**, *17*, 271-280.

437. Snowden, M. J.; Chowdhry, B. Z.; Vincent, B.; Morris, G. E. Colloidal copolymer microgels of N-isopropylacrylamide and acrylic acid: pH, ionic strength and temperature effects. *Faraday Trans.* **1996**, *92*, 5013-5016.

438. Farooqi, Z. H.; Khan, H. U.; Shah, S. M.; Siddiq, M. Stability of poly(N-isopropylacrylamide-co-acrylic acid) polymer microgels under various conditions of temperature, pH and salt concentration. *Arabian J. Chem.* **2013**.

439. Lyon, L. A.; Fernandez-Nieves, A. The Polymer/Colloid Duality of Microgel Suspensions. *Annu. Rev. Phys. Chem.* **2012**, *63*, 25-43.

440. Park, S.; Wang, J.; Kim, B.; Xu, J.; Russell, T. P. A Simple Route to Highly Oriented and Ordered Nanoporous Block Copolymer Templates. *ACS Nano* **2008**, *2*, 766-772.

441. Segalman, R. A.; Hexemer, A.; Hayward, R. C.; Kramer, E. J. Ordering and Melting of Block Copolymer Spherical Domains in 2 and 3 Dimensions. *Macromolecules* **2003**, *36*, 3272-3288.

442. Ma, H.; Dai, L. L. Structure of Multi-Component Colloidal Lattices at Oil-Water Interfaces. *Langmuir* **2009**, *25*, 11210-11215.

443. Aurenhammer, F. Voronoi diagrams---a survey of a fundamental geometric data structure. *CSUR* **1991**, *23*, 345-405.

444. Libal, A.; Reichhardt, C.; Reichhardt, C. J. O. Point-defect dynamics in two-dimensional colloidal crystals. *Phys. Rev. E* **2007**, *75*, 011403.

445. Geisel, K.; Isa, L.; Richtering, W. The Compressibility of pH-Sensitive Microgels at the Oil-Water Interface: Higher Charge Leads to Less Repulsion. *Angew. Chem.* **2014**, *126*, 5005-5009.

446. Pinaud, F.; Geisel, K.; Masse, P.; Catargi, B.; Isa, L.; Richtering, W.; Ravaine, V.; Schmitt, V. Adsorption of microgels at an oil-water interface: correlation between packing and 2D elasticity. *Soft Matter* **2014**, *10*, 6963-6974.

447. Li, Z.; Ming, T.; Wang, J.; Ngai, T. High Internal Phase Emulsions Stabilized Solely by Microgel Particles. *Angew. Chem. Int. Ed.* **2009**, *48*, 8490-8493.

448. Schmidt, S.; Liu, T.; Rutten, S.; Phan, K.; Moller, M.; Richtering, W. Influence of Microgel Architecture and Oil Polarity on Stabilization of Emulsions by Stimuli-Sensitive Core-Shell Poly(N -isopropylacrylamide- co -methacrylic acid) Microgels: Mickering versus Pickering Behavior? *Langmuir* **2011**, *27*, 9801-9806.

449. Destribats, M.; Gineste, S.; Laurichesse, E.; Tanner, H.; Leal-Calderon, F.; Heroguez, V.; Schmitt, V. Pickering Emulsions: What Are the Main Parameters Determining the Emulsion Type and Interfacial Properties? *Langmuir* **2014**, *30*, 9313-9326.

450. Destribats, M.; Wolfs, M.; Pinaud, F.; Lapeyre, V.; Sellier, E.; Schmitt, V.; Ravaine, V. Pickering Emulsions Stabilized by Soft Microgels: Influence of the Emulsification Process on Particle Interfacial Organization and Emulsion Properties. *Langmuir* **2013**, *29*, 12367-12374.

451. Li, Z.; Harbottle, D.; Pensini, E.; Ngai, T.; Richtering, W.; Xu, Z. Fundamental Study of Emulsions Stabilized by Soft and Rigid Particles. *Langmuir* **2015**, *31*, 6282-6288.

452. Destribats, M.; Lapeyre, V.; Wolfs, M.; Sellier, E.; Leal-Calderon, F.; Ravaine, V.; Schmitt, V. Soft microgels as Pickering emulsion stabilisers: role of particle deformability. *Soft Matter* **2011**, *7*, 7689-7698.

453. Masse, P.; Sellier, E.; Schmitt, V.; Ravaine, V. Impact of Electrostatics on the Adsorption of Microgels at the Interface of Pickering Emulsions. *Langmuir* **2014**, *30*, 14745-14756.

APPENDIX A

PARTICLE SELF-ASSEMBLY AT IONIC LIQUID-BASED INTERFACES

1. Introduction

Self-assembly is a unique phenomenon in which objects interact with each other to exhibit a degree of order or structure. The liquid-liquid interface offers a unique self-assembly platform, providing both flexibility and 2D confinement. Traditionally, surfactants have taken the spotlight in these systems, self-assembling at oil-water interfaces with hydrophobic tails immersed in the oil phase and with hydrophilic heads immersed in the water phase [224, 225]. Self-assembly occurs as the surfactant molecules migrate from the bulk phase to the more confined, but energetically favorable, interface. The key is that the surfactants have the right functionality and size to interact with both phases simultaneously. Surfactants, however, are not the only species with this capability; solid colloidal particles can also equilibrate at the liquid-liquid interface due to their dual-wettability.

Being much larger than surfactant molecules (in general), particles are subject to capillary forces at liquid-liquid interfaces. At these interfaces particles can spontaneously self-assemble to form novel and useful microstructures. This process is governed by the fact that solid particles adhere to the interface with an adhesion energy, ΔG, as described in Equation A1.

$$\Delta G = \pi\gamma r^2(1 \pm cos\theta) \qquad \text{(A1)}$$

where γ is the interfacial tension, r is the particle radius, and θ is the 3-phase contact angle depicted in Figure A1(a). For micron-sized particles, this adhesion energy can be on the order of 10^6 kT [226]. After adsorption, the self-assembly process is governed by inter-particle interactions. This phenomenon is widely studied and excellent literature

on the mechanisms and applications are available [227-229]. The most common application, however, is Pickering emulsions. These are emulsions where instead of surfactants, solid particles self-assemble at the droplet surfaces and provide stability. Since these emulsions provided the primary experimental template for this review, a brief overview follows.

Pickering emulsions are surfactant-free systems in which colloidal droplets, typically oil-in-water, are stabilized against coalescence by a protective "armor" of solid particles. Their formulation is fairly straightforward and the droplet surfaces provide excellent liquid-liquid interfaces over which to examine particle self-assembly via microscopy. Ramsden [230] and Pickering [231] were the first to observe this type of emulsion in the early 1900's, but their findings did not receive widespread attention until nearly a century later. Now Pickering emulsions are often encountered in the recovery, separation and cleaning of crude oil [232, 233], wastewater treatment [234], the food industry [235, 236], etc. In the last 20 years, there has been increased interest in Pickering emulsions due to their ease of application to various situations, including, stabilizing emulsions with metal oxide particles for new skincare and sunscreen formulations [237, 238], tuning emulsion stability with paramagnetic solid particles and an external magnetic field [239], using Pickering emulsion droplets as drug delivery vehicles for controlled release of therapeutic substances [240, 241], and utilizing Pd particles in a Pickering emulsion scheme for both the catalysis and separation of products a hydrogenation reaction [242, 243]. Application of Pickering emulsion droplets as templates also offer novel synthetic routes for the synthesis of nanocomposites, with a polymeric core and outer shell of solid particles via a surfactant-free emulsion polymerization method [244, 245]. We have used a similar

method to develop a framework to synthesize temperature responsive core-shell microcapsules for drug delivery [62, 63]. In this review, we focused on using Pickering emulsions as the primary template to experimentally examine particle self-assembly at various liquid-liquid interfaces.

The use of fluorescent microparticles in conjunction with a confocal laser scanning microscope allowed for a simple mechanism by which to study the various morphologies that can result in an oil-in-water Pickering emulsion [246, 247]. Figure A1 shows the rich morphologies of self-assembled polystyrene (PS) microparticles on the surface of poly(dimethylsiloxane) (PDMS, 5 cSt or 5 x 10^{-6} m^2/s) oil droplets in water. This figure presents some representative morphologies commonly seen in this type of Pickering emulsions, which often depend on both the particle concentration, particle size, and surface chemistry. These morphologies consisted of (a, b) aggregated domains, (c) full coverage (with some defects), and (d) ordered lattices. In addition, both homogenous and heterogeneous (size or surface chemistry) mixtures (b, c) of particles also exhibited these morphologies [247]. Of the morphologies shown in Figure A1, the lattice structure was unique in that it incorporated long-range ordering. This was due to the Coulombic repulsion between the particles [248]. It is important to note that most previous theoretical literature on Pickering emulsions assumed monolayer coverage at the interface, and this was seen for these oil-in-water experiments utilizing the PS microparticles. The diversity of morphologies in oil-in-water Pickering emulsions allows for the simple bottom-up approach for the synthesis of novel materials. It should be noted, however, that all of these morphologies had a few common characteristics. First, all morphologies were limited to single, isolated droplets; there were no inter-droplet self-assembly phenomena.

Second, all particles were either observed at the liquid-liquid interface, or in the bulk phase (where they were originally dispersed). No particles crossed the interface into the droplet phase. Our focus in this review is to discuss the prevalence of these two unusual phenomena in a special type of system: ionic liquid-based Pickering emulsions.

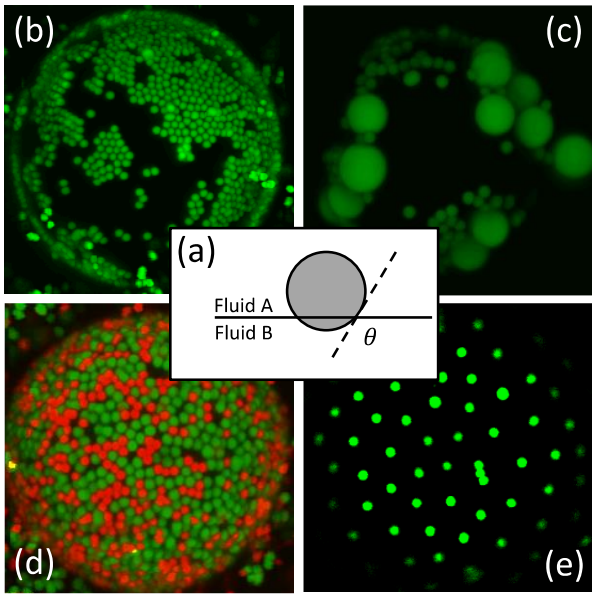

Figure A1. Confocal laser scanning microscope images showing the rich morphology of microparticles at oil-in-water Pickering emulsion interfaces (b) – (e). The solid particles are 1.1 μm in diameter except in (c) which is a mixture of 1.1 and 4 μm particles. The green fluorescence represents sulfate-treated PS microparticles, while the red fluorescence represents carboxylate-treated PS microparticles. Adapted from Reference [247]. Inset (a) shows the definition of contact angle $\boldsymbol{\theta}$ to describe the interfacial position of a colloidal particle between fluids A and B.

An ionic liquid (IL) is an ionic compound that melts below 100 ^{o}C [249, 250]. In contrast to molecular liquids that consist of a single species, ionic liquids (sometimes referred to as “molten salts at room temperature” [251]) are binary mixtures of ions. Unlike

most ionic compounds, the components of ILs are irregularly shaped and do not readily form crystalline lattice structures. Figure A2 gives a basic comparison of ILs to crystalline salts and conventional oils. Two hallmark properties of ILs are their "green" quality and wide tunability. The green quality comes from their near zero vapor pressure over a wide temperature range. Wide tunability of most properties of the IL is possible simply by changing the size, shape, or functionality of one of the constituent ions. Since the liquid state is maintained by the resistance to crystalline packing, one can infer that melting points would be a function of the geometric mismatch of the ions. Some properties for which tunability has been well studied include melting points [250, 252-254], decomposition temperature [255], and water-miscibility[256-258]. ILs can even be tuned for specific applications such as CO_2 absorption [259-267], gas storage [268, 269] and catalysis [270, 271]. By incorporating this new class of liquids with particle self-assembly at the liquid-liquid interface, we desired to be able to exploit the unique characteristics of both Pickering emulsions and ionic liquids to create highly tunable systems that could then be applied to the previously mentioned applications, as well as opening the possibility for new applications.

This review presents an integration of experimental and computational approaches to understanding self-assembly at these unique interfaces. The methods are (1) experimental studies of Pickering emulsions and (2) molecular dynamics (MD) simulations. The latter supported the experimental studies by providing a molecular view of these interfacial phenomena and helped determine how ILs played a unique role. MD simulation is a discreet model that aims to capture intra- and intermolecular behavior with respect to time. MD potential functions capture a variety of interactions including electrostatic and

Van der Waals intermolecular interactions as well as bond and angle stretching and torsions. All of these forces are parameterized in separate functions that are used at each time step of the MD simulation to calculate the total energy and corresponding forces that drive molecular motion. By simulating IL-based interfaces with MD, we obtained a molecular-resolution view of the particle-interface interactions.

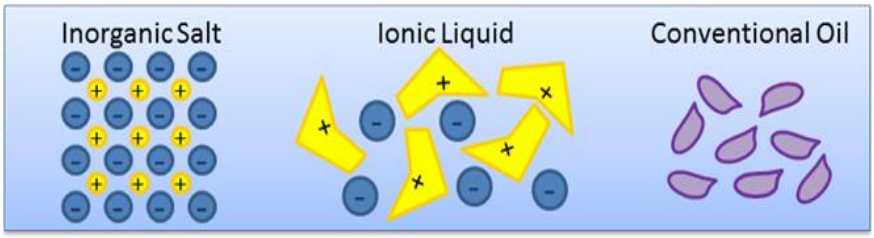

Figure A2. General comparison of inorganic salts, ionic liquids, and conventional oils. Inorganic salts show crystalline packing of the cations (in yellow) and the anions (in blue), while the ionic liquid shows no regular structure of the anions and cations, more similar to the random structure of molecules in oil (in purple).

By employing both experimental and computational methods, we have uncovered and characterized a number of new phenomena pertinent to particle self-assembly at liquid-liquid interfaces. In this way, we hope to emphasize the unique role ILs can play in these systems allowing for ILs to be applied to various applications not previously studied.

2. Materials and Methods

The main materials used in the research discussed in this review article were water, polydimethylsiloxane (PDMS) oil, various types of fluorescent surface-treated poly-

styrene (PS) particles, and various ionic liquids. The water was HPLC grade from Acros Organics or Fisher Scientific. The PDMS oils were the Rhodorsil Fluids 47 V series from Rhodia Silicones, used without further purification; their nominal kinematic viscosities span a range of 5 – 60,000 cSt (5 x 10^{-6} – 0.06 m^2/s) at 25 °C. The particles were FluoSpheres® fluorescent microspheres from Molecular Probes™, purchased as a 2% dispersion in distilled water with 2 mM sodium azide. These particles were surface-modified by sulfate (–SO_3H), carboxylate (–COOH), aldehyde sulfate (–CHO and –SO_3H), or amine (–NH_2) groups. In addition, the sulfate- and aldehyde sulfate-treated particles were relatively hydrophobic and the carboxylate- and amine-treated particles were relatively hydrophilic, based on the information provided by the supplier [272]. More information about the fluorescence and surface charge density of these particles can be found in Table A1. The three ionic liquids that were used were 1-butyl-3-methylimidazolium hexafluorophosphate ([BMIM][PF_6], Sigma Aldrich), ethylammonium nitrate (EAN, Ionic Liquids Technologies), and trihexyltetradecylphosphonium bis(2,4,4-trimethylpentyl)phosphinate ([P_{66614}][Phos], Sigma Aldrich).

Table A1. Properties of solid polystyrene microparticles used in the ionic liquid-based Pickering emulsion experimental work.

Type	Surface Dissociable Group	Diameter (μm)	Surface Charge Density (C/m^2)	Excitation/Emission Wavelengths (nm)
S-PS	Sulfate	1.0 ± 0.031	-0.029	580/605
AS-PS	Aldehyde Sulfate	1.0 ± 0.028	-0.088	505/515
C-PS	Carboxylate	1.1 ± 0.035	-0.325	540/560
A-PS	Amine	1.0 ± 0.023	1.760	505/515

The Pickering emulsions were prepared by combining approximately 1.1 g of continuous phase, 0.1 g of droplet phase, and 0.1 g of particle dispersion in a single vial. The mixture was then emulsified by using ultrasonic agitation (Sonics VibraCell 500W). In the cases where water was not present in the continuous or droplet phases (i.e. oil-in-IL emulsions), 0.1 g of particle dispersion was dried prior to combination with the other components, and the dried particles were then emulsified with the droplet and continuous phases. For emulsions with a binary mixture of particles, each particle type was used in a 1:1 ratio, making for a total of 0.2 g of particle dispersion in the emulsion recipe. Morphologies were recorded using a confocal laser-scanning microscope (Leica SP5) and interfacial tension measurements were taken with a Sigma 701 Tensiometer.

In the MD studies, liquid-liquid interfaces were simulated by placing a two simulated boxes of different liquids adjacent to one another and allowing them to equilibrate. Extra species, such as particles or surfactants, were first dispersed in one of the liquid phases and allowed to spontaneously adsorb to the liquid-liquid interface. This process was relatively fast compared to the total simulation time of 20-50 ns. All simulations were carried out using the GROMACS [273-275] MD simulation package with force fields based on the optimized potential for liquid systems (OPLS) model [276]. The specific force fields [277-283] and simulation parameters are discussed in previous publications [224, 225, 284-286], but the structure of the solid nanoparticles deserves some discussion.

Two types of nanoparticles were used in the MD simulations: a hydrocarbon-based nanoparticle and a silica-based nanoparticle. Both particles were approximately 1.2 nm in diameter. The hydrocarbon nanoparticle (HCP) geometry was truncated from a di-

amond-like lattice structure [225, 281] saturated with united CH, CH_2, and CH_3 groups (two symmetric sites towards one end of the HCP). The force field for the HCP consisted of non-bonded parameters from the OPLS united atom model [276] and bonded parameters from the work of Mazyar and Hase [281] to simulate a rigid hydrophobic nanoparticle. In contrast, the silica-based particle was designed to represent a hydrophilic particle. This particle was truncated to a sphere from a α-quartz structure and the surface was saturated with silanol groups. Interaction potentials for this particle were modeled by a force field developed by Wensink et al. [287] for silica. All particle-interface interactions were modeled using one of these two particles.

3.1. Characteristics of Ionic Liquid-Based Interfaces

Since the excitement about ILs is still rather recent, little is known about the characteristics of IL-based interfaces at the molecular scale. In general, the interfacial tensions of IL-based interfaces are rather low: measured IL/water and IL/oil interfacial tensions are between 10 and 20 mN/m, with IL/water interfacial tension values being about 4 mN/m lower than the corresponding IL/oil interfacial tension values. [288] We have also characterized the interfacial tension between two ILs (ethylammonium nitrate and trihexyltetradecylphosphonium bis(2,4,4-trimethylpentyl)phosphinate) to be 0.952 mN/m. In order to better understand these interfaces at the molecular scale, we performed MD simulations which showed distinct peaks in IL density at a IL/hexane interface, but not at a IL/water interface (Figure A3(a, b)). [286] We hypothesized that some ion ordering at the IL/hexane interface was responsible for this behavior. Ordering was quantified by the ordering parameter S_z, which is described in Equation A2. The value of S_z ranges from -

0.5 to 1.0, corresponding to chain orientation perpendicular and parallel to the z-axis, respectively.

$$S_z = \frac{3}{2}(cos^2\theta) - \frac{1}{2} \qquad \text{(A2)}$$

We examined the ordering of the carbon chain of the [BMIM] cation of the IL. In applying Equation A2, θ was defined as the angle between the carbon chain (N-C vector, where N is the nitrogen attached to the butyl chain and C is the terminal carbon of the butyl chain) and the z axis. Figure A3 compares the ordering of [BMIM] cations at the IL/water (a, c) and IL/hexane (b, d) interfaces, with and without the presence of nanoparticles. In Figure A3(a), S_z fluctuated narrowly around a value of zero, indicating that there was no preferential cation ordering anywhere in the IL/water system. This behavior was also observed by Chaumont et al. [257], who also showed that ordering at the IL/water interface was only exhibited by cations with longer carbon chains. In the presence of nanoparticles, S_z exhibited small peaks of approximately -0.05 (see Figure A3(c)), indicating a slight tendency for the cations chains to orient perpendicular to the z-axis. Closer examination revealed this orientation was exhibited by cations adsorbed to the nanoparticle surfaces, as shown in the inset of Figure A3(c). [BMIM] cations flattened themselves against these surfaces due to hydrophobic interactions.

In contrast to the IL/water systems, significant cation ordering at the IL/hexane interface was observed both with and without nanoparticles (Figure A3 (b) and (d)). Here the carbon chains of the cation extended into the hexane phase, resulting in an orientation parallel to the z-axis. A comparable behavior has been observed at the IL/vacuum interface [289, 290], which becomes more pronounced with cation asymmetry [290]. At the

IL/hexane interface, the parallel orientation was favorable since the hydrophobic chain could interact with the hexane molecules, while leaving the charge imidazolium group to interact with the PF_6 anions.

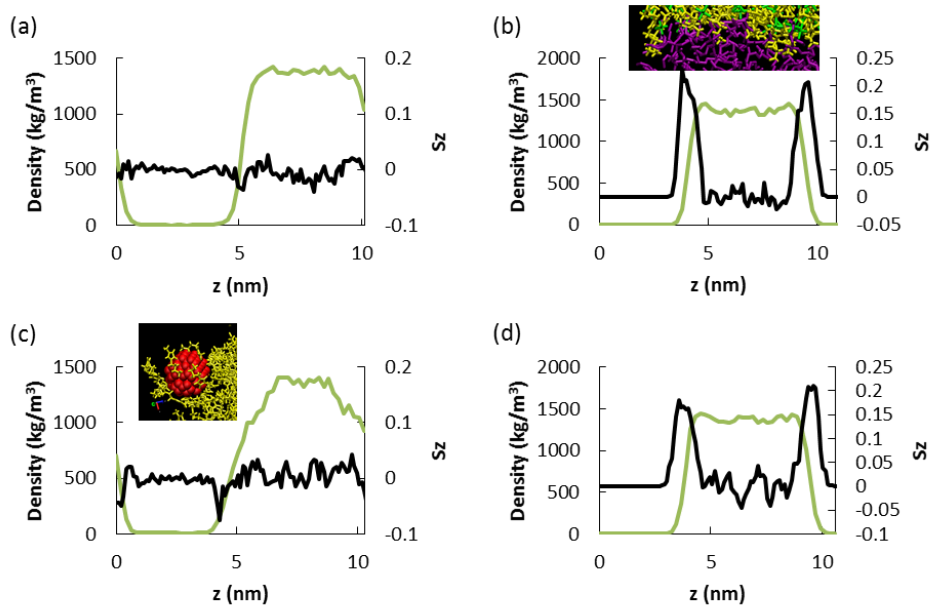

Figure A3. Ordering parameter S_z with respect to box length in IL/water systems without (a) and with (c) nanoparticles and IL/hexane systems without (b) and with (d) nanoparticles. The inset in (b) demonstrates the extension of cation carbon chains into the hexane phase. The inset of (c) shows how the carbon chains of the cations lay across the nanoparticle. Adapted from reference [286].

Furthermore, this orientation allows for more efficient packing due to a reduction in stearic hindrance [290, 291]. Therefore, the peaks in IL density at the IL/hexane interface may be explained by this ordering phenomenon. Another result of this ordering was a small residual net positive charge at the IL/hexane interface [286]. Thus, IL behavior at the interface depended significantly on the opposite solvent and could affect nanoparticle

self-assembly. Upon understanding these molecular-level phenomena, we set out to study how ILs affects self-assembly processes at the micro-level.

3.2. Self-Assembly in Ionic Liquid-Based Pickering Emulsions

3.2.1. Ionic Liquid-in-Water Pickering Emulsions

While IL-based Pickering emulsions had been previously studied by other groups [292, 293], their use of silica nanoparticles did not allow for the particle morphology to be readily seen. Our focus was to use fluorescent microparticles in order to probe the resultant particle morphologies and to analyze the partitioning preferences of free microparticles in the dispersed water and continuous ionic liquid phases [294]. We used a common ionic liquid, 1-butyl-3-methylimidazolium hexafluorophosphate ([BMIM][PF_6]), to create emulsions with either a single type or a binary mixture of PS particles (Table A1). The main systems analyzed contained S-PS (sulfate-treated PS), A-PS (amine-treated PS), AS-PS (aldehyde sulfate-treated PS), S-PS/A-PS, and S-PS/AS-PS particles. Each emulsion would contain droplets with a broad size distribution ranging from several micrometers to tens of micrometers with a varied surface coverage of particles, however, the surface coverage was independent of the droplet size. In Pickering emulsions containing binary heterogeneous particles, both types of particles self-assembled at the droplet interfaces and were randomly mixed without significant phase separation of the particles. Partially covered droplets were observed in all systems, and fully covered droplets were only observed in the A-PS and S-PS/A-PS systems (Figure A4), respectively. The difference in droplet coverage was likely due to the different affinity of particles for the ionic liquid-water interfaces, and the effect of surface charge was hypothesized. Because A-PS

particles were positively charged and all other particles used in this study were negatively charged, the results suggested that the positively charged particles were more easily adsorbed at the interfaces.

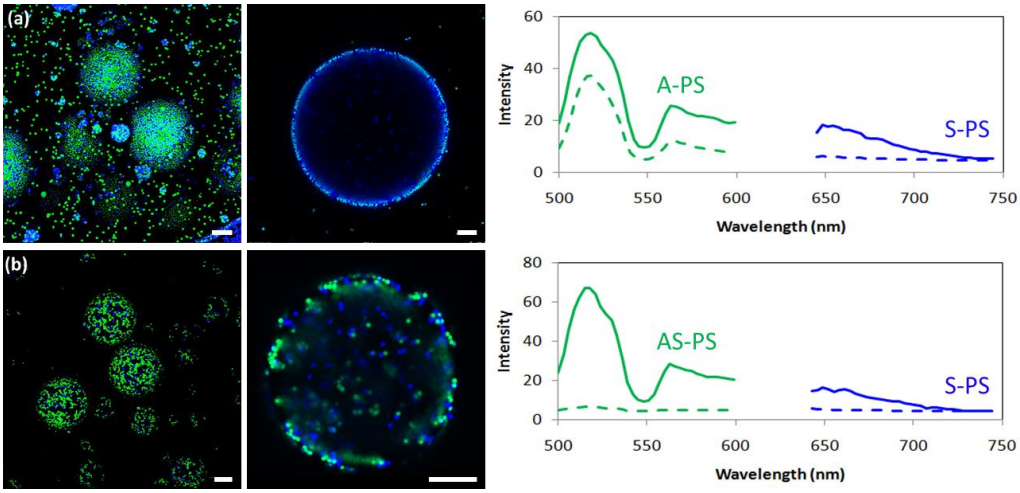

Figure A4. Confocal microscope images of [BMIM][PF_6] emulsion droplets in water with droplet cross-sections and representative fluorescence intensity spectra. (a) The droplet interface is covered with a mixture of S-PS (blue) and A-PS (green) particles, and the [BMIM][PF_6] phase is rich in S-PS and the aqueous phase is rich in A-PS. (b) The droplet interface is covered with a mixture of S-PS (blue) and AS-PS (green) particles, and both types of particles are more concentrated in the [BMIM][PF_6] phase than in the aqueous phase. The scale bars represent 10 μm. In the spectra, solid lines represent before and dashed lines represent after emulsification. Adapted from reference [294].

It is worthwhile to compare the ionic liquid-in-water Pickering emulsions here with the oil-in-water Pickering emulsions previously discussed. First, aggregates of fully covered droplets were frequently observed in ionic liquid-in-water emulsions containing S-PS/A-PS binary particles (Figure A4) whereas oil-in-water emulsions hardly ever contained any fully covered Pickering emulsions droplets, no matter what particle type was

used. The contrast suggests that the S-PS/A-PS particles have a stronger affinity for the ionic liquid-water interfaces than PDMS-water interfaces, although free particles not attached to interfaces were still present in the continuous phase of either emulsion type. The distinction between the ionic nature of the ionic liquid and the molecular nature of PDMS should be at least one of the important factors, if not the primary factor, in determining the affinity of particles to liquid interfaces.

It is also worthwhile to note the differences in interfacial tension values: 39.6 mN/m for PDMS-water and 9.9 mN/m for ionic liquid-water. Secondly, long-range colloidal lattices previously seen in the oil-in-water emulsions were not seen in the IL-in-water emulsions for any concentration value of particles, this was instead replaced by the particles aggregate morphology. When PDMS is substituted with [BMIM][PF_6], the electrostatic repulsion through the ionic liquid phase between charged colloidal particles is screened beyond the Debye length, which is normally is in the range of several nanometers and thus eliminates long-range lattice structure formation at the [BMIM][PF_6]-water interfaces. This observation supports the importance and necessity of Coulombic repulsion through the oil phase for lattice structure formation. The formation of particle aggregates on partially covered droplets might be driven by attractive inter-particle forces although the origin of the attraction is still debatable.

Interestingly, other than equilibrating at the ionic liquid-water interfaces, the microparticles also exhibited a phase preference in either the dispersed or continuous phase, although all particles were initially dispersed in the aqueous phase. Figure A4(a) includes a view of the emulsion landscape and a representative cross-sectional image of an ionic liquid droplet in an emulsion containing a binary particle mixture of S-PS/A-PS. The

droplet interface is covered with a mixture of S-PS and A-PS particles, and the [BMIM][PF_6] phase is rich in S-PS and the continuous (aqueous) phase is rich in A-PS. In contrast, for the S-PS/AS-PS binary system (Figure A4(b)), both types of particles were more concentrated in the [BMIM][PF_6] phase than in the aqueous phase. In the emulsions containing single species of particles, a similar preference was observed: the S-PS and AS-PS particles preferred the [BMIM][PF_6] phase, and the A-PS particles preferred the aqueous phase. The concentration of different species of particles in each aqueous phase was characterized by quantifying the fluorescence intensity over the emission wavelength range of the fluorescent particles, as seen for both binary mixture types in Figure A4. These graphs compare the fluorescence intensity spectra of the emulsion aqueous phase before (solid lines) and after (dashed lines) emulsification. For the S-PS/A-PS system, almost all of the S-PS particles migrated out of the aqueous phase after the formation of the Pickering emulsion, as indicated by the observation that the fluorescence intensity in its emission wavelength range (645-744 nm) fell nearly to the background level. However, the peak fluorescence intensity of A-PS only decreased from 53.6 to 37.2, suggesting that a significant number of A-PS particles remained in the aqueous phase after emulsification. In contrast, the graph in Figure A4(b) shows that for the S-PS/AS-PS system both types of particles were scarcely present in the aqueous phase after emulsification, as seen in the corresponding microscope image.

In addition to these hypotheses regarding the cause of the various morphologies seen in these emulsions, the hydrophobicity and sign of the charge on the particles was considered. The particles in this study were surface treated to have various surface dissociable groups and thus differed in hydrophobicity. The result shows that hydrophobic S-

PS and AS-PS particles preferred the hydrophobic ionic liquid phase whereas the hydrophilic A-PS particles preferred the water phase. However, in PDMS-in-water Pickering emulsions, other than being adsorbed at droplet interfaces, hydrophobic and hydrophilic preferred the water phase, with no particle transfer into the oil phase. Second, the sign of the particle surface charge was hypothesized as an influencing factor on the phase preference, considering the repulsions between the positively charged A-PS particles with the large cations in the ionic liquid. However, additional experiments were performed, and it was found that negatively charged C-PS (carboxylate-treated PS) particles (which are also relatively hydrophilic) can also partition in both the ionic liquid and aqueous phases without a significant preference.

The high transfer efficiency of the S-PS and AS-PS particles to the ionic liquid droplet phase, despite initially residing in the aqueous phase, is also noteworthy. This phenomenon is interesting due to the high free energy cost of removing a particle from a liquid-liquid interface according to Equation A1. Also, while the applications of ILs in the extraction of organic compounds have been studied extensively [295]; investigations in the phase transfer of solid particles, especially in the micrometer size range, are very limited. Gold nanoparticles have been reported to transfer from an aqueous phase to a [BMIM][PF_6] phase more efficiently than to an alcohol phase of the same polarity; and that increasing the ionic strength in the alcohol improved the transfer efficiency [296]. As this particle extraction phenomenon was so unique, we turned to computational studies to examine the energetics of transporting a particle through the interface.

Potential of mean force (PMF) calculations allowed us to examine the changes in free energy as a single particle was pulled through the interface from one phase to the

other. These calculations were performed using the weighted histogram analysis method (WHAM) [297, 298] as described in our previous work [284, 286]. To examine the effect of surface chemistry, we studied PMFs of hydrophobic particles of -4, 0, and +4 surface charges and a silica particle saturated with silanol groups. All hydrophobic particles in the IL/water system exhibited minima in free energy on the IL side of the interface (See Figure A5(a)). The neutral particle exhibited both the deepest embedment into the IL and the greatest decrease in energy. These results may explain why S-PS and AS-PS particles were readily absorbed into the IL droplets, being hydrophobic and having the smallest surface charge density. For the silica (hydrophilic) particle, the minimum in free energy was seen as a shallow well on the water side of the interface with a steady increase in free energy as the particle entered the IL phase. In contrast to the hydrocarbon nanoparticle, the silica particle preferred the water phase, exhibited relatively weak interfacial adsorption energy. Such a profile clearly prohibits any absorption to the IL phase, which explains the behavior of the A-PS particle, which was also hydrophilic.

We took this study a step further to explore what would happen if the water phase was replaced with an oil phase. For the hydrocarbon nanoparticle at the IL/hexane interface, weak adsorption was exhibited by the shallow energy well. Figure A5(b) shows that at this interface, the charged hydrocarbon nanoparticles exhibited deep energy wells straddling the interface and thus strong interfacial adsorption energy. The silica particle experienced a large drop in free energy upon crossing the interface into the IL, but this energy did not significantly increase further, indicating weak interfacial adsorption energy, which has also been reported experimentally [299]. Consequently, it has been shown

that ILs can remove silica particles from crude oil [300-303] and the PMF profile shown in Figure A5(b) for silica points to the energetic favorability of this process.

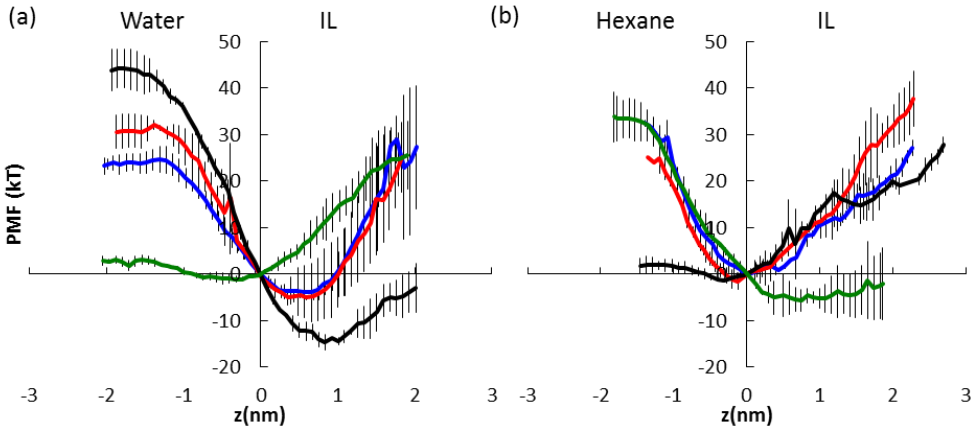

Figure A5. PMF calculation results upon pulling single nanoparticles through the (a) IL/water and (b) IL/hexane interfaces (z = 0). Results from neutral hydrocarbon, +4 charged hydrocarbon, -4 charged hydrocarbon, and silica nanoparticles are shown in black, blue, red, and green, respectively. Adapted from references [284, 285].

We have discussed the location and depth of the energy wells of the PMF calculations, but another important aspect is their respective widths. Equation A1 suggests that interfacial absorption energy should only be felt while a particle is in contact with the liquid-liquid interface. However, Figure A5 shows that most of the PMFs did not "saturate" (flatten out) at 0.6 nm from the interface, the distance at which the particle should no longer have touched the interface assuming it remained flat. Having ruled out finite size effects [284], closer examination revealed that the low interfacial tension of these systems (~10-13 mN/m) allowed for high fluctuation of the interface which could deform enough to form bridges to nanoparticles more than a nm away [284]. Therefore, the assumption of Equation A1 that the interface be flat did not apply well in these systems.

Newer models that include these capillary wave effects as well as line tension have exhibited greater accuracy [304-306]. Therefore, in addition to the energetics favoring particle absorption, the PMF studies also point to large interfacial fluctuations which can affect particle self-assembly. These, along with other features to be discussed, help enable this unique particle transport phenomenon.

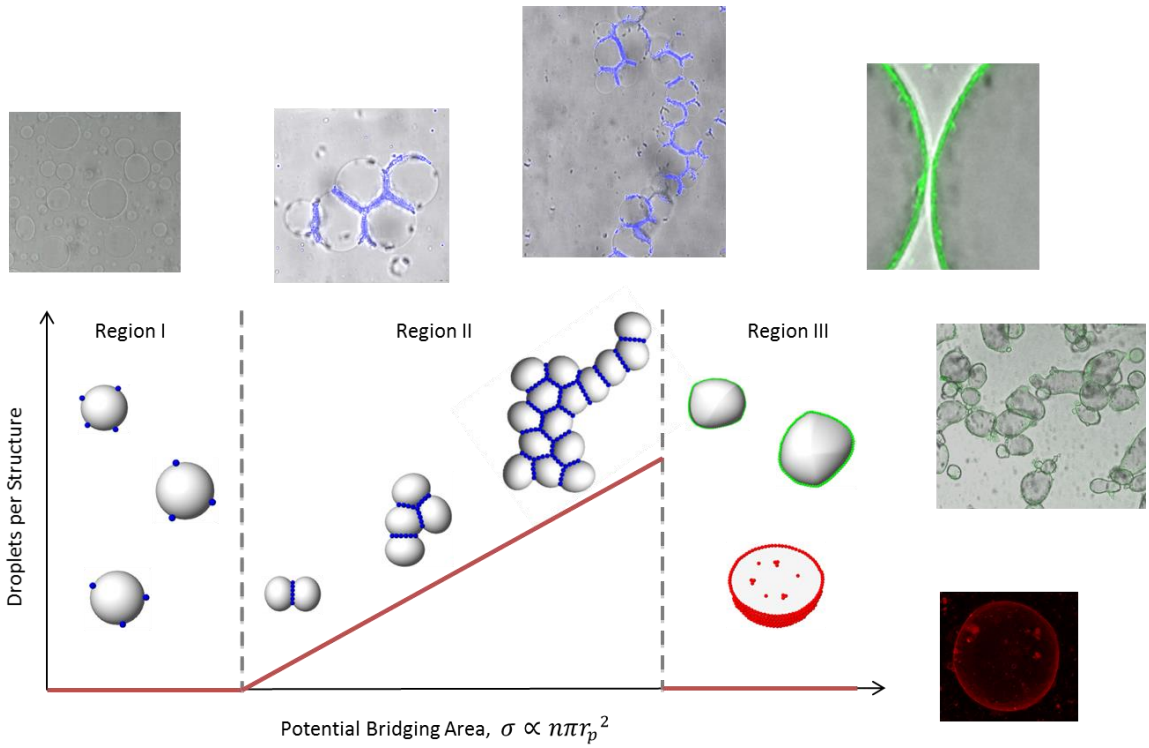

Figure A6. "Phase" diagram of oil-in-IL and water-in-IL Pickering emulsions with representative confocal images for each region. The regimes are denoted as: Region I, single sparingly covered droplets; Region II, bridged clusters of droplets; and Region III, fully covered droplets. The green particles in Regime I and the blue particles in Regime II represent 0.2 μm and 1 μm S-PS particles, respectively. In Regime III, S-PS and C-PS 0.2 μm particles are represented in green and red, respectively. Adapted from references [288, 307].

3.2.2. Oil-in- and Water-in-Ionic Liquid Pickering Emulsions

Further investigation into ionic liquid-based Pickering emulsions led to the discovery of another unique phenomenon in which in PDMS oil- and water-in-[BMIM][PF_6] Pickering emulsions, solid particle bridging occurred between the oil droplets and these particles avoided contact with the liquid-liquid interface: effectively an inter-droplet self-assembly phenomenon [288, 307]. Although the bridges prevented droplet–droplet coalescence, surprisingly, the presence of solid particles disrupted the overall emulsion stability by increasing the rate of flocculation and creaming. Further analysis showed that the morphology of these bridges and the consequent droplet structures depended on the particle surface chemistry, particle concentration, particle size, and whether water or oil was the droplet phase.

The unique, highly visible bridging phenomenon can be seen in the two confocal images for Region II of Figure A6 for 1 μm S-PS stabilized PDMS (20 cSt or 2 x 10^{-5} m^2/s)-in-[BMIM][PF_6] Pickering emulsions, with a 0.8 M particle concentration. Similar bridged morphologies were also seen in emulsions of the same particle concentration with 1 μm AS-PS and C-PS particles [307]. We observed that the particles self-assembled primarily into monolayer bridges across an ultrathin layer of ionic liquid between PDMS oil droplets, creating flocculated droplet structures of varying size and morphology. While there was much variation in droplet size, every oil droplet larger than 3 μm was attached to at least one other droplet. The larger droplets (above about 20 μm) formed chains or large aggregates of droplets, stabilized by many particles. This behavior was in sharp contrast to that of the same solid particles at the IL-in-water or oil-in-water emulsion droplet interface, which showed fully or partially covered droplets as previously dis-

cussed. Here, the solid particles did not generally equilibrate at the oil–IL interfaces, they instead bridge the oil droplets. Since this was the only structure present in these emulsions, we could infer that that the particles halted droplet coalescence by hindering drainage of the inter-droplet film.

These structures were similar to some emulsion systems studied by others [308, 309] in which the bridged droplets formed chains and aggregates. However, most notably, the oil-in-IL systems here differed from other studies in that the oil–IL droplet interfaces were almost completely devoid of particles. Also, droplet deformation at the bridges was much higher in these systems; the bridges occupied more of the droplet surface area. Droplets in other bridging oil–water systems remained mostly spherical with a few particles connecting their interfaces together [308, 309]. Notable also is that despite the low amount of PDMS used relative to the IL, this flocculation was the primary structure present in these systems: no un-bridged droplets of this size were observed except for systems using A-PS particles as a stabilizer.

It should also be noted that no solid particles were transported into the oil phase in oil-in-IL Pickering emulsions. This observation was also in contrast to the previously discussed IL-in-water systems; where a fraction of the particles could cross the interfaces and disperse in the IL phase, although they were initially in the water phase. This, however, is in agreement with the oil-in-water Pickering emulsion morphologies.

As mentioned previously, solid particle bridging plays an important role in the stability of oil–water Pickering emulsions. Surprisingly, although particle bridging inhibited individual droplet–droplet coalescence, it did not promote, but actually distressed, the overall emulsion stability. As a control experiment, we prepared PDMS-in-IL emul-

sions without particles in the same manner as the particle-stabilized emulsions. The oil-in-IL Pickering emulsions were homogenous after sonication but only stable for approximately 2.5 h in the systems using S-PS, AS-PS, and C-PS as stabilizers. At approximately 2.5 h, a distinct cream oil layer with particles formed at the top of the sample and left a light-colored emulsion underneath. The cream oil layer grew as a function of time. In contrast, the stabilizer-free control became cloudy with the formation of oil droplets but was stable for about 23.5 h until a layer of PDMS was clearly visible at the top. It appears, therefore, that the S-PS, AS-PS, and C-PS actually promoted the destabilization of the Pickering emulsions. We hypothesize, that this observation is due to particle-induced adhesion between oil droplets. Due to the low density and large volume (thus the buoyant effect), the aggregated oil droplets quickly rose to the top of the samples. These particles, therefore, did not stabilize the emulsions, but acted as flocculating and creaming agents in the presence of vigorous agitation. The A-PS system did not exhibit these characteristics until later, likely due to a lack of bridging; however, it also worthwhile to note that due to the poor particle coverage at the oil–IL interfaces, the A-PS particles did not provide strong emulsion stabilization. Upon examination of the cream top layer of an emulsion 60 days after sonication we found that the individual droplets had not coalesced, but were still separated by solid particle bridges. Compared to the bridged structure in Figure A6, Region II, these aggregates were much more extensive and the droplets exhibited much higher particle coverage. The latter observation was likely due to particle–particle attraction between bridged particles. Because particles in the inter-droplet bridges severely hinder film drainage, we expected that these droplets will remain in this state for extended periods of time, possibly months or years.

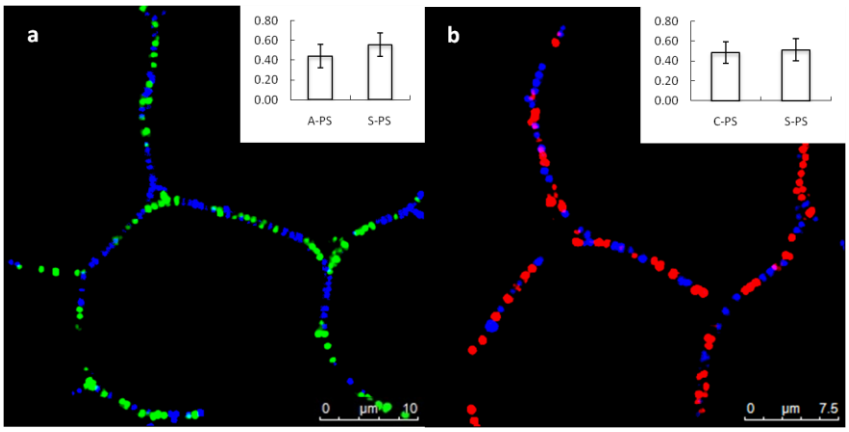

Figure A7. Confocal images of inter-droplet bridges in the Pickering emulsions contain (a) A-PS/S-PS; (b) C-PS/S-PS microparticles. The A-PS, C-PS, and S-PS particles are shown in green, red, and blue respectively. Fractions occupied by each respective particle are shown as insets. Scale bars represent 10 μm and 7.5 μm for (a) and (b), respectively. [307]

To further investigate this bridging phenomenon, oil-in-IL Pickering emulsions with binary mixtures of particles were prepared. The binary systems studied were A-PS/S-PS and C-PS/S-PS in a 1:1 ratio, making for double the amount of particles in the binary system compared to the single particle type systems. Figure A7 shows representative confocal images of the droplet structures that were formed with these heterogeneous particles. The structures seemed to be a hybrid of the structures formed by the respective single-particle systems. Figure A7(a) shows that the A-PS/S-PS system exhibited significant bridging. This is surprising as the A-PS particles did not readily form bridges on their own, but they appeared well incorporated into the bridges with the S-PS particles. The bridges appeared to be monolayers of both A-PS and S-PS particles in nearly equal number. To verify this observation, we analyzed 15 confocal images of such bridges using ImageJ to determine the fraction occupied by each species. We found that in the A-

PS/S-PS system, the fraction of A-PS particles present was 0.44 ± 0.12, indicating that the particles did indeed mix well in the bridges (see inset of Figure A7(a)). Inter-particle interactions between the positively charged A-PS and negatively charged S-PS particles thus were likely responsible for this mixing and stable bridge formation. Similarly, the bridges in the C-PS/S-PS system also showed good mixing between the particles (Figure A7(b)). Such behavior was expected, since both particle types readily formed bridges of this size and packing density in the single particle systems. Analysis (of 8 images) showed that the average fraction of the bridge occupied by the C-PS particles was 0.49 ± 0.11, suggesting good mixing (see inset of Figure A7(b)).

Having explored the effects of this phenomenon, we investigated the "tunability" of the morphology by observing the change in degree of bridging upon altering a number of factors including particle concentration, particle size, and droplet phase type. To quantify the degree of bridging, we obtained distributions of structure and droplet sizes via image analysis with the program ImageJ with the implication that large structures and droplets signified higher degrees of bridging. We observed that at constant particle size, increases in particle concentration resulted in larger bridged structures and wider droplet size distributions (higher degrees of bridging) [288]. At a constant particle concentration, increasing the particle size produced similar results [288]. Clearly, the degree of bridging was dependent on both particle size and concentration. Therefore, it was proposed that the area (σ) of a hypothetical monolayer formed by all of the particles in a given system could be a good predictor of the bridging extent. A system with a high σ would exhibit a greater degree of bridging than that of a lower σ. Assuming that all bridges were planar and circular and exhibited tight packing, the potential bridging area is proportional to the

sum of the cross sectional areas of all particles in the system. Thus, total potential bridging area, σ, is given by

$$\sigma \propto n\pi {r_p}^2 \quad \text{(A3)}$$

where n is the number of particles, and r_p is the individual particle radius. It should be noted that not all particles in a given system self-assembled into bridge structures; many particles remained dispersed in the IL phase. Therefore, σ represents the maximum bridging area attainable by a system. To verify the relation given above, three systems of varying particle size, but identical potential bridging area, were prepared and the degree of bridging was measured. The structure and droplet size distributions of all three systems showed high overlap, suggesting that potential bridging area was an adequate predictor of the degree of bridging. For this reason, σ is used as the x-axis of the phase diagram shown in Figure A6.

It should be noted that the effect of the droplet phase was also tested, but no significant changes in the degree of bridging were observed [288]. Since the particles were known to be stable in water, it was originally hypothesized that the water droplets would reabsorb the particles in a water-in-ionic liquid emulsion, making bridge formation impossible. Surprisingly, bridging occurred with all particle surface chemistries except for the A-PS particles and there was no particle absorption into the water droplets (images may be found in the Supporting Information of [288]). In general, these bridged structures were nearly identical to the oil-in-IL structures. Both cases showed minimal droplet coverage (except for the bridges) and exhibited networks of many droplets. These results

indicate that bridging in IL-based Pickering emulsions was possible over a wide range of droplet phases: from aqueous to hydrophobic.

Another novel particle morphology was seen in these emulsions, single, fully covered droplets, seen in the third regime of the phase diagram in Figure A6. This morphology resulted from emulsions of 100 M particle concentration with either 0.2 μm S-PS particles (Regime III images with green particles) or 0.2 μm C-PS particles (Regime III images with red particles). However, these only occurred with PDMS-in-IL emulsions for the S-PS particles and water-in-IL for the C-PS particles. Normally liquid droplets assume a spherical shape to minimize interfacial area. However, the PDMS droplets stabilized by the S-PS particles were distinctly non-spherical due to the high particle concentration. This phenomenon has been observed experimentally in both liquid droplets and air bubbles and is due to particle ‘‘jamming’’ at the interface [310-314]. A number of droplet shapes have been observed including cylinders, toroids, and saddles [310, 313]. In the water-in-IL C-PS stabilized emulsion, it was seen that once the particle concentration was high enough to prevent any bridging (because the droplets were fully covered), the water droplets began to absorb excess C-PS particles. These particles were relatively hydrophilic, which could partially explain why they were absorbed into the water droplets. We previously observed particle transport across the IL/water interface, but at much lower particle concentrations and the emulsion droplet interfaces were not fully covered [248], but not with C-PS particles in the IL-in-water emulsions.

Bridging was only observed in systems subjected to high mixing (shaking by hand only produced single-sparsely covered droplets). Considering that these conditions would induce an increase in droplet collisions, we hypothesized that bridges were formed as par-

ticles were trapped between colliding droplets [288]. We calculated the adhesive force between two bridged droplets to be on the order of 10^7 kT [288]. The key was to determine the cause behind the self-assembly of particles into bridges between colliding droplets rather than being drained out with the inter-droplet film. Interfacial charge and bulk phase viscosity were considered possibly significant factors, but the most significant effect was the IL-particle interaction, as discussed below.

We hypothesized that this unique bridging phenomenon formed due to the unique ionic nature of the IL. To test this hypothesis, we formulated an oil-in-IL emulsion with 1.0 μm S-PS particles and replaced [BMIM][PF_6] with 1-methyl-1-propylpryyolidinium bis(trifluoromethanesulfonyl)imide ([PMP][Tf_2N]) (TCI America, 98%). [PMP][Tf_2N] has a much lower viscosity (71 cP) and slightly higher density (~1.44 g/cm^3) than [BMIM][PF_6]. In support of our hypothesis, this emulsion formed bridged structures identical to the ones observed with [BMIM][PF_6] [288]. The formation of bridges may have been due to some unique interactions between the particles and the IL. Curiously, only the particles with acidic dissociable groups formed bridges. It is possible that strong hydrogen bonding between the surface groups and the fluorine groups of the anions enhanced the stability of the particle-laden IL film. Furthermore, ionic liquids are known to exhibit a degree of ordering (i.e. layering) upon contact with solid surfaces [315-317]. Confined between tightly packed particles (in bridges), the IL would have interacted with many surfaces may have assumed an ordered structure. Recent AFM studies have indicated that this layering phenomenon is important in IL-particle interactions [299]. The existence of such a structure would also enhance the stability of the inter-droplet bridges. However, it has also been argued that perhaps the particles simply exhibit the correct

contact angle to bridge the droplets. While this seems unlikely given that both water and oil droplets were bridged, the actual measurement of contact angles is quite difficult in liquid systems. Therefore, we again turned to MD simulations to (1) determine how the opposite solvent changes contact angle and (2) investigate any particle-IL interactions that would aid in bridge formation.

In contrast to the oil/water systems, IL-based interfaces offer more configurational degrees of freedom due to the binary nature of the IL. We expected to see a difference in the roles played by each ion in the interfacial self-assembly process. Employing the same hydrophobic nanoparticles, we simulated self-assembly at the IL/water and IL/hexane interfaces [286]. Fortunately, an accurate force field for [BMIM][PF_6] was readily available [279]. The nanoparticles were first placed in the water phase and allowed to equilibrate. The results from equilibration are shown in Figure A8.

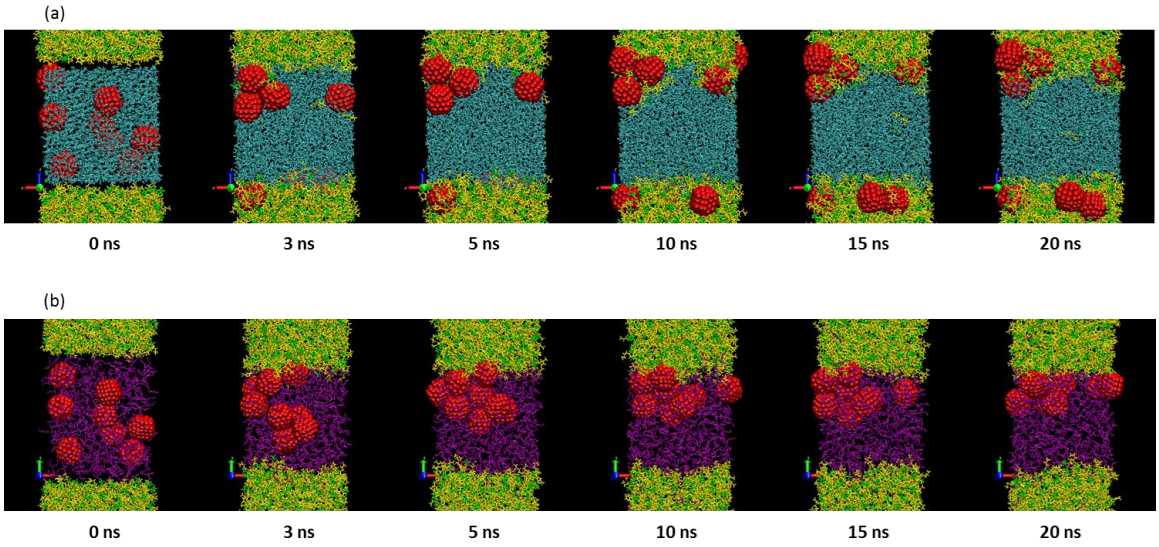

Figure A8. Sample snapshots of (a) the IL/water/HCP and (b) IL/hexane/HCP systems at various time intervals. The water is represented in blue, [PF_6] in green, [BMIM] in yellow, hexane in purple, and HCP in red, respectively. Adapted from reference [286].

In the IL/water system (Figure A8(a)), the particles diffused rapidly toward the IL/water interface, forming some aggregates along the way. Once in contact, the IL ions began to diffuse into the water phase to surround nanoparticles and nanoparticle clusters. The hydrophobic [BMIM] cations oriented themselves such that their hydrophobic tails lay across the surface of the nanoparticles, which was also hydrophobic. To maintain charge neutrality, the [PF_6] anions followed the cations into the water phase to form these surrounding layers, thus causing a net increase in IL concentration in the water. After formation of these surrounding layers, the particles moved further into the IL phase, eventually equilibrating on the IL side of the interface. In contrast, nanoparticles in the IL/hexane system (Figure A8(b)) equilibrated on the hexane side of the interface, indicating relatively higher interactions between the particle surfaces and the hexane molecules rather than [BMIM] cations. The [BMIM] cations, despite the hydrophobic nature of their carbon chains, did not penetrate the oil phase and surround the nanoparticles as those in the IL/water system. The two interfaces did show some similarities, however. Both exhibited interfacial widths of 0.7 to 0.8 nm. This is approximately twice the width of a water/trichloroethylene interface [224]. However, the water/IL interface could be widened to 1.95 nm by the presence of nanoparticles. Since the particles equilibrated on the hexane side of the IL/hexane interface, the interfacial width was not disturbed as much. It was evident, therefore, self-assembly of these nanoparticles depended significantly on the non-IL solvent. Assuming that these particles approximated the PS particle behavior, we can see that contact angles would change drastically between IL/oil and IL/water systems. This is one piece of evidence suggesting that the particles did not simply exhibit ideal contact angles for bridging.

Given that the experimental microparticles did have some surface chemistry, we extended these MD studies to include the effect of particle charge on self-assembly. The surfaces of the hydrophobic particles were modified by adding or removing protons to the protruding -CH_n groups to give them charges ranging from -6 to 6. Figure A9 shows snapshots at 20 ns of IL/water and IL/hexane system of varying particle charges with their corresponding density profiles. In general, the effects of charge were related to the charge magnitude, but independent of charge sign. However, the effects in the IL/water and IL/hexane systems were qualitatively opposite. In the IL/water system, increased particle charge resulted in decreased interaction with the IL, as evidenced by the interfacial position of the particles and the consequent interfacial width (i.e. the IL/water system with zero charge had the most deeply embedded particles and the widest interface) [284]. This is due to the relatively higher polarity of water [318, 319], which interacted more strongly with the charged nanoparticles. In contrast, the IL/hexane system saw increased nanoparticle-IL interaction with higher charge. Charged nanoparticles were more deeply embedded into the IL, resulting in wider interfaces. The IL, being more polar, interacted more strongly with the charged species. This study shows that while varying surface charge could change the interface position of a particle to a degree, the strongest effect was still exhibited by the opposite solvent. The relatively weak effect of particle surface chemistry may explain why similar self-assembled morphologies were experimentally observed with S-PS, AS-PS, C-PS, and A-PS particles in Pickering emulsion systems.

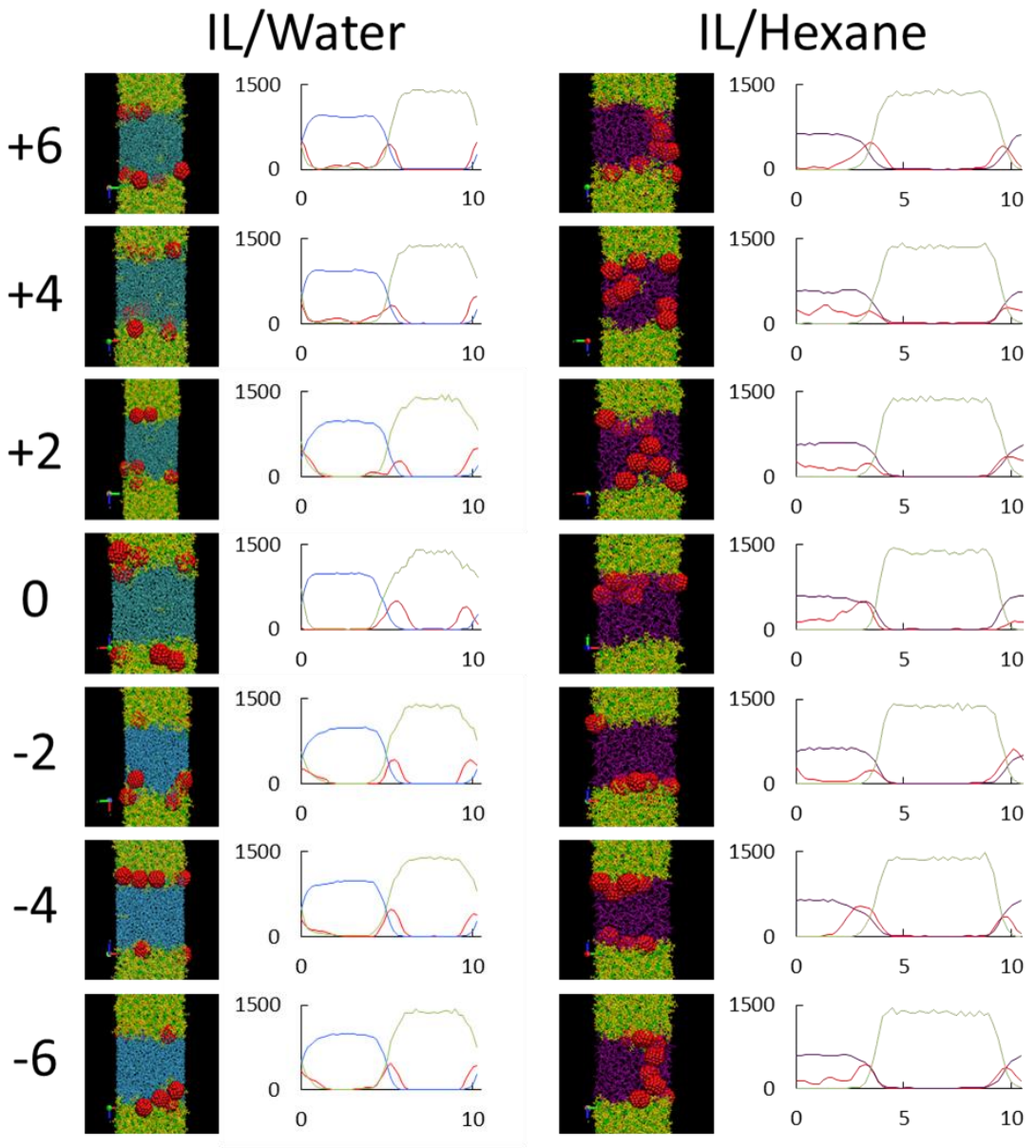

Figure A9. Equilibrium snapshots and density profiles averaged from last 1 ns of 4 parallel runs for the IL/water (left column) and IL/hexane (right column) systems. Y-axes represent density (kg/m^3) and x axes represent z position (nm) in the simulation boxes. The green, blue, purple, and red lines represent the IL, water, hexane and HCPs, respectively. Nanoparticle charges are shown in the left column. Adapted from reference [284].

Next, we examined IL-particle interactions that would affect bridging formation. To this this, we simulated single hydrocarbon and silica particles immersed in [BMIM][PF_6] Figure A10 shows the first solvation layer of IL ions around fully immersed hydrocarbon (a) and silica (b) particles. Corresponding radial distribution functions are also included to describe the rest of the solvation structure. It can be seen that the binary nature of the IL allowed for formation of solvation layers specific to the hydrophobic and hydrophilic surface chemistries. Around the hydrocarbon nanoparticle, favorable van der Waals interactions between the [BMIM] cation and the nanoparticle surface allowed close association and the formation electrically neutral solvation layers [285]. Around the silica nanoparticle, PF_6 anions formed hydrogen bonds with the silanol groups, causing the formation of solvation layers of alternating ions.

ILs are known to exhibit double-layer behavior at charged surfaces [320-322] and similar charge ordering at silica surface [317, 323-325]. The stark differences between these solvation structures point to the adaptive nature of ILs due to their binary structure. Both van der Waals and coulombic interactions played an important role and the individual ions self-assembled to form favorable solvation layers. Interestingly, these solvation layers experienced significantly decreased dynamics, with the PF_6 anions exhibiting solid-like behavior around the silica particle [285]. Assuming that such solvation layers could form around the bridging particles, the decreased dynamics could explain why the particles were able to form bridges. The slower-moving IL film between aggregated particles would hinder their separation as droplets collided around them and allow them to form bridges.

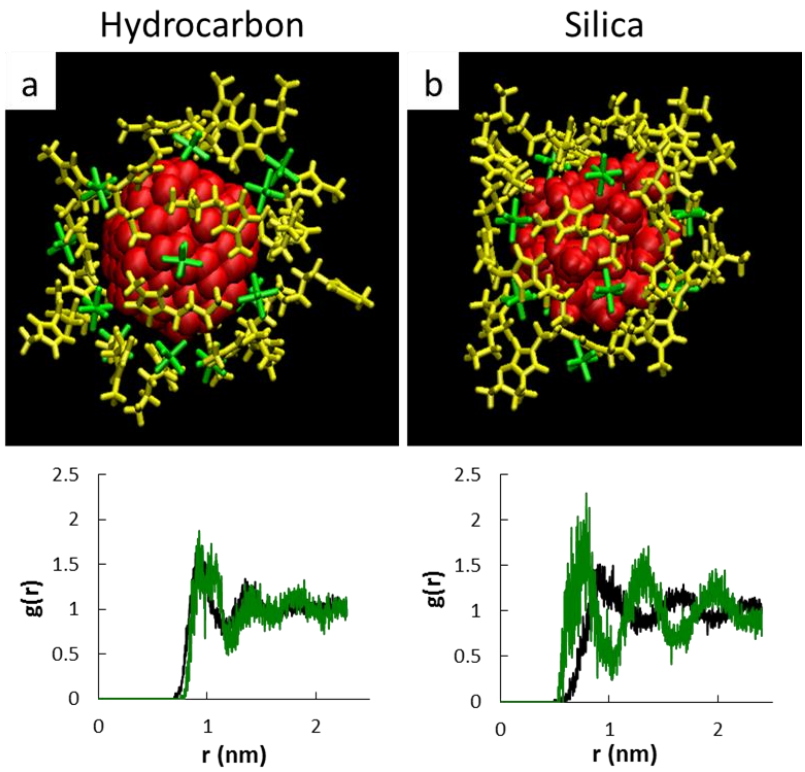

Figure A10. IL solvation shells and radial distribution functions around the (a) hydrocarbon and (b) silica nanoparticles. BMIM, PF_6, and nanoparticles are represented in yellow, green, and red, respectively, in each image and radial distribution functions for the anion and cation are represented in green and black, respectively. Adapted from reference [285].

3.2.3. Ionic Liquid-in-Ionic Liquid Pickering Emulsions

To our knowledge, a Pickering emulsion in which both droplet and continuous phases are ILs has not yet been explored. This section discusses our findings on this type of system, which has not previously been published. Indeed, an IL/IL Pickering emulsion is a novel formulation, and with both phases and particles offering high tunability, the IL/IL Pickering emulsion may be suited for the widest array of applications. Furthermore,

since ILs exhibit negligible volatility and high stability, this type of emulsion may be well suited for extreme environments. The first step in creating this novel emulsion was to determine pairs of mutually immiscible ILs. In the literature, ILs are often mixed completely for enhanced tunability [326], however, mutually or partially immiscible ILs have been reported [327-329]. These immiscible pairs are generally between imidazolium- and phosphonium-based ILs. The mechanism behind this immiscibility is that as the smaller imidazolium ions diffuse into the phosphonium IL they form strong hydrogen bonds that increase the degree of order within the phosphonium IL, resulting in a negative entropy of mixing [328]. We formulated and studied Pickering emulsions of two immiscible pairs: Trihexyltetradecylphosphonium bis-(2,2,4-trimethylphentyl)-phosphinate ($[P_{66614}][Phos]$) / ethylammonium nitrate (EAN) and $[P_{66614}][Phos]$ / $[BMIM][PF_6]$. Viscosities for these ILs were measured using a TA Instruments AR-G2 rheometer at 25 °C, and were 82.4 cP, 2.61 cP, and 22.3 cP for $[P_{66614}][Phos]$, EAN, and $[BMIM][PF_6]$, respectively. Particles used in the Pickering emulsion formulations are described in Table A1.

The first system, $[P_{66614}][Phos]$ in EAN, was quite stable against mixing as long as EAN was the continuous phase of the emulsion. Arce et al. report that smaller ILs are much more soluble in phosphonium ILs than vice versa [328]. The second IL-IL system we emulsified was $[P_{66614}][Phos]$ in $[BMIM][PF_6]$. We observed that $[BMIM][PF_6]$ slowly gelled $[P_{66614}][Phos]$ over time, but interdiffusion between the two ILs was slow enough to allow for droplets to remain for hours. We observed the self-assembled morphologies in these systems using confocal laser-scanning microscopy.

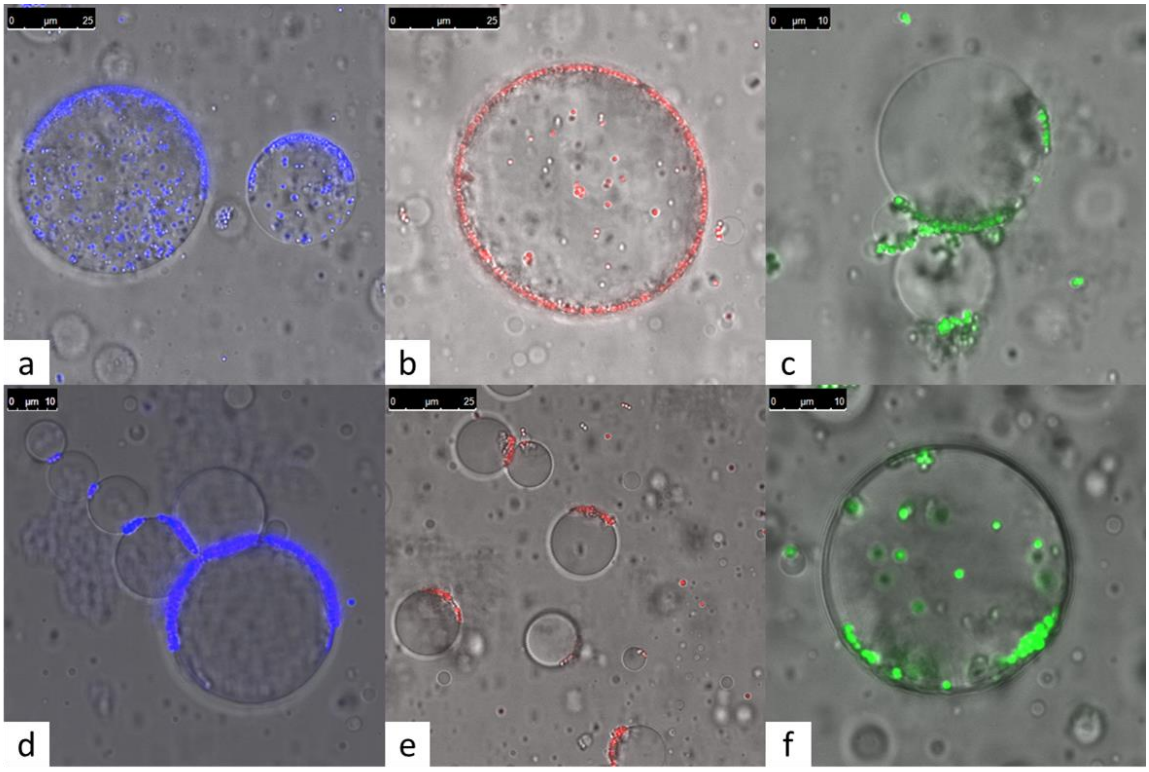

Figure A11. DIC/confocal overlays of [P_{66614}][Phos] droplets in EAN with (a) S-PS, (b) C-PS, and (c) A-PS microparticles and [P_{66614}][Phos] droplets in [BMIM][PF_6] with (d) S-PS, (e) C-PS, and (f) A-PS microparticles.

Figure A11 shows representative confocal/differential interface contrast overlays of both of these emulsion systems with three different particles. For the [P_{66614}][Phos] in EAN system, both S-PS (a) and C-PS (b) systems exhibited morphologies comparable to conventional Pickering emulsion behavior, with the exception that a large number of particles were absorbed into the [P_{66614}][Phos]. The A-PS particles were not absorbed. In a notable similarity, we reported above that in the ionic liquid-in-water Pickering emulsion study [BMIM][PF_6] also absorbed S-PS and C-PS particles, but not A-PS particles, from water [294]. As mentioned previously, this phenomenon is unusual because micron-sized particles are usually strongly bound to the liquid-liquid interface (~10^6 kT desorption en-

ergy) [226]. We suspect for this system as well that the sign and density of the particle surface charge played a primary role in this phenomenon, though the underlying mechanism is still unclear [294]. This similarity in particle "selectivity" in the present system and the IL/water system suggests that particle absorption occurred under the same mechanism for both systems.

While the morphologies of the S-PS and C-PS systems readily compare to that the IL/water Pickering emulsions, the A-PS system does not. Figure A11(c) shows that A-PS particles exhibit some of the bridging behavior reported previously in the oil- and water-in-IL work [288, 307]. Interestingly, the A-PS particles were the only particles that did not form bridges in either the oil- and water-in-IL systems [307]. Thus, we were surprised to see bridging with this particle type. One major difference between this system and the bridging systems reported previously was that the continuous phase here is protic. This is significant because in order for the A-PS particles to assume a surface charge, the amine groups needed to accept a proton (becoming ammonium ions). Consequently, these results support the hypothesis that an active surface chemistry is necessary in order for particles to exclusively form bridges in IL-based Pickering emulsions [288].

Having discussed the first system, we will now move on to the second: $[P_{66614}]$[Phos] in [BMIM]$[PF_6]$. Most obvious is that the particle self-assembly phenomena was a strong function of the continuous phase. In contrast to Figure A11(a), Figure A11(d) shows that S-PS particles in this system were not absorbed, but exclusively formed bridges between the droplets. Likewise with the C-PS particles (Figure A11(e)), though bridging was only an anomaly rather than the dominant morphology. As if to complete reversal of morphologies, A-PS particles did not form bridges (Figure A11(f)),

but were readily absorbed into the [P_{66614}][Phos] droplets. Comparative analysis of these two systems yields important conclusions.

First, it is clear that the phenomena generally unique to IL-based Pickering emulsions: exclusive bridging and particle absorption, may also occur when both phases are ILs. Secondly, these results show that the morphologies can be tuned by the constituent ILs, not just the particles. These phenomena have important implications for IL-based applications. In particle synthesis, phase transfer is often necessary either to place the particles in their working environment or apply additional functionalization [296, 330-332]. These processes usually require additional surface modification of the particles, but our results indicate that such measures may not be necessary in an IL environment. Also, since bridging can be tuned by the continuous phase, this morphology may be used more readily in self-assembly and high internal phase emulsion (HIPE) applications [333-336].

4. Conclusion and Outlook

We have reviewed work on the nature of IL-based interfaces and self-assembled particle morphologies of IL-in-water, oil- and water-in-IL, as well as the new work on IL-in-IL Pickering emulsions with emphasis on their unique phenomena, by way of experimental and computational studies. Particle self-assembly allows for alternative applications to traditional surfactant self-assembly, including the bottom-up preparation of core-shell microparticles [63], the ease of self-assembly of a multitude of particle types for a variety of tasks (metallic nanoparticles for conductivity/catalysis [242, 243], carbon nanotubes [331, 337], virus [338, 339], CdSe/InP quantum dots [228], etc.), the ease of access to the particle morphologies via microscopy, among others. The use of ionic liquid

rather than conventional choice of oil or water in these emulsions allows for the exploitation of the unique properties of ILs including their "green" quality due to their negligible vapor pressure and high chemical and thermal stability, and their ease of tunability for different applications due to the numerous amount of cation/anion pairs.

In the IL-in-water Pickering emulsions, particles formed monolayers at ionic liquid-water interfaces and were close-packed on fully covered emulsion droplets or aggregated on partially covered droplets. In contrast to those at oil-water interfaces, no long-range nearly ordered colloidal lattices were observed. Interestingly, other than equilibrating at the ionic liquid-water interfaces, the microparticles also exhibited phase preference in the dispersed and continuous phases: the sulfate-treated polystyrene (S-PS) and aldehyde-sulfate-treated polystyrene (AS-PS) microparticles were extracted into the ionic liquid phase with a high extraction efficiency whereas the amine-treated polystyrene (A-PS) microparticles remained in the water phase. These experimental findings were supported by PMF calculations, which showed large energy drops as hydrophobic particles crossed the interface into the IL phase.

In the oil- and water-in-IL Pickering emulsions, the S-PS, AS-PS, and C-PS particles mostly formed monolayer bridges among the oil droplets rather than residing at the oil–ionic liquid interfaces, a significant deviation from traditional Pickering emulsions morphology. The bridge formation inhibited individual droplet–droplet coalescence; however, due to the low density and large volume of the droplet clusters (thus the buoyant effect), the aggregated oil droplets actually promoted oil/ionic liquid phase separation and distressed emulsion stability. In investigating the alteration of the particle concentration, particle size, and droplet phase type, three morphology regimes were discovered: (1)

single, sparingly covered droplets, (2) bridged clusters of droplets, and (3) fully covered droplets. The degree of bridging was directly proportional to the total potential bridging area, which could be determined from particle size and concentration. The work identified new self-assembled particle structure and morphology in solid-stabilized emulsions, which contributes to the fundamental understanding of these unique systems. Molecular dynamics simulations revealed aspects of the mechanism behind this bridging phenomenon, including the role of the droplet phase, surface chemistry, and the inter-particle film.

The novel IL-in-IL Pickering emulsions exhibited both of the morphology schemes seen with the IL-in-water and oil/water-in-IL, particle transport with fully covered or aggregated particle domains or droplet bridging with no particle transport. The appearance of these morphologies depended on the particle surface chemistry as well as the ILs used. The key to tuning which morphology was observed was ensuring an "activated" particle surface chemistry, with the acidic particle types having the acidic hydrogen removed by the bulk IL and the basic particle type needing free hydrogen in the bulk IL to be donated. Therefore, these unique behaviors so prevalent in IL-based Pickering emulsions can be controlled using these parameters.

While the field of ionic liquid science has become quite developed in the recent years, the field of particle self-assembly at IL-based interfaces has not seen much interest, especially the 3D interface seen in Pickering emulsions. The reviewed work presents the fundamentals of these interfaces, which have only recently been explored. Applications of these specific systems are yet to be seen, but have the potential to be numerous due to the tunability of the ionic liquids and particles incorporated, as well as the particle morphology by combining certain groups of particle surface chemistry, IL type (protic or

aprotic), and whether oil or water is incorporated as well. The incorporation of particle self-assembly with ionic liquid science allows for new applications at the intersection of these two fields, dependent on the original Pickering emulsion morphology. The single droplet/particle absorption morphology presents a unique method for the bottom-up preparation of core-shell microstructures by polymerization of the internal phase, which could result in novel polymeric ionic liquid microparticles with inorganic particles incorporated at the surface and inside, unique particle separation schemes by the absorption of particles by the IL, as well as novel reaction schemes with catalysis occurring at the particles at the interface and within the IL. The unique bridged morphology allows for interesting application to high internal phase emulsion applications, novel bridged microstructures by polymerization of the internal phase or the particles for membrane formation, self-assembly of bridged droplet chains or rings by microfluidics, as well as Pickering emulsion separation by way of the particles acting as flocculating agents. We expect that the findings concerning the fundamentals behind the systems presented in this review will increase in importance as ionic liquids see more application in self-assembly applications in the coming years.

5. Acknowledgements

We are grateful to the financial support from the National Science Foundation CBET-0922277 and Graduate Fellowship, the Science Foundation of Arizona Fellowship 0447-10, NASA Graduate Fellowship, and the Arizona State University High Performance computing Initiative.

APPENDIX B

PYRROLE-BASED POLY(IONIC LIQUIDS) AS EFFICIENT STABILIZERS FOR FORMATION OF HOLLOW MWCNT PARTICLES

1. Introduction

Carbon Nanotubes (CNTs) have been a material of interest in a diverse set of fields because of their remarkable characteristics such as high thermal, mechanical, and electrical properties, low mass density, etc. However, agglomeration of the nanotubes and their incompatibility with polymer matrices encompass some of the major challenges, which limit their employment in the many proposed applications, especially in the field of nanocomposites. [91-93, 340] The fundamental limitations of carbon nanotubes highlight the need to focus on efficient methods for stable CNT dispersion, without reducing their desired thermal, mechanical, and electrical properties.

Broadly speaking, there are two approaches to disperse CNTs: first is the mechanical dispersion method, and the second is the alteration of the surface energy of the CNTs, either physically through non-covalent treatment, or chemically by the means of covalent bonding. Previously, most of work related to dispersion of CNTs (both single walled and multi-walled) have focused on high powered ultrasonication for dispersing the materials by using a high shear rate. The major drawback of such an approach is the decreased aspect ratio of the nanotubes during the high shear mixing process as well as limited stability. [94] Chemical methods, particularly the covalent treatment method, offer highly stable dispersions due to the chemical functionalization to increase the surface energy, providing repelling forces in between individual nanotubes. [95, 341] Although this method is efficient, it can cause structural defects in the nanotubes, which significantly affects the performance of the CNTs and their potential applications. This occurs due to the aggressive nature of the chemical method, including high reaction temperatures and long reaction times, as well as the added surface pendant interrupting the π-

electron cloud of the CNTs. [97] In this context, non-covalent treatment offers an appealing route to disperse CNTs, mitigating the need for harsh thermal or mechanical treatments and allowing the crucial π-electron cloud of the graphitic nanotube structure to remain completely intact.

Non-covalent surface treatment for CNT dispersions generally comprises of utilizing different types of stabilizers, typically surfactants having both a hydrophilic and hydrophobic group, which are known to facilitate the homogenization of CNTs. [94, 98, 99] One of the major drawbacks of surfactant-based stabilization is the need to use of large quantities of the stabilizers to prevent the aggregation of CNTs for any extended period of time. Secondly, most of the known surfactants used for this application do not share the same properties as CNTs, e.g. high conductivity or thermal stability, which interrupts the inherent property of the nanotubes when these molecules wrap around them. A new option to lessen the effect of the above disadvantages is to use ionic liquids (ILs), liquid salts having both organic and inorganic moieties, as an alternative to create stable dispersants of nanotubes. Recently, Fukushima et al. demonstrated this by dispersing CNTs in different ionic liquids. [100] However, the non-covalent wrapping of the CNTs in ILs does not yield very stable dispersions in water or organic solvents.

Polymerized ionic liquids (poly(ionic liquids), PILs) feature a polymer backbone and pendant ionic liquid groups and can offer enhanced stability over ionic liquids for CNT dispersions. This is attributed to the longer chains of the PILs, which are hypothesized to aid in the wrapping of the CNTs and lead to more stable dispersions. [342] Apart from the stability, PILs also offer extraordinary versatility in terms of hydrophilicity/hydrophobicity, a key factor for utilizing CNTs in different liquid systems. The polari-

ty of the PILs can be tuned by simple anion exchange reactions to produce PILs of the same polymer backbone with a variety of anions, thus they can be solubilized in water to many different polar and nonpolar organic solvents corresponding to the polarity of the selected anion. Furthermore, PILs also offer the unique possibility of different functional backbones. In the present work, we demonstrate how intrinsically conducting polymers (or conjugated polymers, ICPs), such as polypyrrole, can be utilized as a functional backbone in PILs to create PIL-ICP hybrids to act as stabilizers for multi-walled carbon nanotubes dispersions in various solvents. Importantly, we expect to overcome the inherent lack of electronic conductivity in a pure ionic liquid-based system and at the same time aid the electronic properties of nanotubes, through the employment of the polypyrrole backbone, unlike the conventional use of nonconductive surfactants. Additionally, incorporating ionic liquid moieties to create the PIL-ICP hybrid system also solves the largest barrier to the use of ICPs alone, which is the lack of solubility in aqueous or many organic solvents, while allowing for the formation of novel CNT dispersions in multiple, differing solvents with stability in the range of several months.

The formed PIL-ICP hybrid stabilized CNT dispersions also offer unique possibilities in terms of applications. One unique usage of such dispersions is in the area of surfactant-free emulsions or Pickering emulsions, formed by adding an oil phase to the dispersion, to create droplets stabilized by MWCNTs. Due to the incorporated flexibility by the virtue of the PIL-ICP hybrids, different emulsions can be proposed with the same PIL-ICP backbone, such as hexane-in-water or hexane-in-acetonitrile. The Pickering emulsions obtained from this technique demonstrate extended stability and unique characteristics. One of the most unique features of this type of emulsion was the ability to

generate hollow conductive shells via the stabilization of the CNTs at the oil-water/acetonitrile interface. The morphology of the CNT particles formed from the emulsion droplets were studied with confocal microscopy and further characterized after drying by scanning electron microscopy (SEM) to view the shell morphology. The hollow particles can therefore be used as a payload carrier, depending on the solubility of the payload in the oil phase of the Pickering emulsion. In the present work, such an idea was demonstrated with silicon nanoparticles, which have limited solubility in the aqueous phase. Overall, this work proposes a new class of efficient PIL-ICP hybrid stabilizers with controllable hydrophobicity offering extended stability of carbon nanotube dispersions with novel applications in hollow particle formation via Pickering emulsion templating and in placing a payload into the shells.

2. Experimental Methodology

2.1. Pyrrole-based PIL Monomer Synthesis

Synthesis of the monomer was carried out according to literature, by first synthesizing the precursor molecule N-(4-bromobutyl)pyrrole, then using it to yield N-(4-butyl-(1-methylimidazole))pyrrole bromide monomer. [343-345] All materials were used as-in from the suppliers, without further purification. 0.6 g ground potassium hydroxide (Sigma-Aldrich) and 150 mL dimethylformamide (ACROS Organics) were added to a 250 mL round bottom flask, under a nitrogen purge, magnetic stirring, and in an ice bath. 5 mL of 1,4-dibromobutane (ACROS Organics) was added, followed by the addition of 1 mL pyrrole (ACROS Organics) dropwise. The mixture was stirred for 24 hrs. To purify the reaction mixture, 150 mL HPLC water (Fisher Scientific) was added to the reaction

solution and the product was extracted into 300 mL diethyl ether (VWR International). Magnesium sulfate (Alfa Aesar) was used to dry the solution, and then the ether was evaporated under vacuum to yield the precursor molecule, N-(4-bromobutyl)pyrrole. ^{1}H NMR: 6.62, 6.12 (aromatic C-H); 3.92, 3.37 (C-H near Br); 1.99, 1.83 (alkane C-H). 1.2 g N-(4-bromobutyl)pyrrole and 0.59 g 1-methylimidazole (ACROS Organics) were added to 15 mL acetonitrile (Honeywell), heating at 60 °C under reflux, magnetic stirring, and a nitrogen purge two days. The monomer product, N-(4-butyl-(1-methylimidazole))pyrrole bromide, was then recovered after solvent evaporation. ^{1}H NMR: 10.32, 7.87, 7.24, 6.65, 6.12 (aromatic C-H); 4.22, 4.07 (C-H near aromatic); 3.95 (C-H on methyl group on imidazole ring); 1.92, 1.83 (alkane C-H).

2.2. Pyrrole-based Hydrophilic and Hydrophobic PIL Synthesis

The synthesis of the hydrophilic pyrrole-based PIL, poly(N-(4-butyl-(1-methylimidazole))pyrrole bromide) (PPy-Br), and the two hydrophobic pyrrole-based PILs, poly(N-(4-butyl-(1-methylimidazole))pyrrole hexafluorophosphate) (PPy-PF_6) and poly(N-(4-butyl-(1-methylimidazole))pyrrole bis(trifluoromethane)sulfonimide) (PPy-Tf_2N), were carried out according to literature. [345] 2.3 g of Iron(III) chloride hexahydrate (Fisher Scientific) was used as an oxidant and added to 12 mL HPLC water, under a nitrogen purge and magnetic stirring. 0.78 g of N-(4-butyl-(1-methylimidazole))pyrrole bromide was then added. After addition of the monomer, the solution was stirred for two minutes and then kept at room temperature for 24 hours without further stirring. The polymerization was terminated by pouring the mixture into a great deal of acetone. The black power product was then filtered out and washed with acetone and methanol until the washing solution became clear, with subsequent drying under vacuum to yield the

PPy-Br product. To form the hydrophobic PILs, a simple anion exchange procedure was carried out with PPy-Br and two hydrophobic anion containing salts, potassium hexafluorophosphate to create PPy-PF_6 and lithium bis(trifluoromethane)sulfonimide to create PPy-Tf_2N (both salts being from Sigma-Aldrich). 0.02 g of PPy-Br was dissolved in 10 mL HPLC water, and a solution of 0.04 g of the corresponding salt in 10 mL of water was added dropwise to the first solution, under stirring at room temperature for 24 hours. The resulting hydrophobic precipitate was filtered and washed with HPLC water and dried under vacuum to yield the hydrophobic PIL powders.

2.3. PIL-stabilized CNT Dispersion and Emulsion Formation

For stability testing, CNTs were dispersed in various solvents with and without a PIL stabilizer. 5 mg of CNTs and 5 mg of a pyrrole-based PIL were added to 25 mL of HPLC water. The solution was ultrasonicated for fifteen minutes in an ice bath with a Sonics VibraCell 500W to create a stable, homogeneous black solution. For the control without the PIL stabilizer, 5 mg of CNTs and 25 mL of the solvent were sonicated in an ice bath for the same time. To create the hexane-in-water Pickering emulsion stabilized by the PIL-CNT, 1.5 mL of hexane was added to a solution of CNTs stabilized in water by PPy-Br, according to the procedure above. This was then put on a shaker for 10 minutes. Hexane-in-acetonitrile emulsions with PPy-PF_6 or PPy-Tf_2N as the CNT stabilizer were prepared in an identical fashion. A 2.5% w/w suspension of Silicon (Si) nanoparticles in octane was mixed with the CNT suspension at a ratio of 3:5 by volume. The ratio of the weights of Si nanoparticles to CNT was 1:1.

2.4. Material Characterization and Hollow Particle Formation

^{1}H Nuclear Magnetic Resonance (NMR) spectra were taken with a Bruker 400 MHz NMR spectrometer in deuterated chloroform (Cambridge Isotope Laboratories). Fourier transform infrared spectra (FTIR) were generated with a Bruker IFS 66V/S FTIR spectrometer, incorporating the samples into potassium bromide pellets. A TA Instruments Thermogravimetric Analyzer (TGA) Q500 was used to analyze the thermal weight loss under air. The PIL samples were placed in a tared platinum crucible and heated from 25 to 600 °C at a heating rate of 10 °C min^{-1}, while the PIL-CNT emulsion samples were heated from 25 to 900 °C at a heating rate of 20 °C min^{-1}. Microscopic morphologies of the solutions and emulsions were taken using a confocal laser-scanning microscope (Leica TCS SP5), a FEI/Philips XL30 Environmental FEG Scanning Electron Microscope (SEM), and a Philips CM200-FEG Transmission Electron Microscope (TEM). To yield the hollow particles, the emulsion droplets were initially frozen at -18 °C and then freeze dried using a 1L bench top Labconco FreeZone freeze dryer for 24 hours followed by gold sputtering for 100s. The obtained frozen emulsion particles were subsequently studied using the XL-30 SEM for surface morphology.

3. Results and Discussion

3.1. Synthesis and Characterization of Pyrrole-based PILs

The synthesis of the polypyrrole-based poly(ionic liquids) (PILs) was performed following the synthesis of the precursor molecule, N-(4-bromobutyl)pyrrole, and then the creation of the hydrophilic N-(4-butyl-(1-methylimidazole))pyrrole bromide monomer.

This monomer was then polymerized with the aid of iron chloride hexahydrate as an oxidant to create the hydrophilic PIL-ICP hybrid, poly(N-(4-butyl-(1-methylimidazole))pyrrole bromide) (PPy-Br). Simple anion exchanges with the salts potassium hexafluorophosphate and lithium bis(trifluoromethane)sulfonamide, yielded the hydrophobic PIL-ICPs, poly(N-(4-butyl-(1-methylimidazole))pyrrole hexafluorophosphate) (PPy-PF_6) and poly(N-(4-butyl-(1-methylimidazole))pyrrole bis(trifluoromethane)sulfonimide) (PPy-Tf_2N), respectively.

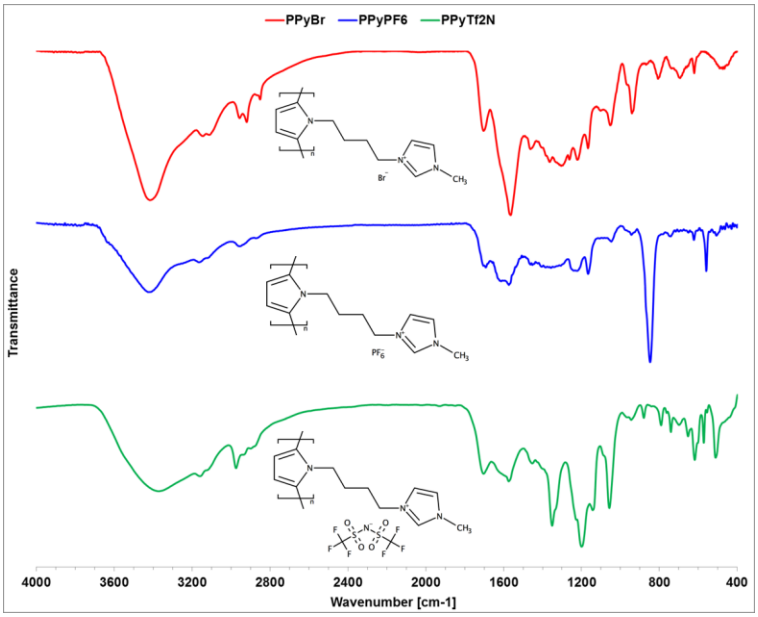

Figure B1. FTIR spectra of the synthesized polypyrrole-based PILs with their respective chemical structures below each curve, from the top down, PPy-Br (green), PPy-PF_6 (red), and PPy-Tf_2N (blue).

Figure B1 shows the FTIR spectra of these three synthesized PILs to show the successful creation of the PILs and anion exchanges. From the FTIR spectra, the characteristic peaks of the poly(pyrrole) (PPy) backbone in the range of 3600 – 3200 and 1700 – 1200 cm^{-1} can been seen. In addition, absorption bands near 1050 cm^{-1} (–NH bending deformation)

and 950 cm^{-1} (-CH out of plane bending) can be observed. This indicates that each PIL has the same PPy backbone.

The anion exchange of the PILs was done to control the hydrophilicity, as the Br anion is highly polar and hydrophilic and can be easily exchanged with nonpolar and hydrophobic anions to yield hydrophobic PILs as precipitates in water to be easily filtered off and recovered. The anion exchange between Br and PF_6 can be seen in the FTIR spectra through the addition of absorption bands in the PPy-PF_6 spectrum at 1169 cm^{-1}, 841 cm^{-1}, and 559 cm^{-1} corresponding to the newly present P-F bonds. [345] The anion exchange between Br and Tf_2N is recognized through the appearance of peaks corresponding to the Tf_2N anion, including 1350 cm^{-1} (SO_2), 1200 cm^{-1} (CF_3), 1150 cm^{-1} (SO_2), and 1050 cm^{-1} (S=N=S))^2, cm^{-1}). [346] With the successful synthesis of three PIL-ICP hybrids of varying hydrophobicity, we sought out to take advantage of these characteristics to stabilize CNTs in various solvents, with subsequent emulsion formation and hollow particle generation.

3.2. Polypyrrole-based PIL-stabilized MWCNT Dispersions

Traditional ionic surfactants, such as sodium dodecyl sulfate (SDS), have long been used as a dispersant for carbon nanotubes. However surfactants such as SDS are not thermally stable for many procedures, including large scale melt-blend processing. As far as aqueous dispersions of CNTs are concerned, long-chain ionic liquids (ILs) can be good alternatives to traditional surfactants. Fukushima first described the efficacy of such materials with imidazole-based IL systems. [100] Surfactant-like long-chain ILs such as 1-alkyl-3-methylimidazolium bromides, butyl-a,b-bis(dodecylimidazolium bromide), car-

bazole tailed ILs (1-n-(N-carbazole)alkyl]-3-methylimidazolium bromide) and imidazolium ion-based ILs with hexadecyl alkyl chains have been found to be quite effective in dispersing CNTs in water.

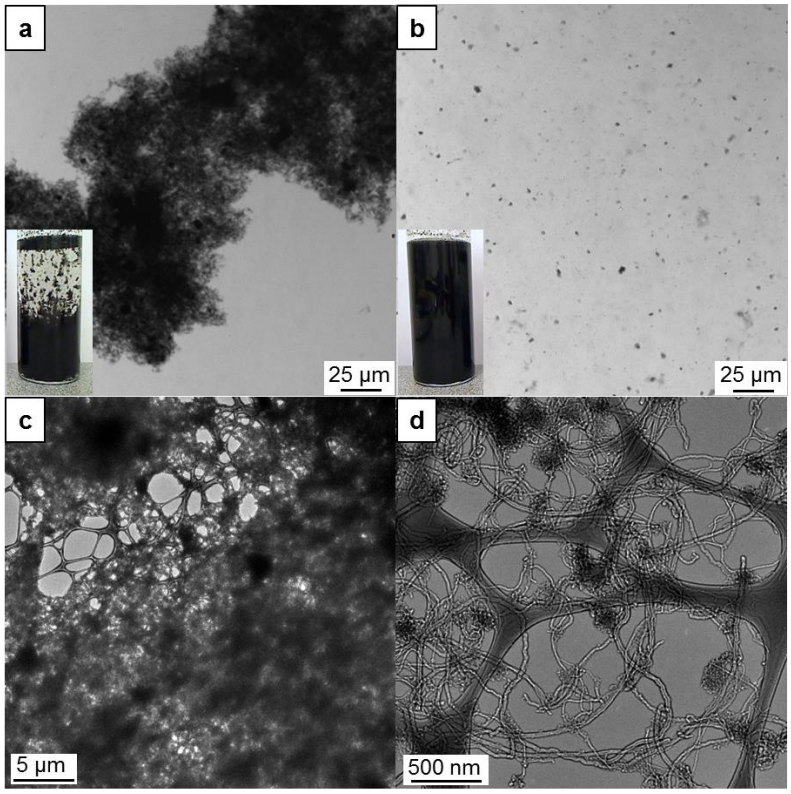

Figure B2. MWCNTs dispersed in water without (a and c) and with (b and d) the PPy-Br stabilizer. a and b: macroscopic stability 8 hr after dispersion (insets left) and corresponding confocal images with 25 µm scale bars, c and d: TEM images of the CNT dispersions with 5 µm and 500 nm scale bars, respectively.

It is also worth mentioning here, that although majority of work utilizes these types of ILs, other combinations are also possible as proposed in literature and several types of long- and short-chain ILs have been investigated to disperse CNTs in aqueous solvents. [342] However, when using short-chain ILs, the stability of the CNT dispersions is not

very long. In the present work, the unique synthesized pyrrole-based PILs were utilized as stabilizers of multi-walled carbon nanotubes (MWCNTs) in order to achieve enhanced emulsion stability, take advantage of the increased thermal and electrical properties of the pyrrole backbone and the tuning of the hydrophobicity by selection of the PIL anion to disperse the CNTs in varying solvents.

Figure B2 compares the stability and resulting microscopic morphology of CNT dispersions in water with and without the hydrophilic PIL, PPy-Br, as the stabilizer. The macroscopic images of the dispersions in Figure B2a and b (left inset) demonstrate the efficacy of the PIL as a dispersant, with these images taken 15 min after ultrasonication. It can be clearly seen that the CNT dispersion with no stabilizer has fully destabilized, while the PPy-Br successfully stabilizes the CNTs to create a homogenous black solution. All of the samples prepared here have dispersion stability greater than 6 months. The confocal and TEM images confirm the micro- and nano-stability, respectively, with large aggregates seen for CNT-in-water without a dispersant for both the micro- and nano-regime. For the dispersion with PPy-Br, no large aggregates can be seen in the confocal images and the resulting TEM images clearly show individual nanotubes, which have been spaced away from each other by the PIL. No large aggregates where seen with TEM for the dispersion with PPy-Br.

Like traditional surfactants, the PIL-based stabilizers adsorb on the CNT surface via their hydrophobic polypyrrole backbone and long alkyl chain orienting the cationic imidazolium groups with the corresponding hydrophilic Bromide anion toward the aqueous phase. The positive charges created on the CNTs prevent them from aggregating and give them extended stability due to the enhanced zeta potential caused by their charged

nature. The high stability is additionally ascribed to longer chains of the polymerized ionic liquid, which can easily wrap around the nanotubes, as illustrated in Figure B3a. This property of the polymerized ionic liquid is different from other non-covalent methods, in that the molecular weight of the PILs is much higher than a simple surfactant or monomeric IL, which generally lead to lower dispersion stability of CNTs in water or organic solvents. This hypothesis is supported by the fact that the dispersing ability of the surfactants generally increases with the increasing length of the alkyl chain, which is reflected by an increased absorbance on the UV–NIR spectrum. [347] For simple ionic liquids, the effect of different groups at the 3-position of the imidazole ring with a hexadecyl alkyl chain has been investigated in terms of CNT dispersing ability. [348] Through a systematic study, it was found that hydrophobic groups (e.g., phenyl group) increased the affinity of the surfactant towards the CNTs, but too hydrophobic of a group decreased the water solubility of the surfactant, thus favoring micelle self-assembly. Results of this study demonstrated that 1-hexadecyl- 3-phenylimidazolium bromide was the most efficient among the investigated surfactants. [348] Hence, a good balance between the hydrophilic and hydrophobic domains is needed to obtain an effective CNT stabilizer, which is easily obtained by the tunability of the PIL-ICP stabilizers in this work. Liu and co-workers showed that IL-based Gemini (dimeric) surfactants, which consist of two imidazole ring head groups and two hydrophobic chains separated with a spacer, were more effective in dispersing CNTs than the IL-based monomeric surfactants. The long alkyl chain ILs formed aqueous dispersions of CNTs, which remained stable for months. Zhou and co-workers investigated the dispersion of CNTs using very small amounts of short-chain ILs in water and found that ILs bearing both an amino group and imidazolium or pyridinium

core are very effective in dispersing CNTs in water. [349] A very small quantity of IL, as little as 1.4 wt%, was sufficient to achieve this. In our work, a 1:1 mass ratio of PIL stabilizer to CNT was used for the dispersions, which is much less than dispersions utilizing conventional surfactants. [350]

Table B1. PIL-ICP polarity importance in dispersing MWCNT in various solvents (stable dispersion denotes a greater than 6 month stability).

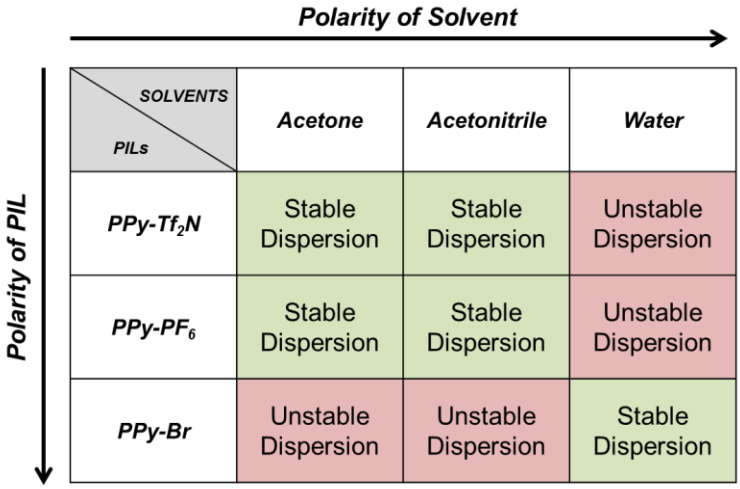

Modifying the polarity/hydrophobicity of the overall PIL by simple anion exchange is one of the major advantages of their use as a stabilizer, with Table 1 demonstrating the dispersion capability of the three synthesized PILs for CNTs in varying solvents, forming stable solutions for longer than 6 months. PPy-Br can easily form stable dispersions of CNTs in water, but was unable to form stable dispersions in acetone or acetonitrile due to the hydrophilic/polar nature of the PIL, a direct result of the Br anion. In contrast, PPy-PF_6 and PPy-Tf_2N were able to form stable dispersions in acetone and acetonitrile, but not water, due to their non-polar hydrophobic nature, with Tf_2N being a more hydrophobic anion that PF_6. [351]

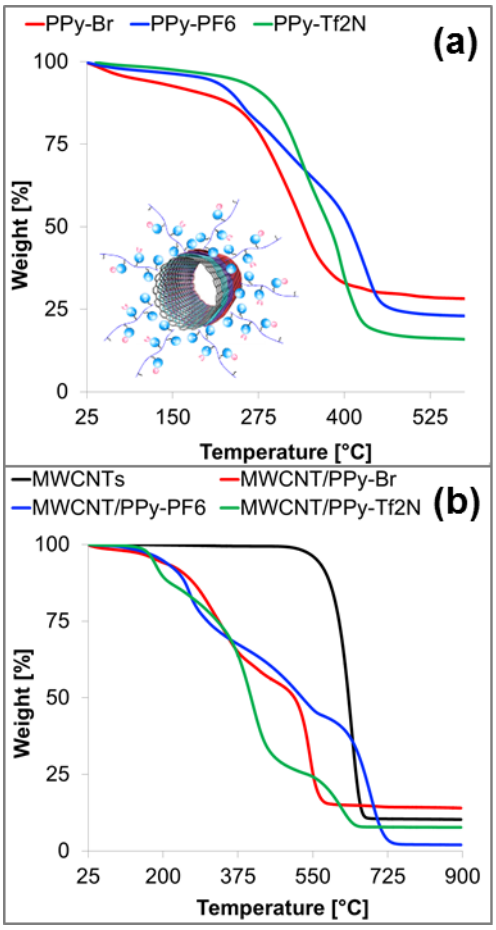

Figure B3. (a) TGA scans showing the comparative degradation of the synthesized PIL-ICP hybrid powders. (b) TGA scans showing the comparative degradation of the respective dried PIL-CNT dispersions with the pristine MWCNTs, showing the interaction between the two materials with the inset schematic showing the proposed interaction between the PIL-ICP hybrid stabilizers and the surface of a MWCNT.

Thermogravimetric analysis (TGA) can been used to probe the interaction between the PIL stabilizer and the CNTs. Figure B3a shows the TGA scans for the neat PIL stabilizers in air, with PPy-Br possessing the least stability, with PPy-Tf_2N possessing the most stability before the decomposition step around 345 ºC, where the trend switches and PPy-PF_6 is the most stable. These differences in stability are directly related to the differ-

ences in the stability of the anion, with the hydrophobic PF_6 and Tf_2N stabilizing the PPy backbone, until there is a drastic degradation of the many function groups in the Tf_2N anion, with the PF_6 anion remaining the most stable to thermal loss. As seen from literature, the quantity of the grafted PIL moiety can be determined from TGA. From Figure B3b, the decomposition temperature of the pristine MWCNT under an air atmosphere near 640 °C. For the CNTs associated with the PIL stabilizers, there are multiple degradation steps, which are associated with the PIL-CNT interactions, as seen in Figure B3c. Interestingly, the CNT decomposition is also determined by the PIL counterion. The stability of PF_6 ion was found to higher than the TF_2N and Br ions, reflecting the stability of the pure powders in Figure B3.

3.3. Oil in water emulsion stabilized by PIL-MWCNT

The poly-ionic liquids synthesized in the previous section demonstrated superior ability of carbon-nanotube stabilization. Along with a conductive backbone the present method of CNT stabilization offers the unique capability of dispersing and stabilizing the CNT for extended period of time.in various conditions; both aqueous and organic. The latter ability of utilizing versatile dispersion solvent is credited to possibility of facile exchange of anions. The replacement of ions has a strong influence on the hydrophilic/hydrophobic character of the PILs. In the present section we explore the idea of utilizing such dispersions as template for stabilizing two immiscible phases, e.g. water and hexane. The present approach of utilizing nanotubes as the stabilizing agent could be bracketed under novel Pickering emulsions technique.

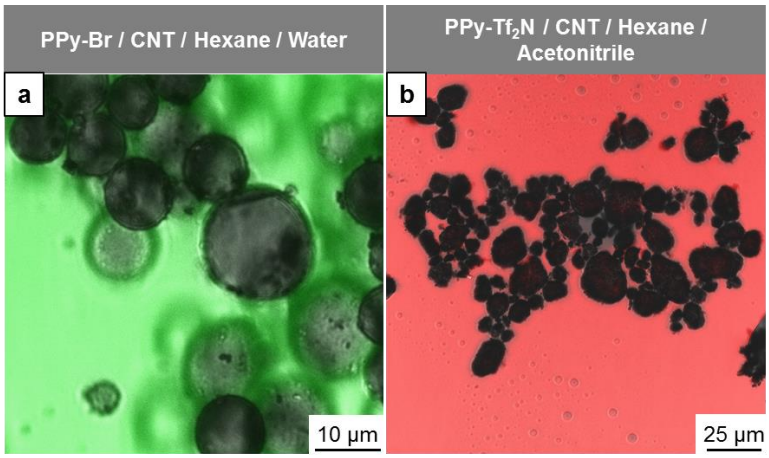

Figure B4. Confocal images of the Pickering emulsions showing the CNT-stabilized droplets. (a) PPy-Br / CNT / water (green color showing fluorescein dye), (b) PPy-Tf_2N / CNT / acetonitrile (pink color showing Rhodamine B dye).

The confocal microscope images in Figure B4 clearly depicting the ability of the nanotube dispersions for formation of emulsion with regular droplet size in two immiscible phase combinations; water-hexane and acetonitrile-hexane. On homogenizing the CNT laden water or acetonitrile phase with hexane, an immiscible solvent, there is quick movement of CNT to the oil and water interface. The fluorescent dyes, green fluorescein for water and pink Rhodamine B for acetonitrile were used to identify the presence of these solvents as the continuous phase, with hexane as the droplet phase (with hexane solubilizing neither dye). Specifically, the aqueous/acetonitrile phase became very clear and transparent, demonstrating that the CNTs had completely transferred to the oil/water interface of the emulsions. Specifically, both the vials contained equal volumes of water and hexane with PIL and CNT in a 1:1 ratio. The emulsion phase accounted for ~40% volume fraction of the total liquid, and was present at the interface between the remaining fractions of the water/acetonitrile-hexane interface. The obtained emulsion was very sta-

ble during storage under ambient conditions, with the droplet size remaining mostly unchanged over 100 h. As gradual evaporation of the organic solvent, some of the CNTs transferred to the wall of the vial and the total volume of emulsion was reduced. Importantly, both these emulsions show good coverage and have considerable homogeneity in terms of droplet size.

To visualize the droplets better, the water was dyed with the hydrophilic compound, sodium fluorescein (Figure B4a). Similarly, in Figure B4b the continuous acetonitrile phase had Rhodamine b incorporated for the distinctive pink coloration. For the water/hexane emulsion, a dye solubility test was performed by tracing the color of the emulsion droplets and the continuous phase after adding the above mentioned green water-soluble dye), and observing that the color remained outside the droplets in the acetonitrile phase only, with no coloration appearing in the droplet phase. Importantly, apart from the visual appearances, the crucial CNT stabilizing molecule is different in both these experiments: PPy-Br (Figure B4a) and PPy-Tf_2N (Figure B4b). The studies clearly reveal that both these previous CNT dispersions are compatible enough for emulsion formation. Moreover, such studies acquire novelty in terms of ease of formation and stability (greater than 100 hours) in versatile media. Such diversity and tunability has not been achieved previously by other methods and thus possesses the possibility of expanding the utilization of these emulsion for diverse applications. Previously, certain pure ionic liquids have tried to demonstrate similar capability of being used as dispersant and replacing surfactant for formation of novel Pickering emulsions. However, these studies require addition of certain additives or particles; e.g. silicon to aid in stabilizing the immiscible phases and therefore cannot be classified as pure CNT stabilized emulsions. [352] Furthermore, stud-

ies were undertaken to probe the ability of the above synthesized PILs as dispersant by themselves, but showed limited ability to do so.

Among, the other studies in this field, Gao et al. utilized acid treated dispersions of CNT along with pure ionic liquid as a similar template for Pickering emulsion process. [353] They suggested that the ionic liquids can be used to stabilize two immiscible phases, water and cyclohexane with the aid of acid treated nanotubes. The hydrophobic ionic liquid, e.g. 1-butyl-3-methylimidazolium hexafluorophosphate, is useful in helping to tune the highly hydrophilic character of the acid treated nanotubes to mix the nanotubes with the oil phase which was cyclohexane in their case study. Although, such studies clearly indicate the efficacy of ionic liquids as good dispersant; the nanotubes still need prior treatment before their use as Pickering emulsion stabilizers. Therefore, the present use of poly(ionic) liquid could be considered superior to the method proposed by Gao and co-workers as it allows the option of utilizing various solvents. Moreover, the use of acid treatment for previous methodology is expected to decrease the aspect ratio of the CNT, a fact which has been verified before. [94] Also Figures A4a, A4b demonstrate that the PILs stabilized nanotubes are considerably more efficient than their ionic liquid alternative is able to form the emulsion droplets of considerable uniform size. Importantly, ratio of the CNT to poly(ionic-liquid) is 1:1 to form these emulsions droplets which considerably lesser than the surfactants required (> 5 times) for similar purposes. The microscopic image taken for the liquid droplets acquired from the emulsion phase shows that the average emulsion droplet sizes appear to be around 3-20 μm, tens of times smaller than those prepared by only MWNT.

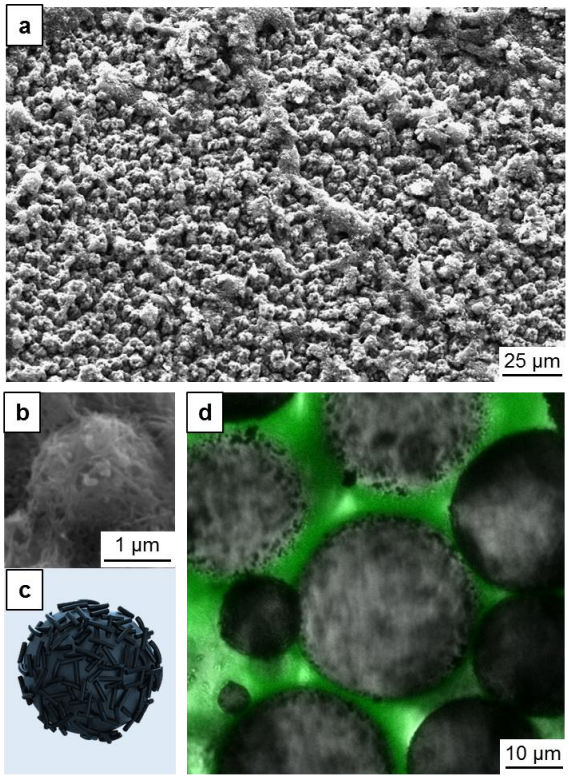

Figure B5. (a), (b) SEM images of the formed hollow particles from the PPy-Br / CNT / water Pickering emulsions. (c) Schematic showing the morphology of the CNT shell. (d): Confocal image depicting Si nanoparticle incorporation in the CNT stabilized hexane droplets.

3.4. Formation of Hollow Particle Shells

The formed emulsions in Figure B4 demonstrated that ability of using different PILs for formation of versatile emulsions with the help of nanotubes. The nanotubes are dispersed only at the interface due to the effect of PILs which are wrapped on the surface of the CNTs. Figure B5, elucidates a facile method of forming hollow particle using the same Pickering emulsion as discussed above. The method relies on the controlled evaporation of the water and hexane phase with the CNT particles clubbed carefully at the interface, as seen in the schematic in Figure B5c. Unlike the previous work of Panhuis et al.

which suggested the cross-linking of emulsion by glutaradehyde for formation of hollow CNT particles, the present method does not on involve chemical cross-linking. [354] Instead the self-assembly nature of the CNT allows the formation of homogenous droplets. To understand the morphology of the droplets, continuous phase was carefully dried with help of freeze-dried and then studied under the SEM, as seen in Figure B5a, b. The SEM studies reveal presence of good stability of the emulsion, as the droplet diameter was uniquely uniform in the experiment.

The hollow nature of such particles presents a unique possibility of incorporating functional particles. Silicon is a unique material, which is been presently studied for high charge retention in electrochemical application. However, such applications are challenged by the enormous expansion of silicon on account of charging. Here, the hollow particles formed before can is used for the encapsulation of silicon nanoparticles. Figure B6d is a confocal image of hollow emulsion droplets with average diameter of ~30 μm, with Silicon nanoparticles present in the droplet shells. By varying the z depth of the confocal image the hollow nature of the particles was clearly seen. The silicon nanoparticles were 50-70 nm in diameter and were mixed with the oil phase (hexane) initially. The oil phase was then mixed with aqueous PIL-stabilized CNT dispersion to create the emulsion as before. The confocal microscope image in Figure B6d shows the hybrid structure in the wet phase, and the silicon nanoparticles, seen as small black dots in the image, are in well distributed in the oil phase. The above reported method offers a simple emulsion-templated directed assembly technique for forming silicon-carbon composite particles, which could be further investigated for energy/electrochemical applications. Using this method, we were able to confine the Si nanoparticles to regions that are surrounded by a

porous carbon nanotube cage and an interconnected conductive carbon nanotube network.

4. Conclusion

Poly(ionic liquid)s (PILs) with an intrinsically conducting pyrrole polymer (ICP) backbone were synthesized and utilized as novel dispersants of carbon nanotubes (CNTs) in various polar and nonpolar solvents. This is due to their highly tunable nature, in which the anions can be easily exchanged to form PILs of varying polarity but with the same polycation. These CNT dispersions were exceedingly stable over many months, and with the addition of hexane, Pickering emulsions with the PIL-stabilized CNTs at the droplet interfaces were formed. Depending on the hydrophobicity of the PIL, hexane-in-water and hexane-in-acetonitrile emulsions were formed, the latter marking the first non-aqueous stabilized-CNT emulsions and corresponding CNT-in-acetonitrile dispersion, further advancing the processability of CNTs. The PIL-stabilized CNT Pickering emulsion droplets generated hollow conductive particles by subsequent drying of the emulsions. With the emulsion templating, the hollow shells can be used as a payload carrier, depending on the solubility of the payload in the droplet phase of the emulsion. This was demonstrated with silicon nanoparticles, which have limited solubility in aqueous environments, but great scientific interest due to their potential electrochemical applications. Overall, this work explored a new class of efficient PIL-ICP hybrid stabilizers with tunable hydrophobicity, offering extended stability of carbon nanotube dispersions with novel applications in hollow particle formation via Pickering emulsion templating and in placing payloads into the shells.

5. Acknowledgements

We gratefully acknowledge the financial support from the Air Force Office of Scientific Research, grant number FA9550-12-1-0331, and Program Manager Dr. David Stargel, the National Science Foundation Graduate Research Fellowship, the Fulton Undergraduate Research Initiative, and the ASU/NASA Space Grant. Also, we acknowledge the Center for Solid State Electronic Research at Arizona State University (ASU). Special thanks to Karl Weiss and staff of LeRoy Eyring Center for Solid State Science at ASU for their help with the SEM imaging, and to Jason Wickham, Ning Ma, Yessica Wirayawan, and Ryan Gunckel.

APPENDIX C

A COMBINED EXPERIMENTAL AND MOLECULAR DYNAMICS STUDY OF IODIDE-BASED IONIC LIQUID AND WATER MIXTURES

1. Introduction

Ionic liquids (ILs) are salts that remain liquid at or below 100 °C, and often at or below room temperature. They remain liquid at such unusually low temperatures due to bulky, asymmetric constituent ions which resist crystalline packing. [355, 356] As they are liquids made up entirely of ions, ILs have unusual properties that make them potentially useful for a variety of applications including polymerization, [357, 358] gas separation, [359] enzymatic reactions, [360] and batteries. [361] One useful aspect of ILs is their tunability—because each ionic liquid consists of a cation and an anion, cations and anions can be mixed and matched to obtain desired properties. [362] The properties of ILs can be further tuned by mixing them with other liquids such as water.

Water/IL mixtures have been explored for use in bio-engineering applications such as dissolving biopolymers, [363] destructuring starch, [364] and pretreating biomass for use in fuels. [365] These mixtures have also found important use in electrical applications, serving as electrolytes for dye-sensitized solar cells [366] and the electrodeposition of zinc films. [367] Adding water to ionic liquids is particularly useful in electrical applications because ionic liquids, while they can function as charge carriers, are highly viscous. This high viscosity limits the diffusion of charge carriers, thus limiting conductivity. Adding a low-viscosity solvent like water, therefore, has been found to greatly improve electrical performance. [368] The most common electrochemical application utilizing iodide ionic liquids, dye-sensitized solar cells, work most effectively with a low water content (about 10% by mole). [366] However, the triiodide/iodide redox couple has been used in other electrochemical devices, many of which do not have the same limits as regards to water content as cells containing dyes. [369, 370] Some of

these applications, such as molecular electric transducer (MET) based sensors [371] currently use water-based electrolytes, but their usefulness could be limited by the working temperature range of water. Furthermore, water can act as a hydrogen bond donor with halide salts such as ILs to greatly lower the mixture transition temperature, [372] potentially creating mixtures with an unusually wide operating temperature. Hopefully, the study of iodide IL/water mixtures will pave the way for the use of ILs in a wider variety of electrochemical devices.

This paper examines mixtures of water with 1-butyl-3-methylimidazolium iodide ([BMIM][I]). While pure alkyl-imidazolium iodide ILs have been widely employed as iodide sources in electrolytes for dye-sensitized solar cells, [373] their usefulness is limited by their particularly high viscosity. Thus, we set out to overcome this limitation by adding water to lower the viscosity of [BMIM][I]. The properties of such mixtures have not been systematically studied or even reported. Here, we combine an experimental study with molecular dynamics (MD) simulations to explore the properties of [BMIM][I]/water mixtures.

In the experimental study, density, melting point, viscosity, and ionic conductivity were reported for a range of concentrations of water in the IL. Trends in these properties were identified. The density measurements were used to tune an all-atom molecular dynamics model describing [BMIM][I], which was then used in MD simulations of the same [BMIM][I]/water mixtures. Similar simulations have been used to study mixtures of other ILs with water [374-377] and allow description of the molecular structure and fundamental physics of these mixtures. In this study, the results of MD simulations were directly compared to the experimentally measured properties, relating molecular-level

physics and structure to the macroscopic behavior of the mixtures. This study does not only provide a greater theoretical standing of ionic liquids and their mixtures—it also allows researchers to tune mixtures for desired properties such as conductivity and viscosity. We also hope that researchers might consider the usefulness of iodide-containing ionic liquids and their mixtures for a wider variety of applications in the future.

2. Materials and Methodology

2.1 Experimental Section

2.1.1. Materials and Mixing

The ionic liquid 1-butyl-3-methylimidazolium iodide ([BMIM][I]) was purchased from Ionic Liquids Technologies Inc. and the water was HPLC grade from Fisher Scientific. Both were used as received, without further purification. The ionic liquid/water mixtures were prepared by ultrasonic agitation for 1 minute with a Sonics VibraCell 500W in an ice water bath at an amplitude of 21%. The mixtures were observed to be homogenous and fully miscible by visual inspection.

2.1.2. Density

Density values were obtained by using a 2 mL specific gravity bottle at room temperature, following calibration of the bottle with pure HPLC water.

2.1.3. Melting Point

The melting points of the mixtures were measured using a TA Instruments Q20 differential scanning calorimeter (DSC). A cooling scan was performed from 20 to -90 °C at a rate of 2 °C min^{-1}, and themelting point was determined with the TA Universal

Analysis software at the large spike in the heat flow signifying the heat of fusion. Tzero pans with lids were used to contain all samples, with air used as the reference.

2.1.4. Viscosity

A TA Instruments AR-G2 rheometer equipped with a 60 mm, 1° cone was used to measure the viscosity via a flow procedure, with the temperature kept at 25°C via a water cooled/heated Peltier plate. A strain rate sweep was performed from 0.1 to 100 s^{-1}. The IL/water mixtures were generally Newtonian fluids with a constant viscosity across sheer rates, and so the viscosity at a sheer rate of 1 s^{-1} was taken to be the viscosity of each mixture.

2.1.5. Conductivity

Conductivity measurements were determined via Oakton PC 700 pH/mV/Conductivity benchtop meter. The instrument conductivity ranges from 0 to 200.00 mS. The instrument has a full scale resolution of 0.5% and an accuracy of ±1%. Throughout the experiment, the sample was placed in a constant temperature water bath kept at 300.0 ± 0.5 K. Each measurement was repeated three times and the average values were evaluated. In addition, prior to each measurement, the instrument was calibrated with corresponding KCl conductivity standard solutions.

2.2 Computational Section

Simulations were performed using the GROMACS 4.6 package. [273, 275, 378] Simulation systems were designed to mirror the same [BMIM][I]/water mixture proportions studied in the experimental section. The total number of molecules in each system was chosen to give a simulation box of approximately 5x5x5 nm. The number of

[BMIM][I] pairs and water molecules in each system is shown in Table C1. In each system, molecules were placed in a simulation box randomly and then allowed to equilibrate for 1 ns.

Table C1. Compositions of simulation systems.

		mole % water					
	pure [BMIM][I]	**10%**	**20%**	**30%**	**50%**	**70%**	**90%**
[BMIM][I] (# ion pairs)	450	450	440	420	400	360	300
Water (# molecules)	0	50	110	180	400	840	2700

Water was described with the extended simple point charge (SPC/E) model. [280] The BMIM molecule was described by the all-atom force field developed by Lopes, et al. [277] and refined by Bhargava and Balasubramanian. [279, 379] In keeping with this force field, h-bonds within the BMIM molecule were constrained by the LINCS algorithm. [380, 381] The Leonard-Jones parameters for iodide were taken from the optimized intermolecular potentials for liquid simulations (OPLS) force field. [276] For both BMIM and iodide, we scaled the partial atomic charges to give total molecular charges of ±0.5. The technique of scaling charges in this manner has been extensively used to capture the effect of charge transfer between cation and anion in ionic liquids when using a non-polarizable force field. [279, 382-386] Models with scaled charges have been found to simulate density and diffusivity of ionic liquids better than models using charges of ±1. [279, 387, 388] In this case, the charges were scaled to fit the simulated densities of [BMIM][I]/water mixtures to the densities measured by experiment. With molecular

charges of ±0.5, densities of each simulation were within 1.6% of the experimental density (as seen in Table C2 in the results section below).

After the initial boxes were generated, 1,000 energy minimization steps were performed using the steepest descent method. Initial atomic velocities were generated with a Maxwellian distribution at an absolute temperature of 300K. Newton's equation of motion was integrated using the leap-frog algorithm with a time step of 0.002 ps. All simulations were carried out under the NPT ensemble using the Berendsen-thermostat [389] to maintain temperature at 300K and the Parinello-Rahman barostat [390] to maintain pressure at 1 bar. The Particle-Mesh Ewald (PME) method was used to account for long-range electrostatic interactions. The cut off distance for Lennard-Jones forces was chosen as r = 1.2 nm to match the cut-off used by the developers of the BMIM forcefield. [277, 279] After the simulation, densities, radial distribution functions, and diffusion coefficients were calculated using GROMACS analysis tools and the simulation systems were visualized using visual molecular dynamics (VMD). [391]

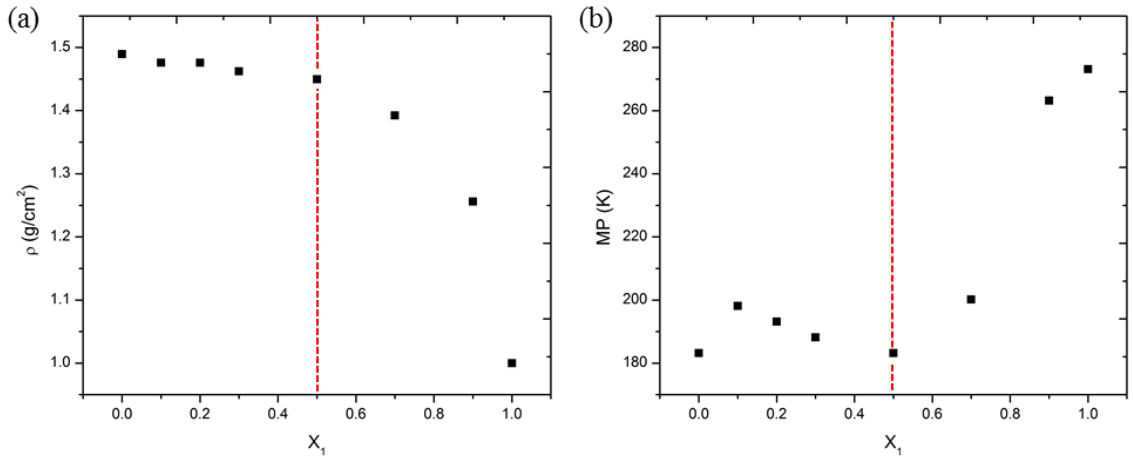

Figure C1. a) Density and b) melting point of binary water/[BMIM][I] mixtures by mole fraction water (X_1). The vertical line at X_1=0.5 for each chart is provided for guidance.

3. Results and Discussion

3.1. Densities and Melting Points of [BMIM][I]/Water Mixtures

Density and melting point were measured as each of these properties is related to the internal structure and molecular interactions of ionic liquids and their mixtures. The values of each for [BMIM][I]/water mixtures containing various percentages of water are shown in Figure C1.

The density of the mixture decreases only slightly (staying almost steady) between 0 and 50% water. From 50 to 100% water, density decreases exponentially with increasing water. The trend in melting points is similar, with one major difference—between 10 and 50% water, adding more water actually *decreases* the melting point, the opposite trend from that which might be expected given the relatively high melting point of water. As more water is added past 50% the melting point increases rapidly.

From these results, it is clear that there are two distinct regions within the range of [BMIM][I]/water mixtures—one encompassing all mixtures up to 50% water by mole, and one encompassing all mixtures from 50% to pure water. Both properties shown above—density and melting point—are related to molecular-level ordering within the liquid. Density depends on the packing-together of molecules, while ionic liquids have unusually low melting points because their bulky structures prevent the formation of crystal structures. Therefore, it is likely that the two regions of IL/water mixtures (above and below 50% water) have different structures on the molecular scale. To explore this phenomenon, we employed molecular dynamics simulations performed in parallel to the experimental measurements.

Table C2. Simulated vs. experimental mixture density at 300K.

	Density		
X_1 (mole fraction water)	**Simulation (g/cm^3)**	**Experiment (g/cm^3)**	**% Difference**
0	1.465	1.489	-1.6%
0.1	1.462	1.476	-0.9%
0.2	1.459	1.476	-1.1%
0.3	1.454	1.462	-0.6%
0.5	1.437	1.450	-0.8%
0.7	1.398	1.392	0.4%
0.9	1.259	1.259	0.3%

The densities calculated from MD simulations of the [BMIM][I]/water mixtures were compared to experimental densities, as seen in Table C2. The difference between the simulated and experimental densities ranges from -1.6% to 0.3%, indicating that the model is adequate to describe the interaction between water and [BMIM][I] molecules.

Figure C2 shows representative snapshots of the simulation system for each of the mixtures. From viewing the system visually, it is possible to make qualitative judgments about the molecular ordering within the mixtures. At low water concentrations, individual water molecules are suspended within [BMIM][I]. Each water molecule is paired with at least one iodide atom, and most have attracted two. At 50% water, the water molecules are beginning to form chains of water-iodide-water. After this point, the overall structure changes drastically with additional water. By 70% water, chains of water reach across the simulation box, and not every water molecule is matched by an iodide atom, though nearly every iodide is attached to a water chain. At 90% water, the system resembles water

with [BMIM][I] dissolved in it more than it does [BMIM][I] with chains of water snaking through.

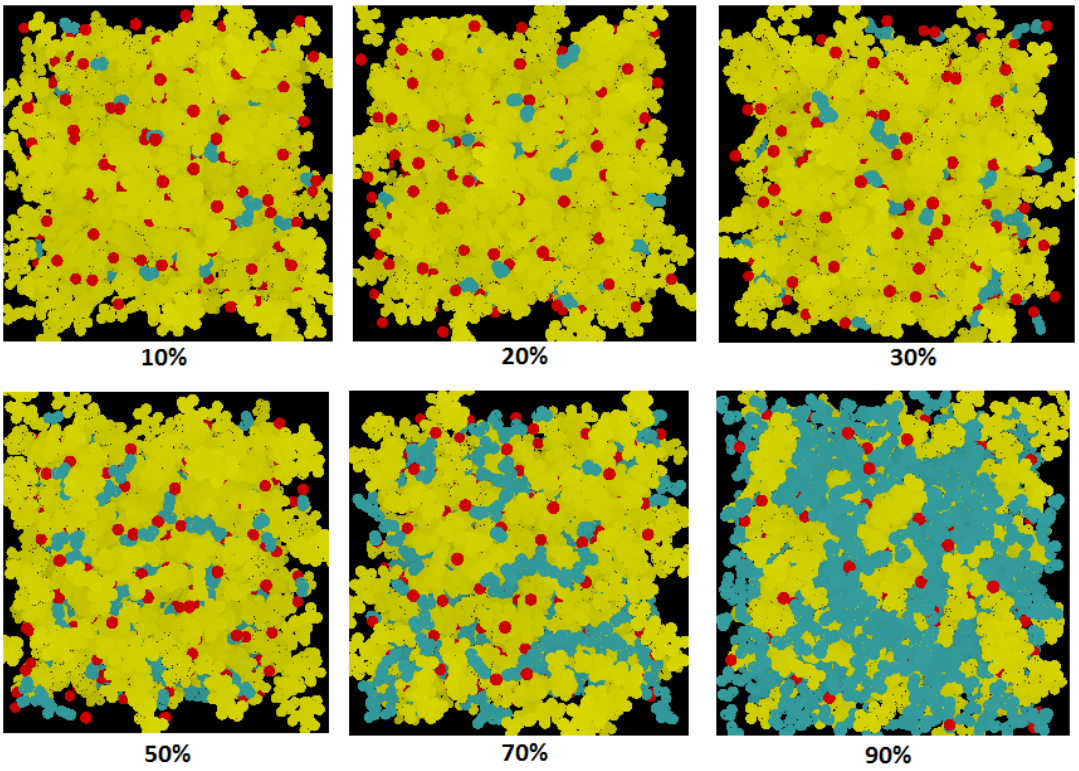

Figure C2. Representative snapshots of MD simulation boxes for mole percentages of water ranging from 10-90%. Each dot is an atom, with yellow representing [BMIM], red [I], and blue water.

These observations offer reasonable insights into the experimental trends illustrated in Figure C1. There are two distinct regions comprising mixtures with less and more than 50% water. At 50% water, the water molecules begin to aggregate, forming chains and then aggregated masses, drastically changing the molecular structure and therefore the macroscopic properties of the mixture as water increases.

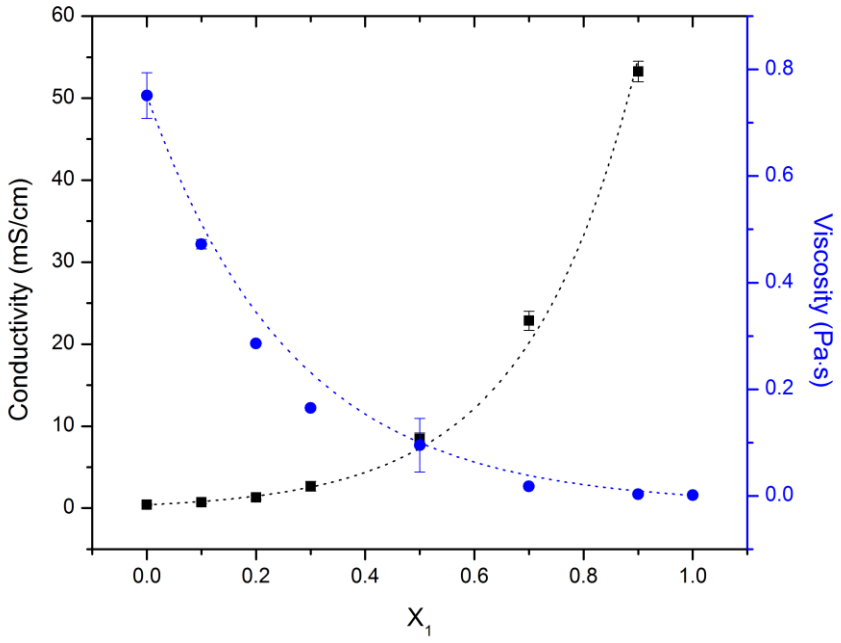

Figure C3. A comparison of the conductivity (in black) and average viscosity (in blue) of binary water/[BMIM][I] mixtures by mole fraction water (x_1).

3.2. Viscosities and Conductivities of [BMIM][I]/Water Mixtures

Viscosity and ionic conductivity were measured as both properties are highly relevant to potential electrochemical applications of [BMIM][I]/water mixtures. These properties are shown in Figure C3.

Viscosity and conductivity are generally related, as high viscosity impedes the movement of ions. Figure C3 confirms this relationship, showing that conductivity increases exponentially as viscosity decreases with a similar trend.

As hydrogen bonding is one of the most significant factors effecting the viscosity of ionic liquids [392], it is not surprising that water content strongly effects viscosity: as water is added to [BMIM][I], the viscosity drops sharply. However, this effect seems to

be more powerful for [BMIM][I]/water mixtures than for aqueous mixtures of other imidazolium ionic liquids.

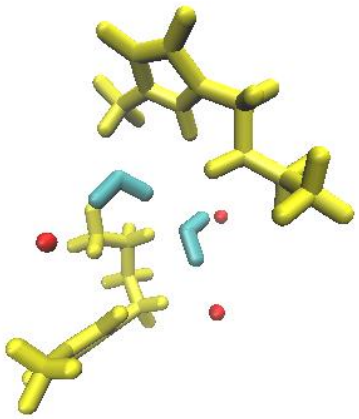

Figure C4. BMIM (yellow), iodide (red), and water (blue) from simulation, showing hydrogen bonds.

For example, neither [BMIM][SCN], [393][EMIM][$EtSO_4$], [EMIM][OTf], nor [EMIM][TFA] [394] show such a steep drop in viscosity at compositions below 50% water. The viscosities of all of these ionic liquids decrease with added water, but more slowly. From this observation, it can be assumed that the interaction between iodide and water accounts for the dramatic drop in viscosity with increasing water content and is important to the behavior of these mixtures. The MD simulations bear out this assumption. Figure C4 shows a representative picture of the arrangement of BMIM, iodide, and water from the simulation, making it clear that iodide forms hydrogen bonds with the water. The pattern shown here reoccurs throughout the simulation, with water and iodide effectively forming chains of hydrogen-bonded molecules.

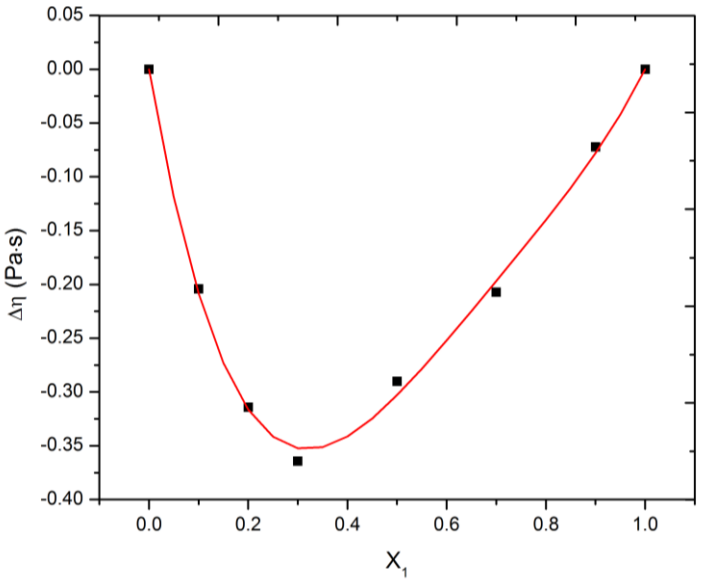

Figure C5. Viscosity deviation vs. mole fraction water (x1). The line is a Redlich-Kister polynomial [392] fit to the data by least-squares regression. Redlich-Kister polynomials describe excess molar quantities such as excess molar volume and viscosity deviation. It is the form $Q_{ij} = x_i x_j \sum_{k=0}^{m} B_k (x_i - x_j)^k$ where i and j are any two components, B_k are parameters fit by regression, and m is the degree of the polynomial expansion. In this case a third order polynomial was used.

The intermolecular interactions within the mixtures are further illustrated by the viscosity deviation—a measure of how the mixture viscosity differs from the viscosity of an ideal mixture. Viscosity deviation is calculated by the equation [395]

$$\Delta\eta = \eta - x_1\eta_1 - x_2\eta_2 \qquad \text{(C1)}$$

where η is the mixture viscosity as measured by experiment, x_n is mole fraction, η_n is the viscosity of the pure components, and n = 1 for water and 2 for [BMIM][I]. It is shown in Figure C5.

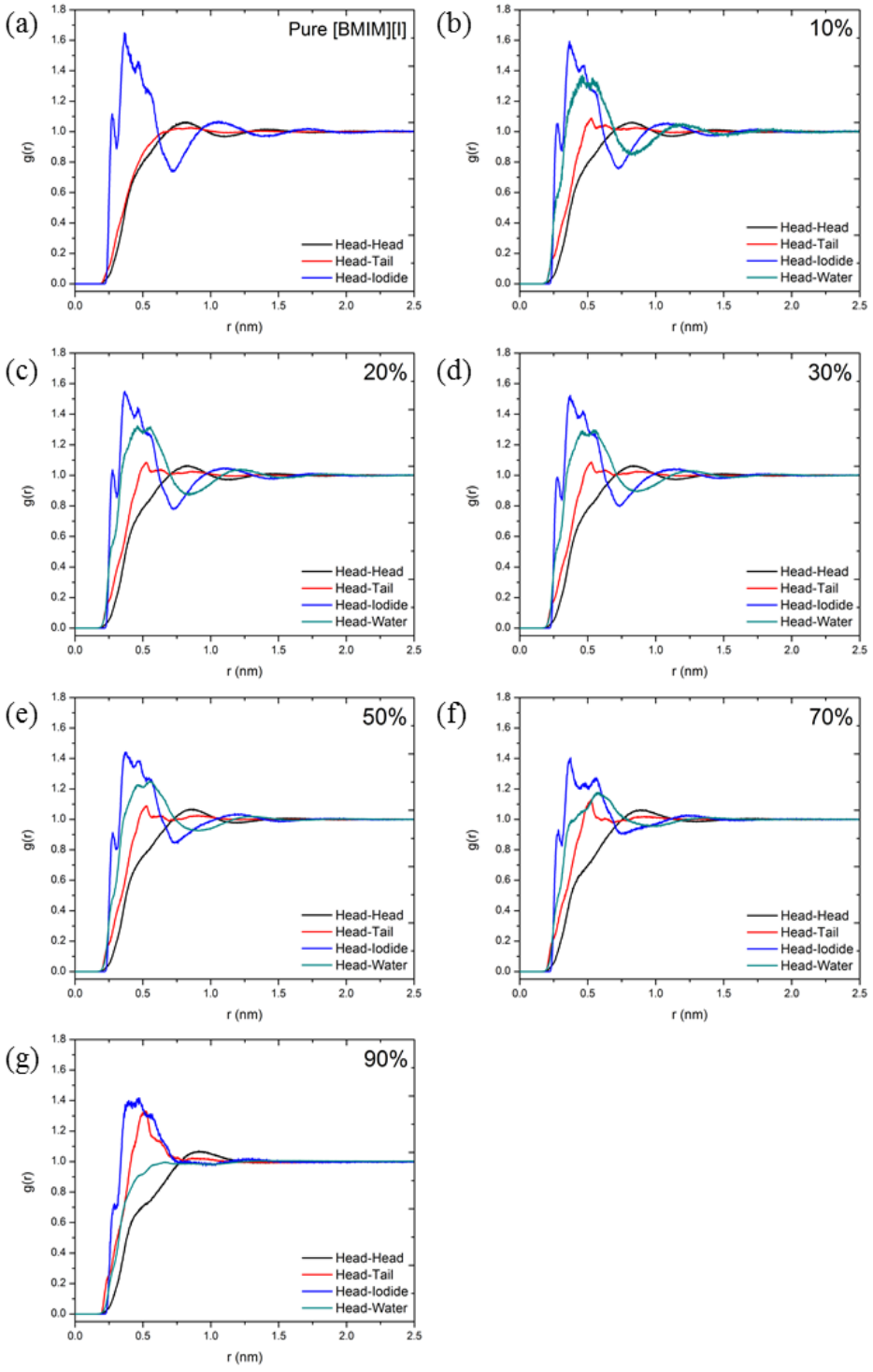

Figure C6. Radial distribution functions around the cation head. "Head" refers to the imidazolium ring within BMIM while "tail" refers to the butyl chain.

In an ideal mixture, each component behaves as if it were in a pure liquid, so the viscosity deviation represents the interaction of the components in so far as those interactions affect viscosity. In this case, the viscosity deviation is negative for all mole fractions of water—the interactions between water and [BMIM][I] reduce viscosity. This is similar to other ionic liquid/water mixtures. [393, 394, 396] However, the magnitude of the deviation is much greater than that of these other mixtures, indicating that the interactions between [BMIM][I] and water are unusually strong. This reinforces the observation made above that small amounts of water decrease the viscosity of [BMIM][I] more than similar ionic liquids with different anions, and so the iodide anion likely interacts more strongly with water than other anions. As can be seen in Figure C5, the viscosity deviation curve is also skewed toward the left with a minimum at about 30% water. This means that a small amount of water effects the viscosity of [BMIM][I] more than a small amount of [BMIM][I] effects the viscosity of water.

3.3. Radial Distribution Functions and Self-Diffusion Coefficients for [BMIM][I]/Water Mixtures

To give a more quantitative picture of the structure of these mixtures, radial distribution functions (rdfs) were calculated from the MD simulations. Figure C6 shows rdfs centered around the imidazolium ring within BMIM. (Each cation molecule consists of a hydrophilic imidazolium ring, the "head," and a hydrophobic hydrocarbon chain, the "tail.")

Adding any water at all changes the molecular ordering of [BMIM][I]. Even 10% water pushes the BMIM tail closer to the head. The water inserts itself into the ordered structure

of the ionic liquid as it is pulled close to iodide through hydrogen bonds. The pattern is similar for all rdfs up to 50% water, when this ordering begins to break down. Between 50 and 90% water, the ordered spacing of iodide anions around the cation head becomes less distinct until the rdf shows one broad, messy peak rather than several sharp ones. The water no longer has a small peak on either side of the iodide peak. By 90% water, the water is not inserted into the [BMIM][I] structure at all, and there is no apparent ordering of water around the cation head.

These rdfs provide further evidence of two distinct behavior regimes below and above 50% water. They may also show why the viscosity deviation plot in Figure C5 is skewed to the left—even a small amount of water inserts itself into the ordering of [BMIM][I], disrupting the intermolecular interactions that account for the IL's unusually high viscosity. Since iodide-water hydrogen bonding has been shown to important for the behavior of these mixtures, rdfs were also calculated for iodide and water surrounding the iodide anion. These are shown in Figure C7. Water arranges itself around iodide in two peaks which probably represent two hydrogen atoms drawn to the iodide by hydrogen bonds. The magnitude of these peaks decrease as the water content increases. This is because, in low water content mixtures, every single water molecule is drawn close to an iodide atom. As more water is added, some of the water molecules are close to other water molecules instead. Since the rdf is normalized against the all the water in the system, the size of the peaks around iodide decrease. More interesting is the radial distribution function of iodide around itself. At low concentrations of water, there is a broad peak indicating that iodide molecules tend to stay at a similar distance from each other, but only somewhat. As more water is added, another peak appears closer to the center iodide as

the water molecules draw the iodide atoms closer together than they would otherwise arrange themselves. This peak becomes distinct at 50% water (the divide between the two composition regions identified above) and only becomes more so as the water concentration rises to 90% and every single iodide is hydrogen-bonded to water (the reverse of what happens at low water concentrations).

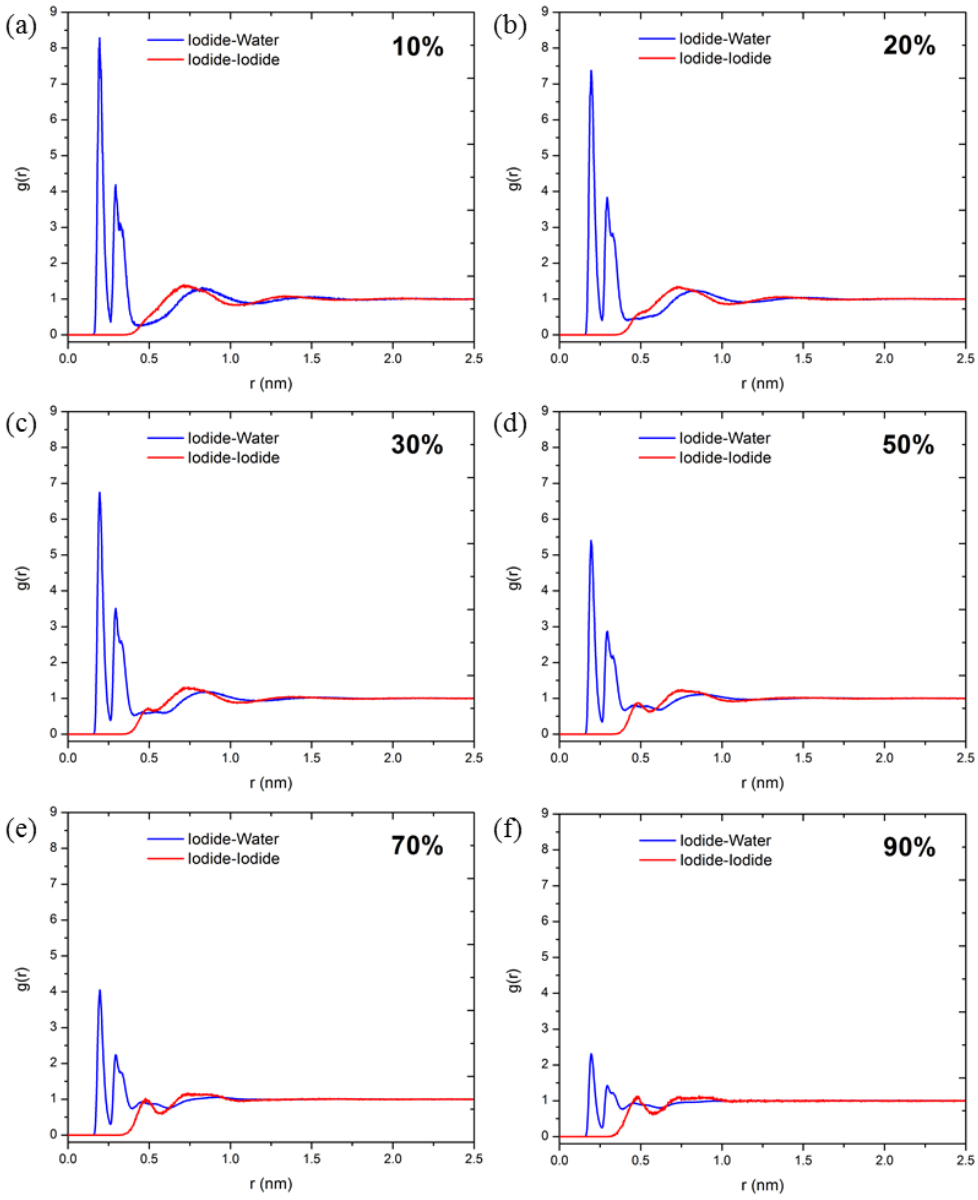

Figure C7. Radial distribution functions of iodide and water around the iodide anion.

Finally, in order to examine the dynamics of the MD simulation systems, self-diffusion coefficients were calculated for the cation, anion, and water. These are shown in Figure C8. In the 0-50% water region, increased water concentration decreases the mobility of all species (though the diffusion coefficient of BMIM does rise slightly at $X_1 = 0.2$). Like the melting points shown in Figure C1, this is the opposite of the expected trend. At higher water concentrations, the diffusion coefficient for BMIM dips even lower before rising to a value slightly below that for pure [BMIM][I]. The diffusion coefficients for water and iodide, on the other hand, rise as water aggregates into a bulk phase, allowing for high mobility. At 90% water, iodide anions move much more freely than the cations they are paired with as they are pulled along by their strong attraction to water. This complements the experimental measurement of ionic conductivity, which found that increasing amounts of water dramatically increased conductivity, particular at concentrations greater than 50%.

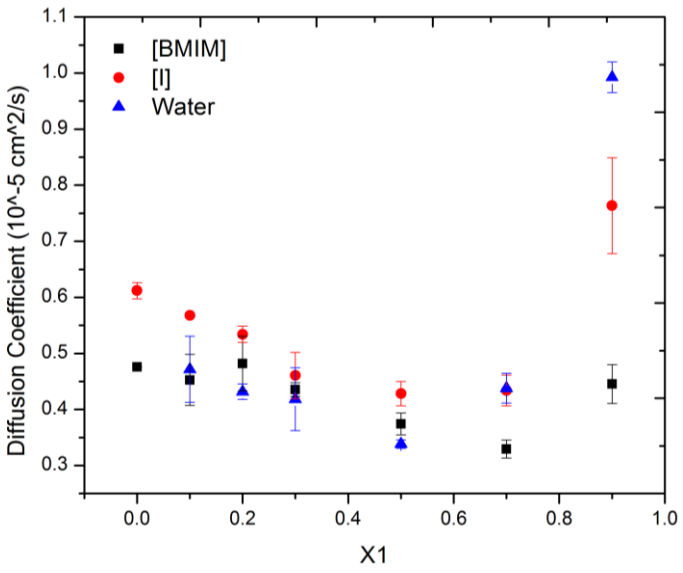

Figure C8. Self-diffusion coefficients versus mole fraction water (X_1).

4. Conclusions

Density, melting point, viscosity, and ionic conductivity were measured for [BMIM][I]/water mixtures with various concentrations of water. Density was found to change little at water concentrations below 50 mole%, but drop dramatically with additional water at concentrations above 50%. Melting point was found to increase with the addition of any water (compared to pure [BMIM][I]) but to decrease slightly with more water up to 50%, after which it increases rapidly. Viscosity was found to decrease exponentially with added water, while conductivity (a related property) was found to increase exponentially. Viscosity deviation was calculated and found to be negative and to skew toward lower water compositions. This indicates that the interactions between [BMIM][I] and water were disproportionately strong at small water concentrations.

Molecular dynamics simulations showed ordering within the IL/water mixtures. At low concentrations, water molecules were found to insert themselves into the ordered cation/anion structure. However, at 50 mol% water this complicated ordering began to break down until, at high concentrations of water, the mixtures resemble water with regions of [BMIM][I] dissolved within. This distinction—between low and high water concentration regions—may explain the observed trends in density and melting point of these mixtures. Hydrogen bonding between water and iodide were found to be strong and important for understanding mixture behavior, particularly the dramatic increase in conductivity at higher water concentrations.

This paper is the first systematic study of [BMIM][I]/water mixtures, either experimentally or through simulations. It begins the work of understanding these mixtures so that they may be better tuned for future applications.

5. Acknowledgements

We are grateful for financial support provided by the National Aeronautics and Space Administration (NASA) through the award NASA-PICASSO-NNX14AI41G. We are also grateful for financial support through Fulton Undergraduate Research Initiatives (FURI) provided by Arizona State University. Furthermore, we also would like to acknowledge the contributions of Benjamin Shindel.

APPENDIX D

COLLOIDAL LATTICES OF ENVIRONMENTALLY RESPONSIVE MICROGEL PARTICLES AT IONIC LIQUID-WATER INTERFACES

1. Introduction

In recent years, ionic liquids (ILs) have drawn significant amount of attention as tunable "green solvents" used in the interdisciplinary fields of biotechnology and chemistry due to their high thermal stability, [255, 397, 398] non-flammability, [399-401] extensive electrochemical window [402, 403] and negligible vapor pressure properties. [404-406] They are currently utilized in a vast array of applications including catalysis, [407, 408] CO_2 absorption, [264, 409, 410] gas storage, [411, 412] and as promising solvents for selective extraction processes. [413-415] While recent work has established the versatility of ILs as novel extraction media, their efficient use in the extraction of chemically sensitive active species still remains largely absent. Thus, the implementation of emulsions with intrinsically large surface area is highly advantageous for the tailored development of IL-based extraction system. [416, 417] These formulated emulsions must be able to remain stable against coarsening via Ostwald ripening while maintaining the ability to demulsify in order to obtain the extracted product absorbed into the IL-phase. The task to form IL-water emulsions is challenging due to low interfacial tension derived from the inherently large miscibility of the two phases along with the highly structured IL-water interfaces resultant of charge hydration and correlations. [418, 419]

Traditionally, surfactants have taken the spotlight for the preparation of thermodynamically stable IL-water microemulsions. However, for the design of selective extraction processes, most of the desired requirements are not met due to the inherent water solubility of most ILs leading to Ostwald ripening and ultimately emulsion destabilization. [420, 421] The employment of surfactants may also interact adversely with a variety of biomolecules inducing irreversible changes to the targeted bioproducts, especially for

the extraction of compounds such as lipids, [422, 423] organic acid, [424, 425] and amphiphilic proteins from biological fluids. [426-428] Meeting these requirements to develop a robust approach to create IL-in-water emulsions is highly sought-after for the advancement of IL-based extraction applications. Particle-stabilized emulsions, also referred to as Pickering emulsions, [231] are surfactant-free metastable dispersions of two non-miscible fluids like oil and water. These emulsions display high stability, which makes them very attractive for storage applications. Recently, there has been growing interest in utilizing soft particles like microgels as emulsifiers for the design of responsive Pickering emulsions, which evolve "on demand" via an external stimulus. [429, 430] While previous works have established the adaptability and versatility of microgel particles in stabilizing oil-water interfaces, the details of its adsorption mechanism at these liquid interfaces and their interfacial packing conformation still remains a matter of much debate. [431-435]

In this work, we demonstrate that soft stimuli-responsive composite microgel particles can be effectively utilized to stabilize IL-water interfaces. The microgel particles that we used in this investigation contain a fluorescent polystyrene core embedded in a thermosensitive and pH-responsive gel-shell composed of poly(N-isopropylacrylamide-co-acrylic acid). The rationale behind the design of the particle system is that it allows for non-invasive in-situ visualization of the structure of microgel-laden IL-water interfaces, while preserving their interfacial and multi-responsive properties. We investigate the impact of the microgel particles' charge and hydrophobicity with their emulsification performance by varying solution temperature and pH. The morphology of the adsorbed soft gel-particles is characterized via direct macroscopic visualization, confocal microscopy

observations, and cryo-SEM studies of the droplet interfaces. To determine the main structural parameters of these colloidal lattices, we have constructed Vornoi diagrams and statistically analyzed the defect number, concentration, and configuration in the light of various possible scenarios for the adsorption mechanism of prepared particles at the interface. Moreover, the self-assembled and densely packed layer of composite microgel particles at the IL-water interface does not hinder their potential application in IL-based extraction processes, as the interface remains permeable.

2. Experimental Section

2.1 Materials

For the composite microgel particle synthesis, co-monomers N-isopropylacrylamide (NIPAm, Acros), acrylic acid (AAc, Sigma-Aldrich), styrene monomer (99.9%, Sigma-Aldrich), cross-linking regent N,N'-methylene-bis-acrylamide (MBAm, MP), initiator potassium persulfate (KPS, Acros) were all used in the polymerization without further purification. Laboratory grade ionic liquid 1-butyl-3-methylimidazolium bis(trifluoromethanesulfonyl)imide ([BMIM][NTf_2], ≥99%, IoLiTec Inc.), water (HPLC grade, Fisher Scientific), and fluorescent dyes Pyrromethene 556 (PM-556, Exciton) and Rhodamine B (>98.0%, TCI America) were also used as received.

2.2 Composite Microgel Particle Synthesis

Composite gel-particles are prepared in a two-step procedure. Firstly, a fluorescent polystyrene core is synthesized through emulsion polymerization. This synthesis was carried out in a 3-necked (250 mL) round bottom reaction vessel along with 150 mL of

water, fitted with a reflux condenser, a magnetic stirrer, a thermocouple and a nitrogen inlet. Overall, the concentrations of styrene monomers in the reaction mixtures were controlled at 90.19±0.37 mol% while the NIPAm monomers were adjusted to be 9.79±0.21 mol%. The concentrations of PM-556 and initiator in the reaction mixtures were kept at 0.02-0.04 mol% and 0.08-1.2 mol%, respectively. In a separate vial, the free-radical initiator KPS was dissolved in 5 g water. This initiator solution was slowly added after the monomer mixture was immersed in a water bath set at 70 °C and purged with nitrogen for 45 minutes. The synthesis was left to proceed under nitrogen gas for 8 hours. After reaction was complete, the mixture was then allowed to cool to room temperature and was subsequently purified against deionized water via centrifugation (Eppendorf 5810-R), followed by decantation and re-dispersion in fresh water solvent at room temperature. Secondly, a non-fluorescent environmentally-responsive microgel shell is grown around the previously synthesized core via free radical precipitation copolymerization. This synthesis was carried out in a 3-necked (125 mL) round bottom reaction vessel, fitted with a reflux condenser, a magnetic stirrer, a thermocouple and a nitrogen inlet. Typically, 40.5±0.11 mol% NIPAm monomer, 58.42±0.14 mol% AAc monomers, and 1.15±0.08 mol% MBAm, were added into the reaction vessel along with 100 g of water and ~0.2 g (determined via freeze-drying) of the fluorescent core. In a separate vial, a varying amount of KPS was dissolved in 2 g water. Then, the monomer solution was immersed in a water bath set at 75 °C. The reaction mixture was purged with nitrogen for 45 min. After the temperature reached equilibrium and the purge stage was complete, the initiator solution was introduced. The polymerization reaction was left to proceed while being purged by nitrogen gas for 5 hours. After polymerization was complete, the particle dis-

persion was then allowed to cool to room temperature and was subsequently dialyzed (Spectra/Por Membrane, MWCO: 12-13 kD) against deionized water changed daily for one week at room temperature to remove any residual monomers from the resulting reaction mixture.

2.3 Preparation of IL-in-Water Droplets Stabilized by Composite Microgel Particles

Stock solutions of prepared microgel particles at the desired solid content were prepared via dilution. When required, the pH was adjusted via the gradual addition of 0.1 M HCl or KOH. The background electrolyte added was 10 mM KCl. In a typical batch, the composite particle-stabilized IL droplets were prepared using an ultrasonic processor, Ultra Turrax T25, at constant speed (8500 rpm), sonicating the dispersion of composite microgel particles in water with [BMIM][NTf_2] (weight ratio 8:2) for 45 seconds at room temperature. The total weight of each dispersion was ~5 g. Moreover, facile dilution tests and visual inspections of the creaming or sedimentation behavior due to the density mismatch between IL and water were applied. Prior to qualifications all dispersions were left to equilibrate overnight at room temperature.

2.4 Characterization

The mean hydrodynamic diameter and electrophoretic mobility of the prepared particles were determined via dynamic light scattering (DLS) and electrophoretic light scattering techniques using PSS NICOMP 380 ZLS. Scanning electron microscopy (SEM) images of the synthesized fluorescently-labeled core particles were obtained using FEI/Philips XL30 Environmental FEG SEM. The interfacial colloidal arrangement was imaged using a confocal laser-scanning microscope Leica TCS SP5 under controlled temperature conditions. The fluorescence intensity spectra were acquired via a wave-

length scan over the range of 500-599 nm for the composite microgel particles and dye adsorption under excitation at 488 nm. The spectra for the aqueous phases after the emulsification were obtained under the same laser intensity and at nearly the same depth within the prepared samples. The particle coordinate center positions, the fast Fourier transform (FFT) pattern, and the Voronoi diagrams were analyzed and constructed via ImageJ and Fiji software.

The cryo-SEM experiments were conducted using FEI Nova 200 Focused Ion Beam and SEM equipped with Gatan Alto 2500 cryogenic cooling stage and vacuum transfer chamber. About 0.5 μL drop of the dispersion was placed on top of a 1 mm diameter copper cylinder that was mounted to the cryo-shuttle that was attached to the end of the transfer rod. The whole assembly was plunge frozen in liquid nitrogen slush, which was made by partially evacuating a chamber with liquid nitrogen. The sample was held in the liquid nitrogen slush until bubbling around the rod ceased (about 30 s). Subsequently, the freezing chamber was evacuated and sample was moved to the cooled and evacuated transfer chamber. To reveal inside of the IL-in-water droplet, the top of the frozen droplet kept at about -140 to -160°C was fractured off using a cooled blade. To provide a better view of microgel particles at the drop-water interface, a layer of water was selectively sublimated by raising temperature of the sample within the evacuated transfer chamber to -90°C for 30 minutes. Afterwards, the sample temperature was again decreased to -140 to -160°C and sample was in situ sputtered coated with a thin grounding gold-palladium layer. The grounded samples were transferred to the cooling stage mounted within the SEM chamber and kept at -140 to -160°C for the remainder of the experiment. SEM im-

aging was performed with energy of 2 to 5 keV and current of 0.21 to 0.4 nA with a working distance of 5 mm.

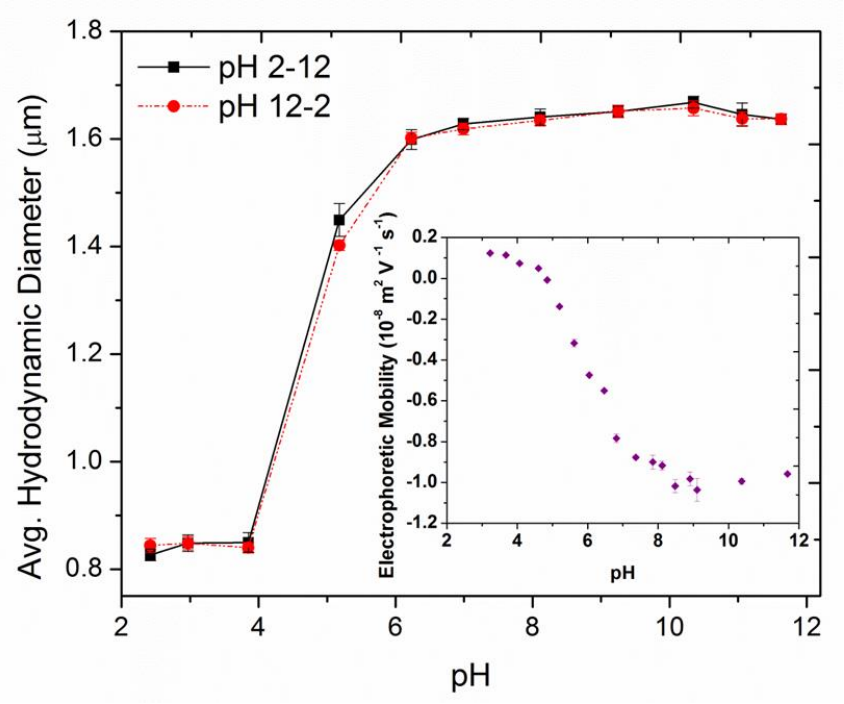

Figure D1. Illustrates the pH dependence of the average hydrodynamic diameter of the composite microgel particles in an aqueous dispersion at room temperature. Inset: displays the pH dependence of the electrophoretic mobility of the prepared particles.

3. Results and Discussion

3.1 Synthesis and Characterization of Composite Microgel Particles

To verify the environmental-responsiveness of the prepared composite particles, the average hydrodynamic diameter of these particles as a function of both pH and temperature was characterized via dynamic light scattering. Figure D1 illustrates that at room temperature, the size of the composite microgel particles swell continuously from pH 4 to

higher pH values. This steep swelling transition originates from the deprotonation of the residual carboxyl groups distributed within the gel network of the composite shell. As expected, at pH values less than 4 (pka of AAc polymer is 4.25[436]), the prepared composite particles are largely uncharged as an equilibrium size of the particles is set through the intricate balance among the elasticity of the crosslinked gel-network and the internal osmotic pressure of the hydrated acrylic acid monomers. [220, 437]

On the other hand, at pH values greater than 4 the electrostatic repulsion generated between the negatively charged carboxylic groups leads to an increase in the hydrophilicity among the gel network in turn triggering the prepared composite particles to be capable of uptaking larger amounts of polar solvent [438] and a larger equilibrium hydrodynamic size results. The correspondingly electrophoretic mobility results were also obtained to illustrate the charging of the composite microgel particles as residual carboxyl moieties are ionized at higher pH, shown in the inset of Figure D1. We also investigated the temperature-induced phase transition of composite microgel particle systems. For neutrally charged composite particles, at pH 3, we found a volume phase transition temperature (VPTT) of 33 °C, which shifts to a higher temperature and broadens by increasing the pH as demonstrated at pH 10 in Figure D2. These characterization measurements indicate the incorporation of a fluorescent polystyrene core does not alter the environmentally responsiveness of the prepared composite gel-particles.

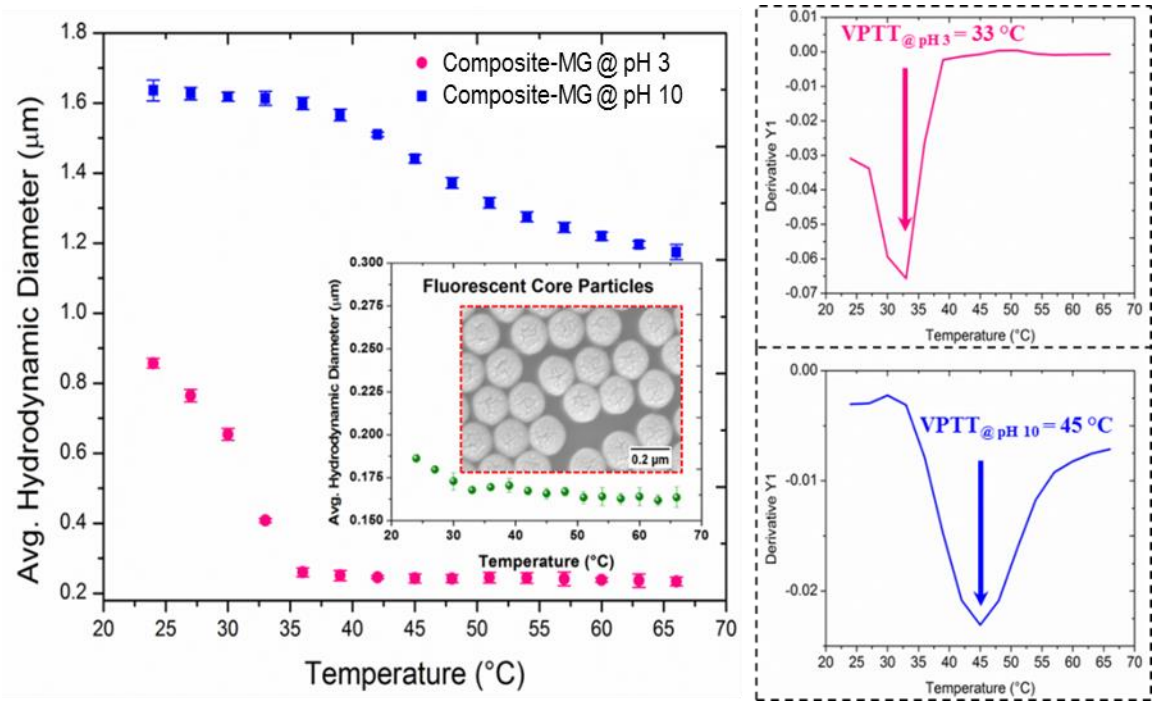

Figure D2. Temperature dependence of the average hydrodynamic diameter of the composite microgel particles measured at pH 3 and pH 10. Leftmost inset: shows the SEM image of dried fluorescent core particles along with the average hydrodynamic diameter of those particles as a function of temperature. Right insets: the thermally induced VPTT is defined as the temperature which the first derivative of the mean hydrodynamic diameter versus the temperature curve reaches a minimum value.

3.2 Structure of Colloidal Lattices at IL-water Interfaces

Figure D3a-d shows representative confocal microscope images obtained at under high magnification of IL-in-water droplets stabilized by the composite microgel particles at various pH and temperatures. We observed that the surface coverage is quite high and that the interface appears highly fluorescent presence of the particles at the interfaces. In addition, under confocal microscopy, the imaged microdomains of the droplets show that the adsorbed microgel particles appear not to be in close contact, however, through opti-

cal microscopy they are closely packed. This observation of inhomogeneous spatial distribution of the fluorescent intensities is evident of integration of fluorescently-labeled cores within the composite particles which allows accurate detection of the particle center-of-mass. Clearly, the composite microgel particles are able to adsorb and effectively stabilize the IL-water interface While the mechanism with which microgel particles adsorb remains uncertain, it has been established that it is different from classical Pickering stabilization, and embodies features of both particle-like anchoring and polymer-like adsorption, as explained by Lyon and Fernandez-Nieves in a thorough review of polymer/colloid duality of microgel suspensions. [439] While we observe adsorption of our soft microgel particles at the investigated IL-water interfaces, in more conventional Pickering emulsion schemes with for solid colloid particles, fine-tuning of the chemistry is required. This is achieved by altering the hydrophobicity, the charge density, or the surface functional groups.

Figure D3a represents confocal microscope images of the colloidal lattice at pH 3 at 24 °C. The inset FFTs of the images show six distinct first-order peaks with multiple higher-ordered reflections. This pattern is similar to those observed on polystyrene-polyvinylpyridine block copolymer films with very ordered colloidal lattice and can be interpreted as an indication of the close-packed-ordered structure. [440, 441] Moreover, the colloidal microgel particles within the lattice oscillate around their equilibrium positions, hypothesized as the result of constrained motion due to the underlying lattice constraint and thermal fluctuation. Figure D3b illustrates representative confocal microscope images of the colloidal lattice at pH 10 at 24 °C. The FTTs display a diffuse ring, which is similarly observed on poly(dimethylsiloxane)-in-water Pickering emulsions containing

sulfate-treated and aldehyde-sulfate-treated polystyrene particles when assembled into less ordered microdomains and was inferred to the presence of a large fraction of defects. [442] From the FFT analysis and the visual inspection, the colloidal lattices of the prepared pH 10 samples is less ordered than the pH 3 samples at these varying temperatures.

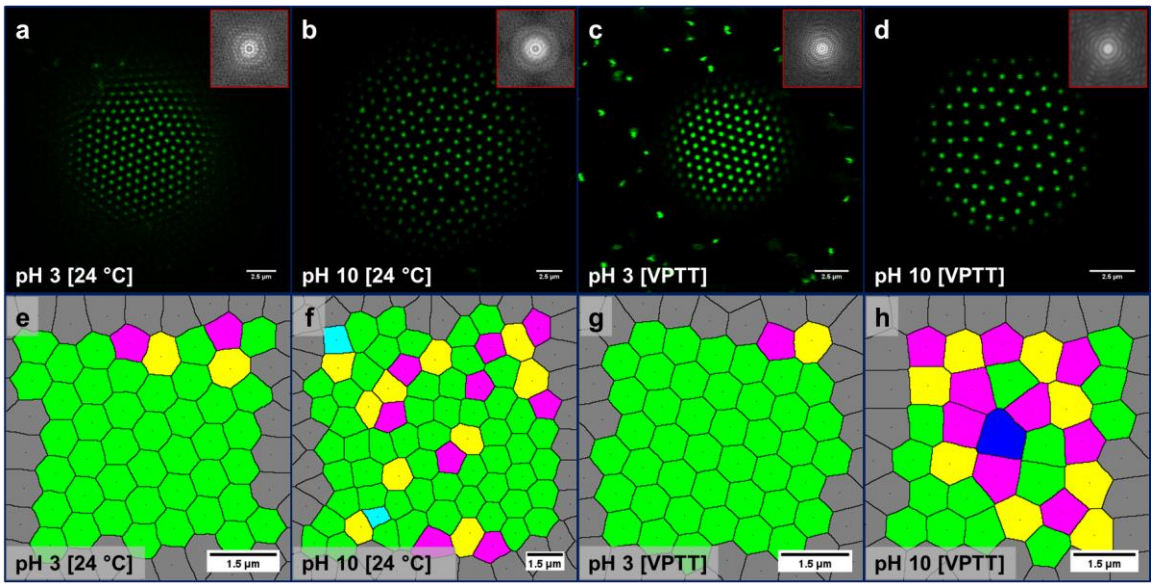

Figure D3. The top row illustrates confocal microscope images of colloidal lattices (a-d) at droplet surfaces at varying pH and temperatures. The insets show the FFT of the associated confocal microscope images. The bottom row shows the constructed Voroni diagrams of the colloidal lattices at the droplet surfaces (e-h) at varying pH and temperatures. In e-h, the cyan, magenta, lime green, yellow and blue fills represent, fourfold, fivefold, sixfold, sevenfold, and eightfold sites, respectively; the gray fills represent incomplete cells at the edge of the lattice and were not taken into account during data analyses.

The differences in the colloidal lattice organizations are postulated to be due to the effect of surface charge of the microgel particles at the IL-water interfaces. At pH 3,

the particles are neutrally charged and thus oscillate around their equilibrium positions in an ordered, closely-packed lattice. In contrast, at pH 10, where the carboxyl groups of the AAc moieties are fully ionized, the prepared particles carry a net negative charge thus oscillate outside the equilibrium positions seen within the formed lattice at pH 3, which are additionally spread further apart, influenced by strong interparticle electrostatic repulsion. Remarkably, upon elevating the temperature to their respective VPTT, the caliber of colloidal lattice organization was visually maintained at both pH 3 and 10, illustrated in Figure D3c and 3d.

To further characterize the structure of these colloidal lattices, we have constructed Voroni diagrams and evaluated the defect number and configurations. Voroni diagrams divide the space into polygons with shared sides having equal distances to the two adjacent particle center locations. [443] For this study, they were constructed via the particle centers in snapshots of the confocal microscope images to assist in visualizing lattice topology. Please note, the number of polygon sides reflects the coordination number of a particle, in turn yielding the number of nearest neighbors. [444] For an ideal triangular lattice, all particles should have a coordination number of 6. Fourfold, fivefold, sevenfold, and eightfold coordinated sites observed in this investigation are defined as defects, akin to previous defect analyses focused on experimentally observed colloidal lattices in our previous work. [442] Figure D3e-h, shows the color-coded Voronoi diagrams of the IL-in-water Pickering emulsion droplets containing the prepared composite microgel particles at various pH and temperatures. The distorted hexagonal cells designate low local hexagonal symmetry of the lattice. In fact, organized semi-perfect hexagonal symmetry was more readily observed in the droplets stabilized by the microgel particles at pH 3.

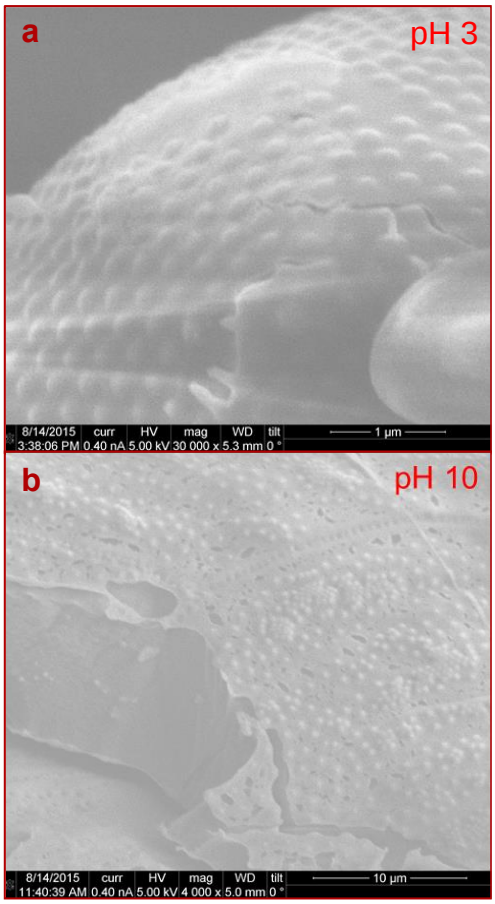

Figure D4. Cryo-SEM images of the interface of IL-in-Water droplets covered by composite microgel particles at pH 3 (a) and pH 10 (b) after sublimation.

This is hypothesized to be a result of localized minimum oscillation of these particles, displayed in Figure D3e and 3g. The number of defect sites was more prevalent at pH 10 where the continuous oscillation was augmented via electrostatic repulsion, shown in Figure D3f and 3h. Upon rapid tuning of the pH, either from pH 3 to pH 10 or vice versa, no variation in dispersion stability is detected. However, colloidal packing pattern changes are observed. Upon increasing the temperature to the VPTT, for the pH 3 particle packing, no changes in the lattice structure were observed from an analysis of the Voronoi diagrams. For the pH 10, there was an increase in the defects observed, which is like-

ly due to increased Brownian motion as there is space between the particle for some freedom of motion.

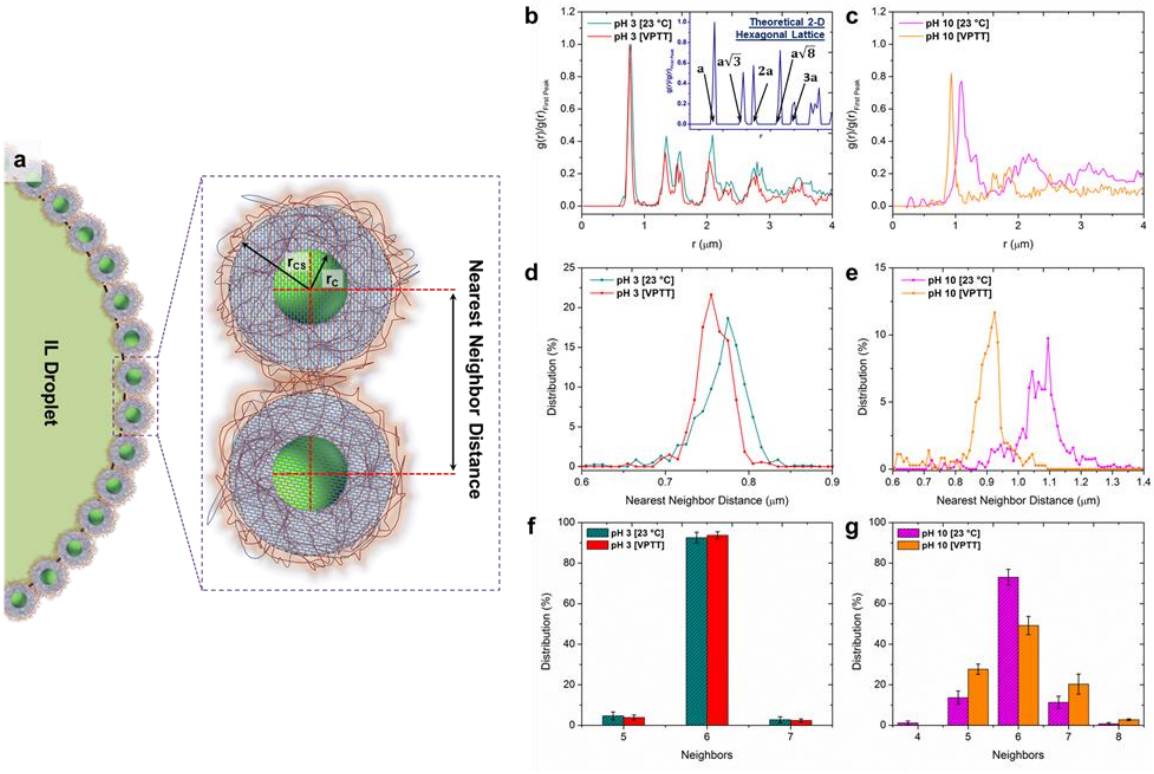

Figure D5. Influence of pH on the interfacial assembly of the composite microgel particles at varying temperatures is as follows: scheme illustrates the particle arrangement at the interface and the nearest neighboring distance (a), normalized pair correlation function $g(r)/g(r)_{\text{First Peak}}$ at pH 3 (b) and pH 10 (c), histograms of nearest neighbor distance on the colloidal lattices at pH 3 (d) and pH 10 (e), the bar charts represent the distribution of four-to-eight-sided polygons in the colloidal lattices at pH 3 (f) and pH 10 (g). All analysis was derived from the Voronoi diagrams of twenty different droplets. Inset: shows the normalized pair correlation function $g(r)/g(r)_{\text{First Peak}}$ of a theoretical 2-D hexagonal packed lattice.

Additionally, Cryo-SEM imaging was utilized to capture the surface topography of these droplets prepared at pH 3 and pH 10, shown in Figure D4. As the micrographs suggest, self-assembly of the swollen microgel particles at the IL-water interface under these conditions leads to distinctive densely packed coverage of the IL droplets with the stabilizing composite microgel particles.

To quantify the impact of pH and temperature on the interfacial packing, we carried out additional in-situ interfacial structural analysis through a non-invasive visual inspection. In contrast, previous studies required sample treatments such as vitrification and freeze-fracturing for these same analyses. [445-447] By the in-situ methods, we have confirmed that there is an increase in the interparticle separation distance (defined also as the nearest neighbor distance, shown in Figure D5a scheme) upon increasing pH. To evaluate this, the normalized radial distribution functions of the composite microgel particle positions g(r) were generated from twenty different droplets. As expected, the colloidal lattice structure at pH 3 demonstrated the distinctive pattern for 2-D hexagonal packing, with characteristic peaks at a, $a\sqrt{3}$, $2a$, $a\sqrt{8}$, and $3a$, where a is the nearest neighboring distance, shown in Figure D5b. In contrast, at pH 10, we assessed more disorder in the characteristic peaks, which denotes a more random packing-structure. In addition, upon increasing the pH to 10, the interparticle distances increase as evidenced from the corresponding peak shift to larger values of r. To characterize the colloidal lattice packing organization and particle spread at the interface, we normalized g(r) with the average hydrodynamic diameter, Dh, of the prepared particle dispersion of the same pH via dynamic light scattering. This method collapses the nearest-neighbor peaks of all pair correlation functions into a single peak at a normalized distance r/Dh ~0.95 and r/Dh

~0.66 at room temperature for pH 3 and 10, respectively. These ratios suggest that our composite microgels shrink when adsorbed at the IL-water interface.

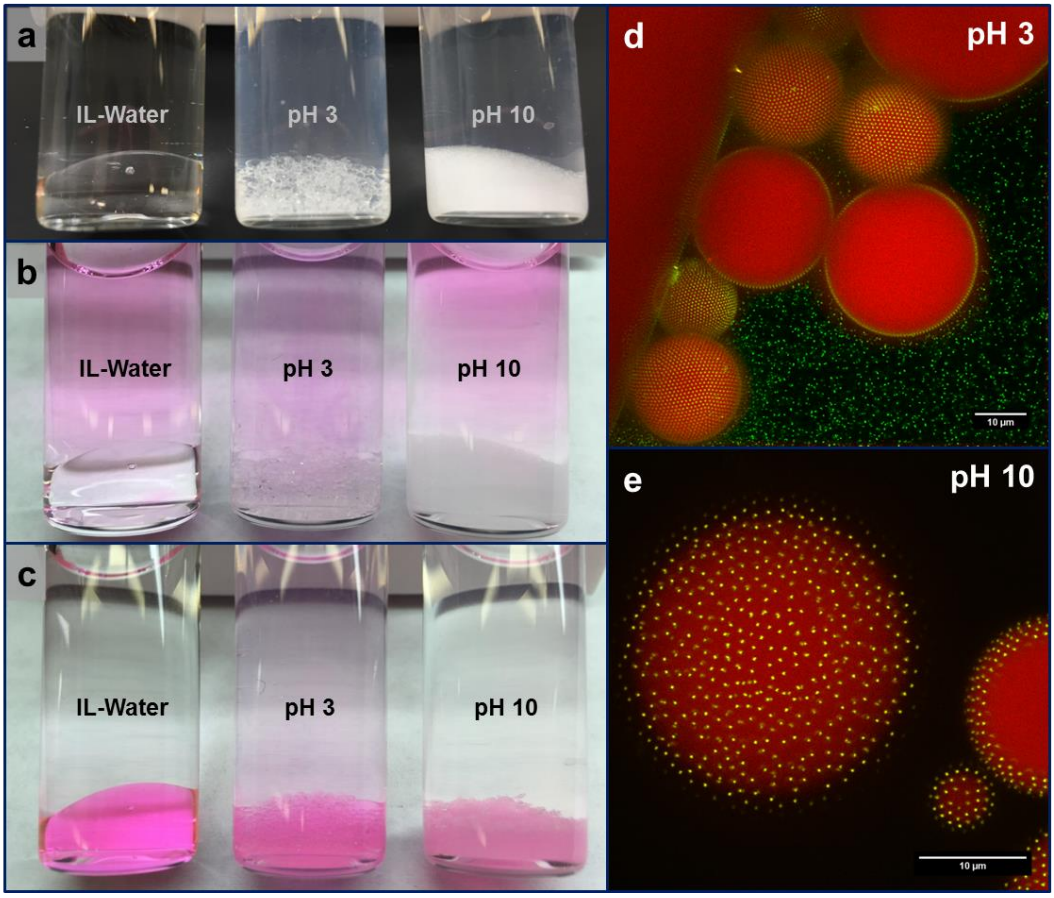

Figure D6. Macroscopic pictures of IL-in-water and IL-in-water droplets stabilized with composite microgel particles at pH 3 and pH 10 (a), immediately after the addition of 0.02 mM Rhodamine B (b) and upon pigment diffusion into the IL (c). 3-D Stacked confocal microcopy images of the successful diffusion of Rhodamine B into the IL-in-water droplets at pH 3 (d) and pH 10 (e); the IL is colored red and the composite particles are yellow-green.

Prior studies have demonstrated that microgel particles can spread, remain un-deformed, or shrink, at an oil-in-water interface reliant on a variety of factors such as interfacial ten-

sion, [448, 449] shear history, [450, 451] particle size, [221, 452] and charge density. [453] Please note that previous observation for homogenous microgel particles are made with potentially invasive techniques in which the sample, containing thermo-responsive particles, is first cooled and then freeze-fractured, while our observations are made in-situ. Others have investigated the packing of similar core-shell particles, with a silica core, using scanning force microscopy. In this case, the imaging occurs under artificial conditions, requiring drying of the sample inducing changes to the surface structure.

To investigate the effect of temperature on interfacial structure, we introduced in-situ localized heating during confocal microscopy imaging. The histograms of nearest neighboring distance of over 400 counts in approximately twenty droplets for each system at room and elevated temperatures are shown in Figure D5d and 5e. It appears that the colloidal lattices at pH 10 have a wider particle spacing distribution than the studied colloidal lattices at pH 3, prior to heating and after heating to the VPTT. The distribution histograms of the pH 3 systems show similar peak width, while the histograms of the pH 10 system demonstrate a much broader peak. When we focus on the increased temperature effect of both systems and sort the nearest neighboring distance, we find that on the same droplet the interparticle distance between adjacent composite microgel particles at pH 3 and pH 10 are always larger at room temperature than at their respective VPTT. To further elucidate the effect of temperature on the lattice structure, we present a bar chart of the counts (distribution %) of the number of nearest neighbors for the adsorbed composite microgel particles for pH 3 and 10 at both room and elevated temperatures. Interestingly, the distribution of the number of neighbors was not impacted by increasing the temperature for both systems, as depicted in Figure D5f and 5g. Upon increasing the

temperature to the VPTT, there was an in-situ decrease in droplet size, and the interparticle distance between adjacent adsorbed particles reduced without changes in organization of the colloidal lattice. However, when we later heated both systems significantly over the VPTT (~70 °C), the dispersion became unstable and effectively de-mixed to two macroscopic phases. Upon increasing the temperature substantially higher than the VPTT for both of the microgel particle stabilized droplets, the particles deswell and become adhesive. While this thermo-induced destabilization mechanism remains undefined, we tentatively postulate the following: the surface coverage decreases and the two interfaces, divided by a thin film of water, become attractive. This attraction removes both the thermodynamic and kinetic barriers inhibiting coalescence, akin to the studies conducted for microgel particle behavior at the oil-in-water interface.

After extensive study of these pH- and temperature-responsive IL-water interfaces, we sought to develop a robust approach for the advancement of IL-based extraction applications. A significant requirement for extraction is that the interface between IL and water remains permeable. To investigate this, we add fluorescent dye, rhodamine B, to the water phase of the samples containing the IL-in-water droplets stabilized with prepared microgel particles illustrated in Figure D6. Immediately upon the addition of the dye, the pigment is found in the IL phase (Fig. 6c). To better visualize the uptake of small molecules across a microgel-laden interface for both pH systems, we utilized confocal microscopy at room temperature. Intriguingly, we found that all of the dye is located in the IL droplets and none remains in the water phase (Fig. 6d and 6e). This shows that despite the densely packed interface, small molecules can easily permeate across the porous adsorbed gel-particle layer.

4. Conclusion

In this study, we report the self-assembly of composite microgel particles at IL-water interfaces. When spontaneously adsorbed at the liquid-liquid interface, these soft and environmentally responsive particles display an interesting duality in their interfacial behavior attributed to both a Pickering-like anchoring and a polymer-like adsorption. The incorporation of a fluorescently labeled core into the microgel particle allows non-invasive and in-situ visualization of an unanticipated correlation between the gel-stabilizer's charge and interfacial colloidal lattice packing in response to external stimuli such as pH and temperature. Moreover, destabilization can be triggered at high solution temperature, due to the removal of both the kinetic and thermodynamic barriers preventing coalescence. Additionally, we demonstrated the densely packed layer of gel-particles remains permeable at the IL-water interface for absorption of active species. Thus, through the utilization of stimuli-responsive microgel particles as emulsifiers we are able to create highly tunable systems, which may open up novel extraction applications.

5. Acknowledgements

We are grateful for financial support provided by the Gulf of Mexico Research Initiative (GoMRI), specifically from the Science and Technology of Dispersants as Relevant to Deep Sea Oil Releases Consortium led by Dr. Vijay T. John. We acknowledge the use of facilities within the LeRoy Eyring Center for Solid State Science at Arizona State University.